TECHNIQUES FOR FABRICATING INTEGRATED OPTICAL COMPONENTS ON LITHIUM NIOBATE

A Thesis

Submitted to the Faculty of Engineering

of the University of Glasgow

for the degree of

Doctor of Philosophy

by

Alan C.G. Nutt, B.Sc.(Eng.)

October 1985

DEDICATED TO MY WIFE, ROSANNE

ACKNOWLEDGMENTS

I would like to thank Professor J. Lamb for his interest in this project as well as the provision of research facilities in the Department of Electronics and Electrical Engineering.

I am greatly indebted to Professor P.J.R. Laybourn for many fruitful discussions and his skilful supervision of this work and to Dr. R.M. DeLaRue for his help and enthusiasm as well as his assistance in making available many of the materials analysis techniques in the proton exchange research.

I am greatly indebted to Barr & Stroud Ltd and to the S.E.R.C. for the provision of the C.A.S.E. award. I would like to especially thank Dr. I. Andonovic and Dr. N. MacFadyen of the Integrated Optics Section at Barr & Stroud for their interest in the research as well as the provision of all the lithium niobate material used in this work. I would also like to acknowledge helpful discussion with Dr. M.B. Holbrook and Dr. S.P. Beaumont.

I would like to thank our Italian collaborators for the materials analysis processing of the proton exchange layers, and also for the resulting detailed and extremely interesting discussions. (A complete acknowledgment for the above researchers is at the beginning of the relevant text (chapter 6)). I would also like to warmly thank Professor M. Armenise for discussions and in-plane scattering measurements on proton exchanged planar waveguides.

The excellent work of Mr. G. Boyle and Mr. R. Harkins in preparing the photolithographic masks is appreciated as is the end-polishing skilfully carried out by Mr. K. Piecowiak. The photographic work and the preparation of slides by Mr. J. Clark and Mr. K. Melville is also greatly appreciated.

The technical advice and assistance from Mrs. L. Hobbs, Mr. J. Young, Mr. J. Crichton, Mr. H. Anderson and the workers of the mechanical workshop was greatly appreciated.

TABLE OF CONTENTS

SUMMARY

This thesis encompasses the development of a fibre/waveguide coupler using ion milled alignment grooves on lithium niobate and the materials and optical investigation of a novel form of high index waveguide in lithium niobate (called proton exchange, PE).

Systems are discussed for the ion etching of masking layers suitable for Ion Beam Etching (IBE) deep structures in lithium niobate substrates. The parameters discussed are etch rate, anisotropy and mask quality. It was discovered that a 20% solution of polyimide could be spun in even layers to thicknesses of 15µm at a spin speed of 2000 rpm. The polymer layer is delineated, after curing, by a Reactive Ion Etching (RIE) process with oxygen. The RIE process gives a highly anisotropic etch which transfers the pattern on an aluminium masking layer faithfully into the polymer layer. Side-wall ripples in the masking layer were found not to be a function of the RIE process.

Argon IBE of lithium niobate masked with patterned polyimide is examined. The polymer pattern is anisotropically reproduced in the lithium niobate substrate but the 6µm deep slots exhibited side wall ripples of a similar form to that on the masking layer. The etch rate of lithium niobate is typically 500Å/min, however during a process run the etch rate drifts and the final groove depth cannot be defined accurately. Solutions to this problem such as end-point detection are discussed. Redeposition effects are highlighted. The grooves were found to be of suitable quality to be used in a prototype fibre/waveguide coupler.

Problems and loss mechanisms inherent in a fibre/waveguide alignment groove coupler are discussed, specifically scatter losses, alignment losses, a localised Fabry Perot effect, fibre etching, optical field mismatch and component realisation. The component was made and tested at a wavelength of 1.3µm and a net insertion loss of 2.56dB was measured. The insertion loss is split up into the quantifiable constituent losses and loss reduction is discussed.

Optical aspects of planar PE waveguides on X-cut and Z-cut lithium niobate at wavelengths of 633nm and 1152nm are examined. The waveguide refractive index profile is a step with an index change of approximately 0.125 (at 633nm) and 0.096 (at 1152nm) for the extra-ordinary index and -0.04 (at 633nm) for the ordinary index. The exchange parameters (melt temperature and time) and hence waveguide depth is directly related to an Arrhenius type diffusion process and the diffusion coefficients determined. Various optical characteristics of PE waveguides are investigated such as propagation losses, anisotropic light propagation, waveguide stability, surface damage and the evaluation of tapered regions formed for use in hybrid coupling.

Materials analysis techniques have found that the proton depth profile (measured by nuclear reaction techniques), the distorted exchanged region (measured by Rutherford Back Scattering techniques), and optical waveguide depth are all comparable for a given waveguide. It is shown that there is approximately a 70% lithium/proton exchange in the waveguide region although the exchange region cannot be defined thus; $Li_{1-x}H_xNbO_3$. The strains within the lattice are complex and may be related to the high amount of optical scatter. The inter-relationship of the analysis techniques are discussed.

A materials and optical analysis of post-annealed PE waveguides is presented. The annealing properties are considered with respect to initial waveguide depth and annealing parameters (annealing temperature, atmosphere and gas flow rate). The materials analysis pinpoints the probable mechanisms from which waveguide instability occurs and suggests methods of reducing waveguide scatter by reducing strain within the lattice. The modification of the waveguide profile is related to the migration of protons and lithium ions within the lattice.

The findings of this work will be useful in the developement of practical integrated optical couplers and good quality high index waveguides in lithium niobate substrates, which have numerous applications in optical sensor and communication systems.

INTRODUCTION

1.1 General Introduction

The technology of coherent light communication has advanced rapidly over the past fifteen years. Single mode fibre technology has made available large communication bandwidths which are being capitalised upon rapidly [1.1]. Active devices in an optical communication system could be fabricated on or in substrates which possess electro-optic, acousto-optic, magneto-optic or pyroelectric properties. In 1969 Miller proposed a miniature form of laser circuitry which he called integrated optics [1.2]. If the expression integrated optics is to be taken literally, it is desirable to manufacture all the required optical devices on one chip and interface the chip with the communication system (via single-mode fibre). Ferroelectric materials such as lithium niobate (LiNbO$_3$) have special physical properties that make them desirable for both active and passive devices. They possess large electro-optic coefficients, large non-linear optical coefficients and are strongly piezoelectric [1.3]. The main disadvantage of using lithium niobate is that light sources or detectors cannot readily be formed on the substrate. Coupled with this disadvantage, the term 'integrated optics' is somewhat misleading as the bulk of devices and components which come under this term, formed on lithium niobate and on other substrates are discrete [1.4,1.5,1.6]. Therefore two main problems will have to be seriously addressed before the potential of these components is realised and these are device integration (i.e. having more than one device on the same chip) [1.7] and inter-device coupling or device pigtailing [1.8].

1.2 Fibre/Waveguide Coupling

Considering fibre to integrated optical waveguide coupling, the light transfer between the two mediums can be obtained in two

main ways. The first is transverse or evanescent field coupling [1.9] in which the evanescent field from the fibre interacts with, and excites, a guided mode in the waveguide. This effect is usually enhanced with the aid of a taper in the waveguide along the interaction region. This effect, called taper velocity coupling, [1.10,1.11] provides the necessary degree of phase matching between the fibre and the waveguide to allow optimum power transfer. The second method is longitudinal or butt coupling [1.12] in which the optical field emerging from the end of a cleaved fibre is launched into the polished end of the optical waveguide. The spatial matching of the optical fields of the fibre and the waveguide, Fresnel reflection and their longitudinal misalignment are largely responsible for the amount of power transfer between the two lightguides. Of the two coupling methods the one favoured is butt coupling due to its relative simplicity.

In butt coupling the alignment of a single-mode fibre to a single-mode waveguide is a complex procedure as the alignment tolerances are in the submicron scale. A single fibre can be aligned to the polished waveguide end-face by varying their relative positions with micro-manipulators while monitoring and maximising the output [1.13], the fibre can then be bonded to the waveguide. However this process requires a semi-skilled operator and has to be repeated for each fibre to be aligned which multiplies the alignment complexity. The fibre is also only supported at the interface region which makes the bond delicate and unstable. The use of silicon V-grooves substantially overcomes the alignment and support problems [1.14,1.15]. The V-grooves are fabricated so that when fibres are placed in them (after the V-grooves have been aligned to the waveguide) no micro-alignment is needed. For the coupling of fibre arrays this method is far more acceptable than plain butt coupling [1.15]. However the method has problems; the need for accurate and repeatable V-groove etching, accurate alignment of V-grooves to waveguides and the considerable difference in thermal expansion coefficients of lithium niobate and silicon gives rise to undesirable instabilities.

A more attractive arrangement was proposed by Mclachlan et al. [1.16,1.17] making use of ion milled alignment grooves which are positioned on the device substrate surface. The groove is longitudinally positioned to the waveguide and when the fibre is placed in the groove there is no need for extra alignment. The position, depth and quality of the groove control the fibre alignment to the waveguide. There are many possible advantages of this type of coupling component; the alignment groove is in the waveguide substrate surface so thermal expansion should not pose much of a problem, using alignment grooves negates the need for waveguide end-face polishing, the fibre is supported by the base and side walls of the groove so the coupler should be rigid, the grooves are defined by conventional photolithography so any number of grooves can be defined with one process step and if the groove parameters can be suitably controlled then repeatable and high efficiency coupling is expected. The alignment groove coupler will be discussed in the first part of this thesis.

1.3 Proton Exchanged vs. Ti:diffused Waveguides

The most firmly established method of forming waveguides in lithium niobate substrates is the indiffusion of titanium ions [1.16,1.18] and most integrated optical waveguide devices have been fabricated using this technique [1.5,1.6]. However, titanium diffused waveguides have some limitations. Such waveguides are very susceptible to the photorefractive effect (optical damage) [1.19,1.20] and in addition the index change in the waveguiding region is small (in the region of 0.002). Considering device integration, due to the small waveguide index change caused by Ti:diffusion the smallest waveguide bend that can be fabricated has a radius of curvature of 1cm, without making considerable changes to the waveguide structure [1.21,1.22], which makes the true integration of devices more difficult.

In the initial stages of research, work was based on the investigation of the alignment groove fibre/waveguide coupler.
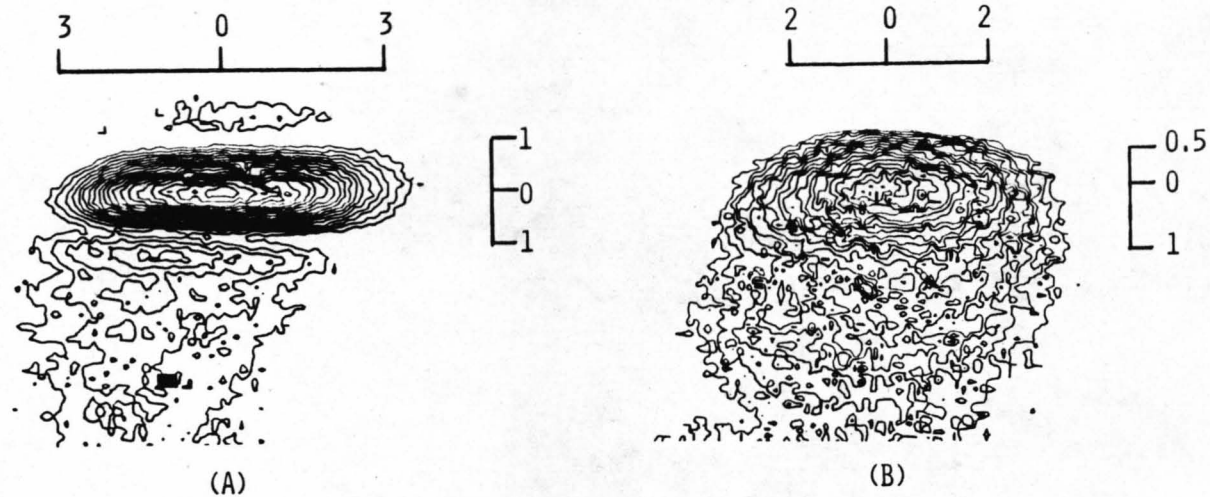
FIELD INTENSITY DISTRIBUTIONS OF X-CUT H$^+$:LiNbO$_3$ STRIPE WAVEGUIDES 0.497 μM (± 0.01) DEEP AND 5 μM WIDE

AT   (A) λ = 0.633 μM

      (B) λ = 1.15 μM

Figure (1.1):

One of the main loss mechanisms in such a component is field mismatch [1.23,1.24]. The problem occurs since the single-mode fibre field profile is symmetric and the Ti:diffused waveguide profile is asymmetric in the axis normal to the surface plane [1.23,1.24]. At this time field profiles were noted which were taken from a novel form of high index waveguide, called proton exchange [1.25] (see figure (1.1)). As can be seen from figure (1.1) the field distribution of a proton exchange channel waveguide has two-fold symmetry and with subsequent optimisation should be much more easily matched to the fibre profile. In single mode operation however the waveguide field profile is much smaller than the fibre profile [1.28]. To make the proton exchange channel waveguide larger without modifying its single mode properties requires a knowledge of the proton exchange process.

Proton exchanged waveguides have an index change in the waveguiding region of approximately 0.12 at a wavelength of 633nm and are very resistant to optical damage [1.26,1.27]. Such waveguides when used in integrated optics could overcome problems which are inherent in Ti:indiffused waveguides.

Because of the possible advantages in fibre/waveguide coupling and in waveguiding properties, the investigation of the optical characteristics of proton exchanged waveguides was undertaken in the second part of this thesis.

This thesis is, as a result of the above, in two experimental parts: firstly considering,

FIBRE TO WAVEGUIDE COUPLER FOR INTEGRATED OPTICS
ON LITHIUM NIOBATE USING ION ETCHING TECHNIQUES

and secondly considering,
PROTON EXCHANGED WAVEGUIDES ON LITHIUM NIOBATE

1.4 Aims of Research Described in this Thesis

1.4.1 Ion Etching for Integrated Optics

The first aim was to find a suitable masking layer and etching
process so that high quality grooves could be etched into lithium
niobate substrates. The grooves ideally had to have smooth side
walls and the process had to be uncomplicated and thus amenable
for industrial implementation.

The second aim was to realise the first alignment groove
fibre/waveguide coupler with a total insertion loss of less than
1dB. The coupler had to be shown to be better than any existing
form of coupling component. It was hoped that the coupler would
be stable, easy to make, suitable for array coupling, and be the
obvious choice for fibre sensor and communication systems.

The third aim was, once the ion etching technique was perfected,
to design and test other components which would benefit from the
delineation possibilities on lithium niobate substrates.

1.4.2 Proton Exchanged Optical Waveguides in Lithium Niobate

The main aim was to investigate the optical characteristics of PE
waveguides on lithium niobate. The work was directed towards
determining whether or not this form of waveguide would be of
practical use in integrated optics. The materials analysis of
such waveguides was initiated in an effort to understand the
process and if any problems arose from the analysis to try to
overcome them. The initial optical and materials analysis would,
by necessity, be done on planar waveguides and if there was time
it was hoped that PE channel waveguides could be fabricated
having field intensity distributions which would match well with
single mode fibres and hence possibly improve the alignment
groove fibre/waveguide coupler.

CHAPTER 1 - REFERENCES

[1.1]   J.E. Midwinter
        Optical Fibre Communications, Present and Future
        The Clifford Paterson Lecture, 1938
        Proc. R. Soc. London, pp1-29, 1984

[1.2]   S.E. Miller
        Integrated Optics: An Introduction
        Bell Syst. Tech.J., vol 48, No.7, pp2059-2069 Sept 1969

[1.3]   A. Rauber
        The Chemistry and Physics of Lithium Niobate
        Current Topics in Materials Science, vol 1, ch7
        F. Kaldis Ed., 1978

[1.4]   R.C. Alferness
        Waveguide Electro-Optic Modulators
        IEEE Trans. MTT, vol MTT-30, No.8, pp1121-1137,
        8th August 1982

[1.5]   R.C. Alferness
        Guided Wave Devices for Optical Communications
        IEEE J. QE., vol QE-17, No.6, pp946-959, June 1981

[1.6]   D. Botez and G.J. Herskowitz
        Components for Optical Communications Systems: A Review
        Proc. IEEE, vol 68, No.6, pp689-731, June 1980

[1.7]   P.G. Flavin, B.E. Daymond-John, K. Preston, R.C. Booth
        An Approach to $LiNbO_3$ Wafer Scale Integration
        IEEE Int. Workshop on Intgr. Opt. and Related Technol.
        for Sig. Proc., Technical Digest, pp13-16, Sept. 1984
        Florence Italy

9

[1.8]   O.G. Ramer, C. Nelson and C. Mohr
Experimental Integrated Optic Circuit Losses and Fiber
Pigtailing of Chips
IEEE J. QE., vol QE-17, No.6, pp970-974, June 1981

[1.9]   H.P. Hsu and A.F. Milton
Single Mode Coupling Between Fibres and Indiffused
Waveguides
IEEE J. QE., vol QE-13, No.4, pp224-233, April 1977

[1.10]   G.Stewart, R.H. Hutchins and P.J.R. Laybourn
Hybrid Integration of Active and Passive Devices
3rd Int. Conf. on Int. Opt. and Opt. Fibre Commun.
San Fransisco, U.S.A., April 1981

[1.11]   G. Stewart and A.C.G. Nutt
Formation and Analysis of Tapers in Proton Exchanged
Lithium Niobate Waveguides
3rd E.C.I.O., Session B: Materials and Fabrication,
pp57-61, Berlin (West), Germany, May 1985

[1.12]   J.C. Campbell
Coupling of Fibre to Ti-diffused $LiNbO_3$ Waveguides
by Butt-Joining
Applied Optics, vol 18, No.12, pp2037-2040, June 1979

[1.13]   R.C. Alferness, V.R. Ramaswamy, S.K. Korotky
M.D. Divino and L.L. Buhl
Efficient Single-Mode Fiber to Titanium Diffused
Lithium Niobate Waveguide Coupling for λ = 1.32um
IEEE J. QE., vol QE-18, No.10, pp1807-1812, Oct. 1982

[1.14]   H.P. Hsu and A.F. Milton
Flip-Chip Approach to Endfire Coupling Between Single-
Mode Fibers and Channel Waveguides
Electron. Lett., vol 12, No.16, pp404-405, Aug 1976

[1.15]   E.J. Murphy and T.C. Rice
          Low-Loss Coupling of Multiple Fiber Arrays to Single
          -Mode Waveguides
          J. Light Tech., vol LT-1, No.3, pp479-482, Sept 1983

[1.16]   A.D. McLachlan
          Ph.D. Thesis, University of Glasgow, 1981

[1.17]   I. Andonovic, M.B. Holbrook and A.D. McLachlan
          End-Fire Coupling Between Optical Fibres and Stripe
          Waveguides
          1st E.C.I.O., pp8-11, London, Sept 1981

[1.18]   W.K. Burns, P.H. Klein, L.E. Plew and E.J. West
          Ti Diffusion in Ti:LiNbO$_3$ Planar and Channel Optical
          Waveguides
          J. Appl. Phys., vol 50, No.10, pp6175-6182, Oct 1982

[1.19]   J.P. Nisius, P. Hertel, E. Kratzig and H. Pape
          Optical Damage Effects in LiNbO$_3$:Ti Waveguides
          Proc. S.P.I.E., vol 480, Integrated Optics III,
          Virginia, April 1983

[1.20]   R.L. Holman and P.J. Cressman
          Optical Damage Resistance of Lithium Niobate Waveguides
          Opt. Engineering, vol 21, pp1025-1032, 1982

[1.21]   W. Doldissen, H. Heidrich and D. Hoffman
          Reduction of Bend Losses in Integrated Optical Devices
          3rd E.C.I.O., pp210-214, Berlin (West), Germany 1985

[1.22]   S.K. Korotky, E.A.J. Marcatili, J.J. Veselka
          R.H. Bosworth
          Greatly Reduced Losses for Small Radius Bends in
          Ti:LiNbO$_3$ Waveguides
          3rd E.C.I.O., pp207-209, Berlin (West), Germany 1985

[1.23]   J. Noda, O. Mikami, M. Minakata and M. Fukuma
          Single—Mode Optical—Waveguide Fiber Coupler
          Applied Optics, vol 17, No.6, pp2092-2096, July 1978

[1.24]   L. McCaughan and E.J. Murphy
          Influence of Temperature and Initial Titanium
          Dimensions on Fibre—Ti:LiNbO$_3$ Waveguide Insertion Loss
          IEEE J. QE., vol QE-19, No.2, pp131-135, Feb 1983

[1.25]   J.L. Jackel, C.E. Rice and J.J. Veselka
          Proton Exchange for High Index Waveguides in LiNbO$_3$
          Appl. Phys. Lett., vol 44, No.7, pp607-608, Oct 1982

[1.26]   J.L. Jackel et al.
          Damage Resistant Lithium Niobate Waveguides
          J. Appl. Phys., vol 55, No.£, pp269-270, Oct 1984

[1.27]   R.L. Holman, D. Hicks and J. Busch
          Laser Power Handling and Electro—Optic Preformance of
          Proton Exchanged Lithium Niobate Waveguides
          Proc. S.P.I.E., vol 460, paper No.19, Los Angeles
          California, U.S.A., January 1984

[1.28]   A.C.G. Nutt et al.
          Proton Exchange Lithium Niobate Slab and Stripe
          Waveguides: Characterisation and Comparisons
          2nd E.C.I.O., IEE Conf. Publ. No.227, pp53-56, Oct 1983
          Florence Italy

PART 1

FIBRE TO WAVEGUIDE COUPLER FOR INTEGRATED OPTICS
ON LITHIUM NIOBATE USING ION ETCHING TECHNIQUES

CHAPTER 2

ION ETCHING TECHNIQUES FOR PATTERN DELINEATION

2.1 Introduction

In integrated optical devices and components, a large range of
two and three dimensional structures are used to facilitate the
many and varied system requirements. Although many of the thin
film layers on lithium niobate substrates may be amenable to wet
chemical etching [2.1], lithium niobate itself is not
[2.1,2.2,2.3]. Therefore, ion etching techniques ('dry etching')
must be used to pattern the lithium niobate substrate and/or
surface layers. Ion etching techniques also allow a high degree
of directionality (anisotropy) in the etch depending on the
process chosen.

Assuming a high quality etch process can be evolved, many
components would benefit from ion etching flexibility.
Components and processes which would (and to some extent do)
benefit from various forms of ion etching techniques include
alignment grooves in lithium niobate for fibre/waveguide coupling
[2.4,2.29], integrated optical reflectors [2.5,2.6], Bragg
reflectors and beam deflectors[2.7,2.15], optical light isolators
[2.8], rib waveguides [2.9,2.10], etched slots for deposited
silica guides [2.11], acoustic Bragg gratings [2.12], polarisers
[2.13], delineation of titanium stripes for channel waveguides
[2.14] and the formation of high aspect ratio masking layers or
structures [2.23]. Dry etching is also much more amenable to
industrial implementation and although the process can be
physical and/or reactive the direction of the etch does not
depend on crystal orientation (although the etch rate may).

This chapter is concerned with the definition of various ion
etching techniques, so that the advantages and disadvantages of
each process are acknowledged. The chapter is intended as an
introduction to chapter 3 where the processes will be discussed

for the specific task of delineating patterns in lithium niobate substrates.

2.2 Plasma Etching (PlE)

Plasma etching [2.16,2.17,2.18] is a mainly chemical technique and involves the creation of a glow discharge to generate chemically reactive species by dissociating relatively inert molecular gases, for example;

$$CF_4 + e^- -> CF_3 + F + 2e^-$$

or
$$O_2 + e^- -> O + O + e^-$$
$$or \quad -> O^- + O$$
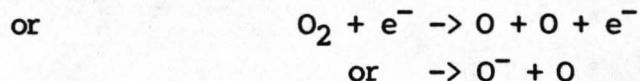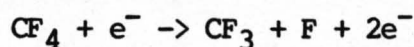
The products react chemically with the surfaces immersed in the discharge and if the by-products of the reaction are volatile, the pumping system removes them and fast etching is achieved. The plasma etching systems used are of two different configurations. One is a barrel plasma etching system (figure (2.1)) and the other is a parallel plate system (see figure (2.2)). In both systems electrodes are energised at high frequency at about 187kHz (in the case of the Electrotech RD600) to produce a chemically active plasma. In the case of the barrel asher the sample is placed centrally in the plasma on a cylindrical sample holder whereas with parallel plate PlE the sample is positioned on one of the plates. Plasma etching with a parallel plate system is also dependent on the pressure at which the system operates. Ideally plasma etching is done at pressures of about 300mTorr or higher in a parallel plate system. Lower pressures, less than 100mTorr, can push the etching process into a physical process by the creation of an ion accelerating 'dark space' [2.16,2.19,] (assuming that the samples are mounted on the cathode where the 'dark space' occurs).

The main drawback with PlE is that it is isotropic - highly unsuitable for pattern delineation which requires high aspect

R.F. COIL

LiNbO$_3$

PLASMA

SAMPLE
BOAT

GAS
INLET

MATCHING NETWORK

R.F. GENERATOR

GAS
OUTLET
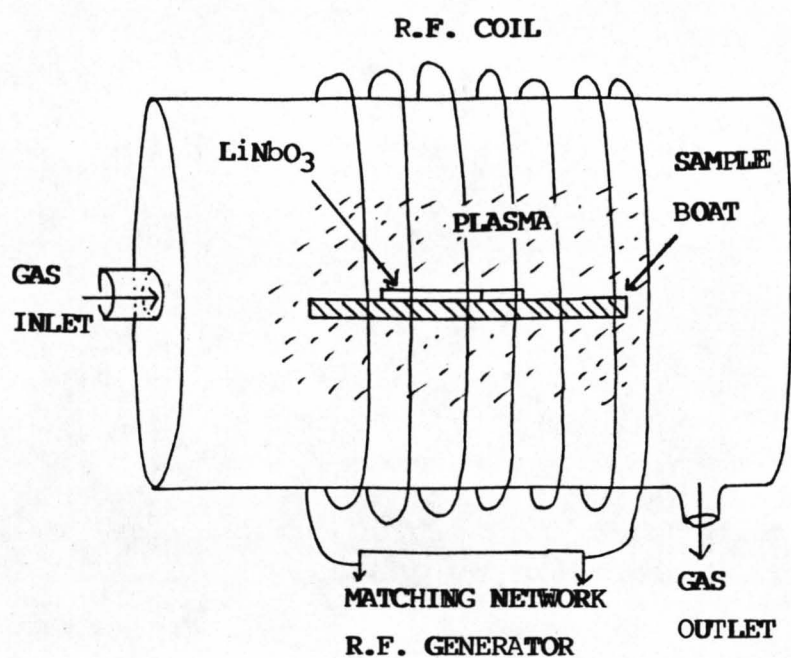
Figure (2.1): Schematic Diagram of Plasma Etching System
(Barrel Asher)
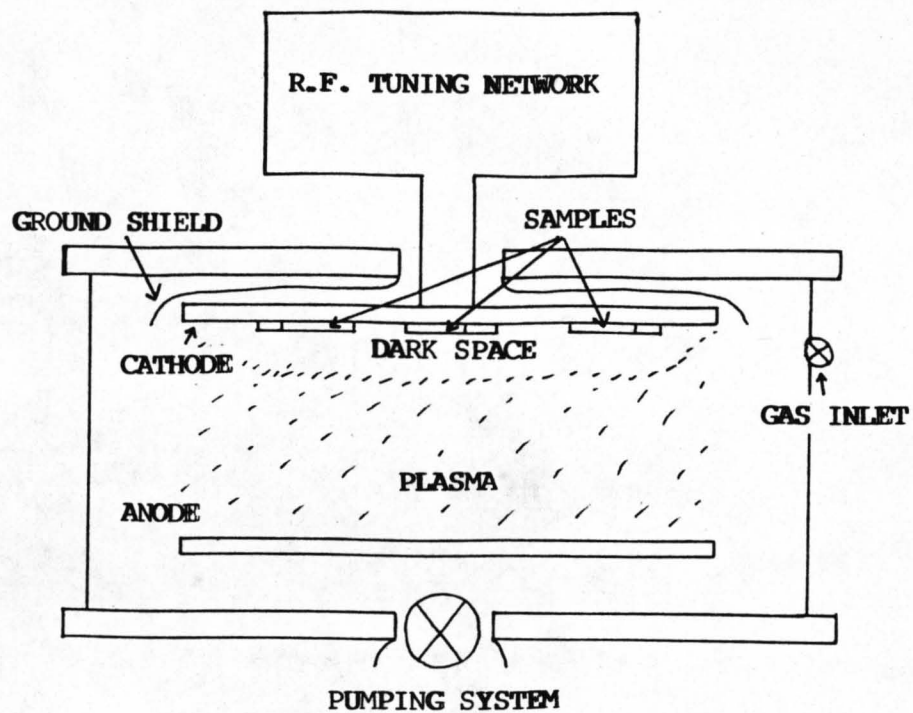
Figure (2.2): Schematic Diagram of a Parallel Plate Etching System. It is Possible to use Both Plasma Etching and Reactive Ion Etching in the System Depending on the Etch Parameters Used.

ratio and/or anisotropic profiles. However it is useful for the wholesale removal or stripping of redundant carbonaceous thin films e.g. photoresist [2.20,2.21].

2.3 Reactive Ion Etching (RIE)

RIE [2.16,2.17,2.18,2.21] is an extension of the purely chemical plasma etching technique. As well as having the work surface immersed in a chemically active plasma RIE incorporates the bombardment of the work surface by energetic ions of the same chemical species. To create the environment in which a RIE process can exist the main requirements are: the existence of a D.C. bias between the parallel plates of a plasma etcher, and the system operating at low pressure. The D.C. bias, which can be created by having the cathode plate smaller than the anode (self-biasing) or the inclusion of a capacitance between parallel plates (see figure (2.2)), creates a dark space (ion sheath) around ths smaller of the parallel plates or the cathode (as defined by the capacitor), through which ions are drawn resulting in physical as well as chemical etching of the work surface. The D.C. bias is wholly across the dark space at the cathode. The dark space is also limited by the ion density which is governed by the system pressure, therefore accurate control of the gas pressure is necessary.

Typical reactive gases used in this process as well as with plasma etching are mixtures of Freon 12, 14 (CCl_2F_2, CF_4), CHF_3, O_2 and Ar.

The advantages of RIE are that the resultant etch is anisotropic, physical (which can be controlled by the D.C. bias), as well as reactive. The main disadvantages of the process are:-

1) the angle of incidence cannot be varied. Since the ion sheath is always parallel and close to the plane of the cathode the ion momentum is normal to the surface.

2) the incident ions have a broad energy spectrum. Low energy ions only heat the sample and do not remove material.

3) atomic collisions in the plasma at the operating pressure (10^{-2} Torr) result in the scattering of impinging ions. The lack of collimation of the beam flux may limit the resolution of the sputter etching mechanism.

2.4 Ion Beam Etching (IBE)

IBE or ion milling is purely a physical sputtering phenomenon. Sputtering occurs when a beam of inert gas ions is directed from an external ion source onto the sample positioned in a high vacuum chamber. The most commonly used ion source in ion milling systems is the Kaufman source [2.24,2.25] (see figure (2.3)). The previous etching processes discussed have relatively simple ion source systems whereas the operation of the Kaufman source is more complex. There are comprehensive papers and books discussing the source operation therefore only a brief system description will be given [2.16,2.17,2.18,2.22, 2.23,2.26].

Inert gases used in IBE are typically nitrogen and in our case argon. The ionisation of Ar does not require a high energy; electrons from the cathode need only attain an energy of about 70eV. A plasma is thus created by the thermal emission of electrons from the cathode which collide with the neutral argon atoms:

$$Ar + e^- \rightarrow Ar^+ + 2e^-$$
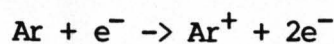
The configuration of the ion source is shown in figure (2.3) and the IBE system in figure (2.4). All electrodes in the ion gun are insulated from each other which allows the independent alteration of any potential in the ion beam source. The system basically consists of two plasma regions, a discharge plasma region, where the ions are generated, and the extraction region,

ROTATION

AXIS

GAS

INLET

BODY

ANODE

CATHODE

MAGNET

PLASMA REGION

SCREEN GRID

ACCELERATOR GRID

NEUTRALISING WIRE

EXTRACTION

REGION
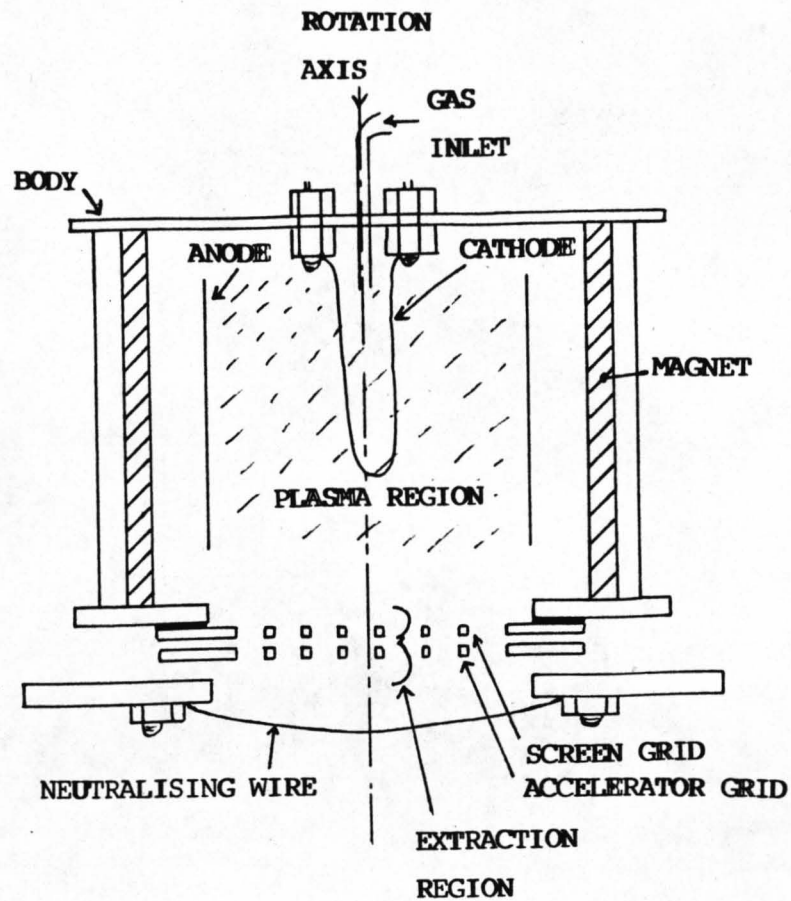
Figure (2.3): Schematic Diagram of a Kaufman Ion Source used for Ion Beam Etching (Ion Milling).

through which the ions are accelerated to form a plasma beam. The cathode potential is typically 30-50V lower than the anode potential, the difference corresponding to the discharge voltage of argon.

The ion energy of the plasma beam is a very important parameter in the sputtering rate. The yield (i.e. the etch rate) being exponentially proportional to the ion energy. To achieve a high energy beam (the Ar ions are assumed to attain the anode potential) the anode potential is increased typically to 950V, thus ensuring high potential ions. The ion (anode) potential with respect to ground (0 volts) is termed V_{net}. The body, screen grid and cathode are held 30-50 volts below V_{net} at about 900V to maintain the discharge potential. The source and plasma now therefore float at about 950 volts.

The accelerator grid is set to a negative potential, V_a, (about -350V w.r.t. ground). From the potential diagram in figure (2.5) it can be seen that the magnitude of V_a plus V_{net} forms the accelerating potential V_{tot};

$$V_{tot} = V_{net} + V_a$$

The ions are accelerated from the screen grid towards the accelerator grid forming a high energy beam, translating their potential energy to kinetic energy. Some of the ions strike the accelerator grid forming a small current (accelerator current) and the remainder pass through the grid, their velocity maintaining their direction away from the source. Targets in the direct line of the ion beam will therefore be bombarded. Thus targets must be grounded so as to inhibit the build-up of surface charge which would deflect the ion beam.

The neutraliser or immersion wire creates a 'sea of electrons' through which the positive beam of argon ions pass. The negative aura ensures minimal beam divergence which would otherwise be prevalent due to electrostatic repulsion of like ionic charges. The electrons also aid the charge neutrality of the target which
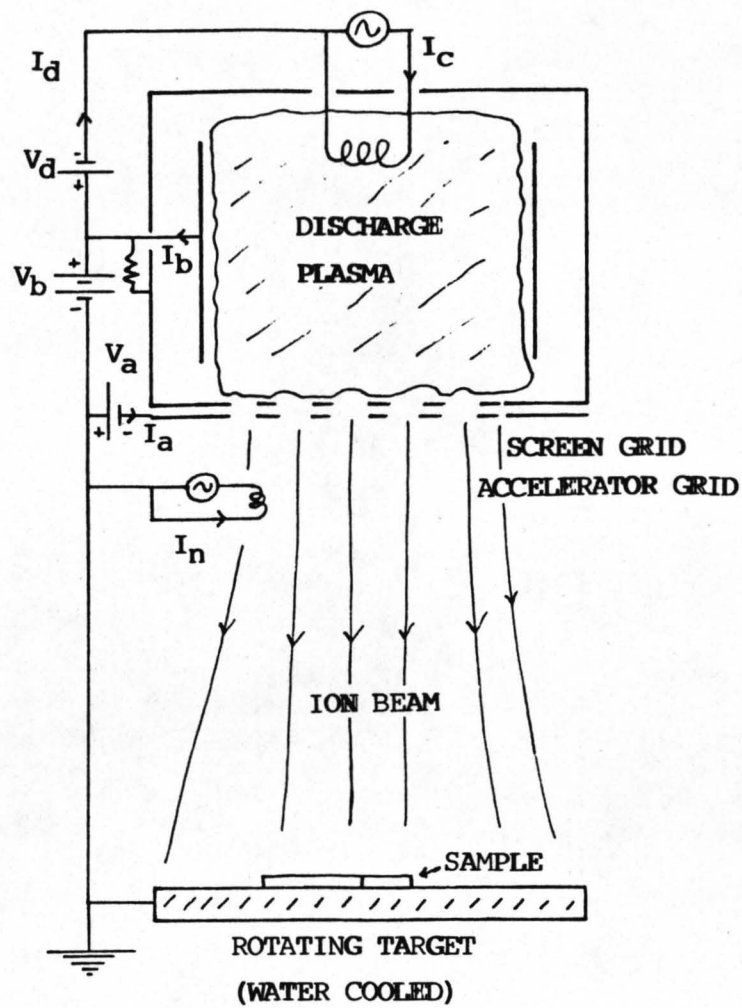
Figure (2.4): Schematic Diagram of an Ion Beam Etching System.
The Diagram Defines the Potentials and Currents
Outlined in Section 2.4 and Table 3.1.
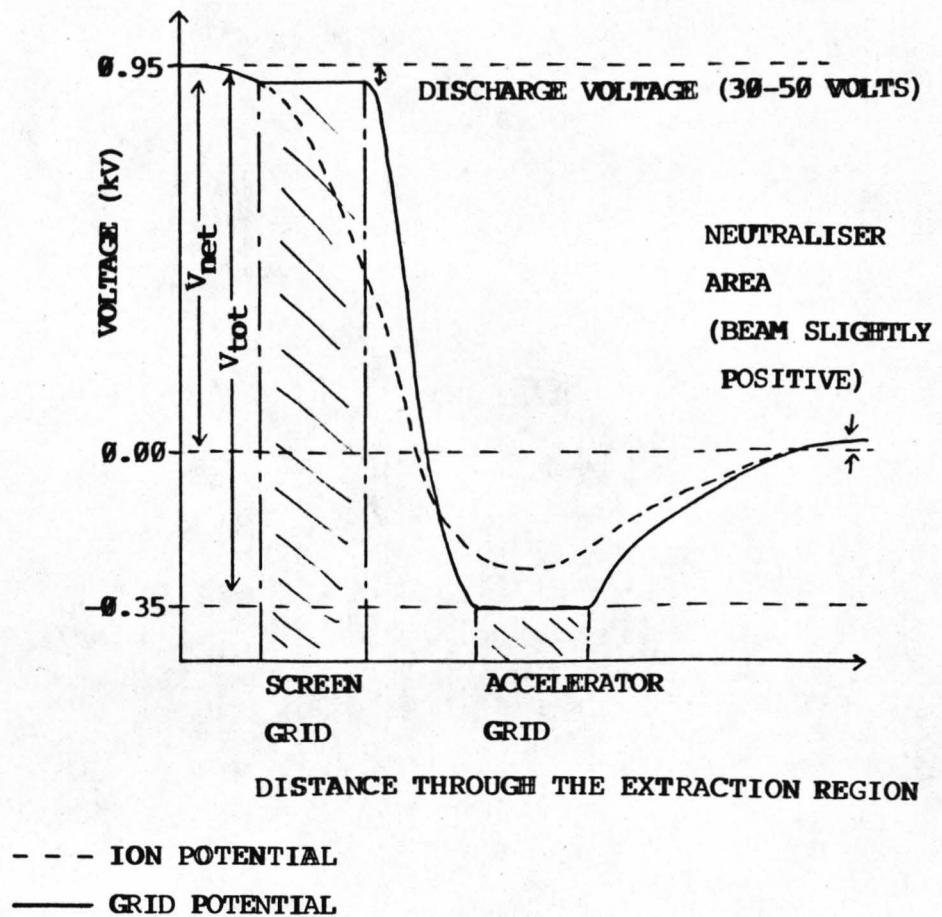
Figure (2.5): Graph Depicting The Potential Fields through which the Ionised Atoms are Accelerated in the Extraction Region.

would otherwise divert the ion beam.

The values of V_{net} and V_{tot} are not arbitrary although the main consideration is a strong potential drop to ensure the production of a high energy stream of ions. Looking at the ratio of V_{net}/V_{tot} the values range typically between 0.5 and 0.8. The lower limit is dependent on electron backstreaming, i.e. the electrons from the immersion wire being attracted into the source. The upper value is limited by the increased divergence of the beam from a parallel or focused beam.

The focussing of the ion beam is very important since the etch rate is dependent on the number of ions per cm^2 as well as the ion energy. The beam divergence can be controlled by adjusting the distance between the screen and accelerator grids, but in the Ion Tech Kaufman source this distance is fixed. The divergence can also be modified by controlling the ion density within the anode-cathode configuration as well as the neutraliser current.

The ion density can be modified in two ways:-

1) If the cathode current is increased it supplies more electrons to the plasma and thus increases the amount of ionisation; the converse happens if the current is reduced.

2) The extraction voltage, if too low, does not remove ions as fast as they are being created and the ion density increases. The converse happens if the extraction voltage is increased.

If the ion beam is collimated there is a minimal amount of ions impinging on the accelerator grid. The amount of accelerator current is an indication of the ion source operation. It is necessary to maintain the accelerator current at a minimum level (typically a few percent of the total beam current). If the accelerator current is higher than a few percent of the beam current it indicates that the beam is not focussed and also that the accelerator grid is being eroded by the ion beam.
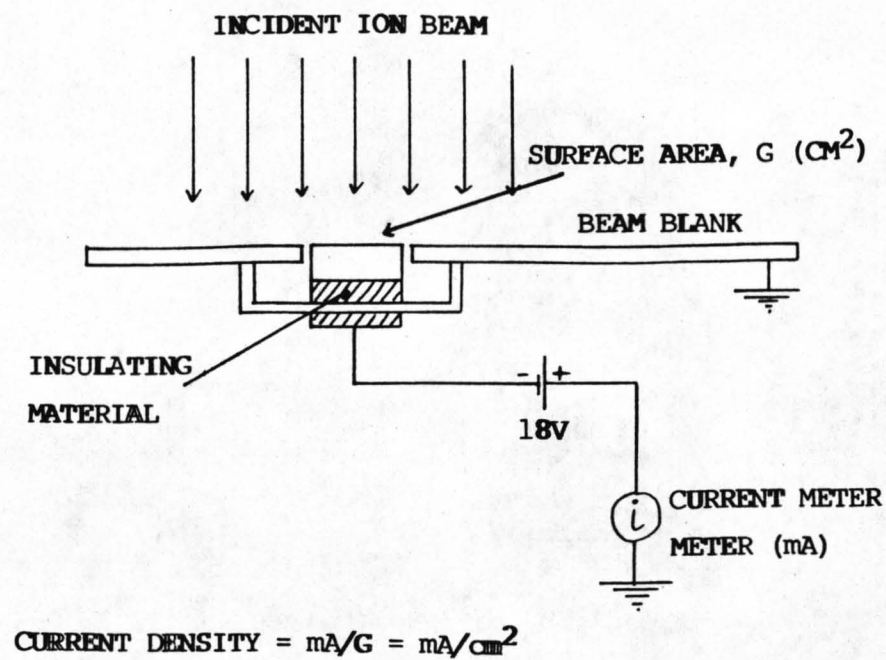
Figure (2.6): Schematic Diagram of Beam Blank Fitted with a Monitor which Measures the Density of Charge Incident on the Target (mA/cm^2).

Although the beam current gives a relative indication of resultant target etch rate, the parameter which truly gives this indication is ion density at the target. The incident ion density at the target is measured by a monitor in the substrate protective shutter, figure (2.6). The detector is positioned above the target and is isolated from the shutter so that all charge incident upon the 1 cm^2 detector can be collected. The detector is biased slightly negative, at about 18 volts, to repel the electron sea and is small enough not to modify the direction of the high velocity ions ensuring a true reading of ion density.

The target is mounted on a water-cooled rotating stage. Sample rotation ensures an even beam density over the etching area and the water cooling alleviates the effects of substrate heating caused by the ionic bombardment of the erosion process.

A photograph of the 'home built' ion milling system is shown in figure (2.7).

2.5 Reactive Ion Beam Etching (RIBE)

The process of ion beam etching can be enhanced with the use of a reactive gas instead of an inert gas [2.16,2.17,2.18]. As a consequence substrate etching is caused by chemical as well as physical processes, although the beam source works in the same manner as in 2.4. Typical reactive gases used are Freon 12 and 14 (CCl_2F_2 and CF_4), CHF_3 and O_2. One major problem with this type of system is that reactive gases which contain carbon in the plasma inhibit the operation of the beam source by attacking insulators or coating them with carbon rendering them ineffective.

Reactive gases are used in the hope that redeposition can be overcome by the chemical process of combining the substrate atoms with the reactive elements of the gas to form volatile products. Care must be taken when reactive gases are chosen e.g. the presence of O_2 while ion etching lithium niobate severely
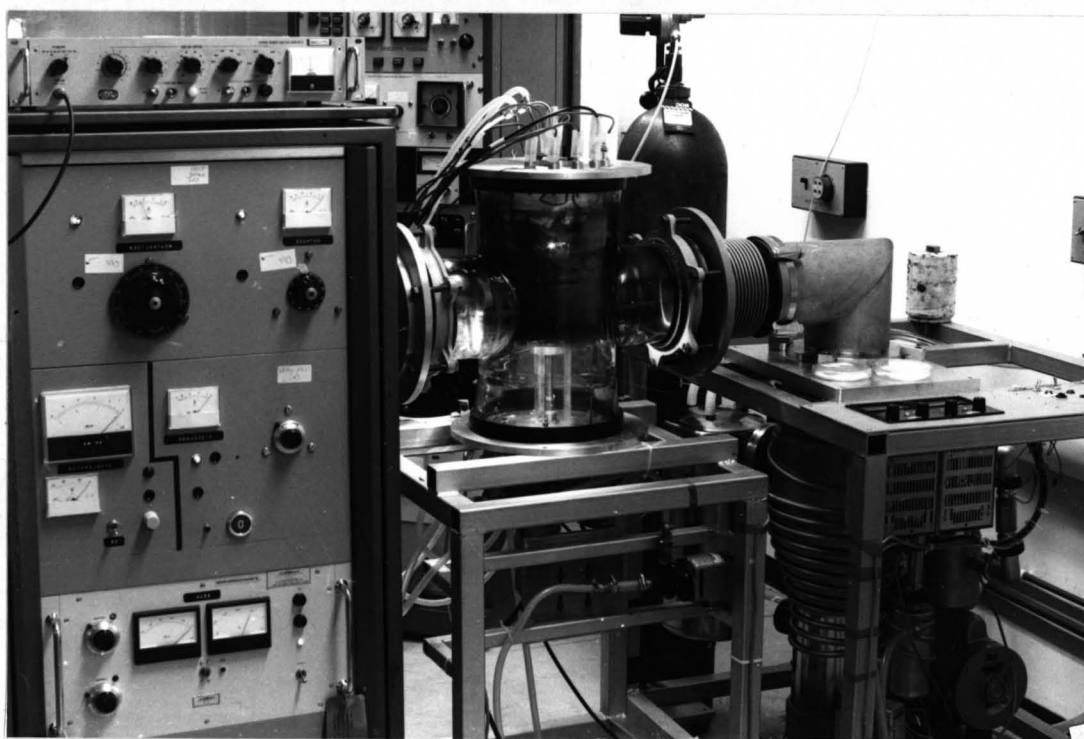
Figure (2.7): Photograph of System used For the Ion Beam Etching of Lithium Niobate Substrates.

inhibits the etch rate [2.29].

The RIBE process was not used in the series of experiments due to the carbon redeposition problem.

2.6 Ion Beam Assisted Etching (IBAE)

One method of overcoming the problems of reactive gases in the Kaufman source is IBAE [2.27, 2.28]. Basically the source acts as a normal inert gas ion beam etching system and the reactive gas is bled onto the substrate surface in the hope that the reactive gas will react with the etched material forming high partial pressure compounds which can be readily removed from the target by being pumped from the system. The etch rate should also be considerably enhanced. Conversely the process has also been used to inhibit the IBE of a metal masking layer rather than increasing the etch rate of the substrate [2.28].

Although there is considerable interest in this type of process, due to the problems of system modification the IBAE process was not investigated.

2.7 Conclusions

The main ion etching processes used for pattern delineation have been discussed. Each process has specific characteristics such as etch directionality, flexibility, physical etching, chemical etching, defined ion energy or combinations of the above. Choosing the correct process for a particular purpose is important so that the resultant etch qualities will be acceptable and not limited by the etching process.

[2.1]   R.C. Booth and C.J. Heslop
          Application of Plasma Etching Techniques to Metal Oxide
          Semiconductor (MOS) Processing
          Thin Solid Films, vol 65, pp111-123, 1980

[2.2]   A. Rauber
          Chemistry and Physics of Lithium Niobate
          Current Topics in Materials Science, Vol 1, Chapter 7
          F. Kaldis Ed., 1978

[2.3]   I. Andonovic, M.B. Holbrook and A.D. MacLachlan
          End-Fire Coupling Between Optical Fibres and Stripe
          Waveguides
          1st E.C.I.O., London, September 1981, pp8-11

[2.4]   A.C.G. Nutt, J.P.G. Bristow, A. McDonach and
          P.J.R. Laybourn
          Fiber-to-Waveguide Coupling using Ion Milled Grooves in
          Lithium Niobate at 1.3-um Wavelength
          Opt. Lett., vol 9, No.10, pp463-465, October 1984

[2.5]   UK Patent Application. No. GB 2096344 A
          S.C. Gratze, Domestic Classification G2J GDA
          13 Oct 1982, Marconi Research Centre, ESSEX

[2.6]   UK Patent Application. No. GB 2100876 A
          C.B. Rodgers and J.S. Heeks, Dom. Class. G2J GDA GDB
          6th Jan 1983, Standard Telephone and Cables Ltd London

[2.7]   B. Zhang, S. Forouhar, S.Y. Huang and W.S.C. Chang
          C_2F_6 Reactive Ion-Beam Etching of $LiNbO_3$ and Nb_2O_5 and
          Their Application to Optical Waveguides
          J. Lightwave Tech., vol LT-2, No.4, pp528-530, Aug 1984

[2.8]   M. Minakata
          Efficient LiNbO$_3$ Balanced Bridge Modulator with an Ion
          -Etched Slot
          Appl. Phys. Lett., vol 35, No.1, pp40-43, July 1979

[2.9]   I.P. Kaminow, V. Ramaswamy, R.V. Schmidt, E.H. Turner
          Lithium Niobate Ridge Waveguide Modulator
          Appl. Phys. Lett., vol 24, No.12 , pp622-624, June 1975

[2.10]   J. Noda et al.
          Electro-Optic Intensity Modulation in LiTaO$_3$ Ridge
          Waveguides
          Appl. Phys. Lett., vol 26, No.6, pp298-301, March 1975

[2.11]   Y. Murakami and M. Ikeda
          Single-Mode Optical Y-Branching Circuit using
          Deposited Silica Guides (DS Guides)
          Electron. Lett., vol 17, No.12, pp411-413, June 1983

[2.12]   W.H. Chen and E.G. Lean
          Grating Acoustic Scanner using Bulk Acoustic Waves
          Electron. Lett., vol 17, No.3, pp141-143, Feb. 1981

[2.13]   J.P.G. Bristow, A.C.G. Nutt and P.J.R. Laybourn
          Novel Integrated Optical Polarisers using Surface
          Plasma Waves and Ion Milled Grooves in Lithium Niobate
          Electr. Lett., vol 20, No. 25/26, pp1047-1048, Dec 1984

[2.14]   P.G. Flavin et al.
          An Approach to LiNbO$_3$ Wafer Scale Integration
          IEEE Int. Workshop on Integr. Opt. and Related Technol.
          for Sig. Proc., Technical Digest, pp13-16, Sept. 1984
          Florence, Italy

[2.15]   M. Stockman and W. Beinvogl
          Planar Bragg-grating Lenses in LiNbO$_3$ fabricated by
          CHF$_3$ Reactive Ion Etching
          Wave Electron., vol 4, No.4, pp221-228, March 1983

[2.16]   J.L. Vossen and W. Kern
         Thin Film Processes
         Academic Press, New York, 2nd Edition, 1978

[2.17]   J.M.E. Harper
         Ion Beam Applications to Thin Films
         Internal Research Report
         IBM Research Labs, Yorktown Heights, New York,
         April 1980

[2.18]   C.J. Mogab
         Ion Beam, Plasma, and Reactive Ion Etching
         Inst. Phys. Conf. Ser. No. 53, pp 37-54, 1980

[2.19]   J.A. Bondur
         Dry Process Technology (Reactive Ion Etching)
         J. Vac. Sci. Technol., vol 13, No.5, pp1023-1029
         Sept./Oct. 1976

[2.20]   R.G. Poulsen
         Plasma Etching in Integrated Circuit Manufacture
         J. Vac. Sci. Technol., vol 14, No.1, pp266-274,
         Jan./Feb. 1977

[2.21]   L.M. Ephrath
         Reactive Ion Etching for VLSI
         IEEE Trans. for Elect. Dev., vol ED-28, No.11, pp1315-
         1319, Nov 1981

[2.22]   P.G. Gloersen
         Ion Beam Etching
         J. Vac. Sci. Technol., vol 12, No.1, pp28-35,
         Jan./Feb. 1975

[2.23]   C.M. Melliar-Smith
         Ion Etching for Pattern Delineation
         J. Vac. Sci. Technol., vol 13, No.5, pp1008-1022
         Sept./Oct. 1976

[2.24] H.F. Kaufman, P.D. Reader and G.C. Isaacson
        Ion Sources for Ion Machining Applications
        AIAA Int. Elect. Propulsion Conf., pp1-5
        Key Biscayne, Florida, Nov 14-17, 1976

[2.25] D.D. Robertson
        Advances in Ion Beam Milling
        Solid State Technol., pp57-60, December 1978

[2.26] R.N. Castellano
        Pattern Delineation by Ion Beam Milling
        Inst. Phys. Conf. Ser. No.54, Chapter 6, pp241-245
        1980

[2.27] M.W. Geis, G.A. Lincoln, N. Efremow and W.J. Piacentini
        A Novel Anistropic Dry Etching Technique
        J. Vac. Sci. Technol., vol 19, No.4, pp1390-1393
        Nov./Dec. 1981

[2.28] M. Kawabe, M. Kubota, K. Masuda and S. Namba
        Microfabrication in $LiNbO_3$ by Ion-Bombardment-
        Enhanced Etching
        J. Vac. Sci. Technol., vol 15, No.3, pp1096-1098
        May/June 1978

[2.29] M. Cantagrel
        Comparison of the Properties of Different Materials
        used as Masks for Ion Beam Etching
        J. Vac. Sci. Technol., vol 12, No.6, pp1340-1343
        Nov./Dec. 1975

CHAPTER 3

THE DELINEATION OF MASKING LAYERS AND THE ION BEAM ETCHING OF LITHIUM NIOBATE

3.1 Introduction

As indicated in chapter 2, if processes can be found which can pattern high quality masking layers and etch high aspect ratio grooves in lithium niobate, many devices and components would benefit.

This chapter outlines the patterning of high quality masking layers mainly needed for the ion beam etching (IBE) of lithium niobate. The properties of the IBE system are discussed with a view to achieving slots which could prove useful in the fibre/waveguide coupling of lithium niobate substrates and/or other components.

3.2 Requirements of a Masking Layer

It can be argued that the most important component in any etching technique is not the actual etching mechanism (although it is obviously of great importance) but the masking layer inhibiting etching of the coated substrate surface and controlling the edge definition of the required pattern. The choice of the masking technique is influenced by the subsequent ion etching technique. The main requirement for a purely physical etch is that the masking layer has a much lower etch rate than the substrate or that a much thicker uniform masking layer can be coated onto the substrate than the required etch depth. With the above requirement the masking layer has to be patterned with a high degree of 'quality', quality meaning that the shape of the required pattern can be faithfully reproduced onto the masking layer with no degradation in pattern either in the plane of the substrate or normal to the substrate surface. This shape transfer can depend on the grain size of the masking material.

Requirements for a mask layer in a chemical or chemical-physical etching process are also modified by the masking material and substrate reaction with the chemical gases used.

3.3 The Suitability of Photoresist (AZ 1350J) as a Masking Layer

Photoresists are commonly used as a masking material [3.9,3.10]. However, even though a resist such as Shipley AZ 1350J can reproduce anisotropic profiles accurately it cannot be spun to a sufficient thickness for use as a masking material for deep slots in lithium niobate substrates [3.9,3.10,3.8,3.2]. Carbon is an excellent masking material due to its relatively low sputter rate (20 Å/min) [3.16] and small grain size. Photoresist has proved to be very useful in masking the dry etching processes for the patterning of semiconductor substrates, where generally submicron depth structures are required [3.11,3.12,3.13].

A series of lithium niobate substrates were coated with photoresist and patterned in the standard manner [3.21]. The etch rate and film thickness of AZ 1350J precluded it from being of any use in delineating deep structures in lithium niobate by IBE, therefore experiments were carried out with RIE using Freon 12. Differential etch rates of as much as 3:1 have been obtained with RIBE etching of lithium niobate and AZ 1350J [3.2]. However due to the angular dependence of the preferential etch rate AZ 1350J must be at least three times thicker than the required vertical sided groove depth [3.10] negating any advantage of using reactive gases in IBE etching of lithium niobate masked with AZ 1350J.

Preliminary experiments showed that the processed samples, RIE etched with Freon 12, were of little practical use. The substrates etched very little within the life time of the mask, due to the formation of lithium salts [3.13,3.14] on the lithium niobate substrate, even though RIE is a physical process and it was hoped that sputtering would remove the etch inhibitor (LiF). The substrate surface quality was also extremely poor.

3.4 The Suitability of Polyimide as a Masking Layer

Since the main problem which precluded AZ 1350J photoresist as a masking layer for IBE on lithium niobate was its thickness, the logical step was to use another material, which also had a high carbon content, as a masking layer. Andonovic in the search for a carbonaceous masking layer investigated several likely polymers [3.15]. He found that polyimide, commonly used in the electronics industry [3.19], was a suitable masking layer which could be patterned by RIE with O_2, similar to previous processes used in IBE with oxygen [3.10,3.17]. The main problem was to achieve a suitably thick and even masking layer. His ultimate decision was to spin several layers onto the same substrate, however this method proved to be unsuitable because of boundary effects between layers and it was decided to investigate another method of producing a polyimide layer of sufficient thickness (of the order of 15 microns). Basically the polymer, to be of any use, had to produce a thick, even layer in one spin coating.

3.4.1 Preparation of the Polyimide Making Layer

Andonovic used a polyimide precursor supplied by the Du Pont Company which, being already in liquid form, was limited to a maximum concentration of 10%. The Du Pont polyimide did not have sufficient thickness, on one spin, for the etch depth required (since the required etch depth was 7 microns as a first approximation a 15 micron thick masking layer was decided upon). Ciba Geigy Ltd. supplied a pre-imidised polyimide XU 218 [3.18,3.20] in powder form which when dissolved in 156/100 V/V of acetophenone/xylene w/w was of the same form as that of Du Pont's polyimide, but with the added bonus of being able to control the concentration and hence the coating thickness.

Figure (3.1) shows the variation of polymer thickness against spin speed for various polymer concentrations. The polymer, even at concentrations of 20%, spun a surface layer free from striations but showing a slight thickness increase (lip) at the
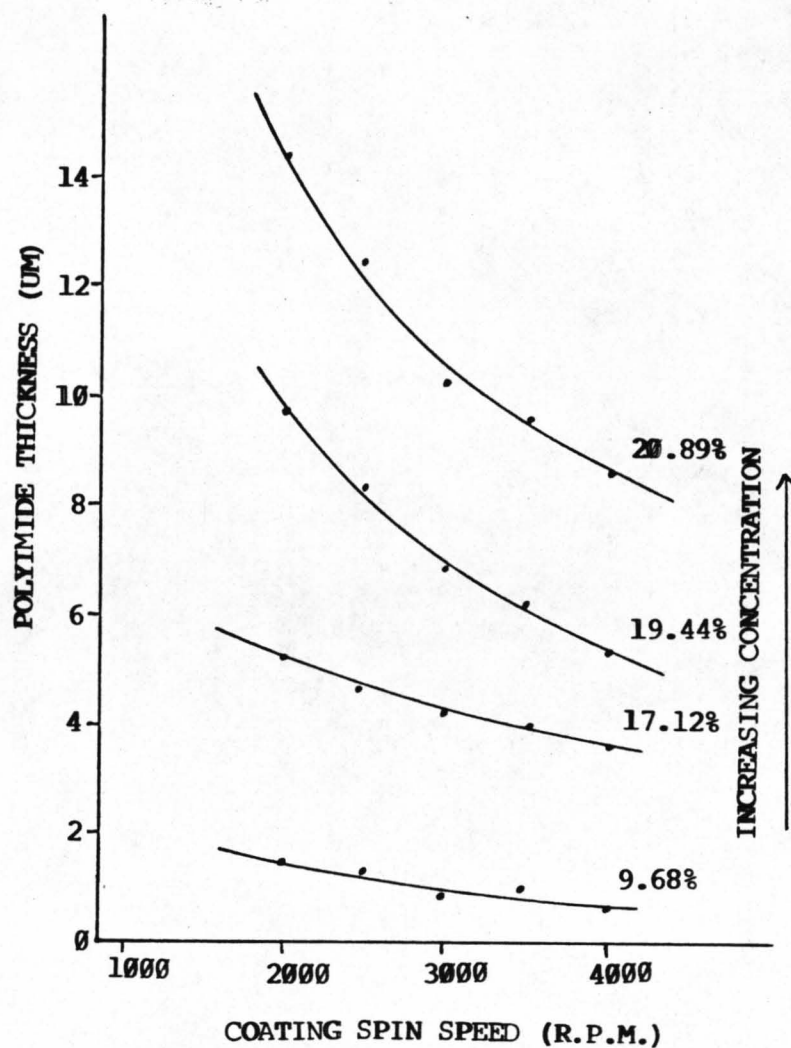
Figure (3.1): Graph of Polymer Thickness vs. Coating Spin Speed
for Various Polymer Concentrations. Polyimide
Dissolved w/w in 156/100 v/v of Acetophenone/Xylene
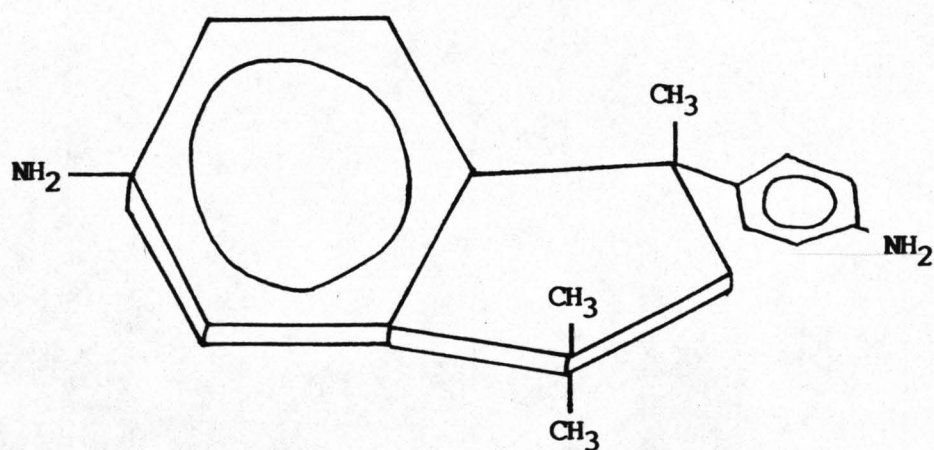
Figure (3.2): Diagram Depicting the Monomer Form
of Polyimide (XU 218)

sample edges. At concentrations of between 10-20% w/w the liquid polymer was extremely viscous and therefore was impossible to filter through the normal resist syringe apparatus. The method used to transfer the polymer from the bottle to the substrate surface was surface tension. A Pasteur pipette was placed in the solvent and extracted with a small amount of polymer adhering to it. On placing the pipette on the cleaned lithium niobate surface the polymer flowed onto the substrate surface in preparation for spinning.

To prepare a surface layer of cross-linked polyimide there are several process steps to follow [3.20], not including the polymer concentration or spin speed, which control the polymer thickness. The spun polyimide layer must be heated to 150°C for 1/2h (which drives off the bulk of the solvent slowly to prevent fast evaporation creating solvent bubbles which damage the masking layer), 250°C for 1h (which dries out the polymer layer totally) and finally to 350°C for 1h 30min (to cross-link the polymer). Figure (3.2) shows the monomer form of polyimide XU 218.

3.4.2 Delineation of the Polyimide Masking Layer

When the polymer is cross-linked it is then ready to be patterned. Figure (3.3) shows the steps used to pattern the masking layer. The masking layer is first coated with aluminium which is patterned using conventional photolithographic processes. On removal of the photoresist, after delineation of the aluminium, the polymer is then ready to be patterned using the aluminium as a mask. An oxygen plasma is used as the etchant as it will react with the polymer but not with the aluminium mask as the formation of an oxide layer quickly inhibits the etch. The etch must be anisotropic to achieve vertical wall profiles and thus a comparison between the various types of plasma etching processes was necessary.

Oxygen plasma etching of polyimide was found to be unsuitable since the etch is mainly isotropic and a high degree of
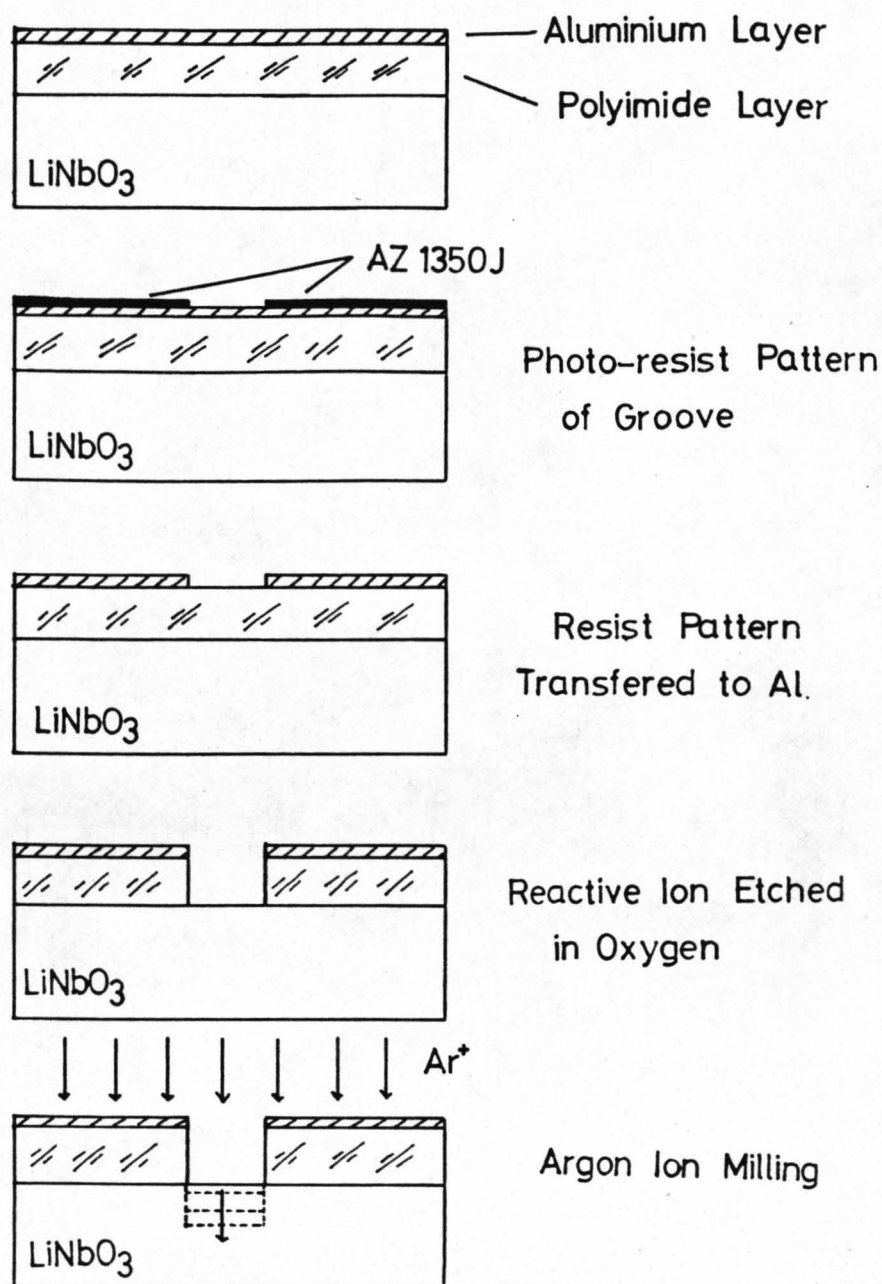
Figure (3.3): Diagram Depicting the Procedure for Delineation of the Polyimide Masking Layer

undercutting of the aluminium masking layer was observed. Oxygen RIE, figure (3.4), proved to be much more satisfactory with vertical walls occuring at the etch aperture. The side walls of the etched masking layer had ripples of the order of 1μm and amplitude of 0.25μm. There was the possibility that the ripples could effect the groove quality of the ion milled groove so in an attempt to reduce the wall ripples various system parameters were investigated in the process.

In the early stages of research into the oxygen RIE of polyimide the machine used was a dual chamber 'home built' parallel plate system. Because of the unknown power split between the dual chambers there was no real indication of power fed into the system. Coupled with this problem was the fact that the systems D.C. bias was not measurable. The resultant etch, see figure (3.4), however was of reasonable quality, once suitable system parameters were found, and the system was used for the main part of the project using the qualitatively defined parameters.

Experiments were also carried out with two other ion etching systems, one a Plasma Technology (PT) PD 80 and the other an Electrotech Plasmafab (EP) 600, and these systems allowed a more quantitative investigation of the etch parameters.

3.4.3 RIE of Polyimide: Experimental Results

Figure (3.5) a) shows the wall quality of a 4μm layer of polyimide etched in the PT. The etch time was 50min with a D.C. bias of 200V, RF power of 110W and a pressure of 10 mTorr. In an effort to investigate the possibility of improving the wall quality, the next sample was run with the same parameters apart from a higher D.C. bias (300V) and a shorter etch time (30min). The shorter etch time was used since it was expected that the increase in D.C. bias would increase the etch rate. The sample prepared under the previous conditions was well defined and the anisotropy of the etch was evident. The second etch resulted in a sample which was not fully etched and whose side walls

Figure (3.4): Scanning Electron Micrograph (S.E.M.) of a
Polyimide Masking Layer RIE in Oxygen. The
Photograph Shows the Vertical Side Walls which are
an Indication of an Anisotropic Etch.
(1um markers)

Figure (3.5): a) S.E.M. of the Side Wall of a Patterned Polyimide Masking Layer. The Sample was RIE in Oxygen at a D.C. Bias of 200V, RF Power 110W, Gas Pressure 10 mTorr and an Etch Time of 50 min. (1um markers)

Figure (3.5): b) S.E.M. of the Side Wall of a Patterned Polyimide Masking Layer. The Sample was RIE in Oxygen at a D.C. Bias of 300V, RF Power 110W, Gas Pressure 10 mTorr and an Etch Time of 30 min. (1um markers)
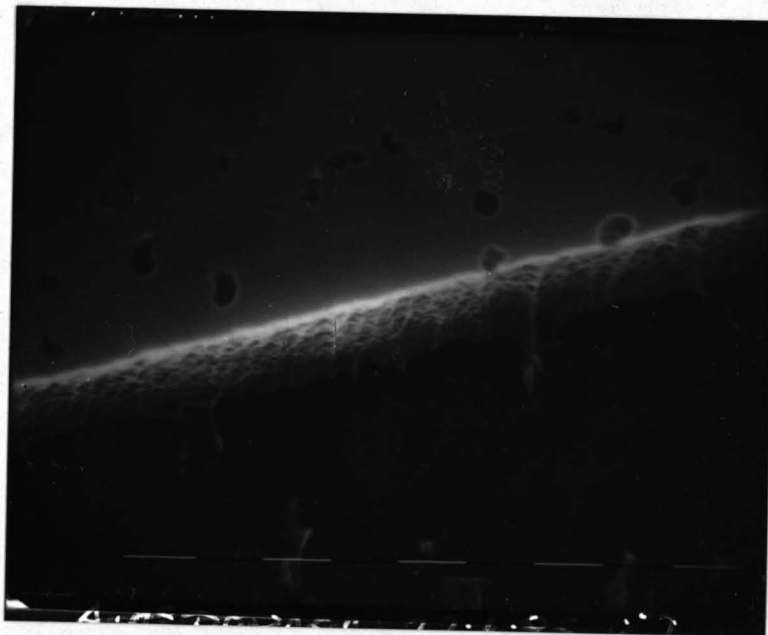
Figure (3.5): c) S.E.M. of the Side Wall of a Patterned Polyimide
Masking Layer. The Sample was RIE in Oxygen at a
D.C. Bias of 300V, RF Power 110W, Gas Pressure
10 mTorr and an Etch Time of 40 min.. (1um markers)

exhibited a definite curve (figure (3.5) b)). A further sample run at the same parameters as above, but with an increased etch time (40min) yielded the results seen in figure (3.5) c). Note that the etch aperture is cleared out and that the walls appear to be vertical, however, the increased D.C. bias and hence increased physical sputtering has eroded the aluminium protective layer and holes have been etched through the polyimide indiscriminately.

From the above data it was noted that D.C. bias is an important factor in the production of an anisotropic etch. Too little voltage can result in undercutting (prevalent especially in thick layers [3.5,3.10]), and too much voltage (>200V) results in undesirable sputtering of the protective metal masking layer, exposing previously protected polymer to reactive oxygen.

Ion etching in the EP yielded far different results mainly due to the fact that the system pressures were much higher [3.5,3.3,3.4]. The first sample run in the machine encountered the problems of cross contamination (see below), coupled with a high system pressure of 190 mTorr. Figure (3.6) a) shows the etched polyimide side wall with RF power 60W, O_2 flow rate 10cc/min and pressure 150mTorr. Note that although the pattern is defined the side walls suffer from undercutting due to the high system pressure producing an anisotropic etch. Reducing the system pressure to its limit, 140 mTorr, and running the machine with the same conditions as above, the result can be seen in figure (3.6) b). Note that although there is a little improvement in the wall concavity, undercutting is still prevalent. Figure (3.6) b) was taken from an area of the sample which had large alignment marks, shape dimensions in the order of 0.4 mm. On the same sample aluminium-delineated windows of much smaller dimensions (in the order of tens of microns) showed markedly different etch properties, see figure (3.7). All patterns of these dimensions exhibited the same effect, namely the etching of a groove around the boundary layer of the aluminium window with the central area relatively unetched. This could be caused by 1) a surface charge effect caused by the small

Figure (3.6): a) S.E.M. of the Side Wall of a Patterned Polyimide Masking Layer. The Sample was RIE in Oxygen at a RF Power 60W, Oxygen Flow Rate 10cc/min, System Pressure 150 mTorr and an Etch Time of 31 min. (1um markers)
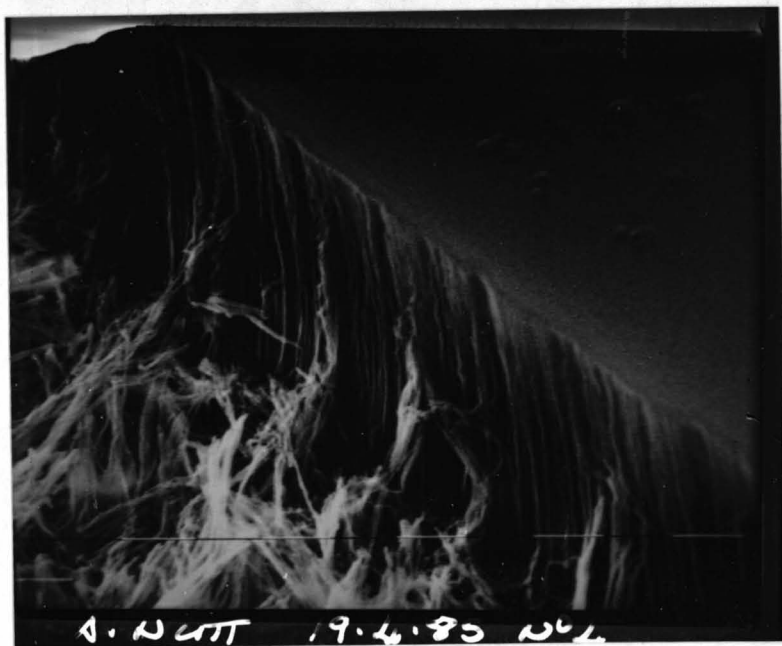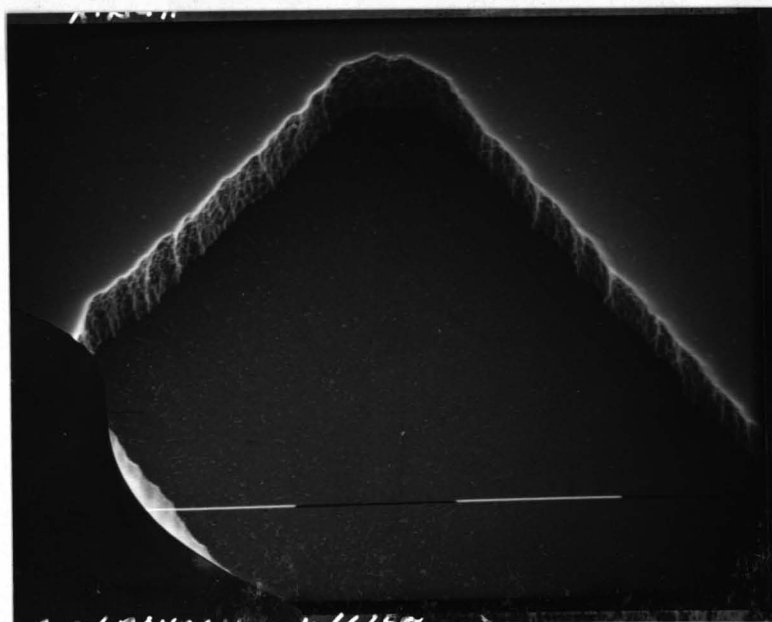

Figure (3.6): b) S.E.M. of the Side Wall of a Patterned Polyimide Masking Layer. The Sample was RIE in Oxygen at a RF Power 60W, Oxygen Flow Rate 10cc/min, System Pressure 140 mTorr and an Etch Time of 30 min. (10um markers)
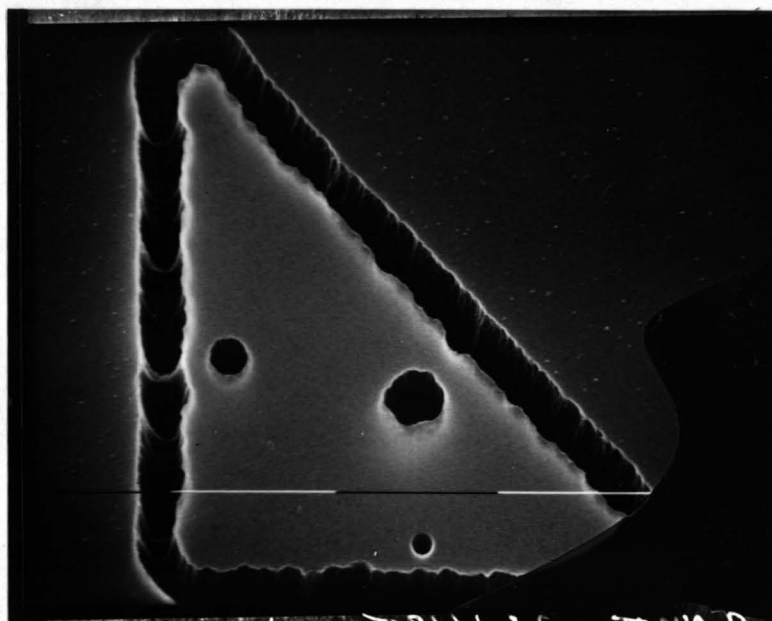
Figure (3.7): S.E.M. of Same Sample as in Figure (3.6) b)
The Very Much Smaller Etch Aperture Exhibits
Remarkably Different Etch Properties.
(10μm markers)

80μm
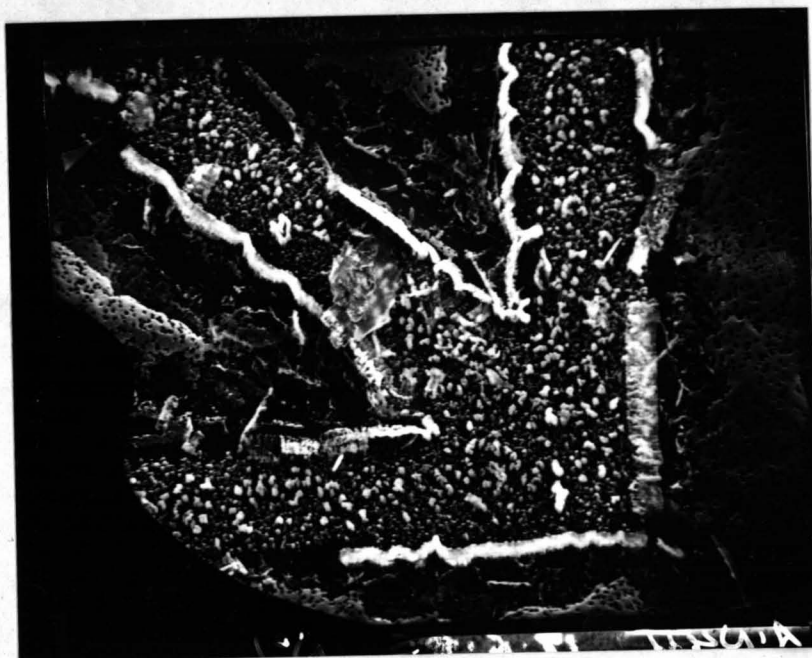
Figure (3.8): S.E.M. Depicting the Damage to a Masking Layer
which can be Caused by High System Pressure (190
mTorr) and System Contamination (Freon 12).

dimensions of the etch window, 2) the etch window still retaining a thin layer of aluminium due to inadequate patterning, 3) system contamination causing the formation of an inert layer on the surface of the exposed polyimide or 4) some above effect combined with the system's high running pressures. This effect, being noticed by other reseachers[1] could obviously be caused by any of the above, as there is not enough information to pinpoint the cause of the effect. However it is unlikely to be 2) or 3) and is most probably caused by a surface charge effect (1) or 4)). The above information highlights the importance of system pressure in an RIE system.

Figure (3.8) shows the effects of having the RIE system contaminated with another reactive gas during the etching process, coupled with a high system pressure. In this case the system was contaminated with Freon 12. The severe damage that resulted was caused by Freon etching the aluminium masking layer and allowing the oxygen to attack previously protected polymer. The result highlights the fact that system parameters must be controlled accurately and that cross contamination can be a problem in a multi-purpose system.

3.4.4 Observations on Polyimide as a Masking Layer

The masking layer is very suitable for ion beam etching (ion milling) and parallel plate ion etching. Care must be taken if reactive gases are used in IBE with this masking layer since gases such as oxygen will greatly degrade the mask effectiveness. Since the mask is mainly composed of carbon the above problem with reactive gases is also somewhat of a boon. Once the polymer has fulfilled its purpose as a mask the excess can easily be removed by placing the sample in an oxygen plasma within a barrel asher in the same way that baked photoresist is removed in the

[1] Discussions with A. McDonach, Research Fellow, Dept E.&E.E., University of Glasgow, Glasgow G12 8QQ.

electronics industry, without damaging the lithium niobate surface. The side wall ripples observed in patterned polyimide could not be removed by the use of different RIE O_2 parameters and may be a function of the material or the inherent structure of the polymer when it is cross-linked. There is also the possibility that the wall roughness in RIE polyimide is caused at the photolithographic stage. If so, it should be possible to pattern the photoresist by an electron beam technique, as that technique should produce no wall roughness on the submicron scale. Electron beam exposure of photoresist in the preparation of the polyimide masking layer would add an unnecessary complexity to the process, which is undesirable should the process be implemented industrially.

Polyimide is quoted in the literature as having an etch rate of 1500 Å/min [3.16] at a power density of $0.3W/cm^2$ in oxygen, which is consistent with our measurements. The patterned polyimide samples, prepared by RIE in O_2, were always overetched. The overetching was to ensure that all the material had been removed from the base of the patterned area (particles left would modify the area to be ion milled). The overetched polymer masks did not show any sign of undercutting, due to the anisotropy of the etching process, which would have compromised the quality of the masking layer.

Recently there have been developments in photosensitive polyimides [3.22,3.23]. The quoted specification of polyimide HTR-2 is that up to 100 microns thickness of polymer can be spun and optically patterned with excellent wall quality and anisotropy. The use of such a polymer would greatly simplify the IBE mask preparation process and hence would make the process even more applicable to industrial implementation. The main problem at the moment is that the polymer is in the development stage and as such is prohibitively expensive.

3.5 Ion Beam Etching of Lithium Niobate

3.5.1 IBE System Limitations and Instabilities

The ion milling system used, as shown in chapter 2 figure 2.7, was built within the department and consisted of a 2.5cm Kaufman ion source mounted face-down onto a water cooled rotating target. The system could be pumped down to 10^{-6} Torr. Since the power supply for the ion source was not microprocessor controlled, during a process run it was necessary to monitor the system and modify the cathode current to keep the accelerator current at a minimum value. Constant monitoring was needed because the ion source was not stable, and the system parameters drifted slowly. Assuming that during a process run the etch rate modified by 50 Å/min (which is a conservative estimate) then the final etch depth, for a 140 min etch, could alter by as much as 0.7µm. When etching submicron structures, the very short etch time allows the system operation to appear stable and graphs of system parameters vs. etch rate can be plotted, however, when approx. 7 micron deep grooves are being etched the resultant etch depth is variable. In an attempt to compensate for the uncertainty in etch rate, in the latter section of research, the beam shutter was replaced for a shutter which could monitor the beam current density at the target. The monitor typically registers current densities of between $1.0 - 3.0$ mA/cm^2. The target current density could be monitored intermittently throughout the etch (each time a reading was taken, by necessity, the ion beam was interrupted). Even with the beam monitor the etch rate still proved to be inconsistent (for no apparent reason) and therefore etch-rate will only be quoted either 'typically' or with a defined set of system parameters.

Since the Kaufman ion source has a beam diameter of 2.5 cm the resultant beam density at the target will vary across the target. The target stage rotates in an attempt to alleviate any changes and give a uniform etch rate across the sample. Two lithium niobate substrates were etched for 25 minutes with system parameters: $I_b = 32$mA, $I_a = 1.5$ mA, $I_c = 6.2-5.4$ A, $I_n = 6.7$ A,

$I_d = 0.33$ A, $V_b = 0.95$ kV, $V_a = -0.35$ kV, $J_c = 2.38$ A/cm^2. One sample was centred in the ion beam and the other sample lay next to it (sample dimensions were 1 x 2 cm^2). The etch rate for the centred samples was 392 Å/min and the etch rate for the adjacent sample was 256 Å/min. Clearly even when the target is rotating the etch rate can vary considerably between two samples etched at the same time. Larger ion sources (10cm diameter) are required to give even etch rates over large areas and allow several samples to be etched at the same time, all resulting in the same etched depth.

The resultant depth uncertainty caused by the above system failings however did not pose any great problem. It was envisaged that if a groove of a defined depth was required, it could be etched to the correct depth (or greater) and the difference could be made up by sputtering the base of the groove with SiO$_2$.

Another factor involved in the etch rate discrepancy was the possibilty of not having lithium niobate of consistent quality. Fortunately, as is mentioned in chapter 4, the coupling efficiency of the ion milled groove coupler appears to be relatively insensitive for up to micron alignment changes.

It would be advantageous to monitor the etch rate of the target during the etch process, and thus be able to have some form of end-point detection. A possible way of doing this is discussed in the conclusions.

3.5.2 Surface Quality of Ion Milled Lithium Niobate

A comparison of ion milling etch surface quality on different lithium niobate crystal orientations was made, as it is known that in anisotropic crystalline materials different crystal orientations etch in different ways [3.24,3.1]. Samples of Z-cut and Y-cut lithium niobate were placed centrally in the ion miller and etched simultaneously. The results can be seen in figure

S.E.M. of the Surface Topography of Y-cut Lithium Niobate
after Ion Beam Etching with Argon (1um markers)
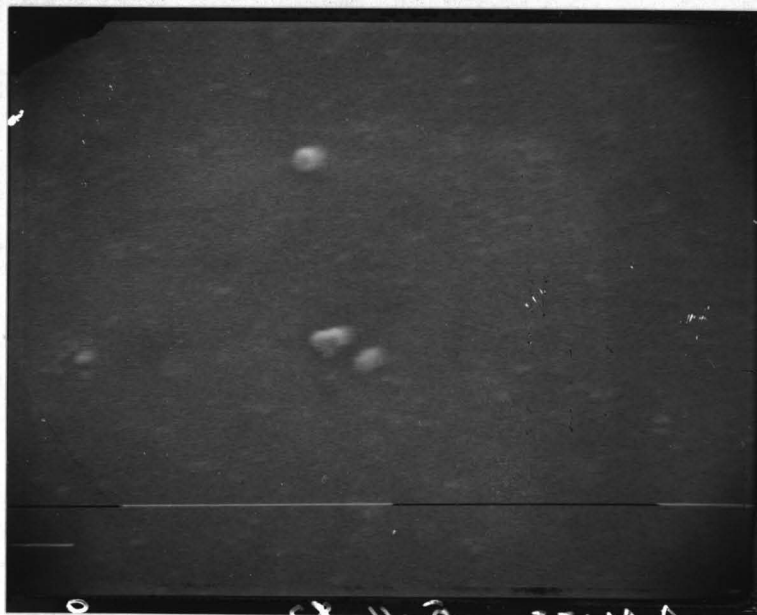
S.E.M. of the Surface Topography of Z-cut Lithium Niobate
after Ion Beam Etching with Argon (1um markers)

Figure (3.9): Comparison of Surface Features on Y-cut and Z-cut
Lithium Niobate under the Same Etch Conditions

(3.9). Basically the Z-cut sample etched uniformly over its surface area whereas the Y-cut sample exhibited a well defined roughness. It could be surmised that the Z-cut lithium niobate etched evenly because over the surface layer the crystal is isotropic whereas the Y-cut lithium niobate sample surface, being anisotropic etched more in accordance with its surface anisotropy. Both samples exhibited discolouration, i.e. both samples were dark grey in colour in the surface region. It is possible that this effect is due to the preferential etching of LiO_2 as compared to Nb in the surface layer [3.15]. This is a reasonable assumption since niobium is a much larger ion than lithium or oxygen and hence the energy to dislodge the larger ion must be much greater (for a purely physical process).

The degradation, and probable index change of the etched layer caused by the ion milling process (possibly leading to LiO_2 depletion) should not affect waveguide properties since waveguides should only be formed on protected areas of substrate.

3.5.3 Redeposition Effects Occuring on IBE Substrates

The erosion process involved in the Ion Beam Etching of lithium niobate was discussed in chapter 2. In order for any dry etch process to be efficient and successful there are several problems to be overcome, and ion milling is no exception.

Firstly, the relative etch rates of the masking material and the substrate are of importance. If, for a required etch depth the masking layer is too thin or the etch ratio too low, then facetting becomes a problem. For normal incidence ion beam etching, facetting first occurs at the mask pattern edges, see figure (3.10). Facetting is caused by a preferential etch rate, occurring at about 45° to the surface of lithium niobate and polyimide [3.24,3.7,3.10], and prevalent at the edge of mask apertures (due to the fact that etch rate has an angular dependence). As the etching process continues this edge effect worsens as the mask is eroded and will eventually open the etch

INCIDENT ION BEAM
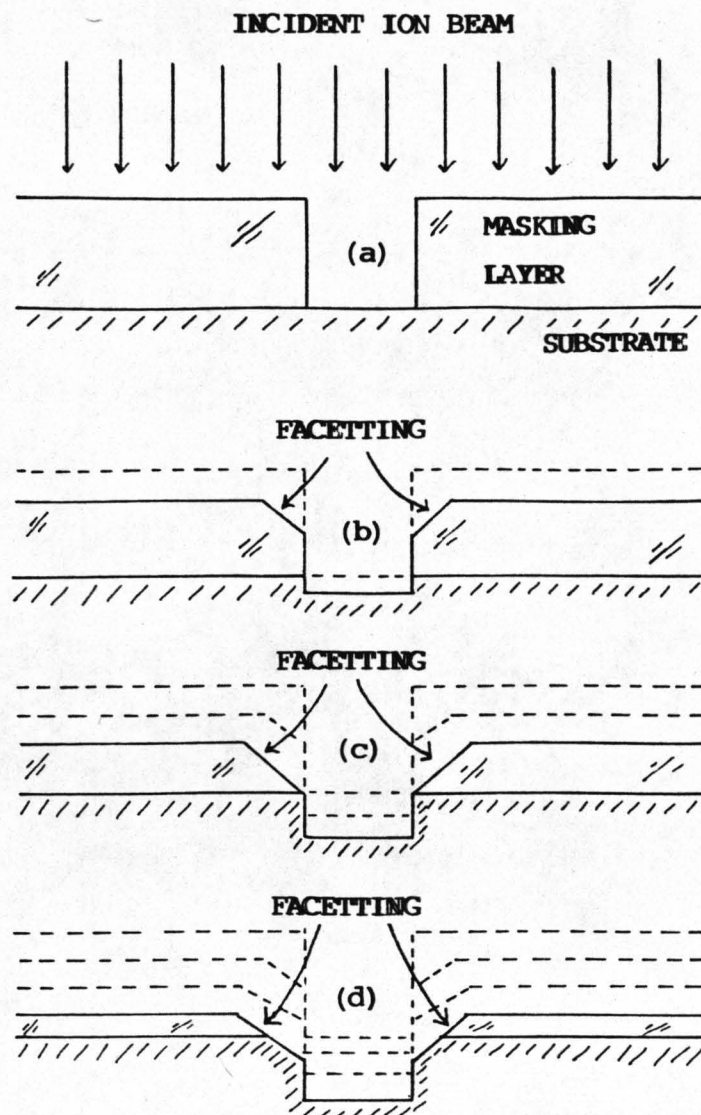
Figure (3.10): Schematic Diagram Depicting the Effect of Facetting
During the IBE Process.

(a) Perfect Masking Layer Before IBE

(b) Facetting Occurs at Mask Edge as it is Etched

(c) Limit to which Sample can be Etched without
Changing Pattern Dimensions

(d) Sample Over-Etched. Resultant Shape of Ion
Etched Slot is Compromised
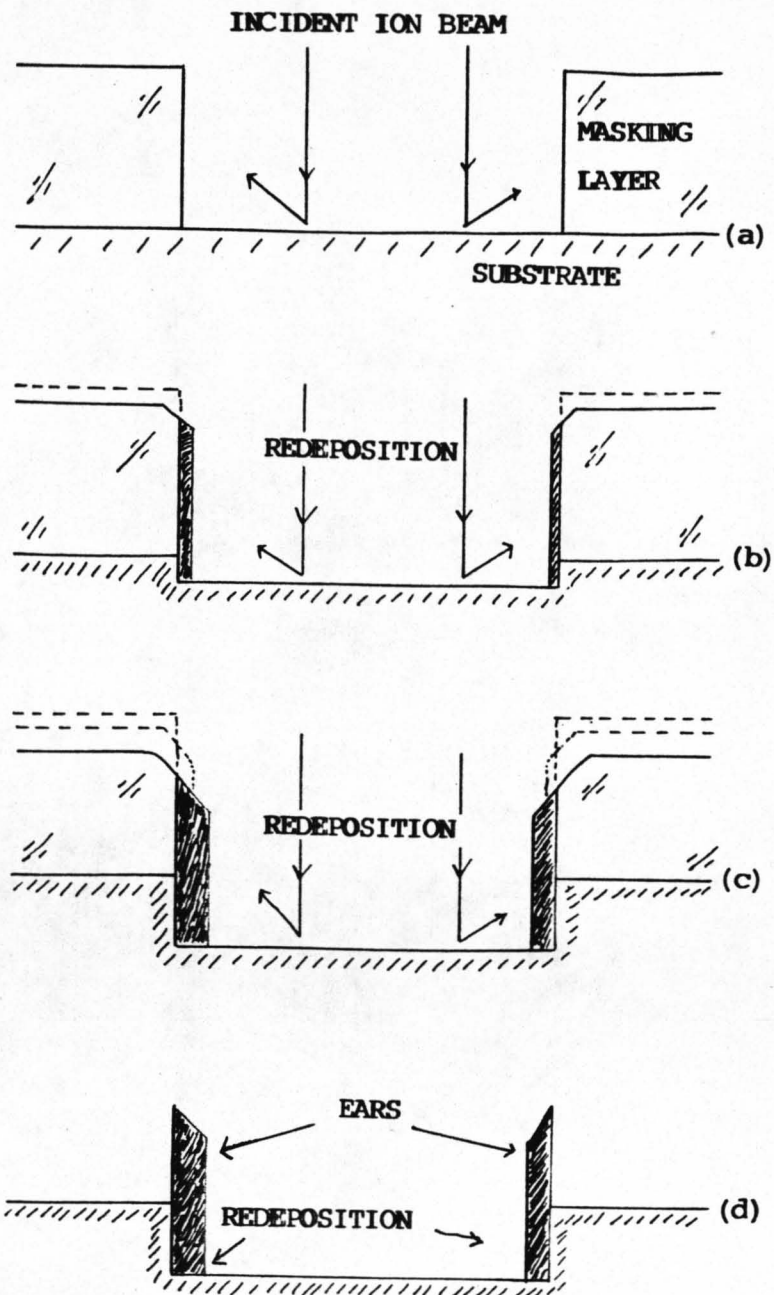
Figure (3.11): Schematic Diagram Depicting the Effect of Redeposition During the IBE Process.
   (a) Perfect Masking Layer Before IBE
   (b) Redeposition Occurs at Mask Edge During Etching
   (c) Amount of Redpositied Material Increases as Does the Facetting
   (d) Masking Layer Removed Leaving Redposition in the Base of the Slot and in the Form of Ears.

aperture to the substrate. The effect is compensated for by coating the substrate with a much thicker layer of polymer than is required for the etch depth, as discussed for the unsuitability of AZ 1350J as a masking layer for deep structures.

Secondly, redeposition [3.24] of masking material and sputtered substrate can result in pattern delineation problems. Figure (3.11) outlines the most common forms of redeposition, which are the formation of 'ears' caused by the redeposition of substrate material onto the side of the masking layer and the redeposition of material from the masking layer and the edge of the substrate into the etch area, this especially occurs when facetting has deformed the mask shape.

Thirdly, foreign material on the etch surface can cause problems due to preferential etching of the area around the particle causing a conical pillar [3.24,3.6]. These particles can arise from insufficient etching of the mask leaving traces of the mask on the area to be etched, dust particles, redeposited material during the etch process or other particles resulting from impurities in the vacuum chamber [3.4,3.24].

Finally, although it may not be a problem in many required patterns, another ion etching defect is trenching. Because the ions are deflected as they strike the interface of the masking layer aperture a higher ion density is created at the base of the masking layer edge [3.3,3.4,3.24]. This increase in ion density causes a greater etch rate and results in a trench being etched along the base of the wall. Trenching is very dependent on the direction of the ion beam as it interacts with the target.

3.5.4 Redeposition on IBE $LiNbO_3$: Experimental Observations

All the above four problems occur with ion milling on lithium niobate. Figure (3.12) illustrates facetting occuring on the polyimide masking layer on a Z-cut lithium niobate substrate (the sample is partially etched). Figure (3.13) illustrates the
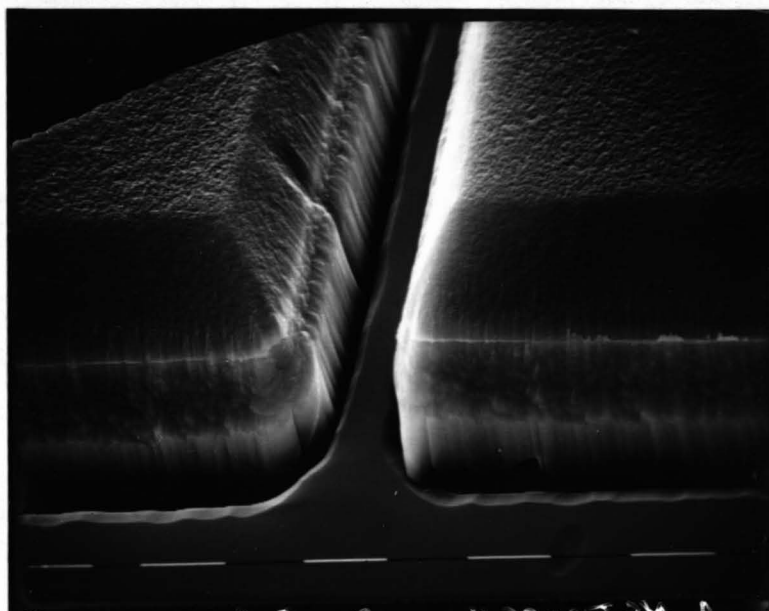
Figure (3.12): S.E.M. of an IBE Lithium Niobate Sample Coated with Polyimide. The Micrograph Shows the Effects of Facetting. (10um markers)
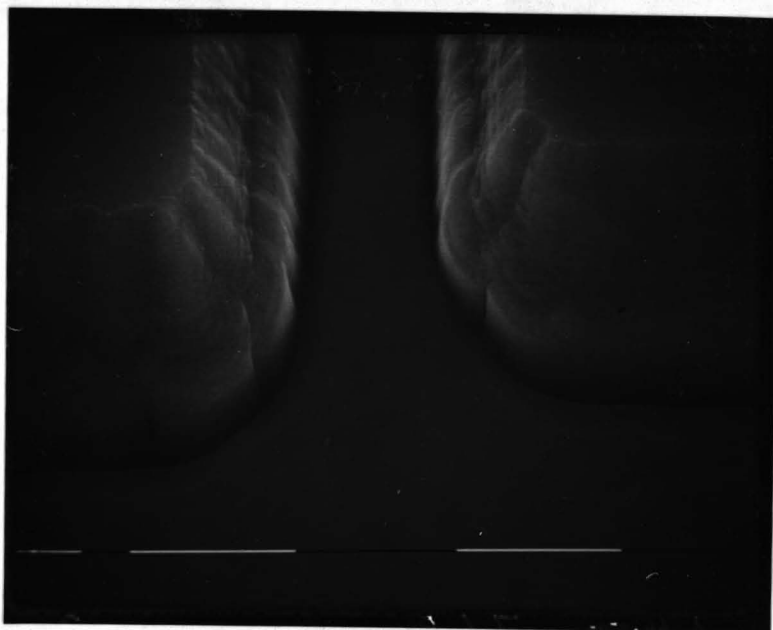
Figure (3.13): S.E.M. of an IBE Lithium Niobate Sample with the Polyimide Masking Layer Removed. The Micrograph Shows the Effects of Facetting and Redeposition. (10um markers)
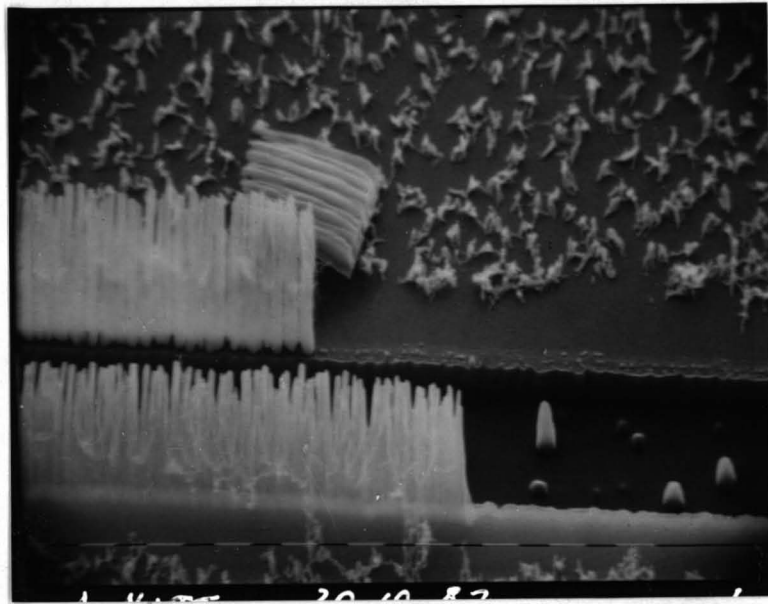
Figure (3.14): S.E.M. of an IBE Lithium Niobate Sample with the Polyimide Masking Layer Removed. The Micrograph Shows Redeposited Ears on the Edge of the Etched Slot. (1um markers)
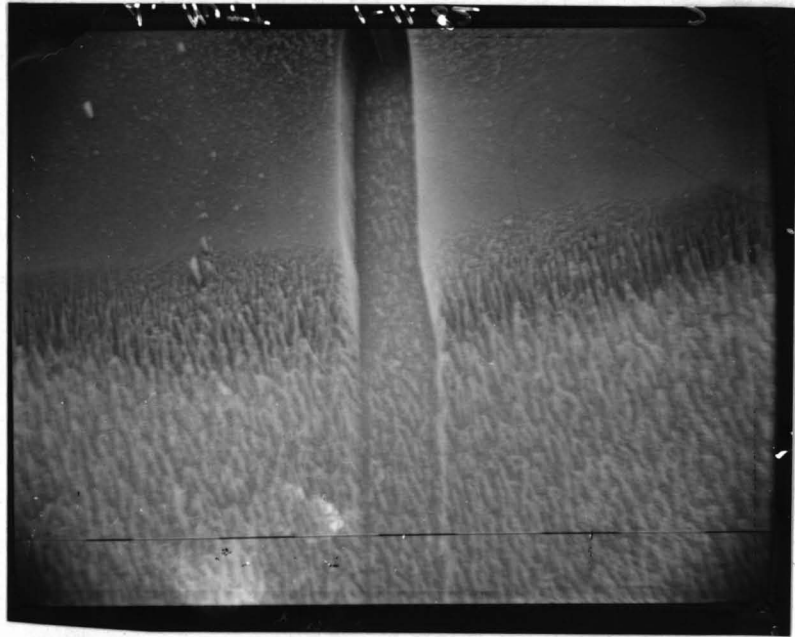
Figure (3.15): a) S.E.M. of the End of a Patterned Polyimide Slot
The Polymer Layer is not Fully Etched Leaving
Material on the Surface of the Etch Area.
(10um markers)
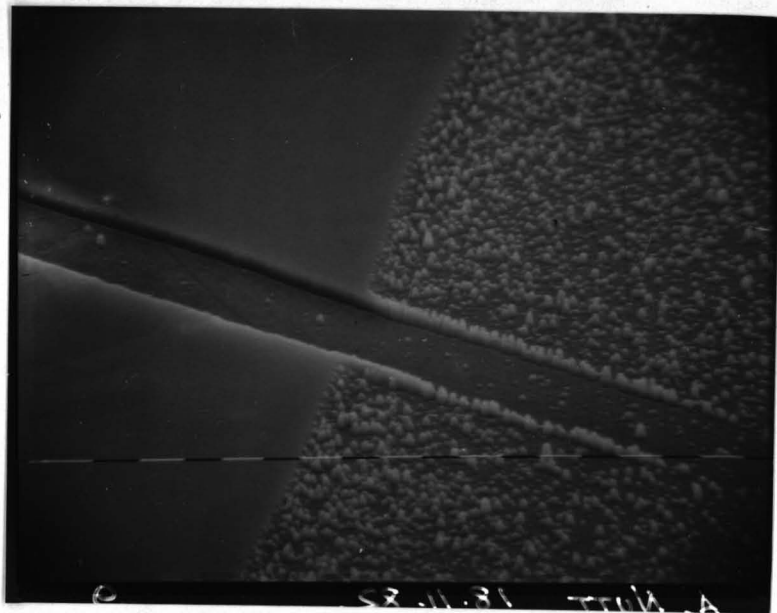
Figure (3.15): b) S.E.M. of the Sample Depicted in Figure (3.14)
after the IBE Process. (10um markers)

detrimental effects of over-etching. The substrate in figure (3.13) clearly shows the effects of side wall facetting (excess polymer being removed from the sample for clarity). As well as facetting, figure (3.13) illustrates the problem of redeposition on the side wall of the grooves (the material being knocked off the wall rim down to the base of the groove). The formation of 'ears' can be seen in figure (3.14); note that after the excess polymer is removed the 'ears' still stand (although they are prone to being dislodged with little force). Figures (3.15) a) and b) illustrate the effects of particles in the exposed area of substrate. Figure (3.15) a) shows the end of a patterned polyimide groove with the polymer not sufficiently removed from the exposed area (the particles could just as easily be dust etc.). After ion milling figure (3.15) b) shows the drastic effects these particles can have on the finished etched substrate. Slight trenching can be seen in figure (3.17) (discussed below) although not all samples exhibited this effect.

The redeposition in the groove and the 'dust' problem can be overcome if care is taken throughout substrate preparation, with the thickness of the masking layer and by removing all traces of the polymer in the exposed substrate region (usually with the help of a sonic bath). However, sputtered 'ears' at the edges of the grooves were always a common occurrence and could be removed simply by re-cleaning the substrate.

3.5.5 Ion Milled Grooves on Lithium Niobate

Ideally an ion etched slot needs to be well defined, of high quality (smooth and square side walls etc.) and the protected region must suffer no surface degradation. Figure (3.16) a) shows an electron micrograph of a patterned polyimide mask, still coated with aluminium, with a rectangular cross-section, and the surface of the Z-cut lithium niobate exposed. Figure (3.16) b) shows a micrograph of the same substrate after ion milling and with the excess polymer layer removed in an O_2 barrel asher. The substrate surface is shown to be well protected and the $10 \mu m$
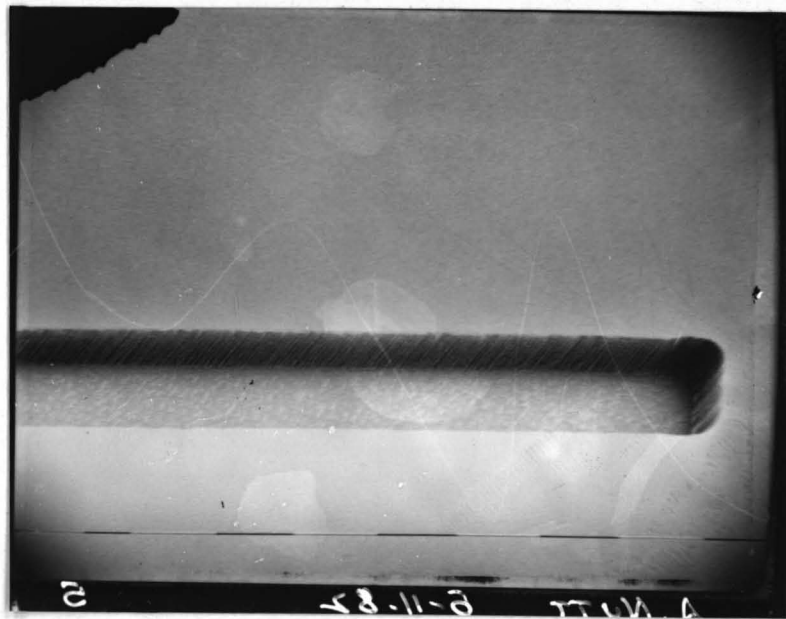
Figure (3.16): a) S.E.M. of a Patterned Polyimide Masking Layer
on Z-cut Lithium Niobate (10um markers)
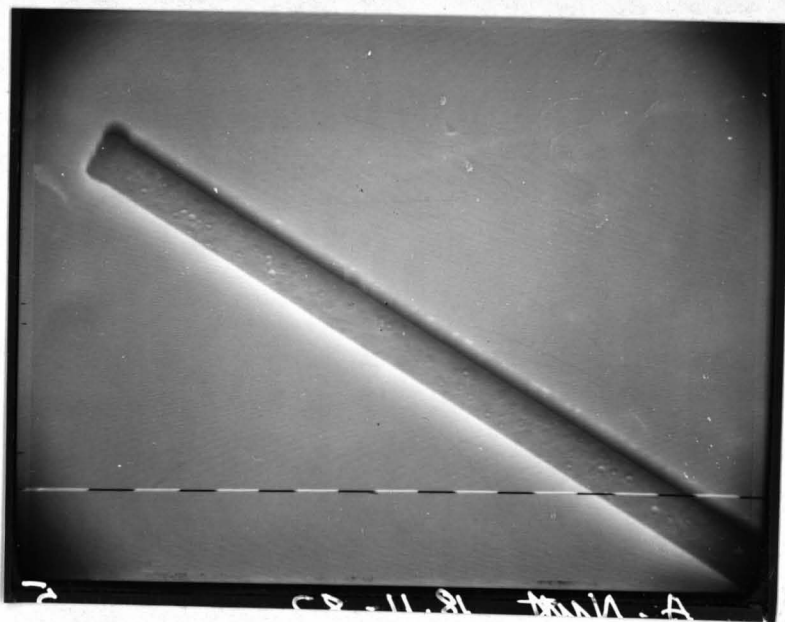
Figure (3.16): b) S.E.M. of the Sample Depicted in Figure (3.16)
a) after the IBE Process and with the Excess
Polymer Masking Layer Removed (10um markers)
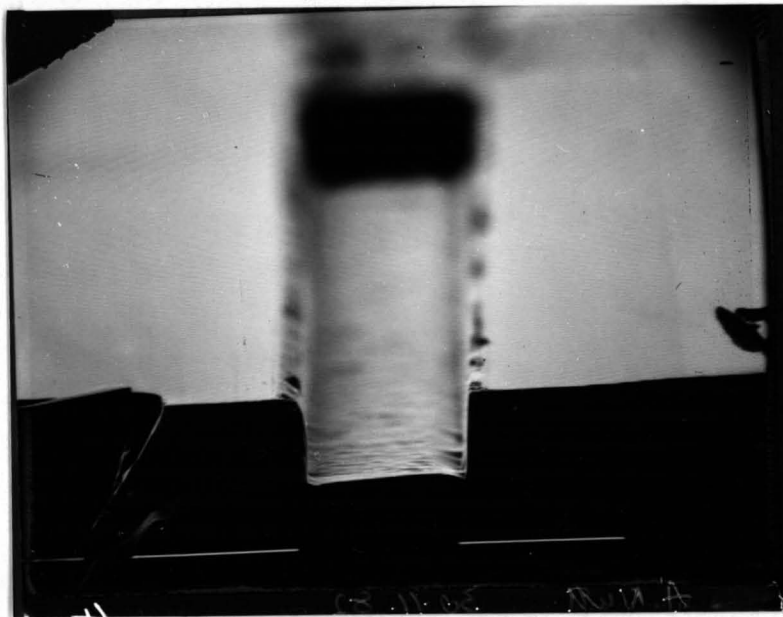
Figure (3.17): S.E.M. of the Cross-Section of an Ion Milled Groove on Z-cut Lithium Niobate (10um markers)
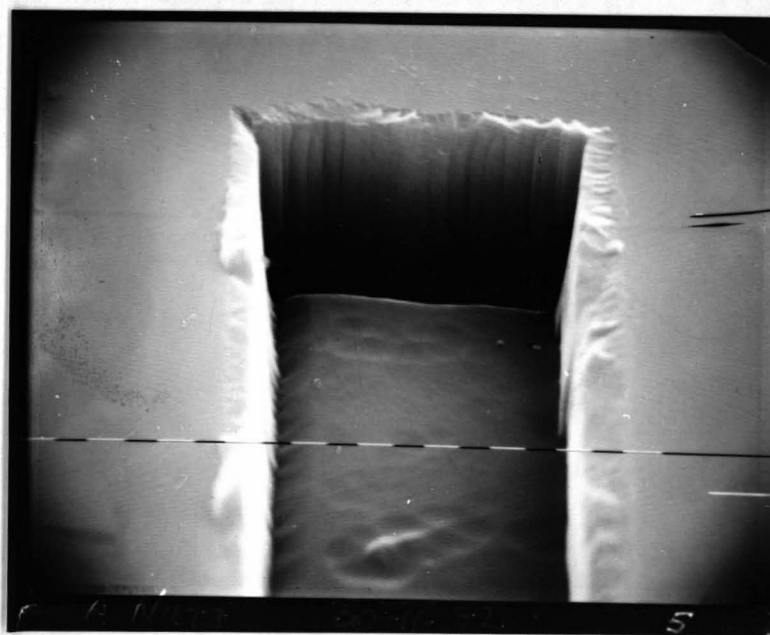
Figure (3.18): S.E.M. of the End-Face of an Ion Milled Groove on Z-cut Lithium Niobate (1um markers)

wide slot well defined (with the 'ears' removed as described above). The sample is of high quality except for a few cones caused by alien particles. The depth of the slot is about 4.0µm, and the etch rate 450Å/min.

Closer inspection of wall profiles and smoothness is necessary before a true estimation of the etch quality can be ascertained. Although lithium niobate does not have a natural cleavage plane along crystallographic axes [3.1], with trial and error, etched lithium niobate samples were eventually split along a plane which allowed the cross-section of an etched slot to be viewed. The important points to note in figure (3.17) are that the base of the slot is flat (apart from slight trenching, see above), the slot cross-section is highly rectangular (although it was not possible to measure the deviation) and the substrate surface has been well protected.

Figure (3.18) shows the end face of an ion milled slot. The sample exhibits a roughness of periodicity 1um and amplitude 0.25µm (approx.). The roughness on the groove rim, in figures (3.17) and (3.18), as in the other samples, was caused by the removal of redeposited 'ears' from the groove edge. It appears that the wall roughness in the ion milled slot is comparable, and maybe caused by the roughness in the polyimide mask.

Although the 'quality' of the final groove structure was a function of the masking layer and substrate preparation the groove depth was not. Different system parameters in the argon ion milling of lithium niobate mainly altered the system etch rate and did not affect the groove shape (assuming normal incidence ions).

Table 3.1 outlines several typical ion milling runs with all the associated source parameters. As the etch rate for Z-cut lithium niobate is approximately 500 Å/min the length of a typical ion milling run is of the order of 120 minutes to produce a 6µm deep groove.

TABLE 3.1

List of IBE Source Parameters During the Etching
of Lithium Niobate

Cathode Current I_c Beam (Anode) Voltage V_b

Neutraliser Current I_n Accelerator Voltage V_a

Beam (Anode) Current I_b Current Density J_c

Accelerator Current I_a Discharge Current I_d

Pump Down Pressure - 2.10^{-6} Torr; Ar gas - 10^{-4} Torr

I_c (A)	I_n (A)	I_b (mA)	I_d (A)	I_a (mA)	V_b (kV)	V_a (-kV)	J_c (mA/cm^2)
6.25	6.8	32	0.31	1.5	0.9	0.30	2.35
5.8	6.8	31	0.34	1.5	0.9	0.35	2.33
5.6	6.8	31	0.33	1.8	0.9	0.35	2.33
5.2	6.8	30	0.33	2.0	0.9	0.35	2.34
4.9	6.4	29	0.33	1.8	0.9	0.35	2.32
4.6	6.4	30	0.34	2.0	0.9	0.35	2.30
4.3	6.4	30	0.34	2.0	0.9	0.35	2.33
4.0	6.3	29	0.34	2.0	0.9	0.35	2.34
3.7	6.2	29	0.34	2.0	0.9	0.35	2.30
3.3	6.0	29	0.34	2.0	0.9	0.35	2.31
2.9	6.0	29	0.34	2.0	0.9	0.35	2.35
2.3	6.0	29	0.35	2.5	0.9	0.35	2.33
1.3	5.9	29	0.36	2.5	0.9	0.40	2.30

Measurements taken every 10 min.

Therefore Total Etch Time = 120 min.

Etch Depth = 5.2 microns

Etch Rate = 433 Å/min

TABLE 3.1 (Continued)

List of IBE Source Parameters During the Etching
of Lithium Niobate

Cathode Current I_c Beam (Anode) Voltage V_b
Neutraliser Current I_n Accelerator Voltage V_a
Beam (Anode) Current I_b Current Density J_c
Accelerator Current I_a Discharge Current I_d

Pump Down Pressure - 2.10^{-6} Torr; Ar gas - 10^{-4} Torr

I_c (A)	I_n (A)	I_b (mA)	I_d (A)	I_a (mA)	V_b (kV)	V_a (-kV)	J_c (mA/cm^2)
6.2	6.8	31	0.30	1.8	0.90	0.35	2.37
5.8	6.7	30	0.30	1.8	0.90	0.35	2.34
5.6	6.7	29	0.30	1.8	0.90	0.35	2.32
5.4	6.7	29	0.30	2.0	0.90	0.35	2.34
5.0	6.7	29	0.28	2.0	0.90	0.35	2.35
4.6	6.7	28	0.28	2.0	0.90	0.35	2.33
4.3	6.7	30	0.28	2.0	0.95	0.35	2.33
3.9	6.7	30	0.29	2.0	0.95	0.35	2.30
3.3	6.6	30	0.28	2.4	0.95	0.35	2.31
2.5	6.6	29	0.26	2.4	0.95	0.35	2.33
1.8	6.6	30	0.25	2.5	0.95	0.35	2.30

---------------------CATHODE CHANGED----------------------------

Etch Time - 99 minutes

-----------------------NEW CATHODE------------------------------

I_c (A)	I_n (A)	I_b (mA)	I_d (A)	I_a (mA)	V_b (kV)	V_a (-kV)	J_c (mA/cm^2)
6.2	6.8	30	0.31	1.8	0.90	0.35	2.32
6.0	6.8	30	0.31	1.8	0.90	0.35	2.34
5.9	6.7	30	0.30	1.7	0.90	0.35	2.35
5.7	6.7	30	0.30	1.8	0.90	0.35	2.33
5.5	6.7	30	0.30	1.8	0.90	0.35	2.29

Total Etch Time = 99 + 21 = 120 min.
Etch Depth = 6.4 microns

Etch Rate = 533 Å/min

TABLE 3.1 (Continued)

List of IBE Source Parameters During the Etching
of Lithium Niobate

Cathode Current I_c Beam (Anode) Voltage V_b

Neutraliser Current I_n Accelerator Voltage V_a

Beam (Anode) Current I_b Current Density J_c

Accelerator Current I_a Discharge Current I_d

Pump Down Pressure $- 6.10^{-6}$ Torr; Ar gas $- 10^{-4}$ Torr

I_c (A)	I_n (A)	I_b (mA)	I_d (A)	I_a (mA)	V_b (kV)	V_a (-kV)	J_c (mA/cm^2)
6.1	5.9	31	0.36	1.2	0.95	0.30	2.43
5.6	5.9	30	0.36	1.2	0.95	0.30	2.40
5.3	5.8	30	0.36	1.2	0.95	0.30	2.37
5.0	5.8	30	0.37	1.3	0.95	0.30	2.41
4.8	5.8	29	0.37	1.1	0.95	0.30	2.43
4.4	5.8	29	0.36	1.2	0.95	0.30	2.40
4.1	5.8	30	0.37	1.4	0.95	0.30	2.45
3.7	5.8	30	0.36	1.2	0.95	0.30	2.42
3.4	5.7	28	0.36	1.2	0.95	0.30	2.39
3.0	5.6	30	0.35	1.2	0.95	0.30	2.41

Time Space Between Each Row of Data is 10 minutes.

Total Etch Time = 90 min.

    Etch Depth = 8.55 microns

Etch Rate = 950 Å/min

3.5.6 Comments and Observations

The deepest groove etched by this method, although the process was not pushed to its extreme limit, was 12.6μm. The sample did not exhibit the same groove 'quality' as in figure (3.17) but this appeared to be mainly due to problems with the bulk crystal at that time. The highest etch rate was also recorded during this run although the system parameters were not different from the usual ones in Table 3.1. It is thought that the high etch rate (>0.1μm/min) could be attributed to the fact that the system was overhauled prior to these measurements, and thus the source parameters (which were dismantled and cleaned) have changed.

Due to the limitations of the home built system no measurements were made with ion angles of incidence other than normal to the target surface.

Ion bombardment has been used to selectively disrupt the surface layers of lithium niobate making it susceptible to wet chemical etching in HF [3.8]. Conversely it may be possible to selectively ion exchange surface regions on lithium niobate and modify the etch rate of those regions. Experiments were undertaken to measure any modification in the IBE etch rate of proton exchanged lithium niobate stripe regions (see chapter 5). If the proton exchanged regions etch at a much faster rate then the process may be useful in enhancing the ion milling process. However it was found that proton exchanged regions on lithium niobate etched typically 5% slower than the unexchanged surface regions. The difference in etch rates are so small that it does not appear to have any practical use.

3.6 Conclusions

It has been shown that good quality ion milled grooves can be etched into lithium niobate substrates with inert gas IBE. The quality of the groove is dependent on the quality of the masking layer. It has been shown that polyimide can be coated evenly

onto lithium niobate substrates with thichnesses of 15μm. The polyimide masking layer can be patterned by RIE in O_2, the resultant etch is highly anisotropic and produces a high quality masking layer which is an accurate reproduction of the aluminium etched pattern.

It was found that when etching deep structures in lithium niobate substrates the etch depth is not fully controllable. The cause of this is mainly due to the long etch times required e.g. 120 min. In a more practical IBE system there is a need to monitor the etch depth throughout the etching process and some method of end-point detection is required. There are several methods of end-point detection in ion etching systems at the present time [3.26]. The method most applicable is optical reflection interferometry. There will be problems with thickness monitoring using interferometry on an IBE system, not least that the target rotates to ensure an even current distribution over the target surface. However, it should be possible to modify the etching system to incorporate the optical reflectometer [3.26].

It would be advantageous to etch deep groove structures more rapidly than the required etch times in the order of 2-3 hours. Intuitively it can be surmised that a chemical etching process would yield much higher etch rates than for the purely physical case [3.25,3.28]. Apart from the possible increase in etch rate, a chemical etch process may have enhanced selectivity and thus thin masks may be used to achieve deep structures. Also reactive gases have been shown to have a polishing effect on the etched surfaces [3.15] which should yield smooth etched walls in the etched slot.

Basic chemical plasma etching of lithium niobate was not considered as viable for the following reasons. Photoresist cannot withstand much more than 15 minutes in a plasma system with reactive gases such as CF_4. Metal or possibly thick layers of polymer would be more suitable as masking materials. An asset of chemical etching with metal masks is that reactions between metals and reactive gases invariably form compounds with a very

low partial pressure (such as AlF) making the compounds difficult to remove and hence making an efficient masking material. However the findings of Lee and Lu [3.14], corroborated by Andonovic [3.15], show that virtually no etch occurs with the lithium niobate surface. The problem is that a 'white powder' forms on the substrate surface stopping the etch, which has to be rinsed off for the etch to continue. The halogenated compounds of niobium (such as Nb_2F_5) have a high partial pressure (i.e. they are highly volatile) and are readily removed from the system [3.27], and niobium metal is known to etch rapidly in CF_4. However, while lithium also reacts with halogens, e.g. LiF, the byproducts have extremely low partial pressures, and hence remain on the substrate inhibiting further etching unless removed by physical means.

Reactive ion etching of lithium niobate seems a more viable alternative to the etching of lithium niobate, since the process combines both reactive and physical etch mechanisms. Andonovic quotes 6:1 etch rate ratio for CF_4 reactive ion and plasma etch processes, stating that for the RIE process there was no evidence of the 'white powder' buffer surmising that it had been removed by the sputter action of the process [3.15]. An interesting observation by Andonovic was that the etch 'quality' of the RIE process is very high, going so far as to suggest that the process might be used for the chemical polishing of lithium niobate.

The bulk of work in the ion etching of lithium niobate should be directed towards the finding of a suitable masking layer for the delineation of lithium niobate by reactive as well as physical ion etching processes.

If we assume that the main problem with reactive ion etching lithium niobate is the formation of lithium salts, the simple solution is to remove the lithium from the region to be etched. This is not as difficult as it seems. Waveguiding regions may be formed on lithium niobate by an ion exchange process called proton exchange (see chapters 5-8). It has been shown that 70%

of the lithium in the exchanged region is removed and replaced with hydrogen. The possible process could be outlined as follows;

1) Pattern the LiNbO$_3$ substrate with a metal masking layer, as would be used in a normal reactive ion etching process.

2) Proton-exchange the patterned substrates in pure benzoic acid to a depth greater than the required etch depth. This process is the same as the process used to form proton exchanged stripe waveguides, where the metal layer protects the substrate with only the substrate exposed at the metal layer aperture exchanging with the acid.

3) RIE the prepared and exchanged sample.

It is expected that a far faster etch will be achieved, due to the lack of lithium in the etched region, and the profile of the groove should follow the shape of the exchanged region, which can be assumed to be rectangular (since planar waveguides formed have a step profile) [3.29,3.30].

CHAPTER 3 - REFERENCES

[3.1] A. Rauber
Chemistry and Physics of Lithium Niobate
Current Topics in Materials Science, Vol 1, Chapter 7
F. Kaldis Ed., 1978

[3.2] B. Zhang, S. Forouhar, S.Y. Huang and W.S.C. Chang
C_2F_6 Reactive Ion-Beam Etching of $LiNbO_3$ and Nb_2O_5 and
Their Application to Optical Waveguides
J. Lightwave Tech., vol LT-2, No.4, pp528-530, Aug 1984

[3.3] J.L. Vossen and W. Kern
Thin Film Processes
Academic Press, New York, 2nd Edition, 1978

[3.4] J.M.E. Harper
Ion Beam Applications to Thin Films
Internal Research Report
IBM Research Labs, Yorktown Heights, New York,
April 1980

[3.5] C.J. Mogab
Ion Beam, Plasma, and Reactive Ion Etching
Inst. Phys. Conf. Ser. No. 53, pp 37-54, 1980

[3.6] P.G. Gloersen
Ion Beam Etching
J. Vac. Sci. Technol., vol 12, No.1, pp28-35,
Jan./Feb. 1975

[3.7] C.M. Melliar-Smith
Ion Etching for Pattern Delineation
J. Vac. Sci. Technol., vol 13, No.5, pp1008-1022
Sept./Oct. 1976

[3.8]   M. Kawabe, M. Kubota, K. Masuda and S. Namba
         Microfabrication in LiNbO$_3$ by Ion-Bombardment-
         Enhanced Etching
         J. Vac. Sci. Technol., vol 15, No.3, pp1096-1098
         May/June 1978

[3.9]   M. Hatzakis, B.J. Canavello and J.M. Shaw
         Single Step Lift-Off Process
         IBM J. Res. Develop., vol 24, No.4, pp452-460
         July 1980

[3.10]   M. Cantagrel
         Comparison of the Properties of Different Materials
         used as Masks for Ion Beam Etching
         J. Vac. Sci. Technol., vol 12, No.6, pp1340-1343
         Nov./Dec. 1975

[3.11]   E.L. Hu and R.E. Howard
         Reactive Ion Etching of GaAs and InP using $CCl_2F_2/Ar/O_2$
         Appl. Phys. Lett., vol 37, No.11, pp1022-1024 Dec 1980

[3.12]   J.D. Chinn, I. Adesida, E.D. Wolf and R.C. Tibero
         Reactive Ion Etching for Submicron Structures
         J. Vac. Sci. Technol., vol 19, No.4, pp1418-1422
         Nov./Dec. 1981

[3.13]   A.P. Webb and C.D.W. Wilkinson
         Ion Beam Etching GaAs for Integrated Optical
         Applications
         Vacuum, vol 34, No's 1-2, pp159-162, 1984

[3.14]   C.L. Lee and C.L. Lu
         CF$_4$ Plasma Etching on LiNbO$_3$
         Appl. Phys. Lett., vol 35, No.10, pp756-758, Nov. 1979

[3.15]   I. Andonovic
         Ph.D. Thesis, University of Strathclyde, 1984

[3.16]   P.D. DeGraff and D.C. Flanders
         Directional Oxygen-Ion-Beam Etching of Carbonaceous
         Materials
         J. Vac. Sci. Technol., vol 16, No.6, pp1906-1908
         Nov./Dec. 1979

[3.17]   I.S. Goldstein and F. Kalk
         Oxygen Plasma Etching of Thick Polymer Layers
         J. Vac. Sci. Technol., vol 19, No.3, pp743-747
         Sept./Oct. 1981

[3.18]   J.H. Batsman, W. Gersey and D.S. Neiditch
         Soluble Polyimides Derived from Phenylindane Diamine: A
         New Approach
         Coatings and Plastics Papers, Presented at the Chicago
         ACS Meeting, vol 35, No.2, pp77-82, 1975

[3.19]   K.C. Vanner, N.F. Jacksond and S.J. Rhodes
         Applications of Polyimides in Microelectronics: RESIN
         AND CHIPS
         Phys. Bull., vol 35, pp158-160, 1984

[3.20]   Polyimide XU 218
         Specification Sheet and Laboratory Coating
         Recommendations
         Resins and Additives Division, Ciba-Geigy Corp,
         Ardesley, New York, 1981

[3.21]   M. Hatzakis, B.J. Canavello and J.M. Shaw
         Single Step Lift-Off Process
         IBM J. Res. Develop., vol 24, No.4, pp452-460,
         July 1980

[3.22]   Polyimide 'Selectilux' HTR-2
         Polimide Precursor Photoresist: Preliminary Data Sheet
         E. Merck, R&D Dept., Frankfurter Str. 250, D-6100
         Darmstadt 1, FRG   1984

- 49

[3.23] H.J. Merrem, R. Klug and H. Hartner
New Developements in Photosensitive Polyimides
ibid [3.42]   1984

[3.24] R.E. Chapman
Redeposition: A Factor in Ion Beam Etching Topography
J. Mat. Sci., vol 12, pp1125-1133, 1977

[3.25] S. Matsui, T. Yamaoto, H. Aritomi and S. Namba
Microfabrication of LiNbO$_3$ byReactive Ion Beam Etching
Jap. J. of Appl. Phys., vol 19, No.8, ppL463-L465
August 1980

[3.26] P.J. Marcoux and Pang Dow Foo
Methods of End Point Detection for Plasma Etching
Solid State Technology, pp115-122, April 1981

[3.27] T. Foxe, B.D. Hunt, C. Rogers, A.W. Kleinasser
and R.A. Buhrman
Reactive Ion Etching of Niobium
J. Vac. Sci. Technol., vol 19, No.4, pp1394-1397
Nov./Dec. 1981

[3.28] J.L. Jackel, R.E. Howard, E.L. Hu and S.P. Lyman
Reactive Ion Etching of LiNbO$_3$
Appl. Phys. Lett., vol 38, No.11, pp907-909, June 1981

[3.29] A.C.G. Nutt, K.K. Wong, D.F. Clark, P.J.R. Laybourn
and R.M. DeLeRue
Proton-Exchanged Lithium Niobate Slab and Stripe
Waveguides: Characterisation and Comparisons
2nd E.C.I.O., IEE Conf. Publ. No.227, pp53-56, Oct 1983
Florence Italy

[3.30] N.A. Sanford and W.C. Robinson
Secondary-Ion Mass Spectroscopy Characterization of
Proton-Exchanged LiNbO$_3$ Waveguides
Optics Lett., vol 10, No.4, pp190-192, April 1985

CHAPTER 4

RIGID LOCATION OF FIBRES ON LITHIUM NIOBATE WAVEGUIDES
USING ION MILLED GROOVES

4.1 Introduction

In order to be able to make practical use of the large number of integrated optical devices demonstrated on lithium niobate [4.1,4.2,4.3], as well as on other substrates [4.3,4.4,4.5], it is essential to produce stable, repeatable and high efficiency coupling between optical fibres and the optical waveguides incorporated into such devices.

The transfer of power between an optical fibre and an integrated optical waveguide occurs in two main ways. The first being transverse or evanescent field coupling [4.6] in which the evanescent field from the fibre interacts with, and excites, a guided mode in the waveguide. This effect is usually enhanced with the aid of a taper in the waveguide along the interaction region. This effect, called taper velocity coupling [4.7,4.8] provides the necessary degree of phase matching which allows maximum power transfer between the fibre and waveguide to occur. The second method of coupling power between an optical fibre and waveguide is longitudinal or butt coupling [4.9] in which the optical field emerging from the cleaved end of the fibre is launched into the polished end of the optical waveguide. The spatial matching of the optical fields of the fibre and the waveguide and their longitudinal alignment are largely responsible for the amount of power transfer between the two lightguides. Of the above two coupling methods the one favoured most is butt coupling, due to its relative simplicity. Tapered velocity coupling on lithium niobate has very high fabrication tolerances [4.10] (although to some extent with proton exchange technology these problems are being aleviated [4.11]). This chapter will discuss the butt coupling process.

In butt coupling, high efficiency can be achieved by varying the relative position of the fibre to the waveguide held in close proximity while monitoring and maximising the output. If attention is also paid to the modal field mismatch [4.12] good coupling efficiencies can be obtained [4.13,4.14,4.15]. However, this method is complex (as intricate micro-alignment stages are needed with 0.1um resolution), unstable (the fibre needs to be bonded to the waveguide with very little support) and since each fibre needs the same degree of alignment the method is unsuitable for multiport devices. The method is also industrially impractical.

The use of silicon V-grooves [4.16] can substantially aid the alignment process and permit low-loss, and to some degree, repeatable coupling. The use of multiple V-grooves has also been shown to facilitate the coupling of fibre arrays to devices [4.17] even to the extent of the production of packaged devices [4.18]. However, the method still has major difficulties concerning the problem of the alignment of the V-grooves to the waveguide array, and these coupled with the considerable difference in thermal expansion coefficients of the silicon compared to that of the lithium niobate substrate gives rise to undesirable instabilities.

A more attractive arrangement was proposed by McLachlan et al. [4.19,4.20] making use of ion milled alignment grooves which are positioned on the device substrate surface. The grooves are defined by conventional photo-lithography. One advantage is that a large number of grooves may be defined on one substrate with no increase in the number of fabrication processes. The groove parameters, if suitably controlled, should provide rigid, repeatable and high efficiency coupling.

Although the groove coupler was proposed, the component that was tested failed to operate due to problems in the ion etching process, these problems have since been resolved (see chapter 3). This chapter is concerned with the realisation and analysis of the proposed groove coupler.

4.2 The Coupling Component

As is shown in figure (4.1), the fibre/waveguide coupling is facilitated by inserting an etched fibre into a square section ion milled groove on a Z-cut lithium niobate substraté. The fibre is held rigidly in the groove, with the groove dimensions and position relative to the waveguide controlling the fibre alignment. The light emerging from the fibre is thus launched into the waveguide.

The fibre has to be etched due to the depth limitations imposed on the ion milled groove by the process parameters (see chapter 3) i.e. the groove depth is limited therefore the fibre diameter has to be reduced to make butt coupling possible.

4.3 Inherent Losses in the Coupling Component

The coupling component (4.1) can be said to have five main loss mechanisms (although the experimentally measured insertion loss has more).

To gain an accurate understanding of how the component functions, each of these four main losses would have to be analysed.

These losses are:

i)   Fresnel loss; the loss due to reflection when the light propagating encounters the index mismatch at the fibre/air and the air/waveguide boundaries. Another effect related to Fresnel loss is the localised Fabry-Perot effect which occurs when a Fabry-Perot-like structure is set up between the flat end faces of the fibre and the waveguide. This effect has been monitored and causes large instabilities in the case of perfect fibre waveguide alignment (see section 4.7).

ii)   Scatter loss; any discontinuity or roughness in the fibre end-face or in the groove walls, base or end-face will cause a perturbation of the evanescent field of the fibre or the longitudinally propagating light resulting in scatter losses.
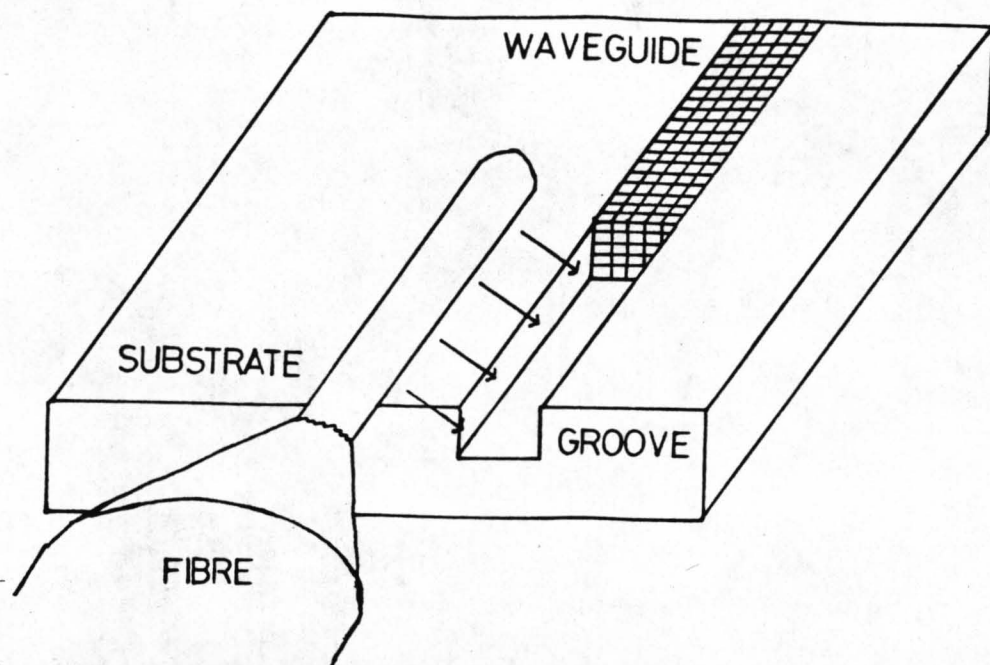
Figure (4.1): Schematic Diagram of Fibre/Waveguide Coupler

Some of these losses can be experimentally measured (see section 4.9).

     iii) Alignment loss; the effects of both positional and angular misalignment on the insertion loss between a fibre and a titanium diffused waveguide. These losses have been quantified by Noda [4.21,4.22] for a titanium diffused waveguide which supported four modes (two TE and two TM). These measurements are repeated in section 4.6 where both a single mode fibre and waveguide is used (at wavelengths of 633nm and 1152nm).

     iv) Field mismatch; for maximum power to be transferred between two optical fields they must be as much alike as is possible. There have been various methods of measuring the degree of optical field mismatch and obtaining the power transfer between such fields [4.12,4.15]. In section 4.5 a new method will be proposed which utilises the complete three dimensional image of the optical fields.

     (v) Mode Sinking; leakage of light into higher index substrate For the total insertion loss to be analysed other loss factors will have to be taken into account, such as the propagation losses and losses in the transition region of the etched fibre taper (see sections 4.4,4.5).

4.4 Fibre Etching

The fibre used in these experiments was produced by British Telecom is single mode at $\lambda = 1.3$ µm wavelength, with a cut-off wavelength of 1.14 µm. The fibre has a 1/e core diameter of 3.88 um and an outside diameter (O.D.) of 100 µm.

Previous work investigating the etching of this fibre [4.23] in buffered hydrofluoric acid had shown that the end of the fibre formed a cone shape, see figure (4.2), which was unsuitable for butt coupling to a waveguide. It is well known that the etch rate of doped glasses is dependent on dopant species and concentration [4.24]. In particular, with hydrofluoric acid as an etchant, the relative etch rate is also dependent upon the buffer (ammonium fluoride) concentration [4.25]. Other workers
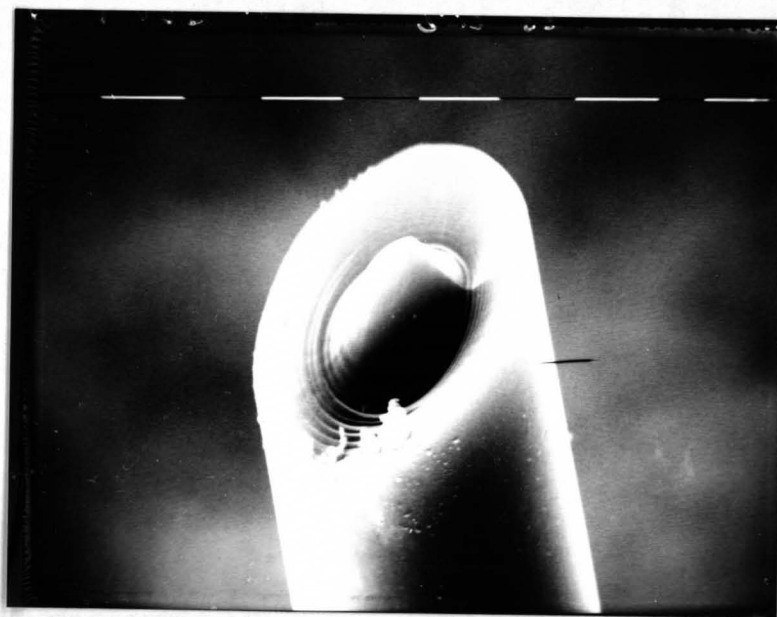
Figure (4.2): S.E.M. of Cone Shape Created at the Fibre End after Etching in Buffered HF (10μm markers)
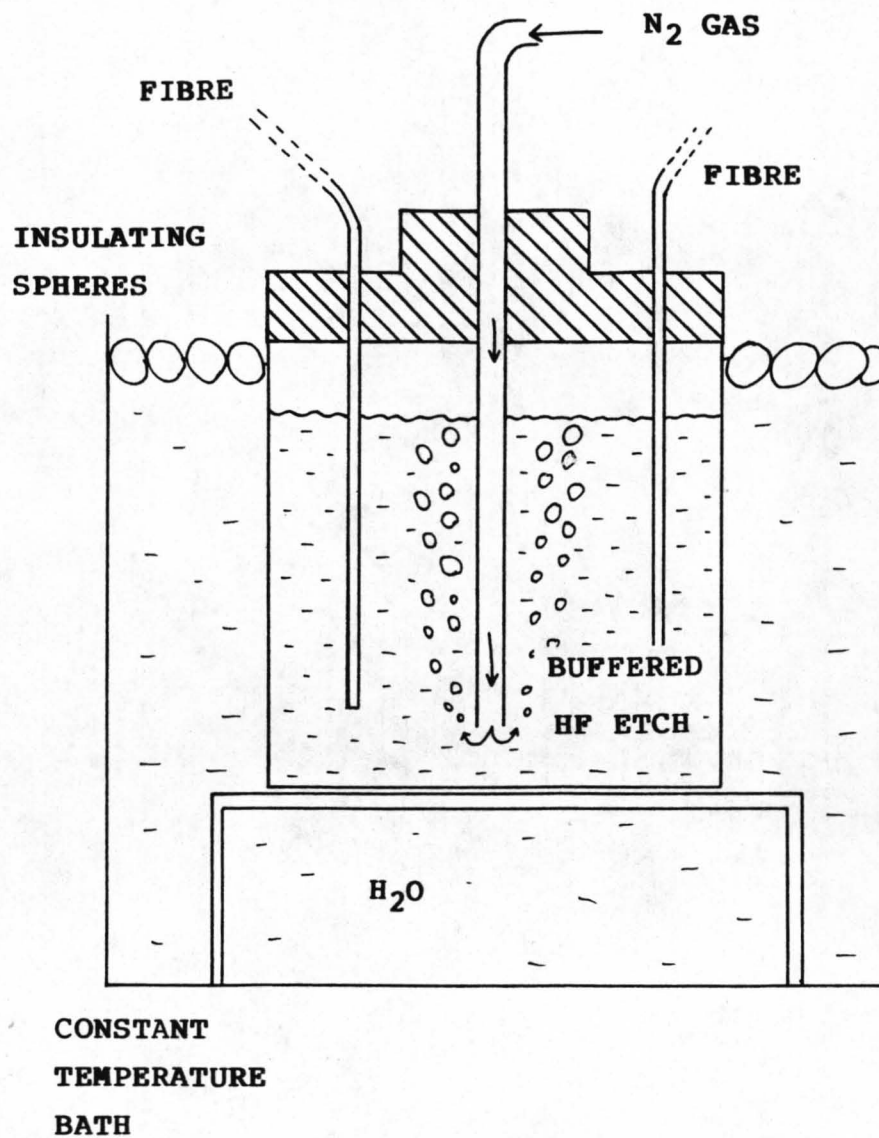
Figure (4.3): Schematic Diagram of Fibre Etching Apparatus
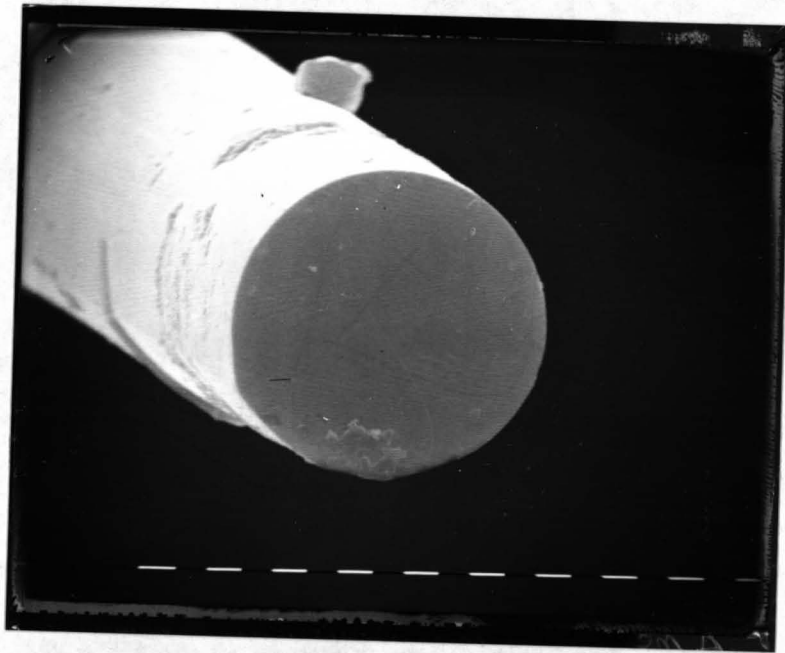
Figure (4.4): S.E.M. of Etched Fibre End-Face after Polishing
(1um markers)

[4.26,4.27] have used this dependency to form chemically, lens shaped end-faces on a fibre and to reduce the fibre diameter to leave the core which then may be used for alignment purposes. The possibilities of forming a micro-lens on the end of the fibre is an interesting section of work, however with the end-polished fibre the constituent losses of the coupler are easier to quantify and it was felt that the inclusion of another factor would detract from the basic problems to be investigated in the coupling component.

With Isoform 7:1 buffered etch, the total etch time to reduce the fibre diameter from 100 μm to 15 μm was approximately 150 min at 40°C. It was found that with acid from the same bath, the variation in the fibre etch rate was less than 5%. Obviously this will result in a possible error of up to $\pm$ 4.5 μm in the diameter of the final fibre, and therefore it is necessary to monitor the process by using test fibres to check the etch progress. With this approach the fibre O.D. may be controlled to within $\pm$ 0.5 μm. The error is determined by the measurement process. Variations in etch rate of up to 17% were found with tests carried out with buffered etchant from batches of different age. A diagram of the fibre etch set-up can be seen in figure (4.3).

Previous work carried out at Glasgow University [4.28] showed that it was possible to achieve a flat fibre end-face by polishing the etched fibre. The fibre is potted in tan wax in a 400 um diameter glass capillary, which is mounted in a mechanical support on a standard polishing jig. After polishing the capillary may be heated and the fibre removed from the molten wax to be cleaned in trichloroethane. A scanning electron micrograph of the polished end of a fibre can be seen in figure (4.4) which can be compared with the unpolished fibre in figure (4.2). For ease of handling the etched fibre was kept mounted in the glass capillary with the etched portion protruding from the end. The unetched to etched fibre transition region, i.e. the taper region, can be increased by reducing the the level of the acid in the bath as the etch procedes. This gives the junction a
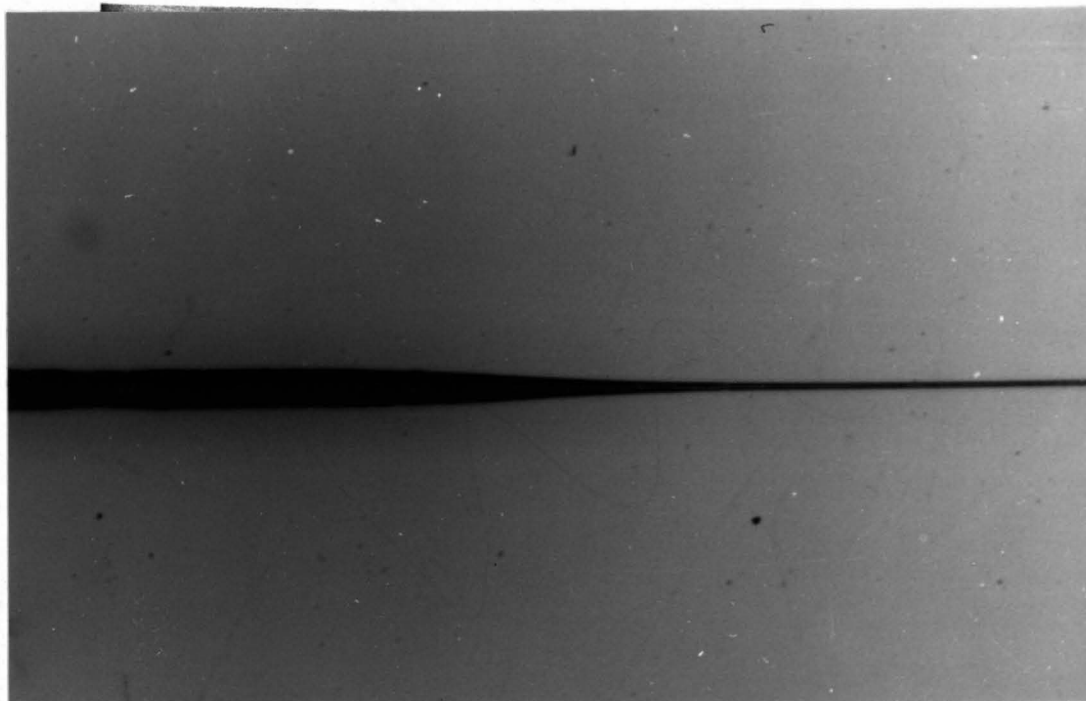
Figure (4.5): Photograph of Fibre to Etched Fibre Tapered
Transition Region

higher degree of flexibility and resilience than in the abrupt junction case, see figures (4.5).

4.5 Field Overlap Calculations

In order to select waveguides which would allow maximum power to be transferred between fibre and waveguide, calculations were performed to determine the loss that is due to spatial mismatch of the two optical fields. Initially it was observed that for a given set of waveguide fabrication parameters more symmetrical field profiles were evident on Z-cut substrates. This may be due to the fact that the c-axis has a slightly larger diffusion coefficient [4.28] which has the effect of pulling the titanium and hence the waveguide profile deeper into the substrate. This being established it was found that Ti:indiffused waveguides formed with an 87nm film of titanium at 980°C and diffused for 40h in wet flowing oxygen produced waveguides which were relatively symmetrical and were an excellent match for the field distribution of the fibre. Waveguides were fabricated under these conditions with widths ranging from 2 - 10 μm. The titanium stripes were patterned using the standard lift-off process [4.29] and were indiffused (as above) in the standard manner [4.30].

The end polished waveguides were excited with a semiconductor laser operating at 1.32μm wavelength, and the resulting near field profiles were imaged by a 40X (0.65 N.A.) microscope objective onto the vidicon screen of a Hamamatsu camera [4.32]. With the associated image analyser and a PDP 11/45 computer it was possible both to display the optical near field pattern and record the intensity at each of a maximum number of 1024x1024 points in the pixel array. The number of pixels used however was only 256x256 which was sufficient because of the limiting resolution of the optics. The resolution of the system was 1 μm which was defined by Abbe's criterion [4.31]. A schematic of the camera set-up can be seen in figure (4.6).

NEAR−FIELD OPTICAL IMAGE PROCESSING SYSTEM
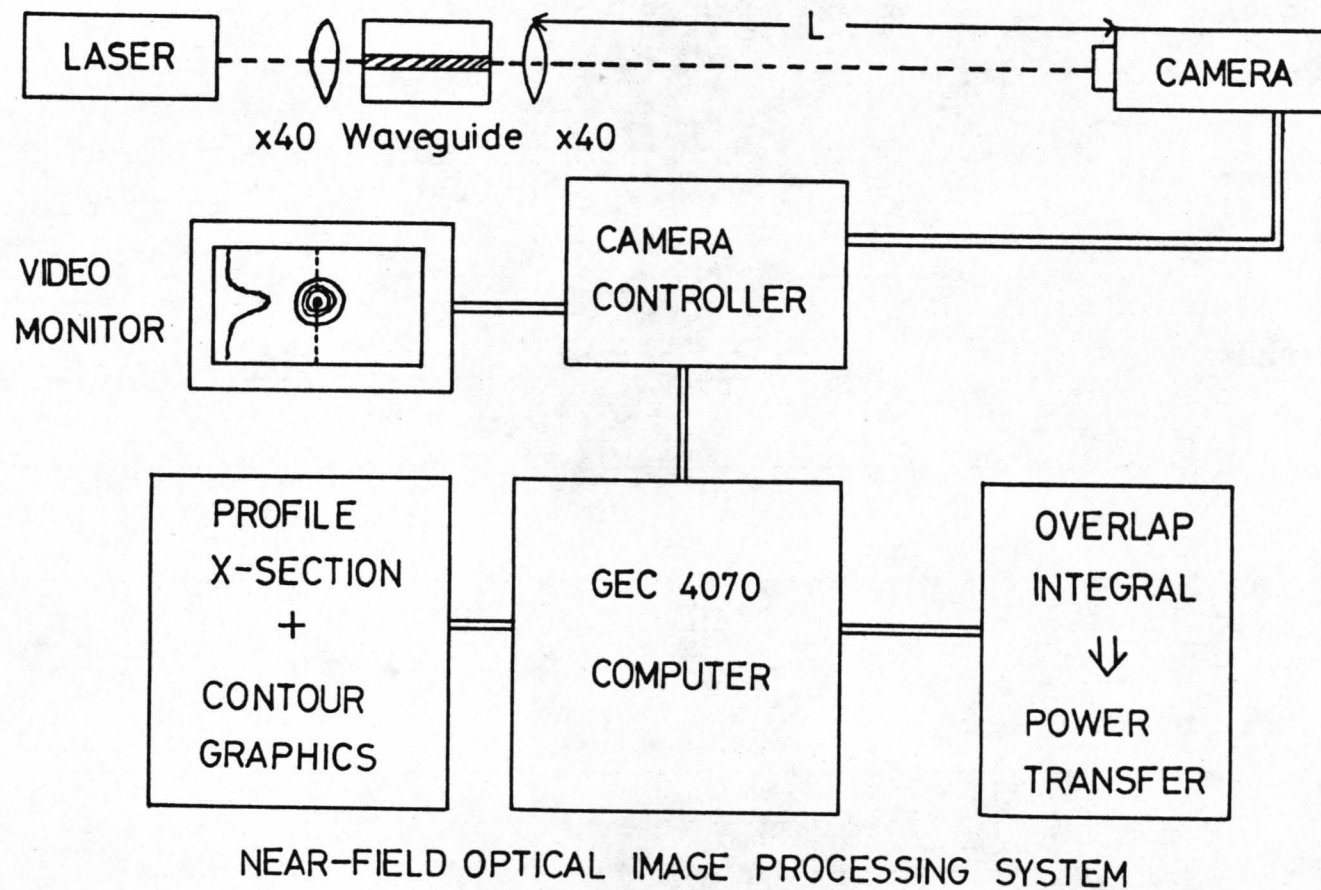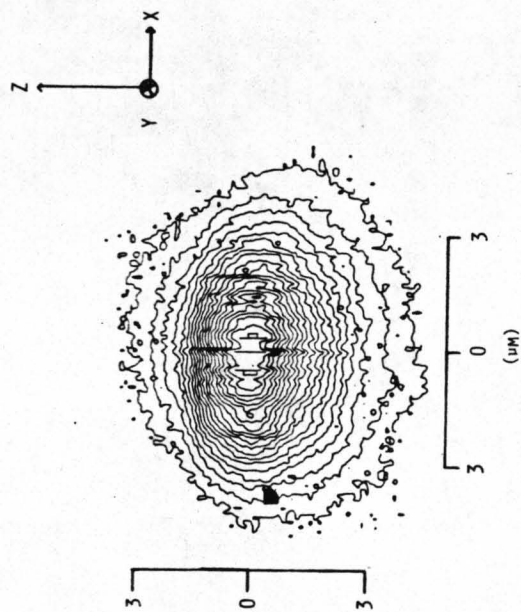
Figure (4.6):

FIELD INTENSITY DISTRIBUTION OF A Z-CUT Ti:DIFFUSED WAVEGUIDE

6 uM WIDE AT λ = 1.3 uM

(A)
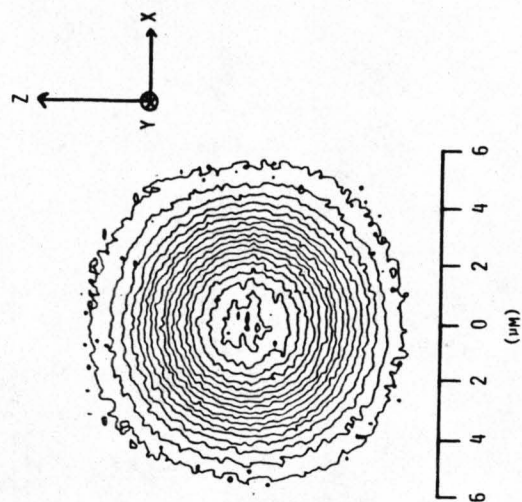
FIELD INTENSITY DISTRIBUTION OF A SINGLE-MODE

FIBRE AT λ = 1.30 uM   AND

CORE DIAMETER = 3.88 uM

(B)

Figure (4.7) :

By transferring the matrix data to a computer with graphics capability, the contour plots shown in figure (4.7) were produced. The plots are of the near field intensity distributions of the cleaved optical fibre and of a 6μm wide waveguide diffused under the above conditions. A conventional definition for the overlap integral may be used to compare the loss that is due to the modal mismatch [4.12] where for optical fields E_1 and E_2 the square of the coefficients η gives the power transfer being defined by

$$\eta = \frac{\displaystyle\int\int_{-\infty}^{\infty} E_1 E_2 \, dxdy}{[\displaystyle\int\int_{-\infty}^{\infty} E^2_1 \, dxdy \int\int_{-\infty}^{\infty} E^2_2 \, dxdy]^{1/2}}$$

However, since the computer records the linear intensity at a finite number of points, the power transfer may be expressed as

$$K = \frac{[\sum_i \sum_j \sqrt{I_1} \sqrt{I_2}]^2}{\sum_i \sum_j I_1 \sum_i \sum_j I_2}$$

where I_1 and I_2 are the values of intensity taken from the Hamamatsu digitised array (I_1 is the profile distribution of the fibre and I_2 is the profile distribution of the Ti:indiffused waveguide), linear polarisation and single mode propagation being maintained throughout.

The field overlap calculation was performed by using the data from each waveguide and from the optical fibre (both cleaved and etched/polished). Figure (4.8) shows the variation of power transfer with waveguide width for the two fibres and eight waveguides. Although the spread of the data was too large to enable an exact value of the optimum width of the waveguide to be found, it is observed that there is a general peak for the
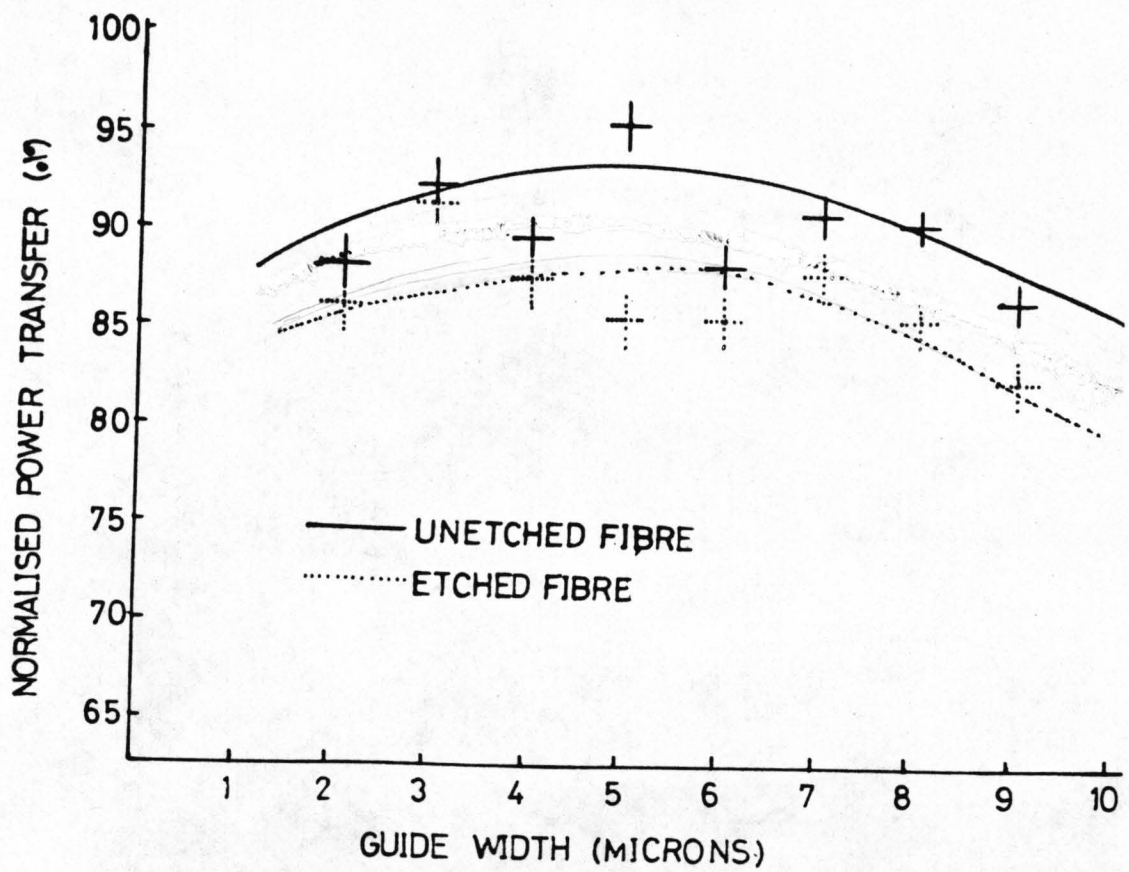
Figure (4.8): Graph of Normalised Power Transfer Calculated from Overlap Integrals of Etched and Unetched Fibres with Ti:indiffused Waveguides on Lithium Niobate (widths ranging from 2 - 8 um).
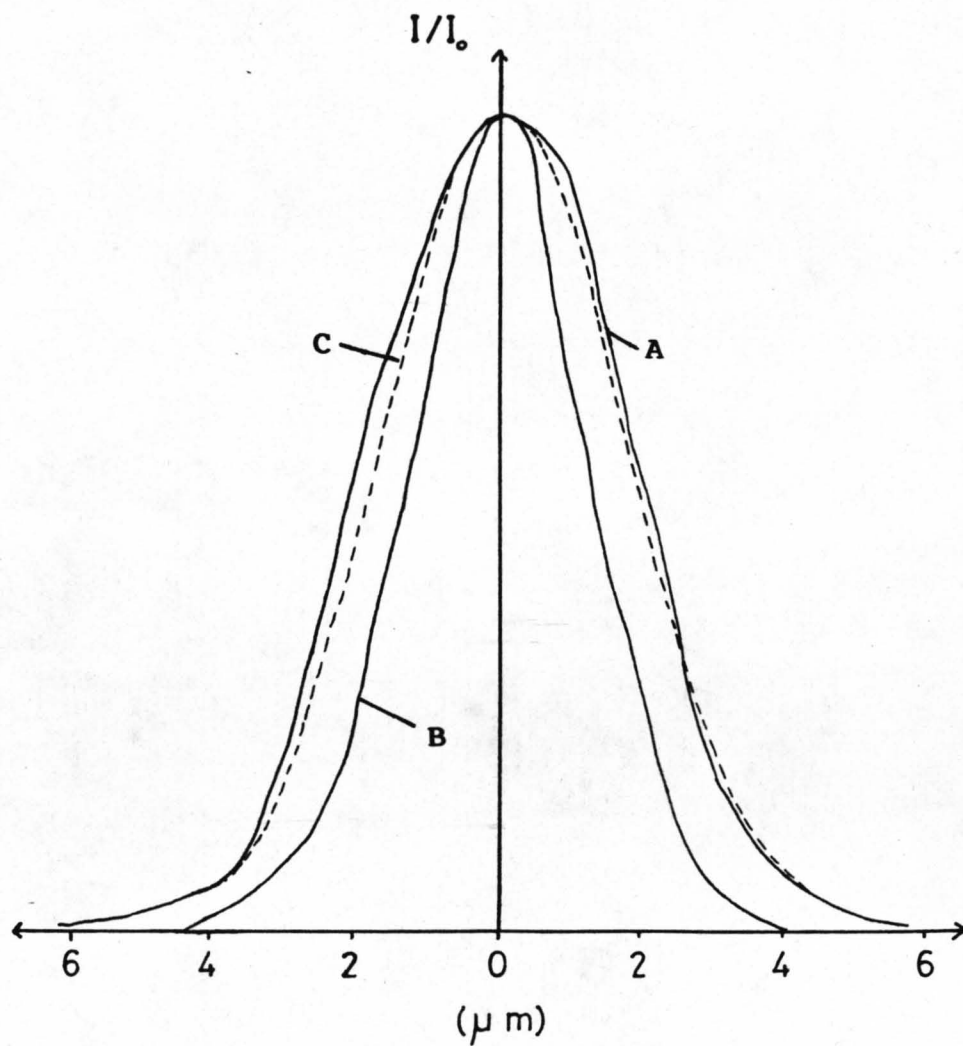
Figure (4.9): Normalised Intensity Distributions of;

      (A) Cleaved Fibre

      (B) Etched Fibre

      (C) Horizontal Distribution of Ti:diffused

           Waveguide on Z-cut Lithium Niobate
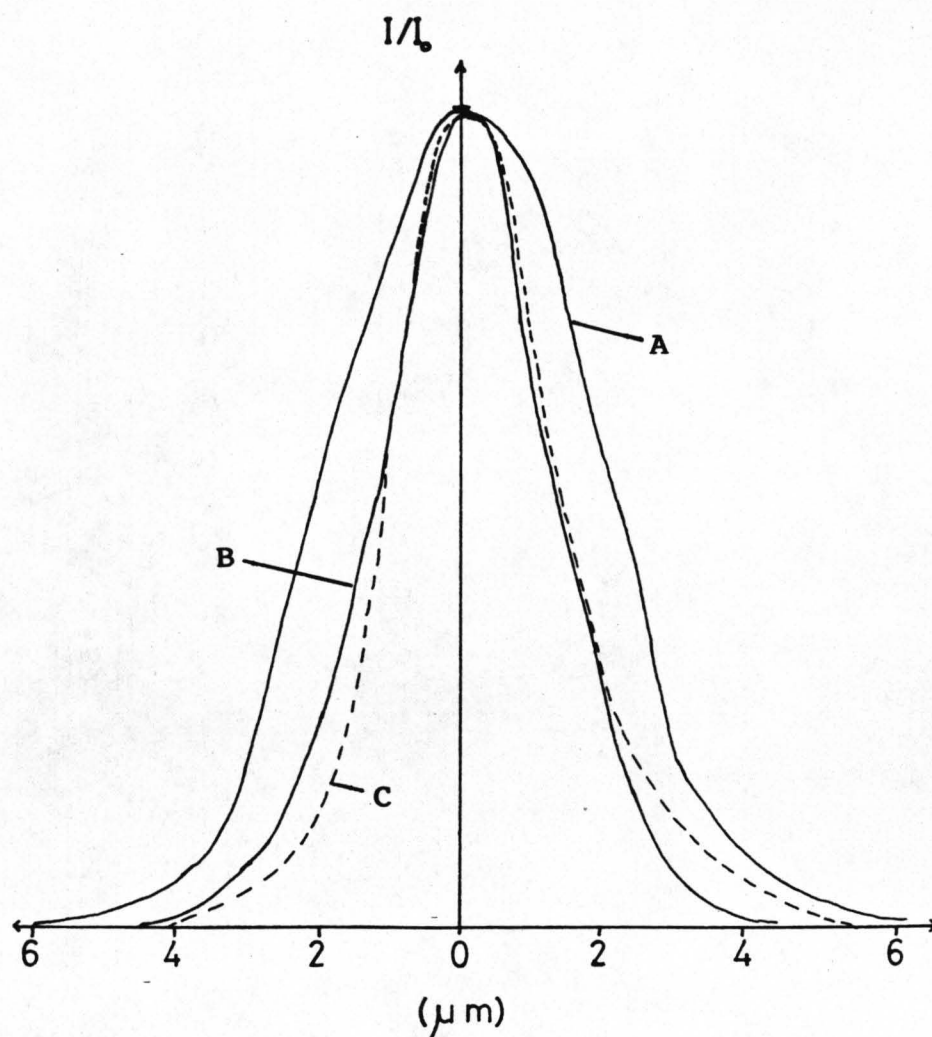
           (6um wide stripe)

Figure (4.10): Normalised Intensity Distributions of;

(A) Cleaved Fibre

(B) Etched Fibre

(C) Vertical Distribution of Ti:diffused Waveguide on Z-cut Lithium Niobate (6um wide stripe)

unetched fibre in the region of 6µm (94% power transfer) and that etching the fibre reduces the power transfer by approximately 5%. This drop of 5% in the power transfer seemed to be very small considering the large change in spot size of the etched fibre as compared with the cleaved fibre.

Contour plots are 3-dimensional and as a result misleading. Figures (4.9) and (4.10) shows normalised cross-sectional distributions of the cleaved and etched fibres as well as for the 6µm wide indiffused waveguide (the titanium indiffused waveguide has both its horizontal, (4.9), and vertical, (4.10), distributions plotted).

In figure (4.9) the match between the cleaved fibre and the horizontal distribution of the waveguide is clearly evident, whereas with the etched fibre there is a definite mismatch between its profile and the other two profiles. This would suggest that the power transfer drop for the etched fibre should be much greater than the estimated 5%. However examination of the vertical distribution of the indiffused waveguide and the fibre distributions shows that now the etched fibre matches closely with the diffused waveguide and the cleaved fibre has a considerable mismatch, figure (4.10).

Two conclusions may be drawn. To achieve a good coupling efficiency between a fibre and a titanium diffused waveguide it is necessary that the two principal profiles of the waveguide matches accurately with the fibre distribution. The difference in loss between the etched and unetched fibres could be attributed to their respective mode field widths. Secondly, the diffusion time and therefore the profile of the waveguide could be made much smaller so that there would be a match between the horizontal distribution of the waveguide and the distribution of the etched fibre. This would result in the component using waveguide dimensions which are more useful for devices, i.e. a more efficient electro-optic and/or acousto-optic interaction.

It must be noted that waveguides fabricated under different

conditions give different coupling properties, and as such the measurements made are only valid for the above material and diffusion conditions [4.34].

The maximum estimated power transfer for the 6um waveguide and the cleaved fibre was 94% and for the etched fibre 89%. These values are only field overlap losses and are not to be mistaken for total insertion loss. The 94% power transfer is the highest value quoted for field distribution matching in the literature for fibres coupling to Ti:diffused waveguides. This value assumes that the profiles are perfectly aligned and that the phase across the field profiles are constant. Other values quoted in the literature are in the range 80 - 85% [4.33,4.34] but these values are obtained from calculations using the profile widths measured from cross sectional field distributions (as in figures (4.9) and (4.10)) and not from the full three dimensional experimental field profiles.

4.6 Ion Milled Grooves

The most important part of the coupling component is the ion etched alignment groove. Delineation of the groove is critical to the operation of the coupler and to its total insertion loss.

Chapter 2 outlines many ion etching processes but the one most readily available at the time of the experiment, and probably the most useful, for the formation of the slot was inert argon ion milling.

The necessary properties of a satisfactory ion etching technique for alignment grooves are:-

1) High Etch Rate; the grooves were limited to a depth maximum of approximately 7μm, and hence the width of the groove was somewhat arbitrarily defined to be 10μm wide. Thus at etch rates of 500Å/min the process would take 140min. Therefore from purely the point of view of process time, slow etch rates are undesirable and higher etch rates desirable. Inert argon ion

milling can easily achieve etch rates of 500Å/min and more importantly polymer masking of the substrate enables the deep grooves to be fashioned.

2) Square Section Groove; in order to achieve the necessary insertion loss the slots must have perpendicular end-face and a square cross-section. Any angular slant on the wall would result in angular misalignment of the fibre and the waveguide i.e. between the fibre and the waveguide would be a sloping interface.

3) Wall/Surface Quality; although other ion etching processes exhibited much better wall quality, it is evident that with 1) and 2) being satisfied by the argon ion milling process, the observed ripples in the wall and end-face of the groove (which will cause scatter losses) are acceptable, at least for the prototype coupler.

4) End-face Flatness; when the shape of the ion milled groove is transferred via photolithography to the aluminium layer (required for the delineation of the polymer masking layer) the corners of the groove, although perfect in the mask, become rounded. This was overcome by making the end of the groove, on the mask, into a T-shape, see figure (4.11), enabling a flat end-face to be repeatably obtained (neglecting the presence of surface roughness).

A 40nm etch rate was obtained with a 1keV beam potential and a beam current density at the target of between 2-3mA/cm^2. This resulted in a series of substrates with groove depths ranging from 4.8µm-7.6µm depending on the etch period. Figure (4.12) shows electron micrographs of a) an argon ion milled groove cross-section, and b) the end-face of an argon ion milled groove. From figure (4.12) the quality of the ion milled grooves can clearly be seen, the emphasis on a) being the 90° wall profile and on b) the amount of surface roughness which is about 1µm period with 0.25µm amplitude. The wavelength to be used in the coupling experiment is 1.3µm therefore the wall roughness is of comparable magnitude with the wavelength and hence will scatter the light propagating in the fibre.
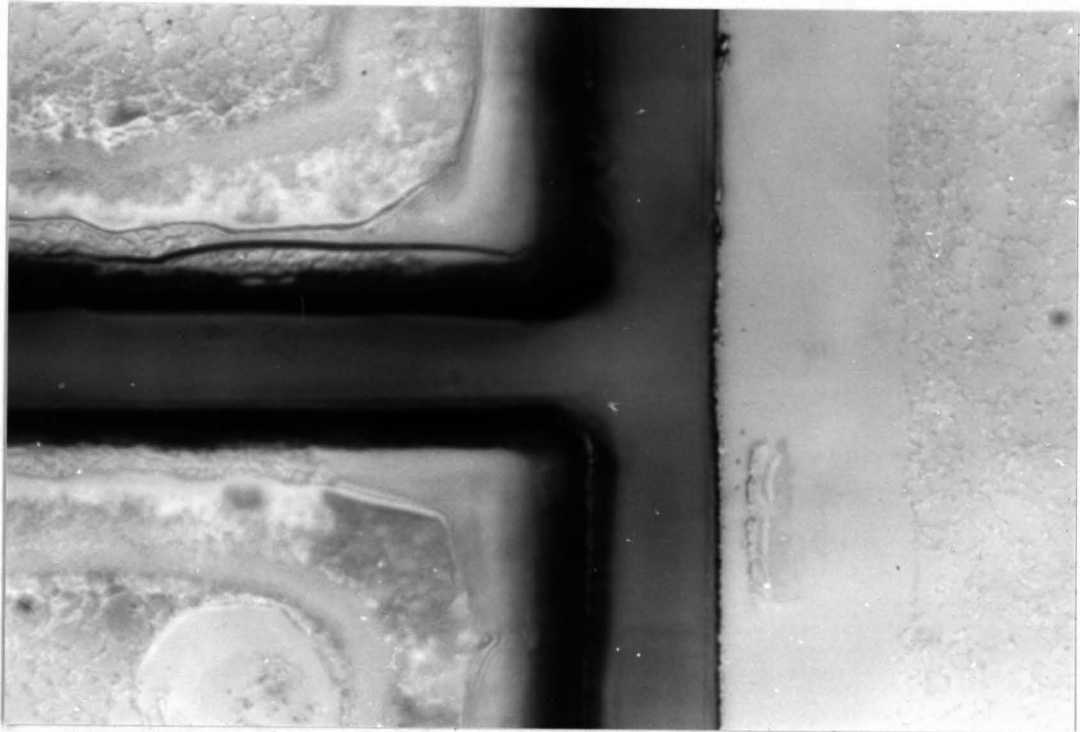
Figure (4.11): Photograph of Revised T-shape Groove to Counteract End-Face Rounding
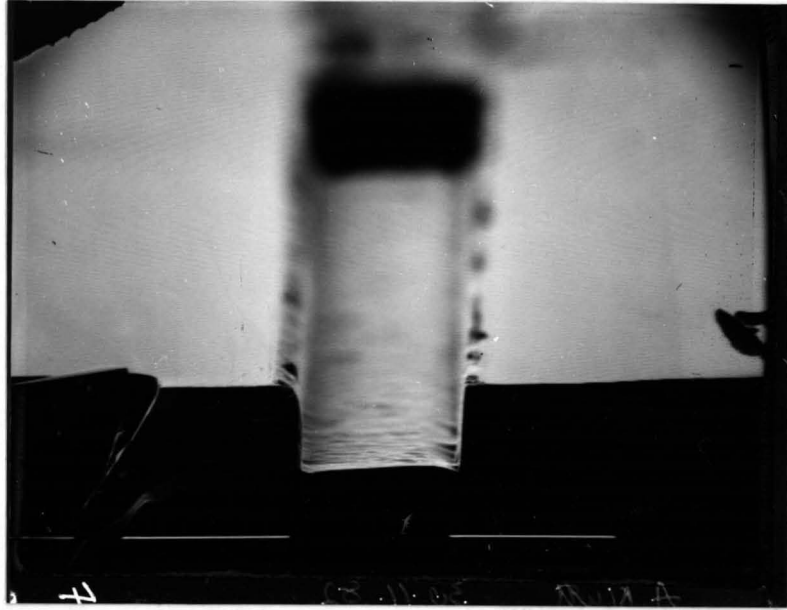
a) S.E.M.of the Cross-Section of an Ion Milled Groove

(10um markers)
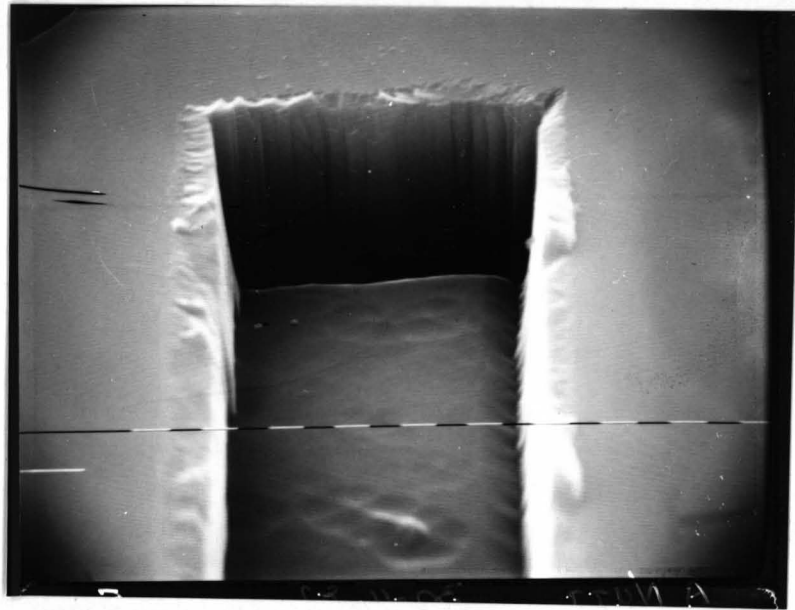
b) S.E.M. of the End-Face of an Ion Milled Groove

(1um markers)

Figure (4.12):

4.7 The Problem of Alignment Related to Losses, Reflection and Chip Realisation

Alignment is of importance in many of the aspects of the coupling component, both in the chip realisation and performance.

In making the chip the main problem was whether to first produce the waveguides then align the grooves to them or to first form the grooves and risk possible edge effects at the groove-waveguide boundary. Experimentally it was found to be extremely difficult, if not impossible, to achieve the former. The main problem was that the groove mask had to be aligned on top of the masking layer which was effectively 20μm above the waveguide surface. This fact meant that it was not possible to focus on the waveguide and groove mask at the same time, hence alignment was impossible (or at best somewhat intuitive).

Aligning the waveguide mask to the ion milled groove proved to be very straightforward, However there was some indication of edge effects at the interface, i.e. the resist pattern and hence the waveguide narrowed slightly. The narrowing, however, did not occur on all substrates suggesting that mask contact with the substrate was to blame. If the problem was persistent a mask could have been made with a small taper or horn at the waveguide end to alleviate the narrowing effect [4.35].

The overlap integral and thus the power transfer between fibre and waveguide were calculated for perfect alignment. The alignment is a function of the component parameters and hence may not be optimum. Investigating the effects of misalignment gave some indication of the required tolerances for angular and positional misalignment as well as an insight into instabilities caused by a localised Fabry-Perot effect, the work mainly covered by G. Henderson, final year student, under the author's supervision [4.36]. The bulk of the alignment measurements were made at 0.633μm, with some measurements at 1.15μm (the 1.3μm laser being unavailable at the time) and gave a clear indication of the tolerances.

The fibre used for the 1.15µm wavelength experiments was the BT fibre since its single mode cut-off was specified to be 1.14µm. The resolution of the goniometers in the series of experiments was 0.1µm for position and 0.1 degree for angular movement. The waveguide used in the infra-red experiment was single mode on Z-cut lithium niobate (865Å of titanium, 2um wide, diffused at 980°C for 20 hours). The results with single mode fibre and waveguide at 0.633µm were very similar to that of Noda [4.21,4.22], and are summarised in Table 4.1, assuming the nomenclature of figure (4.13). The tolerance is quoted as the misalignment necessary to reduce the output power by 5%.

The increase in wavelength (and hence the fibre and waveguide profile dimensions, see Table 4.1) increases the positional tolerances, and at 1.3µm a further increase in tolerances should be expected. Although the angular data was not available at 1.15µm it is to be expected that there will be a decrease in angular tolerance at longer wavelengths [4.39].

Translating the significance of these tolerances onto the groove coupler the following can be surmised, assuming controllable fibre dimensions.

X-axis misalignment occurs at the coupler photolithographic stage. A 6um waveguide has to be aligned with a 10µm wide groove. The quoted tolerance is at least 0.4µm whereas alignment in this axis should be achievable to within 0.1µm, and hence should not be a major contributor to loss.

Y-axis misalignment occurs if the fibre is not placed at the end of the groove or if the ripples in the groove end face allow the presence of a small cavity (see below). The tolerance is at least 0.45µm and should not present any problems, excluding instabilities which will be discussed below.

Z-axis misalignment occurs if the groove depth is either too great or too small. Depth control of the groove is difficult (see chapter 3.4), however since the tolerance is at least 0.5µm the problem can be overcome with the minimum of loss incurred.

TABLE 4.1

List of Tolerances for Fibre/Waveguide Misalignment
at 0.633 µm Wavelength

%I/I_O	X (µm)	Y (µm)	Z (µm)	α (°)	β (°)
95%	0.12	0.14	0.25	0.55	0.25
90%	0.20	0.32	0.40	0.76	0.35

List of Tolerances for Fibre/Waveguide Misalignment
at 1.15 µm Wavelength
(The data does not include angular measurements)

%I/I_O	X (µm)	Y (µm)	Z (µm)
95%	0.40	0.45	0.50
90%	0.72	0.83	1.00

Figure (4.13) Shows the Axes to which Table 4.1 Corresponds.
The tolerances quoted are for misalignment from the centred axis.

Diagram Defining Axis Orientation for
Misalignment

Figure (4.13):

Basically the groove should always be on the deep side allowing the possibility of filling the groove with sputtered SiO_2 to achieve the required depth.

α^o misalignment occurs at the photolithographic stage. The tolerance at 1.3µm can be assumed to be greater than that of 0.633µm i.e. 0.55^o. This alignment problem should not be significant since with the mask aligner 0.1^o alignment offset is easily achievable.

β^o misalignment is a function of the 'squareness' of the cross-section of the ion milled groove. The tolerance at 0.633um is 0.25^o and should be much smaller at 1.3µm. Observations have shown (see chapter 3) that the walls of the ion milled grooves are perpendicular and hence the problem of β misalignment can also be considered minimal.

The concentricity of the fibre core, if not consistent, will cause alignment problems, and this is somewhat of an unknown quantity. From the measurements discussed below it can be surmised that the alignment problem due to the fibre eccentricity is a 2nd order effect and that, with the improvement in fibre technology, it should not add another factor to the constituent losses.

From the above it can be noted that the main problem for alignment is in the groove depth.

A subject very rarely discussed or even mentioned in fibre-waveguide coupling papers is the localised Fabry-Perot effect which occurs between the fibre and waveguide if they are 'perfectly' aligned and in close proximity to each other. The resulting effects are mainly referred to as 'instabilities' [4.14] to be reduced by slight misalignment or the use of an index matching fluid. Indeed what is surprising is that Noda [4.21,4.22] when researching into the effects of fibre misalignment with integrated optic waveguides did not even mention the existence of such effects, which within the series of

experiments he considered should have been easily observable.

Interference instabilities were measured at 0.633μm and 1.15μm in the following manner. Using single mode fibre and waveguides at both wavelengths and utilising the better than 0.1μm movement resolution of the Micro-control goniometer stages the fibre was perfectly aligned to the integrated optical waveguide. The fibre was positioned against the waveguide such that a waveguide output maximum ocurred. This value was therefore the value by which the measurements would be normalised. The fibre was then pulled back axially from the waveguide and the waveguide output was monitored. The results take the form of either values at discreet distances between fibre and waveguide or of a continuous chart recording (which caused problems with distance calibration but which gave a continuous recording of the effects).

Figure (4.14) a) is a plot of waveguide output as a function of fibre/waveguide separation (at 0.633μm), the values of waveguide output being taken at discrete steps and a curve fitted to the data. Figure (4.14) b) is a plot of waveguide output as a function of fibre/waveguide separation (at 1.15μm), the plot is a continous recording of the effect as the fibre is drawn axially away from the waveguide.

From figure (4.15) a) it can be seen that there is a definite fluctuation in the output waveguide intensity over the first micron of separation. From an analysis of the basic operation of a Fabry-Perot etalon using the fibre/air and air/waveguide boundaries as reflectors (chapter 4 appendix) the minimum transmitted intensity is 0.743. However, from the figure, it is noted that minimum transmissions of 0.06 and 0.03 were recorded and these values were steady state and hence were not due to transient effects. The position of the maximum and the two minima were roughly in the $\lambda/4$ area's which did suggest that the effect was similar to an etalon but there must be other much more significant factors which contribute to such a drastic effect.

From figure (4.14) b) the measurement technique was continuous
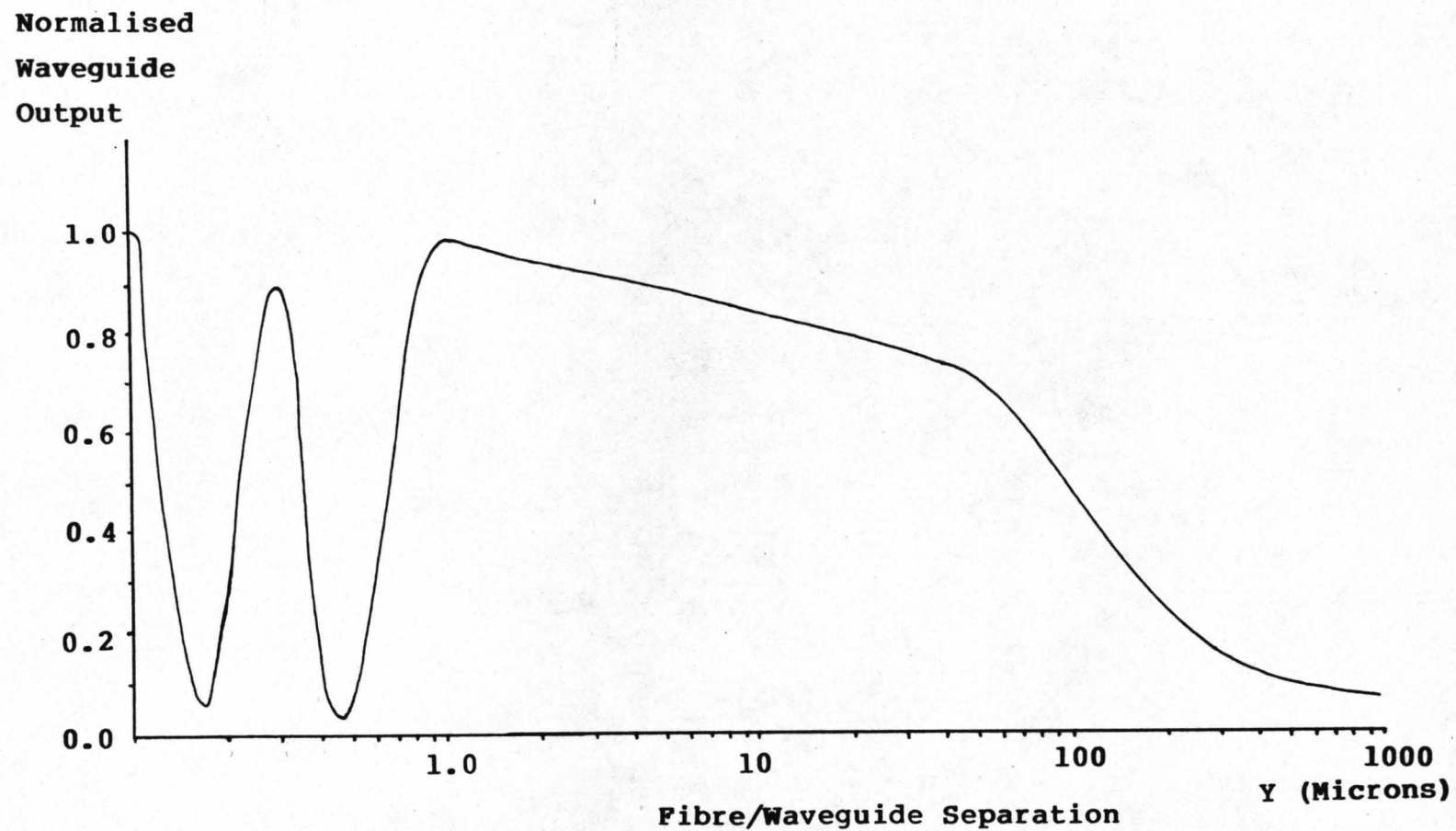
Figure (4.14): a) Plot of Waveguide Output vs. Fibre/Waveguide
Separation; Single Mode Operation at 0.633um
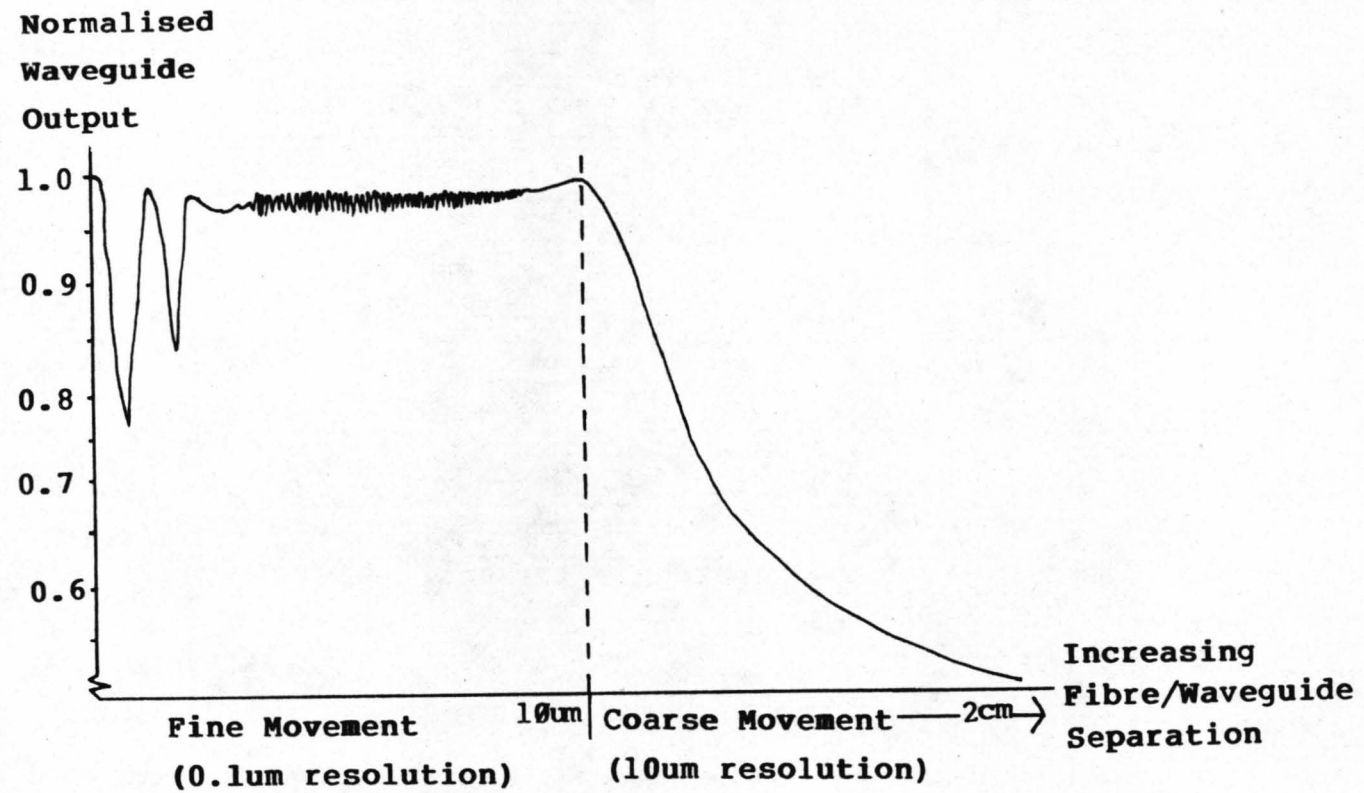
Figure (4.14): b) Plot of Waveguide Output vs. Fibre/Waveguide Separation; Single Mode Operation at 1.15um
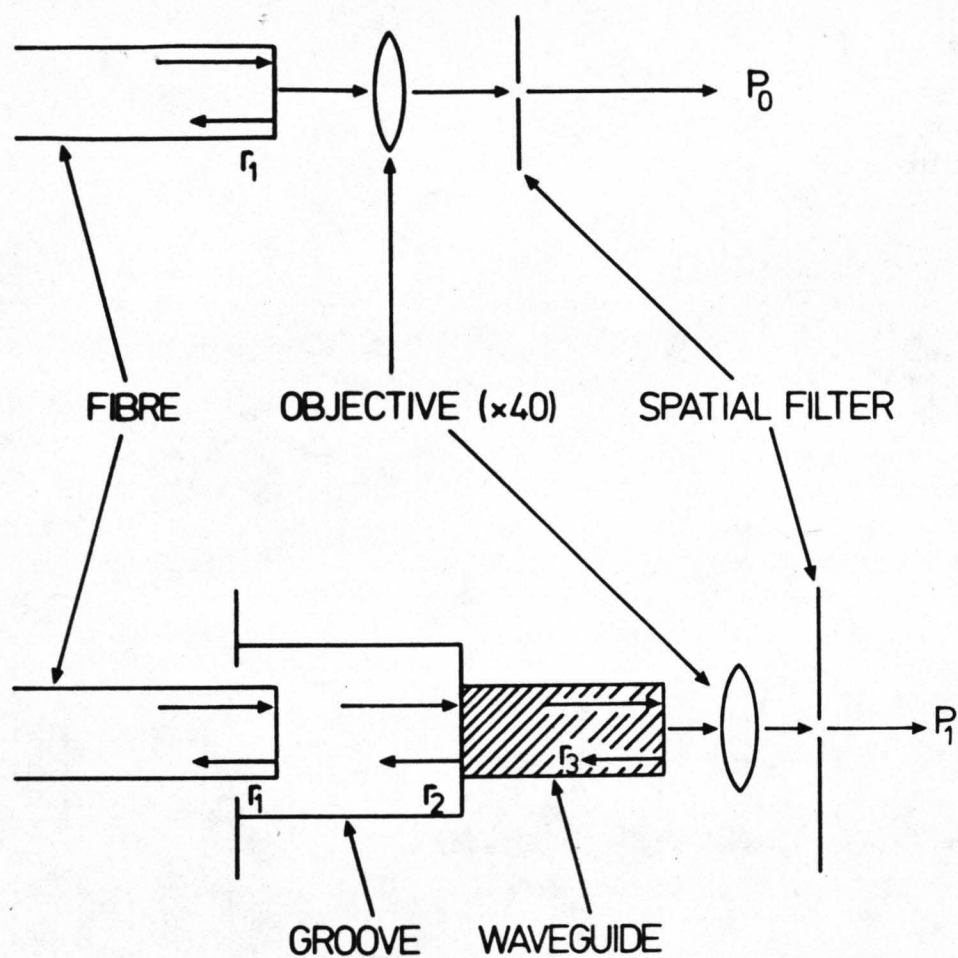
TOTAL INSERTION LOSS $= 10 \log \left(\dfrac{P_1}{P_0} \right)$

Figure (4.15): Schematic Diagram of Fresnel losses inherent in Experimental Insertion Loss Measurements.

The spatial filter is incorporated to block out substrate coupled modes.

with the instabilities monitored on a chart recorder. Basically one minima (or two) were recorded with a sinusoidal effect after. The instabilities were again found to be steady state effects but the minima's position bore no relation to that of the $\lambda/4$ positions. Again theoretically the height of the minima should be 0.749 but recorded minima at 1.15µm ranged from 0.84 to 0.52. The small sinusoidal fluctuations are most probably mechanical effects, however, the initial large dips are an anomally as they do not correspond to Fabry-Perot effects. As yet there is no theory to what is causing this phenomenon.

The longer wavelength was used in the hope that the increased separation between Fabry-Perot resonance dips would yield clearer results. This did not occur, it may be that there is a trade off between fibre/waveguide separation and the numerical apertures of the waveguide and fibre.

Ignoring the instabilities the reflection losses incurred in the coupling component can be seen in figure (4.15). The reflections in the component result in a total 1.36dB ($r_2 + r_3$) which is included in the measured coupler loss. The fibre/air reflection loss, r_1 and the reflection loss at the microscope objective are assumed to be equal in the measurement of P_0 and P_1 and hence are not included in the measured coupler loss.

4.8 Component Realisation

The previous sections in this chapter discuss and explain the various but separate aspects of the coupling component. This section outlines the nature of the experimental set-up and of the realisation of the coupling component.

A photograph of the experimental set-up can be seen in figure (4.16). The fibre, retained for handling ease in the glass capillary, is mounted onto a goniometric rig which allows x,y and z movement (resolution 0.1µm) and θ (in the x-y plane) movement (0.1° resolution). The prepared chip, also shown in figure
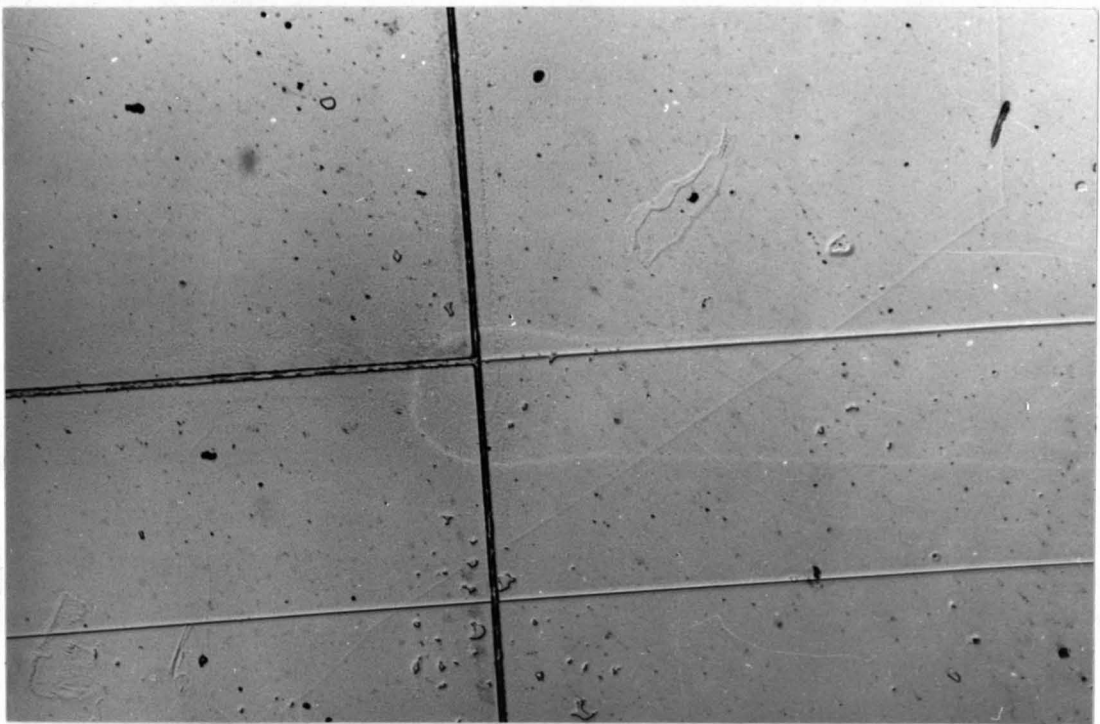
Photograph of Ti:diffused Waveguide Aligned to an
Ion Milled Groove
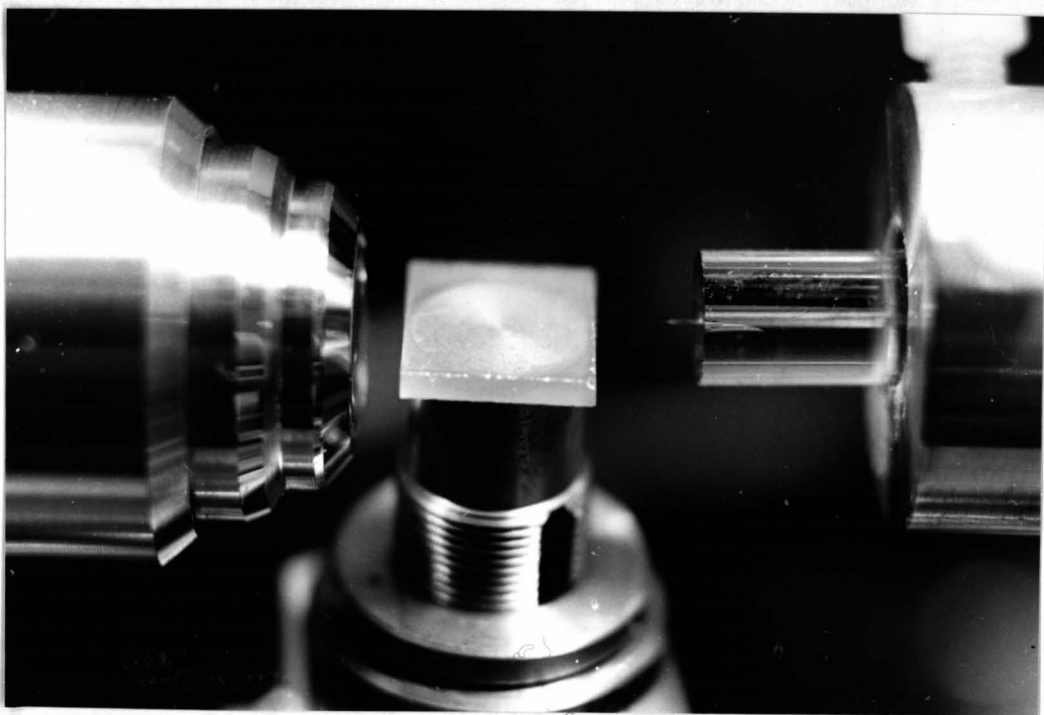
Photograph of the Experimental Arrangement for
Insertion Loss Measurements

Figure (4.16):

(4.16), is mounted on a goniometer which allows the substrate to be levelled i.e. with basic x,y,z movement but with the capacity to move the substrate in pitch,yaw or roll. A 40x microscope objective, mounted akin to the fibre, was positioned so that the waveguide or fibre output could be monitored either on a power meter or the vidicon screen of the Hamamatsu camera.

The 1.3μm laser by itself is very difficult to align, therefore a 633nm tracer was used. Once it was ensured that the red and infra-red beams followed exactly the same path, the tracer was coupled into the optical fibre (which supported 7 modes at 633nm). It then was possible to couple the infra-red into the fibre with the minimum of fuss. A schematic diagram of the complete coupling set-up can be seen in figure (4.17).

Optical insertion loss measurements on the coupler were made by first monitoring the output power of the fibre and then, after placing the fibre in the groove, monitoring the power output from the waveguide. The difference in these values was the insertion loss for that particular component. The power output from the waveguide was measured with the etched fibre butted up against the end-face of the groove in order to minimise any localised Fabry-Perot effect (see section 4.7).

To align and insert an etched fibre (O.D. 10μm) into a 10μm wide groove proved to be relatively simple. The fibre and substrate were observed from above using a stereo microscope with a maximum magnification of 180x with a working distance of 20mm. Using the microscope at a magnification of 60x the fibre is suspended above the groove and angularly aligned with it. The fibre is then lowered onto the waveguide directly in front of the groove. The fibre sags so that the He-Ne output from the fibre can be seen on the substrate surface. The fibre is then lowered until the tip of the fibre touches the top of the waveguide and then lowered a little more so that the fibre is almost level with the substrate surface (this process is easily monitored by observing the red output from the fibre on the substrate surface). Once this process is completed the fibre is simply drawn back towards the
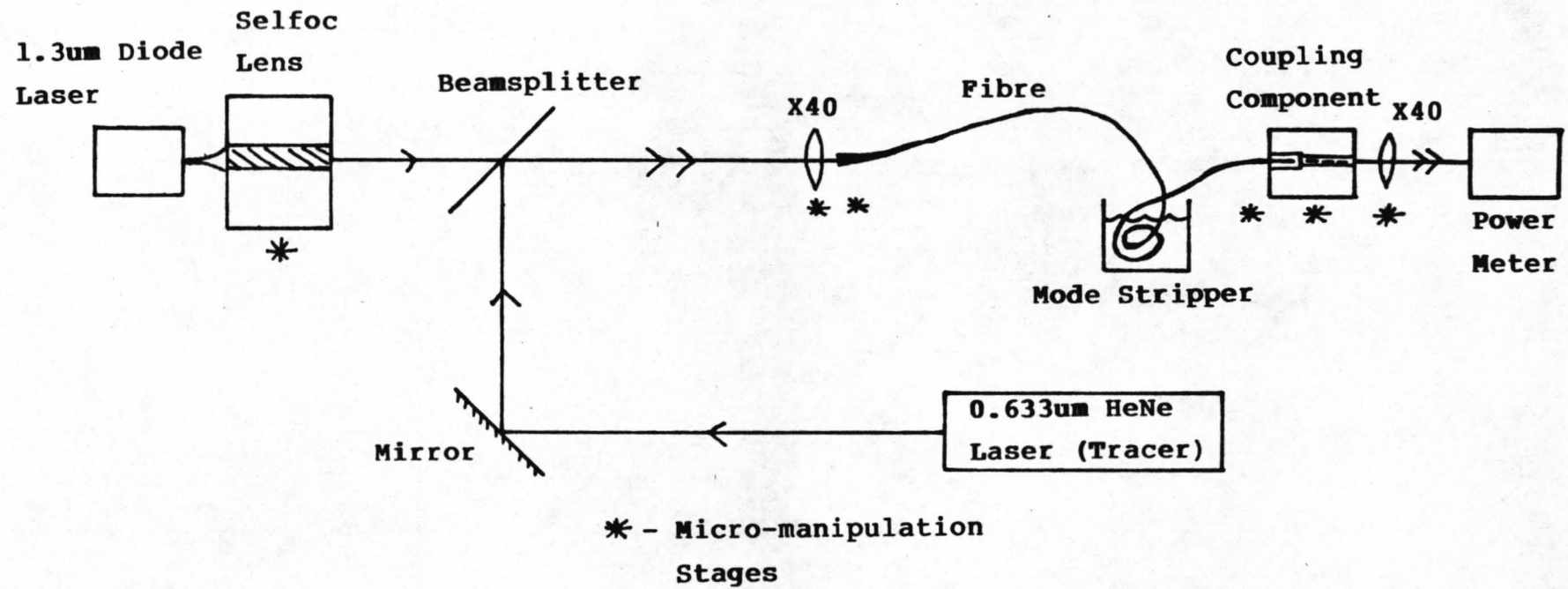
Figure (4.17): Schematic Diagram of Full Coupling Set-up
Including HeNe Laser Tracer
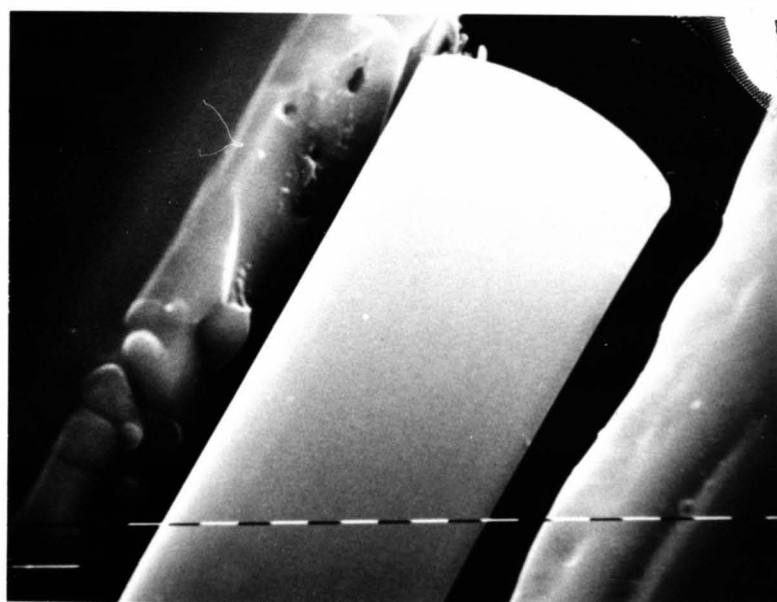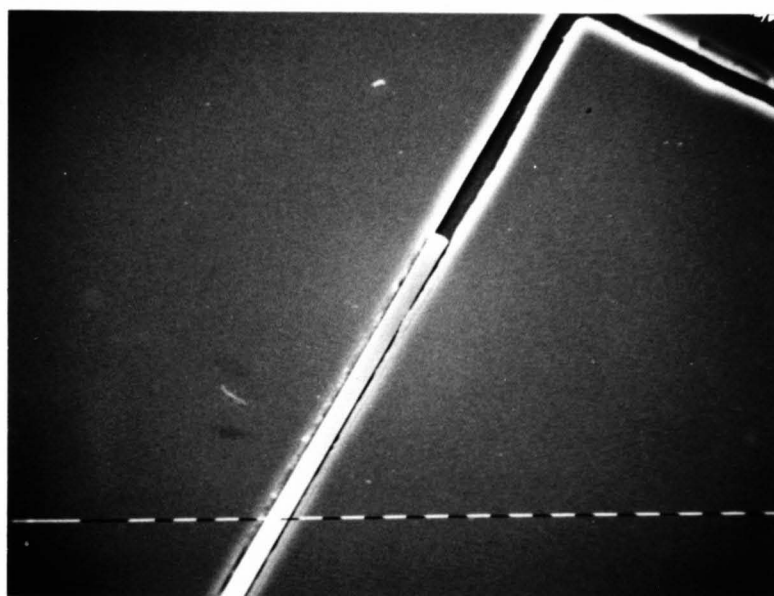
Figure (4.18): S.E.M. of an Etched Fibre Positioned in an
Ion Milled Groove (but not the end-face)
TOP - 10um markers
BOTTOM - 1um markers

MAG. 500x

MAG. 50x
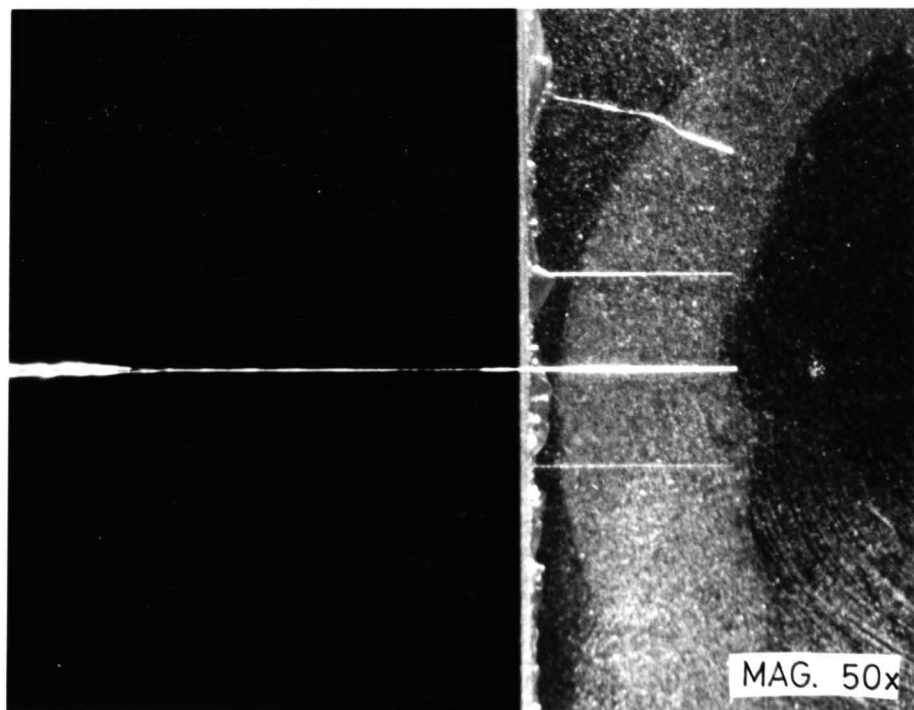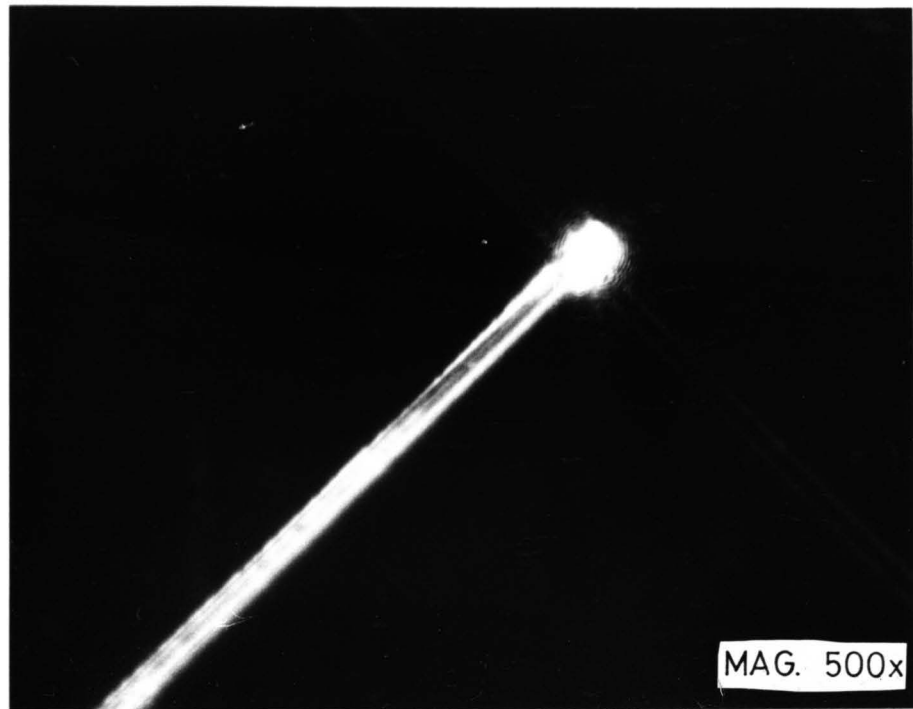
Figure(4.19): Photographs of an Operational Rigid
Fibre – Waveguide Coupler

groove which catches the fibre and guides it until the fibre drops into the groove. The fibre is then pushed forward again until the fibre butts directly against the groove end-face.

This process will normally suffice unless there has been a static charge build up which makes the insertion process much more difficult. Static build up can be counteracted with an anti-static gun, or by earthing the sample occasionally.

A series of processed substrates and fibres was prepared and insertion loss measurements carried out (see section 4.9). During the measurements the etched fibre was held down in the groove with the aid of a cross fibre. The cross fibre ensured the the fibre was fully down onto the base of the groove.

Figure (4.18) a) and b) show S.E.M.s of a 9μm diameter etched fibre lying in an ion milled groove (but not positioned at the end-face of the groove). Figure (4.19) shows the groove coupler in operation. The scattered light is 0.633μm radiation (the coupler was designed to operate at 1.3μm) the end-face scatter caused by ripples in the end-face is clearly visible, the scatter should be much less at the longer wavelength of 1.3μm.

4.9 Results and Loss Analysis of Coupling Component

All the etched fibres used in these tests had an O.D. in the range 9-9.5μm, while the groove widths were in the range 10-10.5μm. The insertion loss measurements were made as in section 4.8. Table 4.2 shows the insertion loss of six ion milled groove couplers compared to the depth of the groove. The results ranged from -3.1dB to -7.6dB (or no discernible output) depending on the component.

Examining the data shows that there is a degree of correlation between the depth of the groove (i.e. the fibre depth misalignment) and the insertion loss. Figure (4.20) shows representative drawings of the six substrates (there was not

TABLE 4.2

List of Insertion Loss Measurements Related
to Component Groove Depth

DEVICE	GROOVE DEPTH	COUPLING LOSS
1	4.8μm	-5.7 dB
2	7.6μm	no output
3	5.6μm	-3.1 dB
4	7.6μm	no output
5	5.4μm	-7.8 dB
6	7.6μm	-6.5 dB

All Insertion Loss Measurements have an accuracy of +/- 0.1dB
or Better
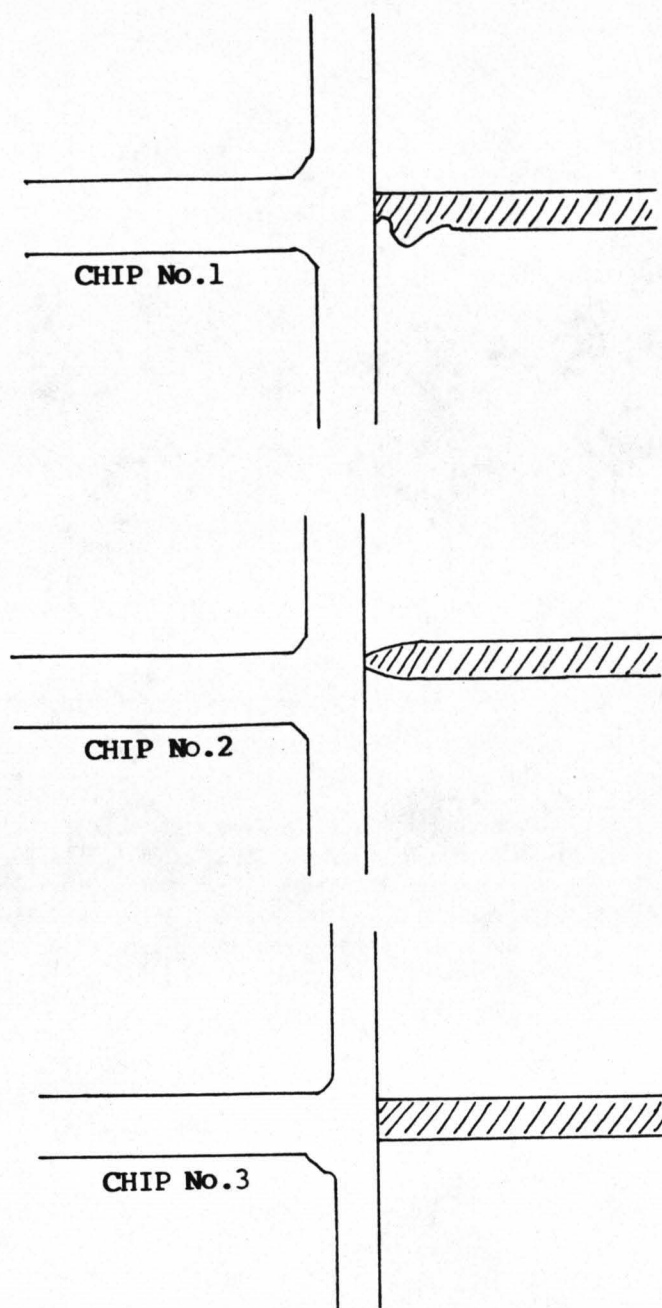
Figure (4.20): Schematic Diagram Depicting the Alignment of Ti:Diffused Waveguides to the Ion Milled Grooves. The Groove Area is Defined by the Solid Lines and the Hatched Area is the Waveguide.

CHIP No.4

CHIP No.5

CHIP No.6
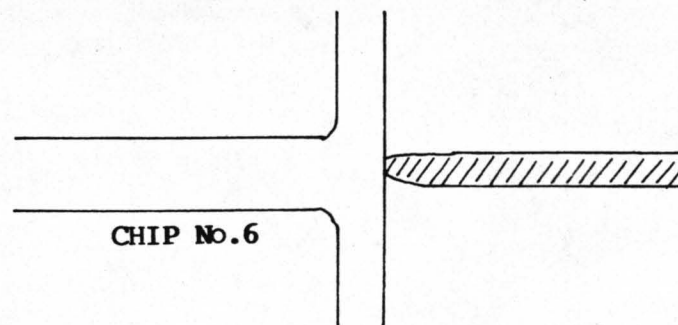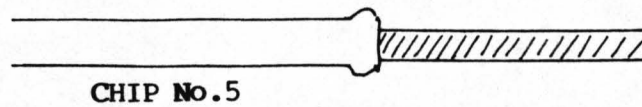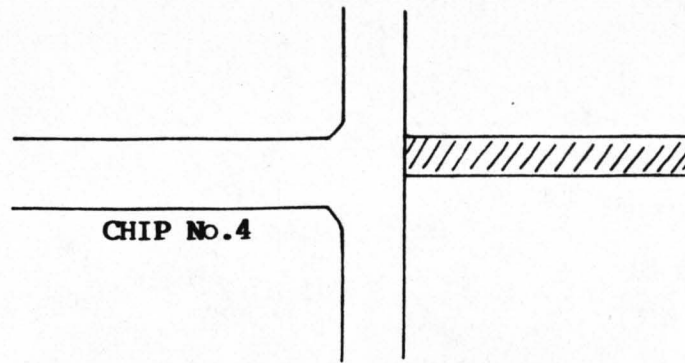
Figure (4.20): Schematic Diagram Depicting the Alignment of
Ti:Diffused Waveguides to the Ion Milled Grooves.
The Groove Area is Defined by the Solid Lines and
the Hatched Area is the Waveguide.
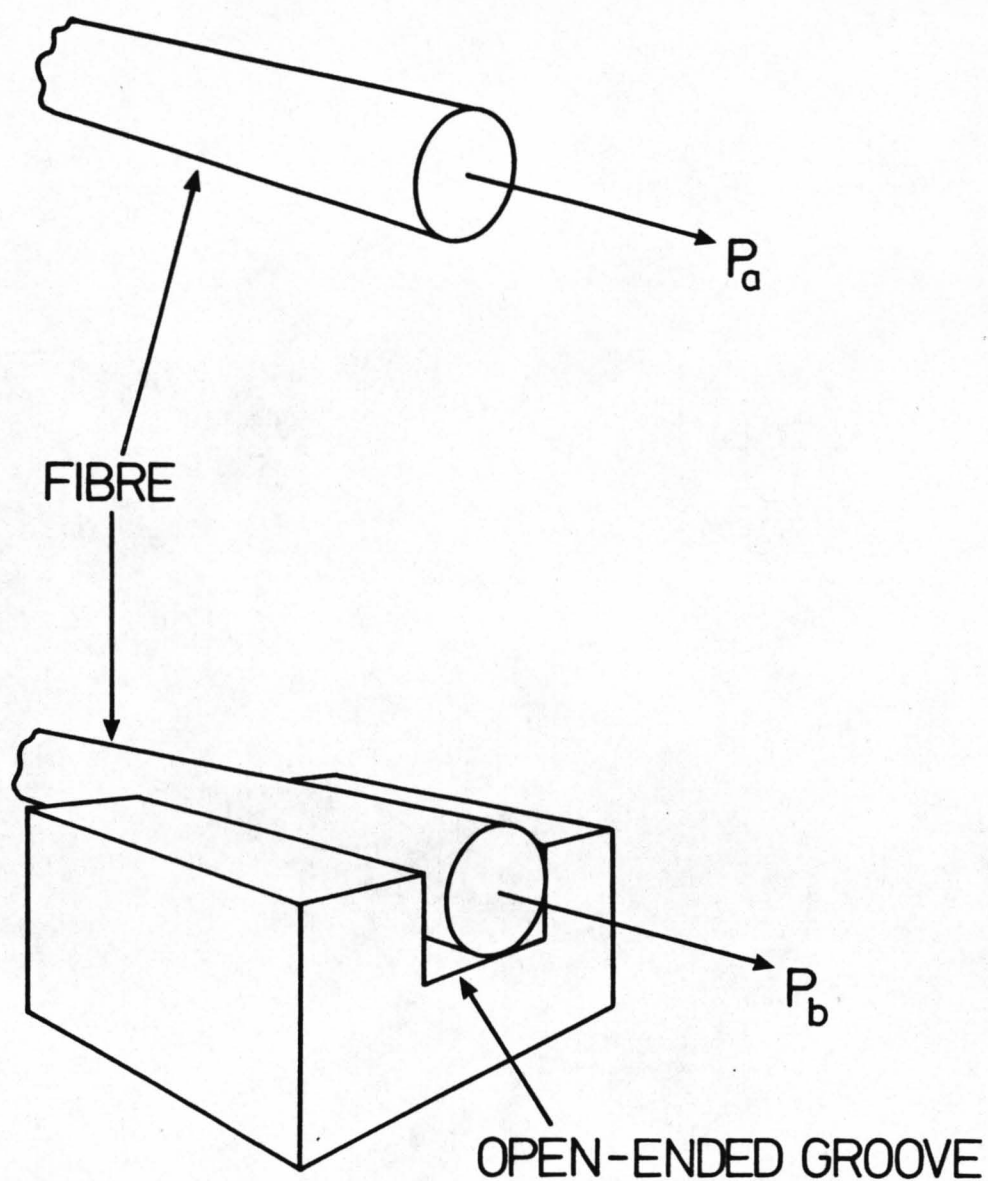
SCATTER LOSS DUE TO WALLS
AND BASE OF GROOVE $\quad 10\log\left(\dfrac{P_b}{P_a}\right)$

Figure (4.21): Schematic Diagram of the Process Involved in
Measuring Groove Scatter Loss

sufficient contrast on the samples to show the waveguides photographically). These drawings highlight another important factor in the loss mechanism. There is an edge effect at the groove-waveguide interface which occurs at the photolithographic stage, causing the waveguide pattern, in some cases, to be deformed. Closer inspection of figure (4.20) also yields the amount of positional misalignment that each waveguide has relative to the coupling groove (i.e. the fibre). Both of these effects explain the difference in insertion loss measured in each component.

To fully understand the component the constituent losses have to be examined. Table 4.3 outlines the constituent losses for the 'best case' coupler. The values were obtained thus:

The Fresnel loss was calculated as in Section 4.7 for the worst possible case but ignoring the localised Fabry-Perot effect.

To measure the scattering losses due to the side walls and the base of the groove an open ended slot was used, see figure (4.21) i.e. the power from the etched fibre was measured before and after positioning in the open ended grooves thus a reasonable estimation of the scatter loss could be obtained (0.5dB/mm).

The field overlap power transfer calculation was obtained from the near field intensity distributions of the etched fibre and the 6µm wide waveguide (see section 4.4).

To monitor any loss in the etched fibre taper region, the power output from the etched fibre was measured, then the fibre was cleaved just behind the taper and the process repeated. Within measurement tolerances, 0.01dB, no power is lost in the transition region although the fibre profile is modified considerably.

Thus the quantifiable losses amounted to 1.87dB of the 3.1dB total. This leaves 1.23dB to be split up between the alignment loss, waveguide loss and end-face scatter loss.

One important aspect of this research, which may not be

TABLE 4.3

Constituents of Experimentally Determined Insertion Loss

Calculated Fresnel reflection loss at waveguide ends		
(2 x 0.68 dB)	1.36	dB
Measured groove scatter loss	0.5	dB
Calculated field overlap loss	0.51	dB
Measured fibre taper loss	0	dB
TOTAL	2.37	dB
Best achieved total insertion loss	3.1	dB
Remainder (end-face scatter loss, alignment loss, waveguide attenuation)	0.73	dB

TABLE 4.4

Net Coupler Insertion Loss

Fresnel Loss (i) waveguide end	0.68 dB
(ii) fibre end	0.16 dB
Groove scatter	0.5 dB
Field overlap	0.51 dB
End-face scatter, alignment (plus waveguide loss)	0.73 dB
Measured Net Total Loss	2.58 dB

PREDICTED:

Reduction by index matching	0.76 dB
Net loss with index matching	1.82 dB

appreciated at this stage, is that of 'ease of use'. Provided that any static charge is negligible, coupling of the fibre to the waveguide may be achieved with the minimum of fuss. The process only requires a 60x magnification to allow the positioning of a 10µm wide fibre into a 10µm wide slot. Futhermore, contrary to expectations, the etched portion of the fibre is relatively strong and robust, and with careful handling is no more likely to break than the bulk of the fibre. Indeed most of the fibre breakages during the experiments have been with the main fibre. The etched fibre resilience may be due to the fact that in the unetched fibre the outer surface has stress cracks which weaken the fibre whereas in the etched fibre, since the outer layers have been removed, the strength of the etched fibre is only limited by the material strength. This phenomenon has been utilised to measure the tensile strength of glass [4.37].

Table 4.4 gives a clearer indication of the true coupler losses, and shows that the net coupler loss is 2.58dB, pointing to the possibility of achieving 1.82dB net loss with index matching. This value of net coupler loss is comparable with recent V-groove technology [4.17,4.38].

4.10 Conclusions

The first realisation of a fibre-chip coupler using ion milled alignment grooves in lithium niobate has been described. The coupler affords rigid location of a reduced diameter fibre with a single mode integrated optical waveguide with the process parameters involved being amenable for industrial implementation. Various aspects of the coupling problem have been highlighted. These include an accurate three dimensional representation of the overlap integral (and hence power transfer), problems involved with alignment tolerances and measured instabilities caused by a localised Fabry-Perot type effect and an investigation of the components' constituent losses.

Even with preliminary measurements on prototype couplers the net insertion loss of 2.58dB (without index matching) is impressive. Since the fibre has only a 10μm O.D. in the coupling region fibres can be array coupled over a smaller area than is possible with standard 100μm diameter fibre.

It is envisaged that with little effort the insertion loss can be reduced even further. Scatter loss (0.5dB) can be reduced by reducing the ripples in the groove end-face and side walls, the latter also being dependent on fibre diameter. If the etched groove depth can be increased by even a modest amount the etched fibre radius can be increased by a similar amount, reducing the evanescent field outside the fibre and hence reducing the scattering losses. Alignment loss and end-face scatter loss can be reduced with an increase in groove quality and delineation, which may involve the use of reactive gases in the etching process. Fresnel losses can be reduced with the aid of index matching fluid or by an anti-reflection coating on the fibre (for one fibre-air-waveguide interface the loss can be reduced from 18% or 0.86dB to 2% or 0.1dB). For the situation in which input and output couplers are formed on an integrated waveguide device, the overall insertion loss may be estimated to be 5.2dB, reducible by index matching to 3.6dB (see Tables 4.3 and 4.4).

It would be envisaged that this coupling method would allow the easy attachment of several fibre pigtails to a single integrated optical circuit. The method, since it is a purely physical phenomenon, should be applicable to other substrate materials such as glass or semiconductor with little modification. This type of coupler negates the need for a complex and time consuming process step, i.e. the end-polishing of the integrated optical waveguides.

CHAPTER 4 - REFERENCES

[4.1]   R.C. Alferness
         Waveguide Electro-Optic Modulators
         IEEE Trans. MTT, vol MTT-30, No.8, pp1121-1137
         8th Aug. 1982

[4.2]   R.C. Alferness
         Guided-Wave Devices for Optical Communications
         IEEE J. Quant. Elect, vol QE-17, No.6, pp946-959
         6th June 1981

[4.3]   D. Botez and G.J. Herskowitz
         Components for Optical Communications Systems: A Review
         Proc. IEEE, vol 68, No.6, pp689-731,   June 1980

[4.4]   G. Stewart
         Recent Developments in Integrated Optics
         SPIE, vol 468 Fibre Optics'84 (Sira), pp74-80, 1984

[4.5]   Y. Suematsu
         Progress in Integrated Optics Lasers
         3rd E.C.I.O., Session C: Semiconductor-Devices, pp82-98
         Berlin (West), Germany, May 1985

[4.6]   H.P. Hsu and A.F. Milton
         Single-Mode Coupling Between Fibres and Indiffused
         Waveguides
         IEEE J. QE., vol QE-13, No.4, pp224-233, April 1977

[4.7]   G. Stewart, R.H. Hutchins and P.J.R. Laybourn
         Hybrid Integration of Active and Passive Devices
         3rd Int. Conf. on Int. Opt. and Opt. Fibre Commun.
         San Francisco, U.S.A., April 1981

[4.8]   G. Stewart and A.C.G. Nutt
          Formation and Analysis of Tapers in Proton-Exchanged
          Lithium Niobate Waveguides
          3rd E.C.I.O., Session B: Material and Fabrication,
          pp57-61, Berlin (West), Germany, May 1985

[4.9]   J.C. Campbell
          Coupling of Fibers to Ti-diffused $LiNbO_3$ Waveguides
          by Butt-Joining
          Applied Optics, vol 18, No.12, pp2037-2040
          15 June 1979

[4.10]   G. Stewart, R.H. Hutchins and P.J.R. Laybourn
          Controlled Growth of Arsenic Trisulphide Films for
          Coupling to Integrated Optical Devices
          J. Phys. D: Appl.Phys., vol 14, pp323-331, 1981

[4.11]   G. Stewart, R.H. Hutchins, P.J.R. Laybourn
          and C.A. MacRae
          Construction of Hybrid Integrated Optical Circuits
          Integrated Optical Waveguide Fabrication
          I.O.O.C.,E.C.O.C.'85, Venezia, Italia, Oct 1985

[4.12]   L. McCaughan and E.E. Bergmann
          Index Distribution of Optical Waveguides from Their
          Mode Profile
          J. Light. Tech., vol LT-1, No.1, pp241-244, March 1983

[4.13]   R.C. Alferness, V.R. Ramaswamy, S.K. Korotky,
          M.D. Divino and L.L. Buhl
          Efficient Single-Mode Fiber to Titanium Diffused
          Lithium Niobate Waveguide Coupling for λ = 1.32um
          IEEE J. QE., vol QE-18, No.10, pp1807-1812, Oct 1982

[4.14]   K.H. Cameron
          Simple and Practical Technique for Attaching Single-
          mode Fibres to Lithium Niobate Waveguides
          Electron. Lett., vol 20, No.23, pp974-976, Nov. 1984

[4.15]   V. Ramaswamy, R.C. Alferness and M. Divino
         High Efficiency Single-Mode Fibre to Ti:LiNbO$_3$
         Waveguide Coupling
         Electron. Lett., vol 18, No.1, pp30-31, Jan. 1982

[4.16]   H.P. Hsu and A.F. Milton
         Flip-Chip Approach to Endfire Coupling Between Single
         -Mode Optical Fibres and Channel Waveguides
         Electron. Lett., vol 12, No.16, pp404-405, Aug 1976

[4.17]   E.J. Murphy and T.C. Rice
         Low-Loss Coupling of Multiple Fiber Arrays to Single
         -Mode Waveguides
         J. Light. Tech., vol LT-1, No.3, pp479-482, Sept 1983

[4.18]   C.M. Gee and G.D. Thurmond
         High-Speed Integrated Optics Travelling-Wave Modulator
         2nd E.C.I.O., Publ. No. IEE 227, pp111-121, Oct 1983
         Firenze, Italia

[4.19]   A.D. McLachlan
         Ph.D. Thesis, University of Glasgow, 1981

[4.20]   I. Andonovic, M.B. Holbrook and A.D. McLachlan
         End-fire Coupling Between Optical Fibres and Stripe
         Waveguides
         1st E.C.I.O., London, Sept 1981, pp8-11

[4.21]   M. Fukuma and J. Noda
         Optical Properties of Titanium-diffused LiNbO$_3$ Strip
         Waveguides and their Coupling-to-a-fiber
         Characteristics
         Applied Optics, vol 19, No.4, pp591-597, 15 Feb 1980

[4.22]   J. Noda, O. Mikami, M. Minakata and M. Fukuma
         Single-mode Optical-waveguide Fiber Coupler
         Applied Optics, vol 17, No.6, pp2092-2099, June 1978

[4.23]   A. McDonach
          Internal Report
          Dept E&EE, University of Glasgow, 1984

[4.24]   A.S. Tenney and M. Ghezzo
          Etch Rates of Doped Oxides in Solutions of Buffered HF
          J. Electrochem. Soc., vol 8, pp1091-1095, 1973

[4.25]   J.S. Judge
          A Study of Dissolution of SiO_2 in Acidic Flouride
          Solutions
          J. Electrochem. Soc., vol 118, pp1772-1775, 1971

[4.26]   L.O. Svaasan, S. Hopland and A.P. Grande
          Slicing of Optical Fibres with a Selective Etching
          Technique
          Fourth E.C.O.C., Genoa, Italy, Sept. 1978, pp304-308

[4.27]   G. Eisenstein and D. Vitello
          Chemically Etched Conical Microlenses for Coupling
          Single-mode Lasers into Single-mode Fibres
          Applied Optics, vol 21, pp3470-3474, 1982

[4.28]   I. Andonovic
          Ph.D. Thesis, University of Glasgow, 1983

[4.29]   M. Hatzakis, B.J. Canavello and J.M. Shaw
          Single Step Lift-Off Process
          IBM J. Res. Develop., vol 24, No.4, pp452-460
          July 1980

[4.30]   Bjorn Bjortorp
          Ph.D. Thesis, University of Glasgow, 1984

[4.31]   Born & Wolf
          Principles of Optics
          Chapter 8.6.3, p417, Pergamon, 1959

[4.32]   Hamamatsu Camera plus associated C1000 controller

[4.33]   W.K. Burns and G.B. Hocker
           End Fire Coupling Between Optical Fibres and Diffused
           Channel Waveguides
           Applied Optics, vol 16, No.8, pp2048-2050, Aug 1977

[4.34]   L. McCaughan and E.J. Murphy
           Influence of Temperature and Initial Titanium
           Dimensions on Fiber-Ti:LiNbO$_3$ Waveguide Insertion loss
           at λ = 1.3um
           IEEE J. QE., vol QE-19, No.2, pp131-135, Feb 1983

[4.35]   A.F. Milton and W.K. Burns
           Mode Coupling in Optical Waveguide Horns
           IEEE J. QE., vol QE-13, No.10, pp828-835, Oct 1977

[4.36]   G. Henderson
           Investigating Fabry-Perot Interference Effects in a
           Fibre-to-Waveguide End-Fire Coupler
           Final Year Project Report, Dept E&EE
           University of Glasgow, March 1985

[4.37]   J.E. Gordon
           The New Science of Strong Materials
           Chapter 3 Cohesion, 2nd Ed., Penguin Books, 1983
           Aylesbury, Bucks.

[4.38]   O.G. Ramer, C. Nelson and C. Mohr
           Experimental Integrated Optic Circuit Losses and
           Fiber Pigtailing of Chips
           IEEE J. QE., vol QE-17, No.6, pp970-974, June 1981

[4.39]   D. Marcuse
           Loss Analysis of Single-Mode Fiber Splices
           B.S.T.J., vol 56, No.5, pp703-718, May-June 1977

APPENDIX TO CHAPTER 4

THEORETICAL ANALYSIS OF THE LOCALISED FABRY-PEROT EFFECT
BETWEEN ALIGNED FIBRE AND WAVEGUIDE END-FACE

When the flat end of a fibre is close to the polished end-face of
a waveguide a Fabry-Perot type structure is set-up (see appendix
figure 1). If the interface region is simplified to the one
shown in appendix figure 2 the effect of the etalon can be
analysed. The experimental measurements in section 4.7 were made
by examining the effects of the etalon on the waveguide output
power and thus the theory will examine mainly the power
transmitted through the etalon to the waveguide output. The
effects of reflection at the waveguide/air interface at the
output are assumed to be negligible.

From appendix figure 2 the optical path difference (OPD) of two
successive reflections A_1 and A_2 (B_1 and B_2) defined as

$$OPD = AB + BC = [\cos(2\theta) + 1].BC$$

$$OPD = \frac{d}{\cos(\theta)} [1 + \cos(2\theta)] = \frac{d}{\cos(\theta)} [1 + 2.\cos^2\theta - 1]$$

Therefore

$$OPD = 2.d.\cos(\theta)$$

The OPD can be defined as follows:

$$OPD = \text{(phase difference/wave number)} \qquad \text{(appendix ref A1)}$$

$$= D/k_n$$

where D is the phase difference and $k_n = \frac{2.\pi}{\lambda}.n$

MULTIPLE

REFLECTIONS

CLADDING

CORE n_1

n_0

n_2

Ti:DIFFUSED WAVEGUIDE

I_t

d

X

Z

Y

LiNbO$_3$

I_t — TRANSMITTED LIGHT
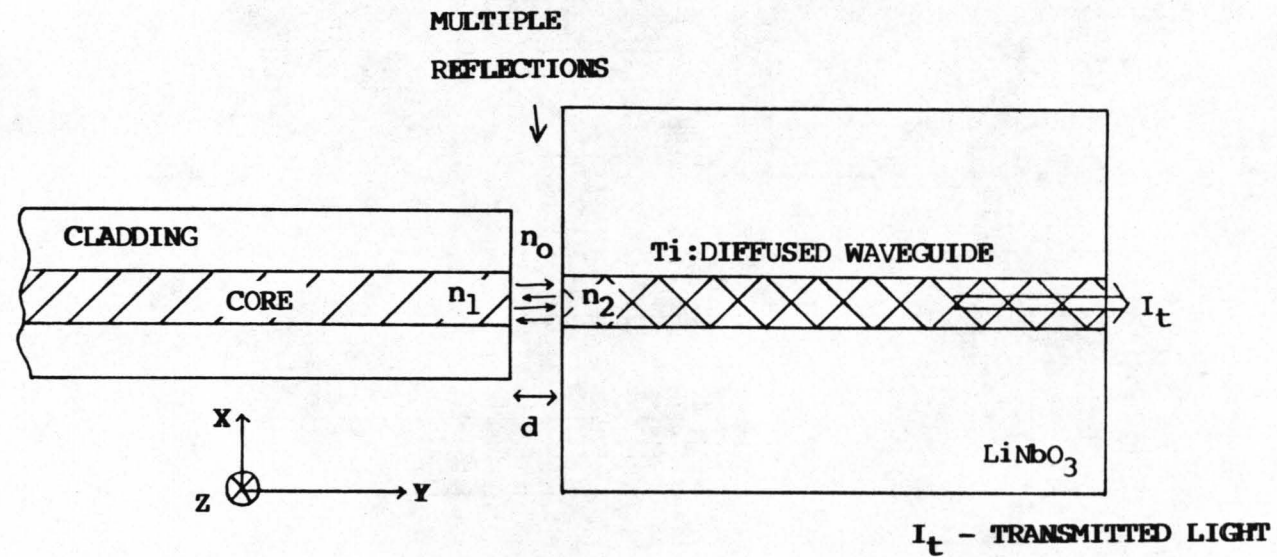
Appendix Figure 1:   Schematic Diagram Depicting the Localised
Fabry- Perot Effect Between a Fibre and a
Stripe Waveguide
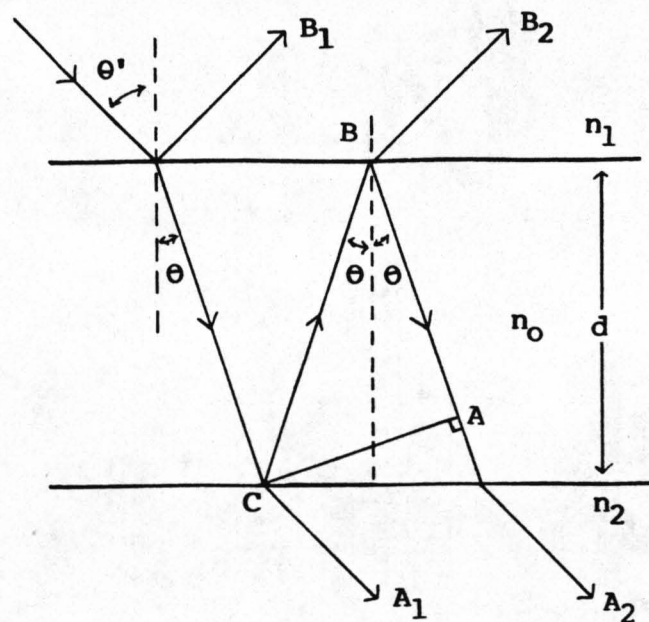
Appendix Figure 2: Diagram Showing Two Succesive Reflections A_1 and A_2 (or B_1 and B_2). The Above Structure Will Be Examined as a Fabry-Perot Etalon

with n the refractive index of the reflection region (in our case air, n = 1) and λ is the wavelength).

Thus the phase difference between A_1 and A_2 is;

$$D = \frac{4.\pi.d.\cos(\theta)}{\lambda}$$ --- (1)

To simplify the following calculation of the transmittance define the following

Let A_i = complex amplitude of incident wave
B_1, B_2 = complex amplitudes of partial reflections
A_1, A_2 = complex amplitudes of partial transmissions

Also, Fresnel coefficients for normal incidence, $\theta = 0^o$ are
r_{1o} = reflection coefficient for waves travelling from n_1 to n_o
r_{o2} = reflection coefficient for waves travelling from n_o to n_2
r_{o1} = reflection coefficient for waves travelling from n_o to n_1

and, t_{1o} = transmission coefficient for waves travelling
from n_1 to n_o
t_{o2} = transmission coefficient for waves travelling
from n_o to n_2

Concentrating on transmitted light

$$A_1 = t_{1o}t_{o2}A_i$$
$$A_2 = t_{1o}r_{o2}r_{o1}t_{o2}A_i\exp\{jD\}$$
$$A_3 = t_{1o}r_{o2}r_{o1}r_{o2}r_{o1}t_{o2}A_i\exp\{j2.D\}$$
$$= t_{1o}r_{o2}{}^2r_{o1}{}^2t_{o2}A_i\exp\{j2.D\}$$
$$A_4 = t_{1o}r_{o2}{}^3r_{o1}{}^3t_{o2}A_i\exp\{j3.D\}$$
and so on....

The complex amplitude of the total transmitted light, A_t, can be found by summing the A_n terms;

$$A_n = A_1 + A_2 + A_3 + A_4 + .. + .. + ...$$

$$A_t = t_{1o}t_{o2}A_i[1 + r_{o1}r_{o2}\exp\{jD\} + r_{o1}^2 r_{o2}^2\exp\{j2.D\}$$
$$+ r_{o1}^3 r_{o2}^3\exp\{j3.D\} + ...]$$

Defining $T_1 = t_{1o}t_{o2}$
$R_1 = r_{o1}r_{o2}$

We get,

$$A_t = A_i.T_1[1 + R_1\exp\{jD\} + R_1^2\exp\{j2.D\} + R_1^3\exp\{j3.D\} + ...]$$

The terms within the square brackets of the above expression form an infinite geometric progression. Adding them gives:

$$A_t = \frac{A_iT_1}{1 - R_1\exp\{jD\}} \qquad\qquad ---(2)$$

Taking the transmitted intensity (watts/m^2) as $A_iA_i^*$ (appendix ref A2) the transmitted fraction of incident light is

$$\frac{I_t}{I_i} = \frac{A_tA_t^*}{A_iA_i^*}$$

$$= \frac{T_1}{1 - R_1\exp\{jD\}} \cdot \frac{T_1}{1 - R_1\exp\{-jD\}}$$

$$= \frac{T_1^2}{1 + R_1^2 - R_1(\exp\{jD\} + \exp\{-jD\})}$$

$$= \frac{T_1^2}{1 + R_1^2 - 2.R_1.\cos(D)}$$

using $\cos(D) = 1 - \sin^2(D/2)$ we get,

$$\frac{I_t}{I_i} = \frac{T_1^2}{(1 - R_1)^2 + 4R_1 \cdot \sin^2(D/2)} \qquad \text{---(3)}$$

Equation (3) can be expressed in the form of an Airy function by letting

$$F = \frac{4R_1}{(1 - R_1)^2}$$

$$\frac{I_t}{I_i} = \frac{T_1^2/(1 - R_1)^2}{1 + F \cdot \sin^2(D/2)}$$

$$= \frac{T_1^2}{(1 - R_1)^2} \cdot \left(\frac{1}{1 + F \cdot \sin^2(D/2)} \right) \qquad \text{---(4)}$$

Note that the factors $\dfrac{T_1^2}{(1 - R_1)^2}$ and F are constants determined only by the relative refractive indices of the materials forming the interferometer. Assuming no absorption losses in the air gap and that changes in phase only result from the OPD then the maximum transmitted intensity will be

$$\frac{T_1^2}{(1 - R_1)^2} \qquad \text{when } \sin(D/2) = 0$$

An expression relating the actual transmitted intensity to the maximum transmitted intensity, I_{tm}, has to be obtained since it is this normalised value which is plotted in the experimental results in section 4.7.

$$I_i = \frac{(1 - R_1)^2}{T_1^2} \cdot I_{tm}$$

Substituting for I_i in equation (4) gives

$$\frac{I_t}{I_{tm}} = \frac{1}{1 + F.\sin^2(D/2)} \qquad\qquad ---(5)$$

Recalling that F is a constant wholly defined by the refractive indices of the three media making up the interferometer, the normalised maximum effects of the etalon can be calculated.

Defining

n_0 = the refractive index of air = 1

n_1 = the refractive index of the fibre core (approx.) = 1.47

n_0 = the refractive index of lithium niobate

at a wavelength of 633nm = 2.28

at a wavelength of 1152nm = 2.23

Assuming TE mode propagation (appendix ref A3)

For a wavelength of 633nm

r_{o1} = 0.19, r_{o2} = 0.39

Therefore R_1 = 0.074

Thus   F = 0.345

This gives

$$\frac{I_t}{I_{tm}} = \frac{1}{1 + 0.345\sin^2(D/2)}$$

Thus the transmitted light is minimised when $\sin^2(D/2)$ is a maximum. This occurs when $D = (2m+1)\pi$ where m is an integer. From equation (1) it is noted that the minimum is a function of the air-gap between fibre and waveguide and thus minima occur for gap distances;

$$d = (2m+1) \; \lambda/4 = (2m+1) \times 0.158 \mu m$$

Minima should occur at gap widths of 0.158μm, 0.475μm, 0.791μm, 1.108μm .....etc.

The maximum percentage dip in the light from the output waveguide caused by the localised Fabry-Perot effect at a wavelength of 633nm is 25.7%.

For a wavelength of 1152nm

$r_{o1} = 0.19$, $r_{o2} = 0.38$
Therefore $R_1 = 0.072$
Thus $\quad$ F = 0.334

This gives
$$\frac{I_t}{I_{tm}} = \frac{1}{1 + 0.334 \sin^2 (D/2)}$$

Thus the transmitted light is minimised when $\sin^2 (D/2)$ is a maximum. This occurs when $D = (2m+1)\pi$ where m is an integer. From equation (1) it is noted that the minimum is a function of the air-gap between fibre and waveguide and thus minima occur for gap distances;
$$d = (2m+1) \; \lambda/4 = (2m+1) \times 0.228 \mu m$$

Minima should occur at gap widths of 0.228μm, 0.864μm, 1.440μm, 2.016μm ·......etc.

The maximum percentage dip in the light from the output waveguide caused by the localised Fabry-Perot effect at a wavelength of 633nm is 25.1%.

APPENDIX TO CHAPTER 4 – REFERENCES

A1   M. Young
      Optics and Lasers
      2nd Edition, New York: Springer-Verlag, 1984
      (Chapters 4,5 and9)

A2   A. Yariv
      Introduction to Optical Electronics
      New York; Holt, Rinehart and Winston, 1971 (Ch. 4)

A3   A. Rauber
      Chemistry and Physics of Lithium Niobate
      Current Topics in Materials Science, vol 1, ch 7 p.531
      F. Kaldis Ed.

PART 2

PROTON EXCHANGED WAVEGUIDES ON LITHIUM NIOBATE

CHAPTER 5

OPTICAL CHARACTERISTICS OF PROTON EXCHANGED PLANAR AND TAPERED WAVEGUIDE REGIONS

5.1 Introduction

Lithium niobate is an electro-optic dielectric material [5.4] of current interest for the fabrication of guided wave devices such as switches, modulators, wavelength multiplexers and demultiplexers [5.1,5.2,5.3]. The essential element of these devices is an optical waveguide consisting of a surface layer which is of a higher refractive index than the substrate. Optical waveguiding layers are typically a few microns thick and, depending on the application, have either a planar or stripe geometry.

Among different waveguide fabrication methods the most firmly established technology in lithium niobate is the indiffusion of titanium ions [5.5,5.6]. Titanium diffused waveguides, although forming the basis for waveguide fabrication in integrated optics on lithium niobate, have some limitations. Such waveguides are very susceptible to the photo-refractive effect (optical damage) [5.7,5.8] and, in addition, the index change in the waveguiding region is small (in the region of 0.002 [5.5]). The small index change results in low confinement waveguides and therefore, in many instances, the electro-optic and acousto-optic interaction efficiencies are not fully optimised [5.9,5.10]. Ti:diffused waveguides, due to the low index change, can only form waveguide bends whose radius of curvature is a minimum of 1cm, without making considerable changes to the waveguide structure [5.11,5.12], and therefore, making the true integration of devices more difficult. These limitations could possibly be eliminated or greatly reduced by a high index waveguide fabrication process, such as proton exchange [5.13].

The proton exchange technique for forming waveguides was employed originally as a way of, supposedly, making new compounds $NbO_2(OH)$ and $TaO_2(OH)$ [5.14]. Jackel first discovered the process of forming high index waveguides in lithium niobate by the total immersion of cleaned substrates in hot carboxylic acid [5.14,5.15]. Since then optical waveguides in X, Y, and Z-cut lithium niobate and X-cut lithium tantalate have been fabricated by the proton exchange technique, using benzoic acid as the source of protons [5.15,5.16,5.17,5.18,5.19]. The attractions of the process are that it is simple and takes place at a relatively low temperature ($< 240^\circ$C). The resultant waveguides have a high index change (approx. 0.12 at a wavelength of 0.633um). After the exchange process only the extra-ordinary index increases, the ordinary index is actually reduced by -0.04 [5.20,5.21,5.22]. This implies that only TE modes are supported in proton-exchanged (PE) X-cut, Y-propagating and Y-cut X-propagating lithium niobate and TM modes in Z-cut lithium niobate. Various researchers have also studied optical waveguides formed in diluted benzoic acid melts (buffered with small percentages of lithium benzoate) [5.23,5.24], as well as the combination of titanium diffusion followed by proton exchange (TIPE) [5.25,5.26] in lithium niobate. These processes allow the refractive index change and the refractive index profile to be modified. Recently the annealing of PE waveguides [5.21,5.27,5.28] has shown that the refractive index profile of the optical waveguide can be changed from a step-like profile to a graded profile after suitable annealing times and temperatures.

Various passive devices such as high efficiency diffraction gratings [5.29], second harmonic generators [5.30,5.31], chirped grating lenses [5.32,5.34], planar lenses [5.33,5.76], polarisers [5.35], temperature sensors [5.73], ring resonators [5.74] and tapered velocity couplers [5.36,5.37] and various active devices such as optical frequency translators [5.38], Mach-Zender interferometers [5.39], acousto-optic deflectors [5.40,5.41] and TE/TM converters [5.42] have been demonstrated in various lithium niobate crystal orientations, using the proton exchange technique of forming optical waveguides.

PE waveguides have been found to be much more resistant to optical damage [5.8,5.43,5.71]. As a result, at a glance, they seem to be a viable alternative to titanium diffused waveguides. However, proton exchanged waveguides will have to be fully characterised before this assertion can be verified.

This chapter deals with the necessary characterisation of proton exchanged planar optical waveguides mainly on X-cut and Z-cut lithium niobate. The main points that are considered are waveguide properties i.e. index change, dispersion curves, losses, stability, anisotropic propagation characteristics, surface damage, and component realisation at 633nm and 1152nm wavelength. The problems inherent with this form of waveguide are discussed. The materials and optical analyses of PE and post-annealed PE waveguides are discussed in chapters 6,7 and 8.

5.2 Waveguide Fabrication Procedure

To ensure that waveguide properties can be reproduced the exchange process has to be accurately controlled. Some researchers therefore favour doing the exchange in sealed ampoules [5.44,5.42], but this was not considered necessary as reproducible results were obtained by the process outlined below.

Single crystal lithium niobate substrates were cleaned and degreased thoroughly using a series of organic solvents. The samples were then mounted in a PTFE or stainless steel sample holder before being placed in 250ml of benzoic acid in a stainless steel beaker placed in a high-temperature oil bath controlled to within $\pm 0.25^{O}C$. Figure (5.1) shows a schematic diagram of the proton exchange apparatus. Use of a stainless steel beaker ensured good thermal contact between the acid and the high temperature oil, while the volume of acid was large enough to provide an effectively infinite source diffusion. Measurements show that the acid and the oil are at slightly different temperatures (typically 1-2 ^{O}C), which is enough to modify waveguide properties if either measurement of temperature
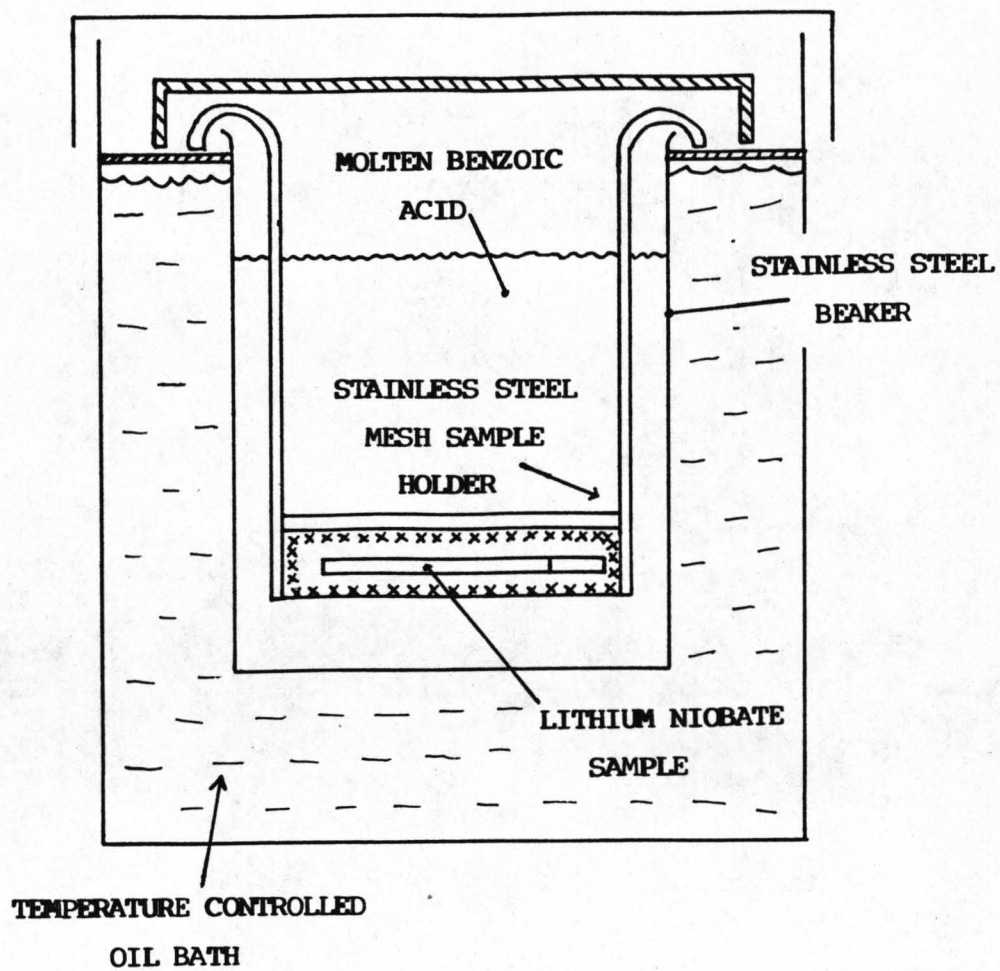
Figure (5.1): Schematic Diagram of Apparatus Necessary for the Proton Exchange Process

is not consistently taken (see section 5.4). The benzoic acid was renewed, at the most, after five exchange runs (typically fewer depending on the exchange times). The re—using of acid was thought to be acceptable because both optical waveguide measurements and IR absorption spectra (when monitoring the OH stretching bond) showed no difference between samples fabricated in fresh benzoic acid and samples from the fifth run (within experimental error). Both oil-bath and exchange-beaker were covered to provide a well-isolated temperature stable enviroment.

Exchange temperatures used ranged from 150°C to 220°C, with sample pre-heating being required at the lowest temperatures. The exchange time was defined as that between immersion of the sample in the benzoic acid and its removal from the acid. Crystallised benzoic acid (benzoic acid has a melting point of 122°C and a boiling point of 249°C), which formed on the lithium niobate substrate because of cooling after exchange, was removed by rinsing in chloroform and/or methanol. The samples were then stored for a long enough period to allow the refractive index of the waveguide region to relax to a stable value (typically for two weeks; see section 5.5). This was normally the case unless the sample was being prepared for post-annealing or device fabrication, where other process steps are involved.

5.3 Optical Analysis Techniques

The optical analysis of proton exchanged waveguides was derived initially using one source of data and one major, but reasonable, assumption. Measurements were made on a comprehensive series of waveguides on X-cut and Z-cut lithium niobate. The waveguiding layers were modified by varying the temperature of the exchange melt and the exchange duration (see section 5.2). Effective index measurements of each guided mode were made using the standard prism coupling technique [5.45], with the correct guided mode (TE for X-cut and TM for Z-cut) and maintaining propagation normal to the c-axis at all times to ensure no anisotropic light propagation on the PE X-cut substrates [5.22].

At the time of the analysis the preliminary papers published suggested that the refractive index profile of a PE waveguide was close to a step. Using this initial assumption and the theory of Kogelnik and Ramaswamy [5.46], which defines universal normalised dispersion curves for a step index waveguide profile, a computer programme was devised. The programme, using the normalised dispersion curves and the measured mode effective indices, estimated the waveguide depth and surface index.

An initial assumption made was that the data corresponded to a step-index slab waveguide model. The applicability of this model was then verified by obtaining consistent results for estimated waveguide depth over a wide range of fabrication conditions and at two different wavelengths (633nm and 1152nm).

For TE modes a normalised guide effective index b is defined:

$$b = \frac{(N^2 - n_f^2)}{(n_f^2 - n_s^2)} \tag{1}$$

where N is the guide mode effective index (determined by measuring prism coupler m-line angles), n_s is the substrate extra-ordinary refractive index (2.2025 at 633nm and 2.1517 at 1152nm) for TE modes on X-cut and Y-cut lithium niobate, and n_f is the (unknown) guiding region refractive index. A normalised guide thickness V is defined:

$$V = kf(n_f^2 - n_s^2)^{1/2} \tag{2}$$

where f is the guiding region thickness and k is the free space propagation constant. Plots of b versus V are obtained from the solutions of the normalised dispersion equation with an asymmetry parameter 'a' given by:

$$a = \frac{(n_s^2 - n_c^2)}{(n_f^2 - n_s^2)} \qquad (3)$$

where n_c is the cover region refractive index (i.e. air).

From a knowledge of the number of modes which the guide supports, an appropriately restricted range of values for V is determined. Within this range a computer scan is carried out to obtain an estimate of n_f for each mode, given an initial estimate of the asymmetry parameter 'a'. b-values from the initial choice of V are obtained from the theoretical plots, and, together with N-values from measurement, are used to obtain sets of estimated n_f values. V is then adjusted (and consequently the set of b-values) until the standard deviation over a set of n_f values is reasonably small (typically 10^{-4} for guides supporting several modes). The value for the asymmetry parameter 'a' given by equation 3 is also refined at the same time. Having obtained an estimate of n_f and its corresponding value of V, the waveguide depth, f, then follows immediately from equation 2.

Strong support for the step index model stems from the fact that the same estimates of depth (to within 1%) are obtained over a range of waveguides at both 633nm wavelength and 1152nm wavelength, with respective values, on X-cut lithium niobate, of $\Delta n = 0.1267$ and $\Delta n = 0.096$. The TE mode analysis described above applies for PE waveguides formed on X-cut lithium niobate, while for the TM modes which occur on Z-cut lithium niobate, some modification of the theory is required [5.46].

Another analysis technique used is the IWKB method [5.47]. The method takes as input the effective index measurements of the PE waveguides and uses an area minimising technique to work out the best-fit effective depth for each mode as well as an estimation of the waveguide depth. The IWKB method requires a waveguide to support at least four modes and as a result is not necessarily suitable for the analysis of waveguides of practical interest (since waveguides of interest only support one or two modes

depending on the application envisaged) however it provides a comparative technique for multimode waveguides and is invaluable when annealed waveguides are investigated (see chapter 8).

5.4 Waveguide Characterisation

PE waveguides may be characterised by estimates of their depth and guiding layer index assuming they have a step index profile. PE waveguides are formed in the manner described in section 5.2.

The values of effective index for each waveguiding mode and the corresponding estimated depth of the waveguide were plotted onto theoretical dispersion curves based on a step index model but assuming the average estimated film index. Figure 5.2 a) and b) are the plotted dispersion curves for PE waveguides on X-cut and Z-cut substrates at 633nm wavelength. The experimental points closely agree with the superimposed 'theoretical' dispersion curves, supporting the step index assumption. Table 5.1 shows typical estimated waveguide properties at the wavelength of 1152nm on X-cut lithium niobate samples with values at 633nm wavelength for comparison. Note the close agreement in estimated waveguide depth, supporting the assumption that the proton exchanged waveguides have a step-like refractive index profile. It must be noted that at the two different wavelengths the ordinary and extra-ordinary bulk refractive indices of both the prism and the substrate differ considerably [5.48,5.49,5.4] and, therefore, the waveguiding indices are also naturally different, although the estimated waveguide depths are approximately equal. Similar results have been obtained on Z-cut lithium niobate substrates.

It is possible to relate the proton exchange process to a diffusion model. To relate the exchange parameters to the estimated waveguide depth, the diffusion parameters must be calculated. Normally the oil temperature is taken as the exchange temperature (at least for the bulk of the measurements in chapters 5,6,7,8), however, to determine any differences in

TABLE 5.1

SUMMARY OF MEASURED WAVEGUIDE PROPERTIES AT 1152 nm WITH
BRACKETED VALUES MEASURED AT 633 nm FOR COMPARISON

TEMPERATURE (^{O}C)	TIME (hours)	SURFACE INDEX N_f	FILM THICKNESS t_f (um)	INDEX CHANGE $\hat{N}$
193	2.5	2.2477 (2.3290)	1.3258 (1.3017)	0.0960 (0.1265)
202	2.0	2.2477 (2.3319)	1.3915 (1.3731)	0.0960 (0.1294)
211	3.0	2.2471 (2.3313)	1.9356 (1.9603)	0.0954 (0.1288)
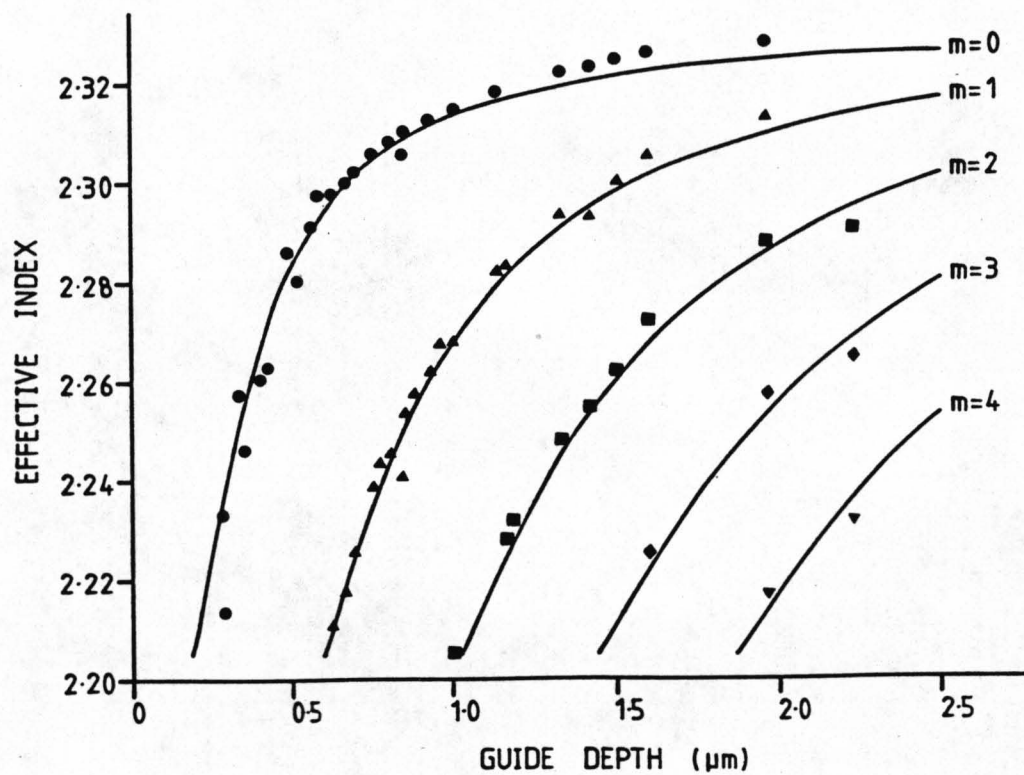
Figure (5.2): a) Experimental Points, on Theoretical DispersionCurves for a Step Index Change of 0.126 at a Wavelength of633nm, taken from X-cut H^+:$LiNbO_3$ Planar Waveguides.
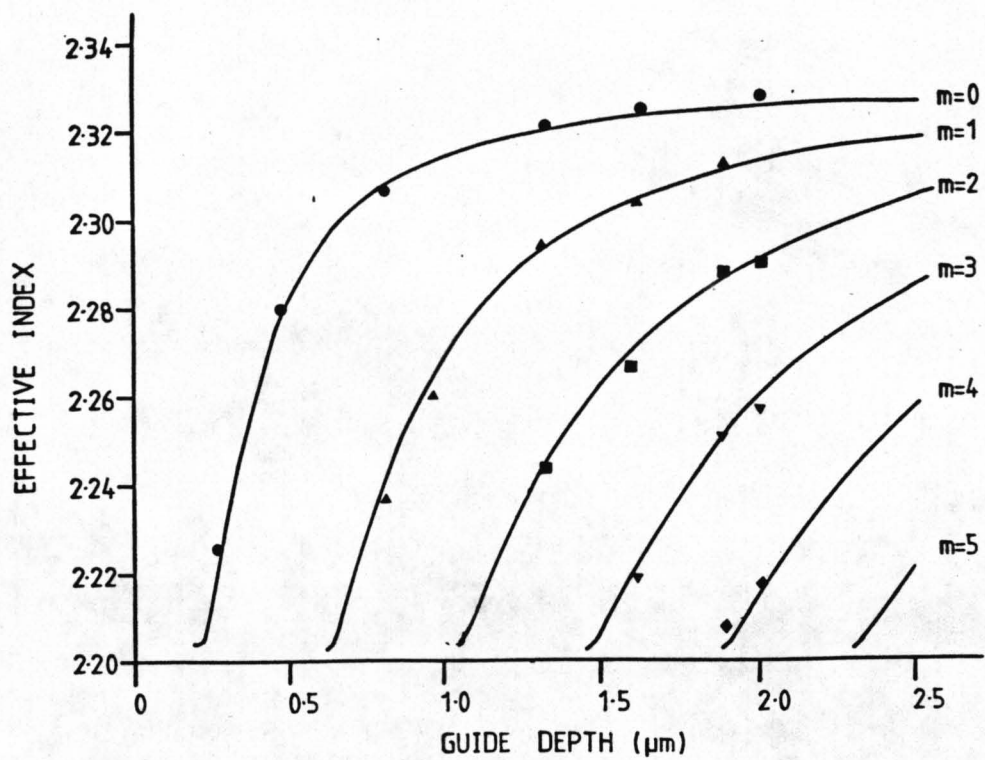
Figure (5.2): b) Experimental Points, on Theoretical Dispersion Curves for a Step Index Change of 0.126 at a Wavelength of 633nm, taken from Z-cut H^+:$LiNbO_3$ Planar Waveguides.

the diffusion coefficents when taking the acid temperature as the exchange temperature, both temperature measurements were made on PE X-cut lithium niobate. As was indicated above the difference in the oil and acid temperatures is $1-2^{\circ}$C. Figure (5.3) a) and b) show plots of diffusion depth versus exchange time, for each exchange temperature, for X-cut (taking the acid temperature as the exchange temperature) and Z-cut (taking the oil temperature as the exchange temperature) substrates respectively. Figure (5.3) a), b) show that the experimental points lie on a straight line indicating that the process is diffusion limited. The gradient of each line yields the diffusion coefficients, $D(T)$, (μm/hr$^{1/2}$) at each exchange temperature, T, (see table 5.2). For comparison Table 5.2 also has values of $D(T)$ on X-cut lithium niobate taking the oil temperature as the exchange temperature.

The values were calculated assuming that the diffusion depth, d, varies as follows:

$$d = 2(t.D(T))^{1/2} \qquad (1)$$

where t is the exchange time.

In equation (1) the dependence of D on temperature is given by the Arrhenius' Law [5.50]:

$$D(T) = D_O \exp(-Q/RT) \qquad (2)$$

where D_O is the diffusion constant for the proton exchange process for each crystal orientation (D_{OX} and D_{OZ} for X-cut and Z-cut lithium niobate respectively), R is the universal gas constant, T the absolute temperature and Q the activation energy for the process (Q_X and Q_Z as above).

If the proton exchange process is diffusion limited (of the form of equation (2)) then plotting the natural logarithm of the diffusion coefficients against the inverse of the exchanged temperature, for which the diffusion coefficient is calculated, should give straight-line plots.
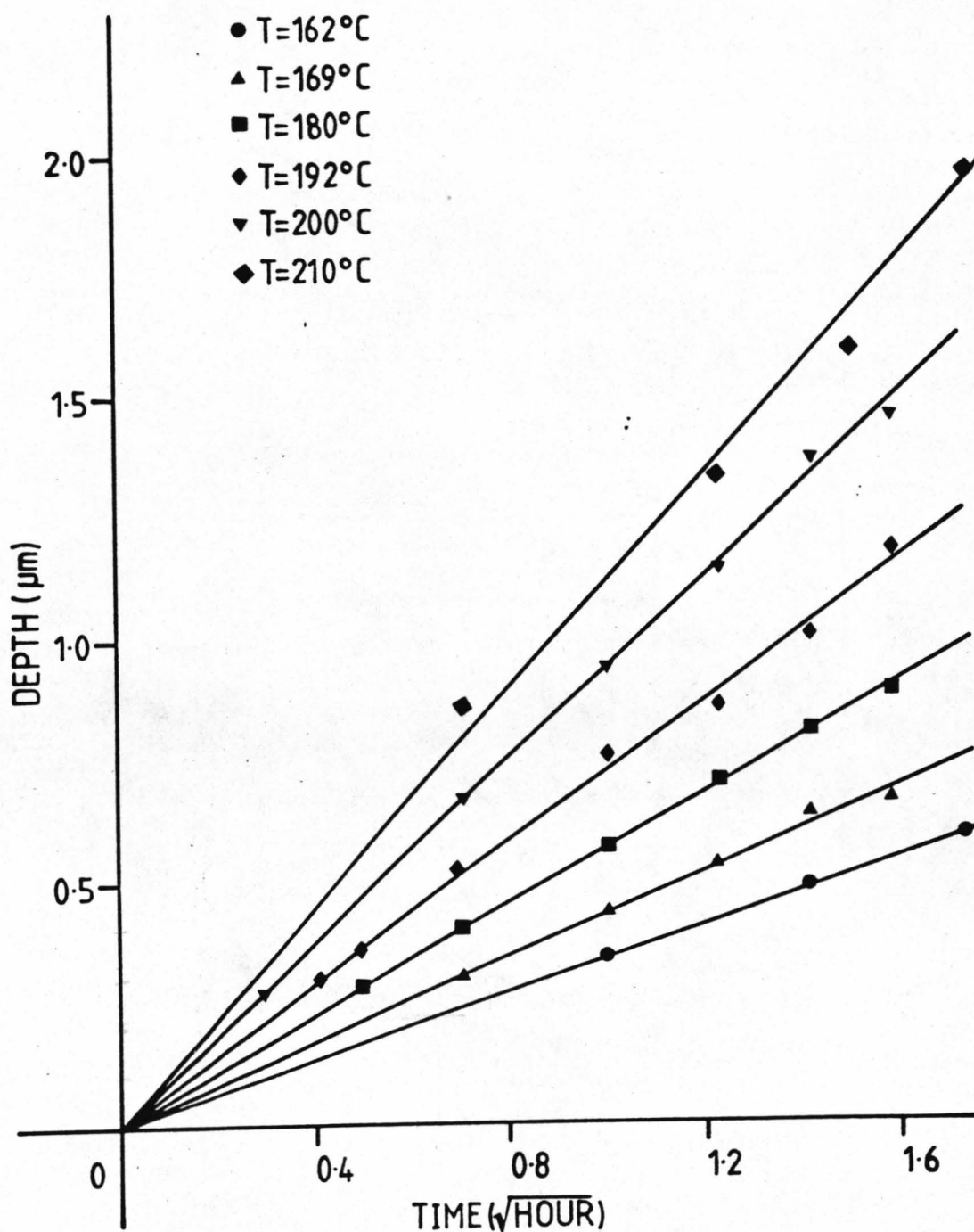
Figure (5.3): a) X-cut H^+:$LiNbO_3$ Slab Waveguides; Experimental Plots of Estimated Waveguide Depth (um) vs. Root Exchange Time ($h^{1/2}$) for Constant Temperature. The Gradient of the Lines Yield the Diffusion Coefficient at the given Temperature.
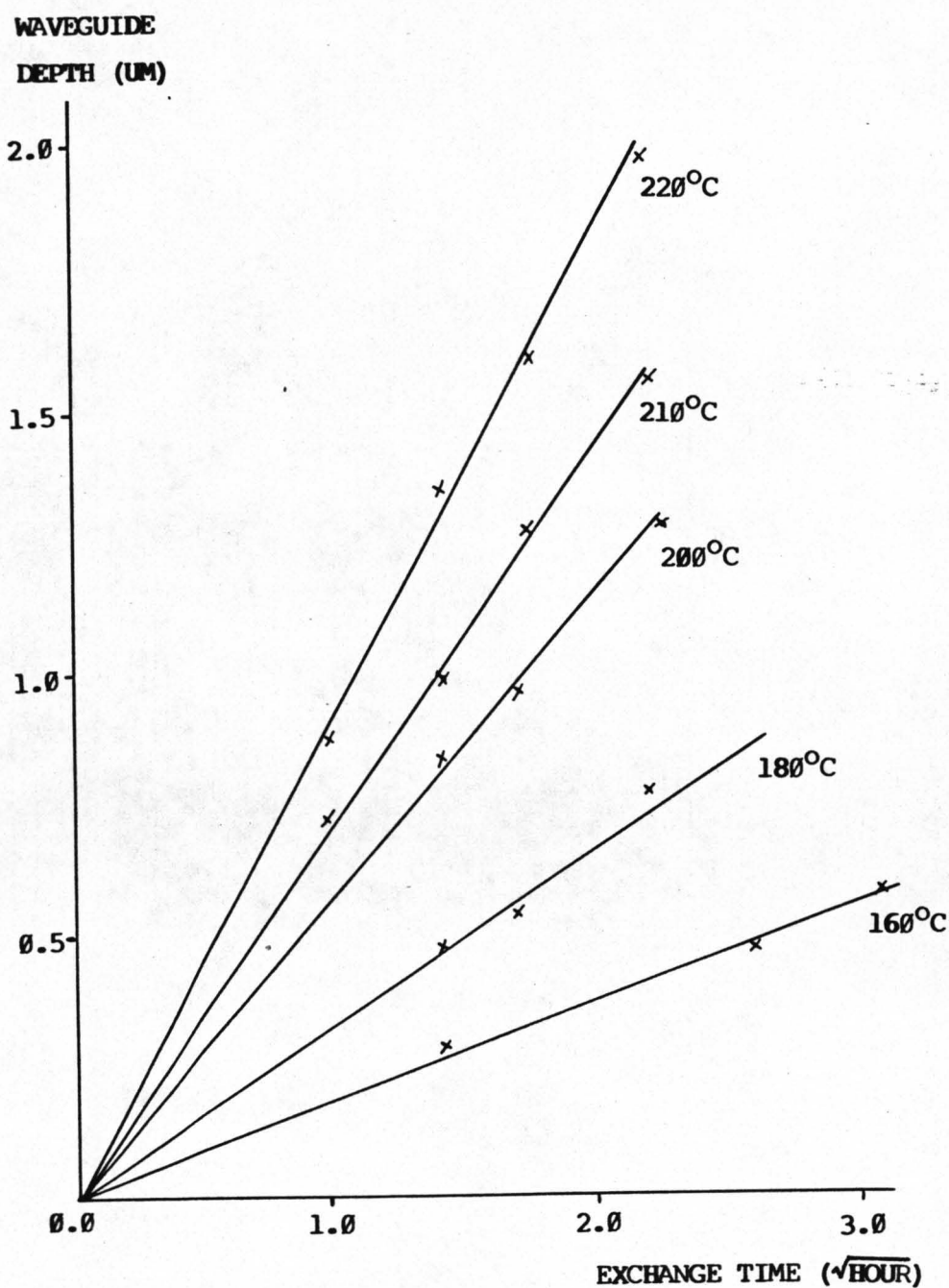
Figure (5.3): b) Z-cut H^+:$LiNbO_3$ Slab Waveguides;
Experimental Plots of Estimated Waveguide
Depth (um) vs. Root Exchange Time ($h^{1/2}$) for
Constant Temperature. The Gradient of the
Lines Yield the Diffusion Coefficient at the
given Temperature.

TABLE 5.2

DIFFUSION COEFFICIENTS FOR THE PROTON EXCHANGE PROCESS IN X-CUT
AND Z-CUT LITHIUM NIOBATE W.R.T. TEMPERATURE

X-cut Lithium Niobate

T (^{O}C) [K]	(a) D(T) (μm^2/h)	(b) D(T) (μm^2/h)
162 [435]	0.029	-----
169 [442]	0.047	-----
180 [453]	0.081	0.048
192 [465]	0.136	-----
200 [473]	0.220	0.153
210 [483]	0.291	0.232
220 [493]	-----	0.351

(a) Exchange temperature is acid temperature

(b) Exchange temperature is oil bath temperature

Z-cut Lithium Niobate

T (^{O}C) [K]	D(T) (μm^2/h)
160 [433]	0.008
180 [453]	0.027
200 [473]	0.081
210 [483]	0.126
220 [493]	0.207

Exchange temperature is oil bath temperature

Figure (5.4) illustrates the relationship between $1/T$ and $\ln D(T)$ and from these plots Q_x, Q_z, D_{ox} and D_{oz} have been obtained;

For X-cut lithium niobate: 1) Q_x = 84 kJ/mole

$$D_{ox} = 4.326 \times 10^8 \ \mu m^2/hour$$

when the acid temperature was taken as the melt temperature and

2) Q_x = 92 kJ/mole

$$D_{ox} = 2.298 \times 10^9 \ \mu m^2/hour$$

when the oil temperature was taken as the melt temperature.

From the diffusion coefficients plotted in Table 5.2 and the values of Q and D_o for PE X-cut lithium niobate calculated assuming either T is the acid temperature, 1), or T is the oil temperature, 2), it can be seen that there is a large difference in values. Even though the difference in temperature between the acid and the oil is at most 2.0^oC, the diffusion equation resulting from the graphs are also considerably different (see below). Therefore it appears that waveguide characterisation of this type is very sensitive to experimental procedure and especially to the exchange temperature.

For Z-cut lithium niobate: Q_z = 94 kJ/mole
(oil temperature) D_{oz} = $1.842 \times 10^9 \ \mu m^2/hour$

Thus equation (1) can be rewritten for the proton exchange process in X-cut lithium niobate, 1), as;

$$d = 4.168 \times 10^4 (t)^{1/2} \exp(-5.052 \times 10^3/T) \ \mu m$$

and for 2);

$$d = 9.587 \times 10^4 (t)^{1/2} \exp(-5.663 \times 10^3/T) \ \mu m$$
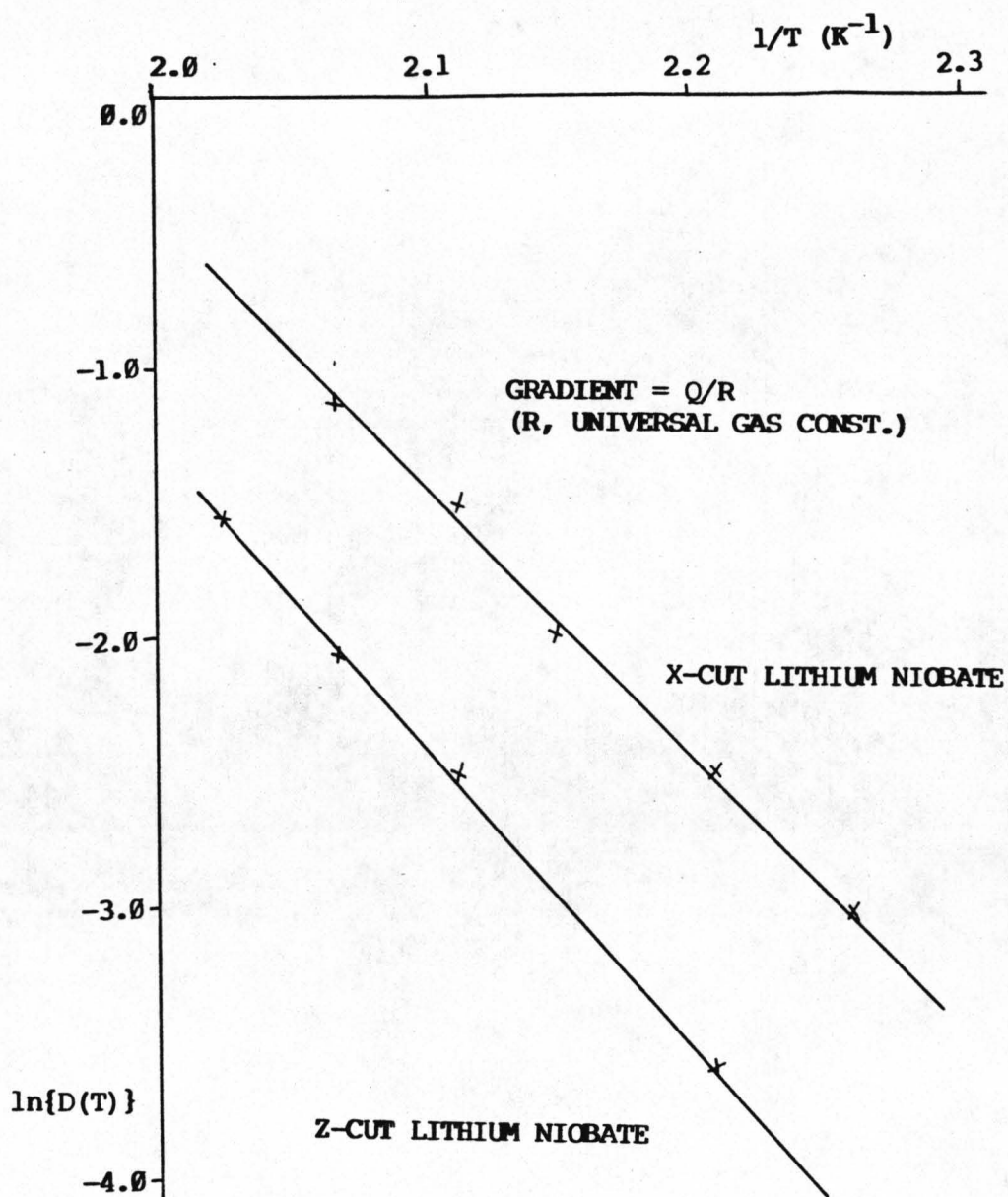
Figure (5.4): Plot of Inverse Absolute Temperature vs. the Natural Log of the Diffusion Coefficient. The Gradient of the Lines Yields the Process Activation Energy (Q) and the Cross-over Point Yields the Pre-exponential Term (D_o). Curves for X-cut and Z-cut $H^+:LiNbO_3$ Waveguides are Plotted.

and in Z-cut lithium niobate as;

$$d = 8.577 \times 10^4 (t)^{1/2} \exp(-5.650 \times 10^3 / T) \; \mu m$$

The index change on both substrates was estimated to be 0.1259 on X-cut lithium niobate and 0.1267 on Z-cut lithium niobate. At the wavelength of 1152nm the waveguide index change was estimated to be 0.0961 on X-cut lithium niobate and 0.0958 on Z-cut lithium niobate. The dispersion curves for the proton exchange process on X-cut and Z-cut lithium niobate can be seen on figure (5.2). In table 5.3 the cut-off depths for the first 6 modes are listed for PE waveguides on X-cut and Z-cut lithium niobate at 633nm and 1152nm wavelength.

The information in this section is sufficient to allow PE waveguides to be manufactured to any defined waveguide depth, with a choice of fabrication parameters. The optical properties of PE waveguides have been defined on X-cut and Z-cut lithium niobate at wavelengths of 633nm and 1152nm.

5.5 Optical Relaxation in Proton Exchanged Waveguides

A problem experienced with proton exchanged waveguides on lithium niobate, first described by Yi-Yan [5.51,5.52], is waveguide stability. This is not surprising since one of the assets of the PE process is that it occurs at low temperature. Yi-Yan outlines the fact that initially, after the exchange process, proton exchange waveguides have a high index change which relaxes to a lower value by as much as 0.0075. This relaxation depends on post-exchange time, and presumably temperature (see chapter 8). Yi-Yan's paper also describes a measured sinusoidal fluctuation with time in the index change. It must be mentioned however that Yi-Yan's assertions are not directly applicable to the waveguides formed in these experiments for the following reasons; The proton exchange process used by Yi-Yan took place in a closed ampoule, and not as described in section 5.2. Except for one sample, all the samples discussed in the paper were exchanged for

TABLE 5.3

TM MODE CUT-OFF SLAB WAVEGUIDE DEPTHS
IN PROTON EXCHANGED Z-CUT LITHIUM NIOBATE

MODE NUMBER	CUT-OFF DEPTH (μm) 633nm, 1152nm
0	0.18, 0.38
1	0.62, 1.28
2	1.03, 2.18
3	1.46, 3.03
4	1.88, 3.94
5	2.30, 4.82

TE MODE CUT-OFF SLAB WAVEGUIDE DEPTHS
IN PROTON EXCHANGED X-CUT LITHIUM NIOBATE

MODE NUMBER	CUT-OFF DEPTH (μm) 633nm, 1152nm
0	0.15, 0.35
1	0.57, 1.23
2	1.00, 2.12
3	1.42, 3.00
4	1.82, 3.89
5	2.25, 4.77

extreme lengths of time e.g. 24h or 36h (at 200°C). If these exchange times were used with the fabrication procedure outlined in section 5.2 substrates would be damaged (see section 5.9). It must therefore be assumed that the closed ampoule PE process has markedly different effects on the lithium niobate crystal from those produced by our process.

The data suggests that only at very long diffusion times does the sinusoidal variation in index become evident. It is possible, when using a closed ampoule process, that the onset of surface damage to alleviate strain in the lattice is replaced either by a change in crystal phase or possibly by a self-annealing effect. A change in phase could very possibly cause the observed effects. The two-moded waveguide on Z-cut lithium niobate, discussed by Yi-Yan, does however exhibit very strange stability characteristics with respect to post-exchange time, the difference in the waveguide formation process might explain why the effects were not observed with our waveguides.

Measurements on waveguide stability using the process described in section 5.2 were as follows;

Figure (5.5) shows a) the variation of effective refractive index and b) the calculated surface index w.r.t. time after the exchange process. The waveguide is on Z-cut lithium niobate and was exchanged for 2h at a melt temperature of 200°C and supports 2 modes. Initially when the waveguide was removed from the melt the waveguide had a surface index much higher than expected. However, after a few weeks, the waveguide refractive indices relax to a stable value. The drop in refractive index is in total in the order of 0.0075. Also in contradiction to Yi-Yan's results the relaxation of refractive index is relatively smooth (whereas his plots fluctuated by as much as 0.001 from point to point). A plot of the time relaxation of a single mode waveguide fabricated by proton exchange on X-cut lithium niobate can be seen in figure (5.6).
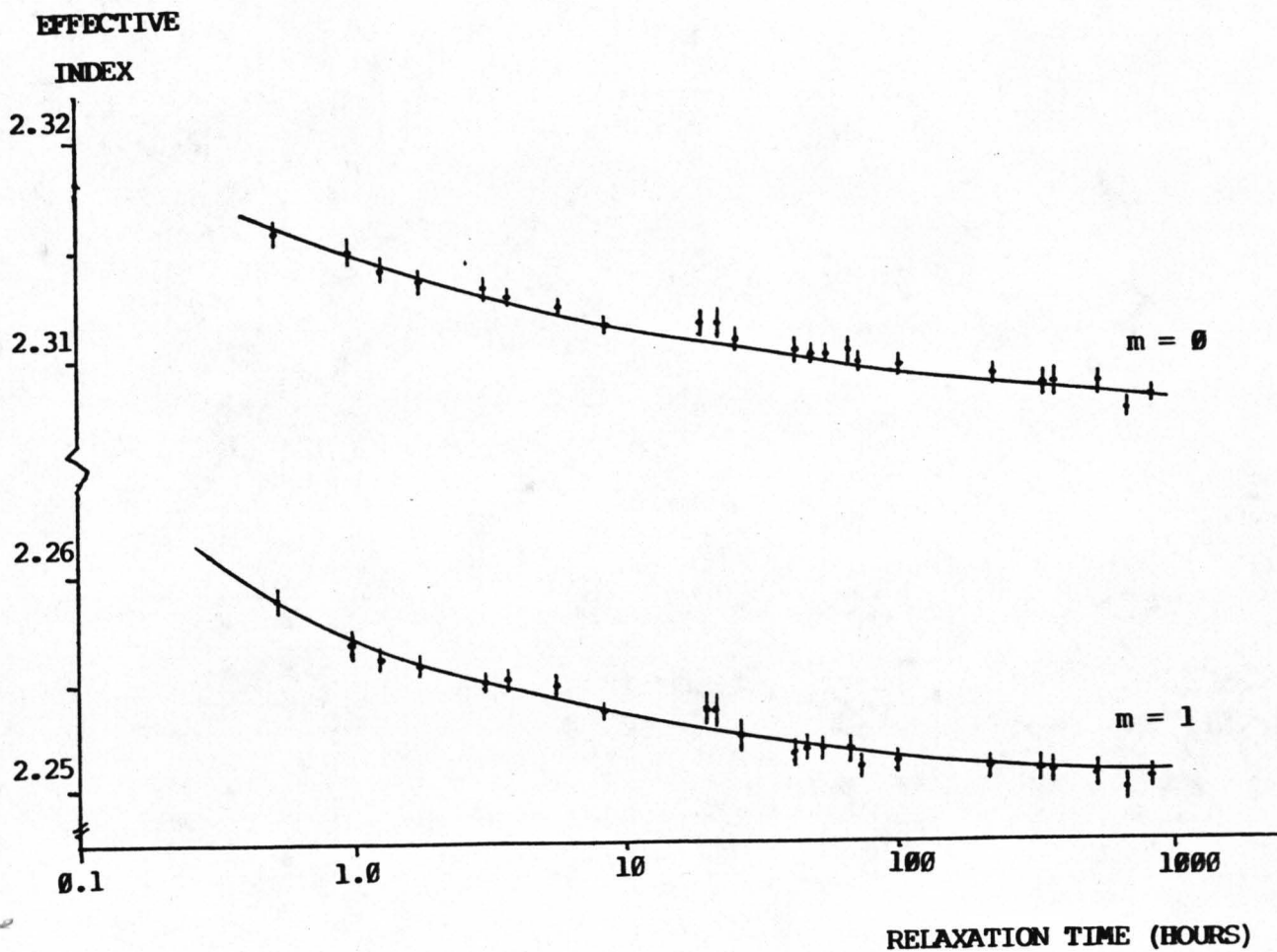
Figure (5.5): a) The Graph Shows the Relaxation w.r.t. Time of Mode Effective Indices After Removal from the Exchange Melt. (Z-cut $LiNbO_3$ Exchanged for 2 hours at 200^oC)
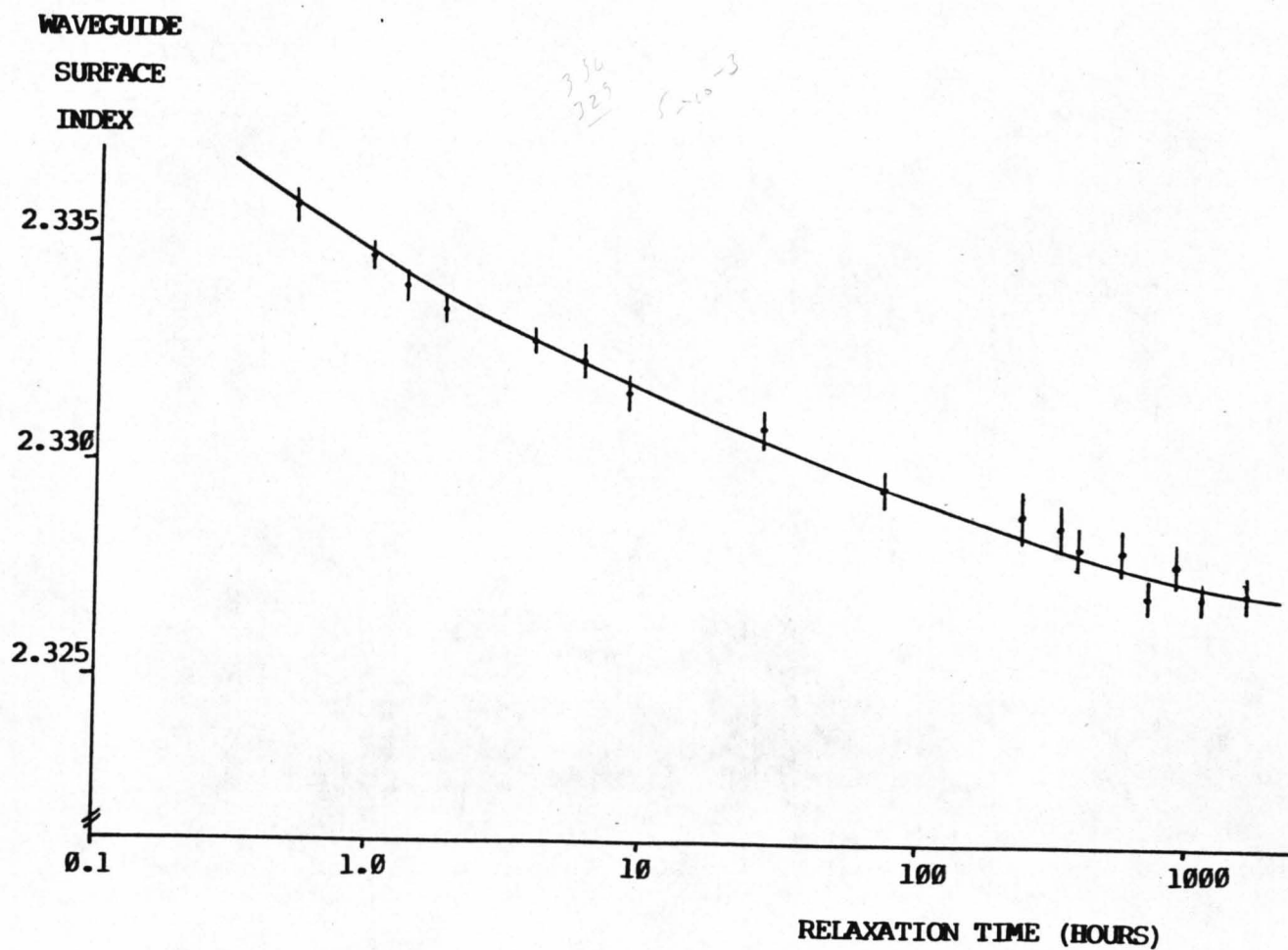
Figure (5.5): b) The Graph Shows the Relaxation w.r.t. Time
of Estimated Waveguide Surface Index After
Removal from the Exchange Melt for the Planar
Waveguide Depicted in (5.5) a)
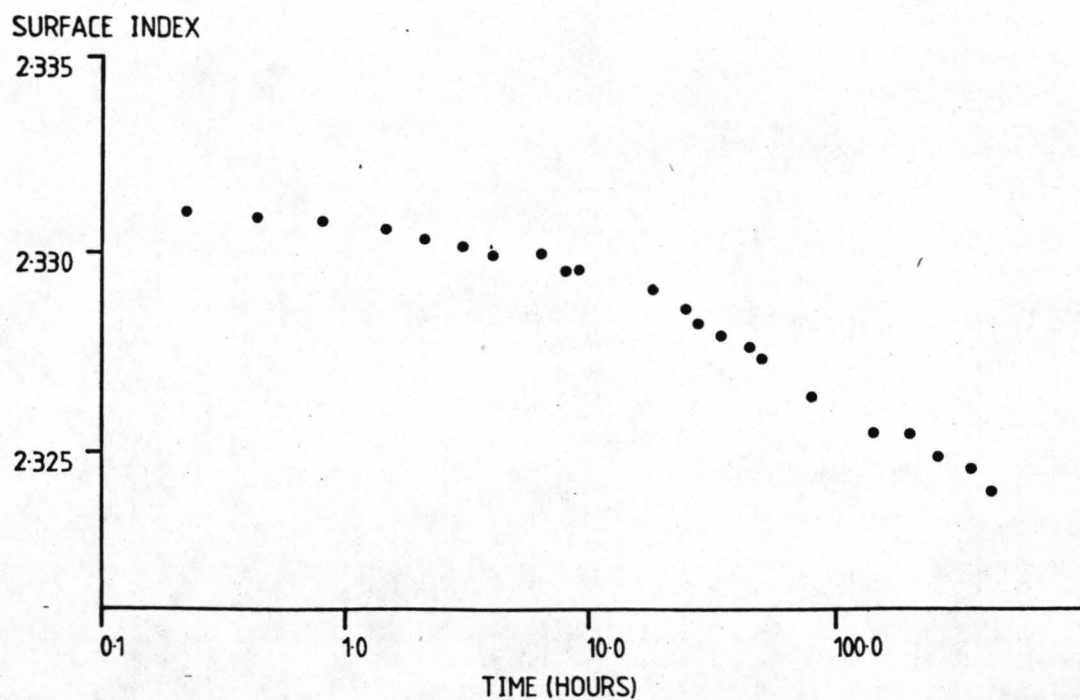
Figure (5.6): The Graph Shows the Relaxation w.r.t. Time of the Estimated Surface Index after Removal from Exchange Melt. (for X-cut LiNbO$_3$ Exchanged at 200°C for 1.0 h)

For further discussion on the relaxation, or possible low temperature annealing, of proton exchanged waveguides see chapter 8.

5.6 Off-Axis Propagation in Anisotropic Proton Exchanged Waveguides

Off-axis light propagation has been investigated in titanium indiffused waveguides examining particularly the creation of leaky modes [5.53,5.54,5.55]. Leaky modes occur in an anisotropic waveguide when the direction of light propagation is off-axis, such that the effective index of the guided mode is less than the higher of the two bulk refractive indices (when considering a birefringent crystal). If the guided mode index, N_{eff}, is less than the higher bulk index, N_o, then at either of the waveguide interfaces a polarisation transformation can occur, if there exists a phase matching condition:

$$N_{eff} = N_o \cos(A)$$

where A is the angle between the axis with the higher refractive index, N_o, and the direction the polarised light which is anisotropically propagating and whose effective refractive index is N_{eff}. For titanium diffused waveguides on X-cut or Y-cut lithium niobate this effect results in a converted mode which also can be supported by the waveguide.

Leaky modes created by off-axis propagation can occur on X-cut and Y-cut lithium niobate since both the guided index (N_e) and the non-guiding index, (N_o), have components in the plane of the waveguide. TM modes in PE Z-cut lithium niobate waveguides propagate isotropically in any direction since the index change is normal to the waveguide surface and the substrate index in the plane of the waveguide is isotropic.

Ctyroky [5.56] has analysed theoretically the effects of anisotropic light propagation on proton exchanged waveguides on

X-cut lithium niobate. However the author failed to take into account the significant effect of the proton exchange process on the ordinary axis, reducing the usefulness of his results. A comparison is made below between Ctyrokys' theoretical findings and the experimental results discussed below.

The effects of off-axis light propagation on PE anisotropic waveguides were determined experimentally. Measurements were made on a 2 inch square, 1mm thick plate of X-cut lithium niobate. The waveguide was formed by exchanging the plate in benzoic acid for 4h at a constant temperature of $182^{O}C$, in the same way as described in section 5.2. After the exchange process, the plate was scanned in an optical thickness monitor to confirm that a uniform thickness exchange layer had been formed (see section 5.10). The guide layer had a refractive index of 2.3276 (i.e. an index increase in the extra-ordinary axis of 0.125), while the ordinary axis was assumed to have a refractive index decrease of 0.04. The waveguide depth was calculated from the melt parameters to be 1.26μm. The waveguide supported 3 TE modes for light propagation normal to the c-axis.

Crystallographic orientation and notation were kept consistent with the theoretical paper by Ctyroky to aid the comparison (see figure (5.7)). The waveguide mode effective indices were measured as a function of propagation direction and the results plotted on figure (5.8). Measurements of mode angles were made at 5 degree intervals from the c-axis. Making use of the waveguide mode-effective indices and the effective substrate index at each propagation angle, the waveguide surface index and the waveguide depth was estimated assuming a step index profile (see section 5.3). The waveguide depth was estimated to be in the range 1.25 ±0.03μm at each propagation angle and these values agree well with the value estimated from the diffusion coefficients.

It can be seen from figure (5.8) that as the propagation angle from the c-axis decreases below 90° each of the waveguiding modes cut off. The position of the cut-off of each mode coincides with
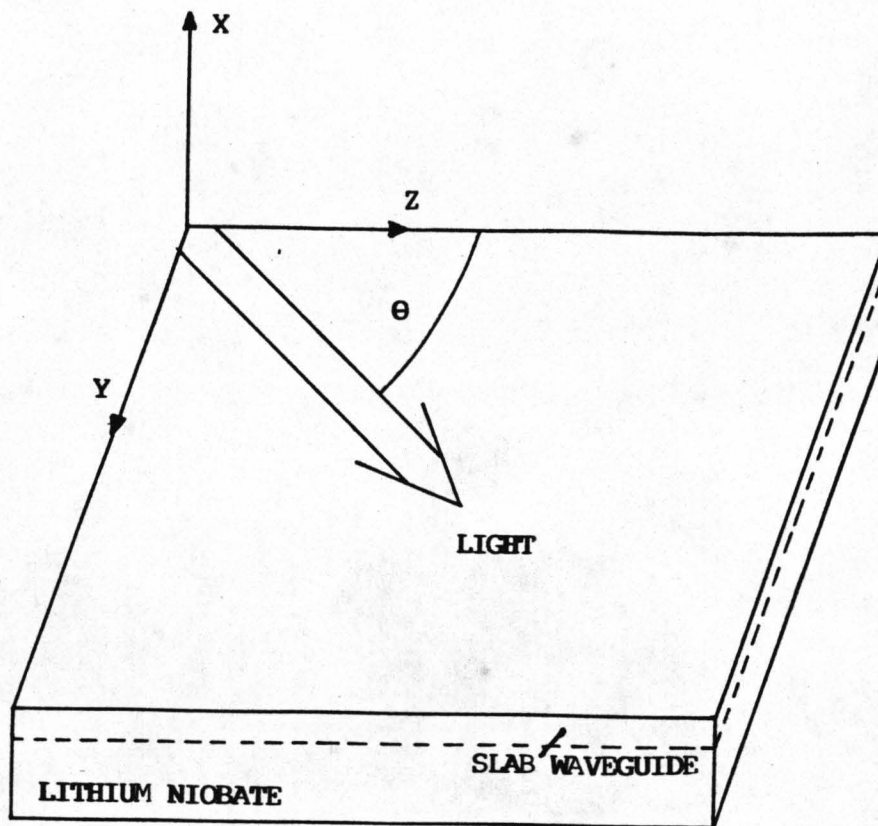
Figure (5.7): Diagram Depicting Crystallographic Orientation used in Figure (5.8) (After Reference [5.56])

Figure (5.8): Experimental Analysis of the Angular Dependence of Effective Refractive Indices of Modes in a Proton Exchanged X-cut Lithium Niobate Anisotropic Waveguide;

N_g - Waveguide Surface Index for Y-axis Propagation;

N_o - Bulk Ordinary Index;

N_o'- Waveguide Ordinary Index Assuming Proton Exchange Modification;

$N_{ef}(\theta)$ - Angular change in Waveguide Index Assuming N_o ;

$N_{ef}'(\theta)$ - Angular change in Waveguide Index Assuming N_o';

N_e - Bulk Extra-Ordinary Index;

$N_{es}(\theta)$ - Angular Dependenceof Effective Bulk Index;

⊠ - Angular Dependence of Mode Effective Indices m = 0,1,2 (Experimental);

θ = 0,1,2 Cut-off Angle for the Waveguiding Mode m = 0,1,2;

Ŧ - Experimental Values of Waveguide Surface Index

Calculated from the Mode Effective Indices at each Angle; Region below Horizontal Dotted Line

- Waveguide Modes are Leaky;

The Region to the Left of the Vertical Dotted Line

- No Guided Modes are Supported
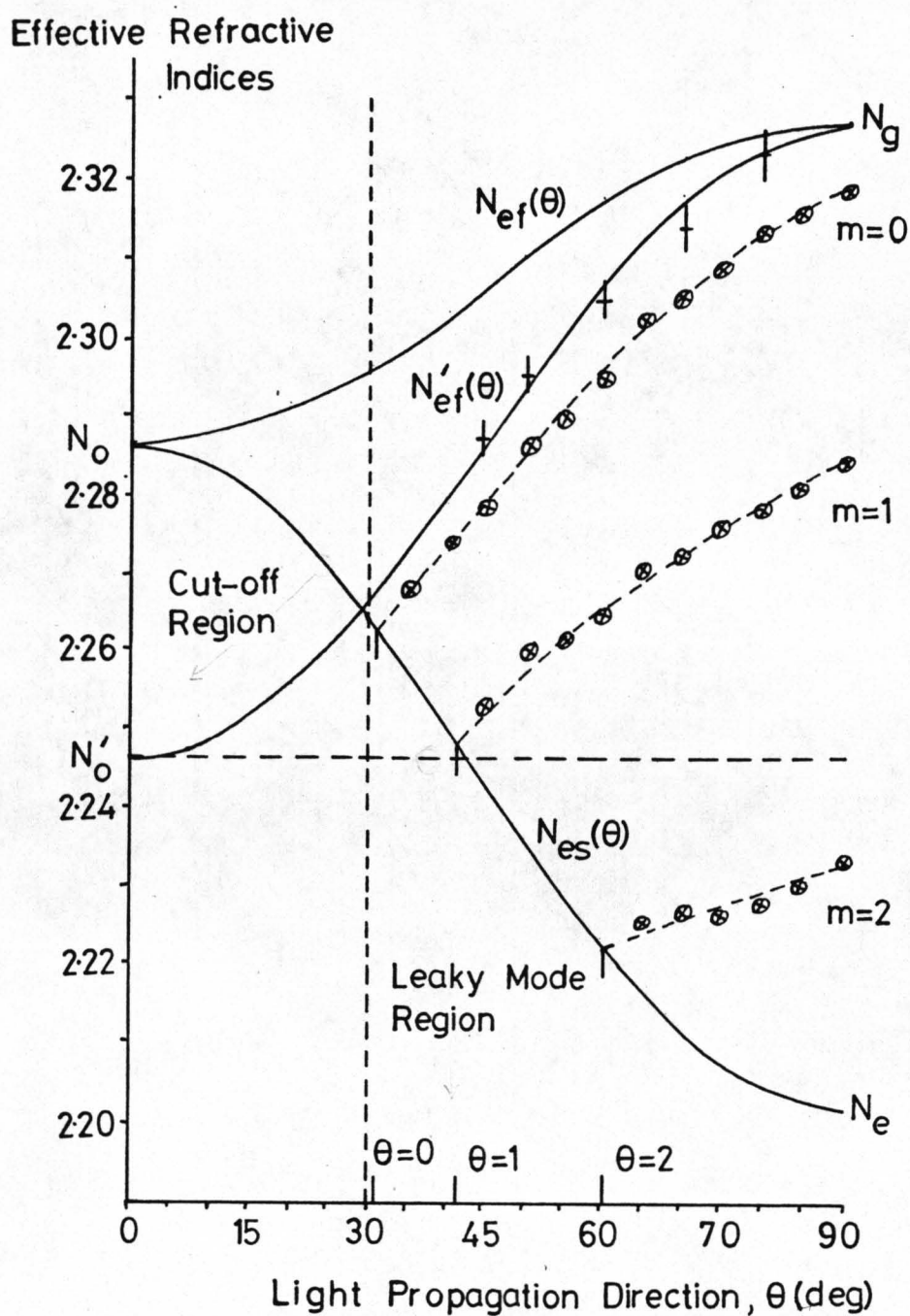
Figure (5.8):

the position of the effective substrate index $N_{es}(\Theta)$ at that angle. The cut-off propagation angle for the modes m=1,2,3 are marked on figure (5.8) with Θ=1,2,3.

Figure (5.8) has two curves plotted for the theoretical change in waveguide index with respect to angular direction of propagation. Curve $N_{ef}(\Theta)$ makes the assumption that the decrease in the ordinary axis refractive index due to the proton exchange process is negligible and curve $N_{ef}'(\Theta)$ takes the -0.04 index change into account. The experimental values of the waveguide index, on figure (5.8), show good agreement with the curve $N_{ef}'(\Theta)$ and indicate that the negative index change must be taken into account to obtain an accurate representation of the actual experimental situation. This fact clearly modifies the conclusions to be obtained from reference [5.56].

Different authors have published the negative change in the ordinary axis caused by the proton exchange process as either -0.04 or -0.05 [5.25,5.52]. The results on figure (5.8) indicate that if a -0.05 index change was assumed for the curve $N_{ef}'(\Theta)$ then the waveguide index values would not agree with the experimental data. The value of -0.04 is therefore closer to the true value of this phenomenon. Guided modes propagating off-axis and having an effective index of less than 2.2467 will be leaky as indicated in figure (5.8). This implies that a larger range of propagation angles and number of guided modes will propagate without becoming leaky than indicated in reference [5.56].

Many of the possible uses of proton exchanged waveguides on Y-cut lithium niobate (due to its efficient acousto-optic interaction, forming Bragg cells and possibly spectrum analysers in this material is attractive) and in X-cut lithium niobate require that waveguides support only a single mode. This means that there is still a very good chance that useful waveguides will support leaky modes along off-axis propagation directions. For Θ close to 90° (+/- 5°) this effect should be unimportant as indicated by the fact that useful device performance has already been obtained [5.40].

The above conclusions were based on the assumption that leaky modes in PE waveguides were generated in a manner similar to that of Ti:diffused waveguides i.e. polarisation conversion only occured at the air/waveguide interface due to the high index discontinuity.

This assumption was tested when Ctyroky published a theoretical paper on anisotropic light propagation (taking the negative ordinary index of PE layers into account) [5.57]. In fact leaky modes theoretically do exist for mode indices less than the higher of the two substrate indices and not 2.2467 as discussed above. The main reason for this is that the assumption discussed above (forming the basis of reference [5.22]) is incorrect. In PE layers there is a considerable index discontinuity at the waveguide/substrate interface as well as the air/waveguide interface and as such polarisation conversion occurs at that boundary also. Theoretically it appears that the larger of the two effects is at the waveguide/substrate interface [5.57]. For propagation angles that give a small deviation from normal to the c-axis the effect is negligible [5.22,5.57], and more importantly if larger deviation angles are required, modification of the waveguide profile (i.e. by annealing) can alleviate the leaky mode loss to some degree [5.57].

5.7 Waveguide Losses (In and Out of Plane Scattering Measurements)

The measurement of planar waveguide propagation losses is critical to the analysis of the waveguide 'quality'. The three main types of non destructive loss measurement on planar waveguides are:-

1) Out-of-plane Scattering: This method is based on the assumption that the power scattered outwards from the surface of a light propagating waveguide is proportional to the power propagating in the waveguide. The out-of plane scattering from light propagation in an optical waveguide can be imaged on the
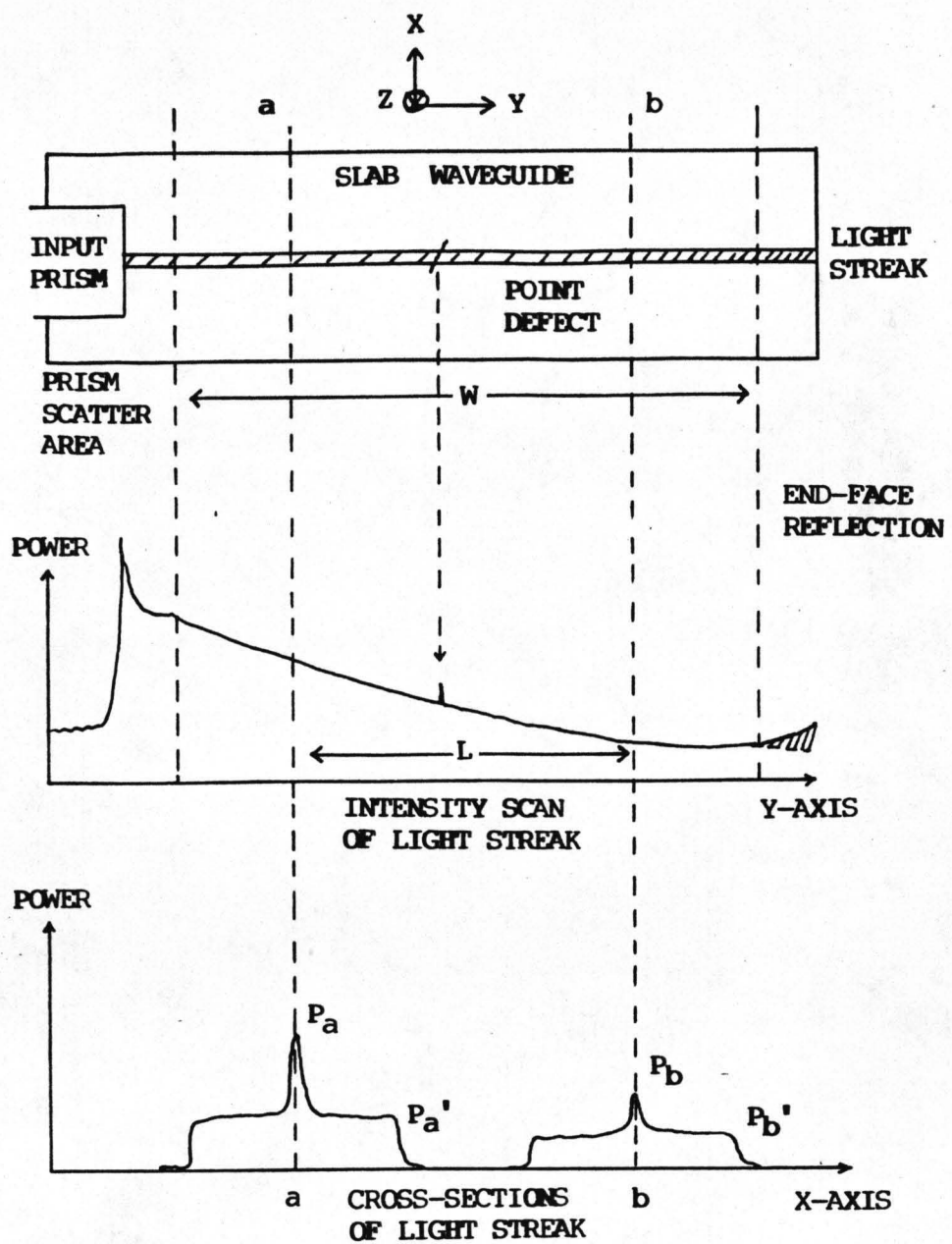
Figure (5.9): Schematic Diagram Depicting Information Available from the Line Scan of a Hamamatsu Vidicon Camera and Associated C1000 Control

screen of a vidicon camera and the light streak monitored transversely with the aid of a linear scan, similar to the method proposed by Okamura [5.58,5.59] and used, essentially, by many others before Okamura's publication. Figure (5.9) shows a schematic diagram of typical data obtained from a line scan both parallel and perpendicular to the direction of propagation. From (5.9) it can be seen that the range of useful information is 'W' which is limited by input prism light scatter and the back reflection from the waveguide end-face. Although a longitudinal scan of the light streak does not give the loss (because the substrate noise level is not determined) it does define the working area of the line scan and highlights any waveguide point defects (which if unnoticed would cause spurious results. Along the useful length of the light streak, the power can be monitored at any point (by means of a transverse line scan) e.g. the maximum streak power at point 'a' is P_a and the background power at point 'a' is P_a'. Taking the power of the light scattered from the light streak (P_a-P_a') and at subsequent points (such as point 'b'), and knowing the distance between each point (i.e. between 'a' and 'b' the distance is L cm) , the propagation loss in the waveguide can be estimated;

$$10 \times \log \left[(P_b-P_b')/(P_a-P_a') \right]/L \quad dB/cm$$

This method is not mode selective in the sense that even though a single mode may be excited in a waveguide it cannot distinguish between that mode and the modes originating from mode coupling at scatter points. The method is also more suitable for waveguides which have a large amount of scatter. Losses below 1dB/cm are difficult to detect with this method.

2) Two Prism and Three Prism method [5.45,5.60]: this method makes relative positional measurements of the output prism coupled power along the length of the waveguide. It measures directly the propagation loss in the waveguide and since the output prism distinguishes between modes, the mode scattering loss as well as the coupled mode propagation loss can be measured.

The basic two prism technique has to assume that the coupling efficiency of the output prism is consistent for each positional measurement taken, which it may not be. The three prism technique, with the extra prism at the waveguide end, monitors the coupling efficiency of the output prism and hence it can be compensated for when calculating waveguide loss.

The three prism technique is not more accurate than the two prism technique but it is less dependent apon experimental competence. Propagation losses as low as 0.1dB/cm can be measured using this technique.

3) In-plane Scattering [5.61,5.62]; this method is based on the assumption that the light scattered sideways in a planar optical waveguide is relative to the quality of the waveguide. The sideways scattered light as well as the unscattered light can be 'made available' for measurement by output prism coupling, the output coupled scattered light is commonly known as an m-line. Figure (5.10) shows m-lines (i.e. out-put coupled waveguide modes) for a PE waveguide on Z-cut lithium niobate. From the scan of an m-line shown in figure (5.11) it can be seen that the central peak is the waveguide mode and the 'moustache' on either side is the in-plane scatter. A convention is clearly needed to define the method of measurement of the level of in-plane scattering. In this case, the assumption is made that the in-plane scattering levels will be measured at an angle of 1.0° from the m-line centre. Again, as in 2), relative positional measurement of in-plane scattering levels are made to determine the waveguide figure of merit ΔI (dB/cm), as defined by Armenise [5.61,5.62].

Measurements of waveguide propagation loss by the out-of-plane scattering method (as in '1)' above) yielded propagation losses (at λ = 0.633um) typically between 2.4 and 4.8 dB/cm on Z-cut lithium niobate PE waveguides. At 1.15um the best measured propagation loss was 2.1 dB/cm. For X-cut lithium niobate the best propagation loss measured at 0.633μm was 1.4 dB/cm and at 1.15μm it was 1.3dB/cm. All the results above had an error of
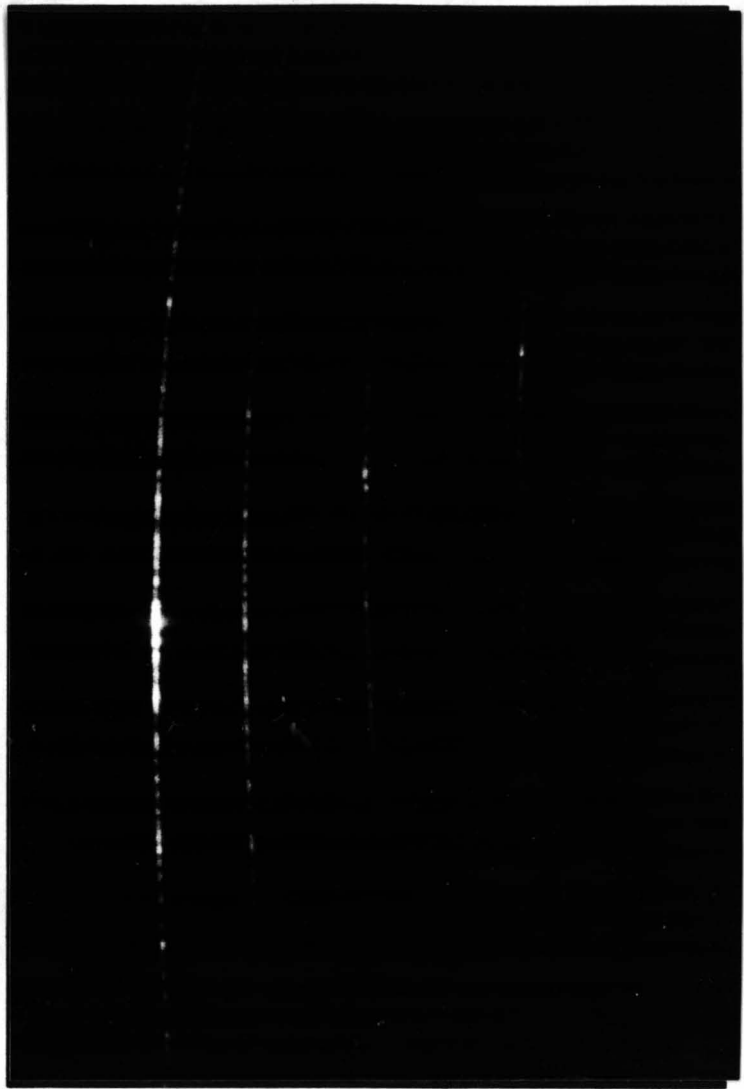
Figure (5.10): Photograph of PE Waveguide Modes Output Prism Coupled, Depicting Intermodal and Inplane m-line Scatter (Z-cut Lithium Niobate Exchanged for 1.5 hours at 220°C, waveguide supports 4 modes)
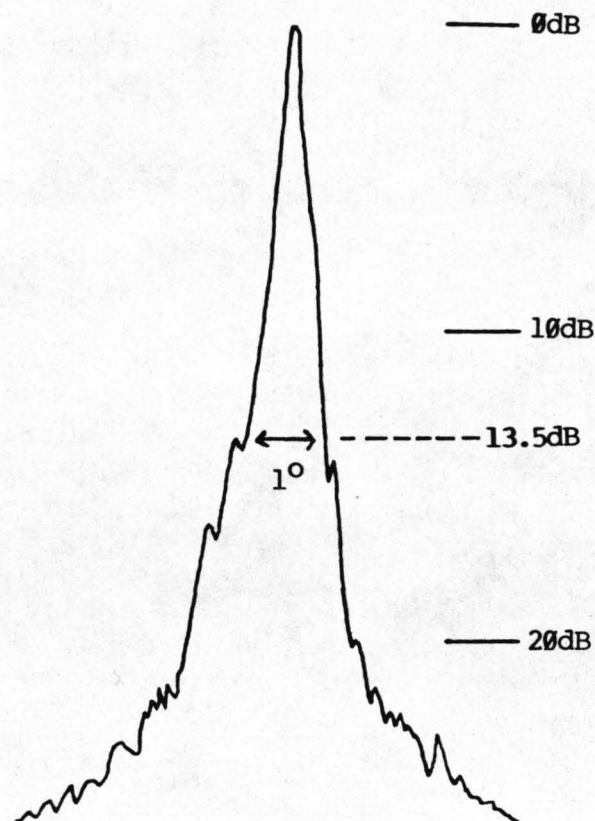
Figure (5.11): Intensity Scan of a m-line on PE Z-cut Lithium
Niobate. The Scan is of the Fundamental Mode of a
Four Moded Waveguide Exchanged at 220°C for
3h 55min. The 1° Intensity Drop is 13.5 dB at a
at a Distance of 0.5m and an Operating Wavelength
of 633nm.

+/- 0.3dB/cm and in all cases the values did not follow any clear trend with respect to fabrication temperature, time or waveguide depth. Jackel has reported loss measurements on X-cut lithium niobate PE waveguides [5.15] of 0.5dB/cm. This value is very low and neither the research done at Glasgow University [5.63] or elsewhere [5.64,5.65] has ever reported such low losses on PE waveguides.

Measurements of propagation loss using the two prism method, 2)[!]. Loss measurements on a three moded PE wavguide on Z-cut lithium niobate fabricated at 221°C for 2h were as follows:

fundamental mode 2.27 +/- 0.24 dB/cm
first order mode 3.24 +/- 0.57 dB/cm
second order mode 4.46 +/- 1.0 dB/cm

The propagation losses increase as the mode order increases. This is reasonable since the higher order modes have successively more reflections on waveguide boundaries. Chapter 7 shows that there is a surface damaged layer on PE waveguides on lithium niobate (about 500 angstroms thick). It may be that the damaged surface layer on the waveguide is the main loss mechanism.

These typical values compare well with those obtained by out-of-plane scattering measurements. No measurements were obtained by the three prism method.

Preliminary in-plane scattering measurements indicate that in all cases scattering levels in PE waveguides are much higher than in Ti:diffused waveguides. Titanium diffused waveguides have an in-plane scattering level (ΔI) of approximately 1.1dB/cm (or greater) whereas PE waveguides can be as high as 15dB/cm and only as low as 5.2dB/cm [5.66,5.40]. It is clear that in-plane scattering, levels are lower in PE waveguides in X-cut lithium

[!] Thanks are due to Dr Al-Chalabi for loss measurements on PE waveguides using the two prism technique, Dept E&EE, University of Surrey, Guilford.

niobate than in guides in ~~z~~-cut lithium niobate.

When output prism coupling a PE waveguide mode, scattering manifests itself in the form of three basic phenomena (neglecting absorption).

1) In/Out-of-Plane Scattering: Input prism coupling is mode selective therefore as the light is coupled into the slab waveguide initially only one mode is excited. This propagating mode has inplane scattering i.e. there is a visible m-line rather than a pure output coupled spot.

2) Intermodal Scattering: Secondly all the other waveguided modes supported by the waveguide are visible in the output coupled light i.e. as the mode propagates in the slab, defects and discontinuities in the waveguide cause the mode to scatter into the other modes (which is evident from figure (5.10)).

3) Polarisation Transformation: Thirdly it has been observed that a second faint set of m-lines are visible from the output coupled light. Initially this light was thought to be a reflection from the prism but on further investigation it was discovered that the faint modes were of the opposite polarisation to the waveguided modes. This is strange because PE waveguides are highly polarised and couple the orthogonal mode directly to the substrate. The faint m-lines are -30dB down on the intensity of the coupled modes. This effect could be caused by distortion at the prism/waveguide interface or scattering points in the waveguiding structure. It is conceivable that light converted to the non-guiding polarisation will remain in the guiding region for a long enough period to be output coupled, and as the waveguides are very lossy, polarisation conversion at scattering points is a possibility.

Further investigation of waveguide loss mechanisms is necessary to help quantify and hence reduce PE waveguide losses.

5.8 Waveguide Surface Damage

Surface deterioration in the form of cracks results in badly coupled and lossy optical waveguides were first noticed for the proton exchange process on Y-cut lithium niobate [5.67,5.15]. The effect is so severe that even for exchange periods of 10 mins surface damage can occur. This means effectively that only single mode waveguides can be made by PE in Y-cut lithium niobate [5.16]. Thus waveguide characterisation and computation of diffusion parameters cannot be undertaken on Y-cut crystals by an optical analysis technique, unless the process is modified to allow deep, damage free, waveguiding structures in Y-cut lithium niobate.

The damage is also evident on X-cut and Z-cut lithium niobate. However, X-cut lithium niobate exhibits surface damage typically after 5h at 210°C and Z-cut lithium niobate after 17h at 220°C. These conditions result in extremely multimode waveguides which as such have limited applications to integrated optical devices working at a wavelength of 0.633μm. Unfortunately waveguides for operation in the infra-red need deeper waveguiding structures and hence surface damage could become a problem for PE in X-cut and Z-cut lithium niobate. The onset of surface damage appears to be dependent upon the exchange depth. X-cut and Z-cut lithium nionate samples exhibit surface damage when exchanged to a depth of greater than 3μm.

A materials analysis and explanation for the occurrence of surface damage on Y-cut lithium niobate will be discussed in chapter 7.

5.9 Formation and Analysis of Tapered Regions in Proton Exchanged Lithium Niobate Waveguides

Stewart et al. [5.68,5.69,5.70] have explored the possibility of constructing hybrid integrated optical systems using directional coupling techniques to interconnect waveguides in different

materials. Coupling between glass and lithium niobate guides (with As_2S_3 overlays) has been demonstrated , but difficulties were encountered due to the need for exact phase matching of the guided modes [5.68]. Proton exchange, however, will allow taper velocity coupling methods to be employed [5.36,5.37,]. Furthermore, proton exchange waveguides and tapers could be formed over existing Ti-indiffused waveguides (TIPE guides) thus allowing coupling to existing devices formed with the Ti-indiffused waveguide [5.37].

Proton exchanged tapered waveguiding regions such as those illustrated in figure (5.12) (inset) may simply be formed by partially immersing the lithium niobate substrate in benzoic acid, the taper being formed at the meniscus of the acid. The taper length is not controllable and is defined by the temperature and time of the exchange process for a required waveguide depth.

In order to analyse the tapers, the apparatus illustrated in figure (5.12) was used [5.36]. The output from the laser (633nm wavelength) is first passed through a polariser and then focussed to a 25µm spot size. The reflected beam, consisting of reflections from upper and lower surfaces of the proton exchanged layer is passed through a second polariser and then to the detector. Interference between the two reflected components results in variation in the beam intensity when the beam is scanned along a taper region. The change in intensity of the scanning beam can be directly related to the shape and index magnitude of the taper. The theory below makes the assumption that the waveguide/substrate interface is a step.

The reflectivity is given by [5,68]:

$$R = \frac{r_{12}^2 + r_{23}^2 + 2.r_{12}r_{23}\cos(2B)}{1 + r_{12}^2 r_{23}^2 + 2.r_{12}r_{23}\cos(2B)} \qquad (1)$$

where r_{12} is the amplitude of the reflected light from the
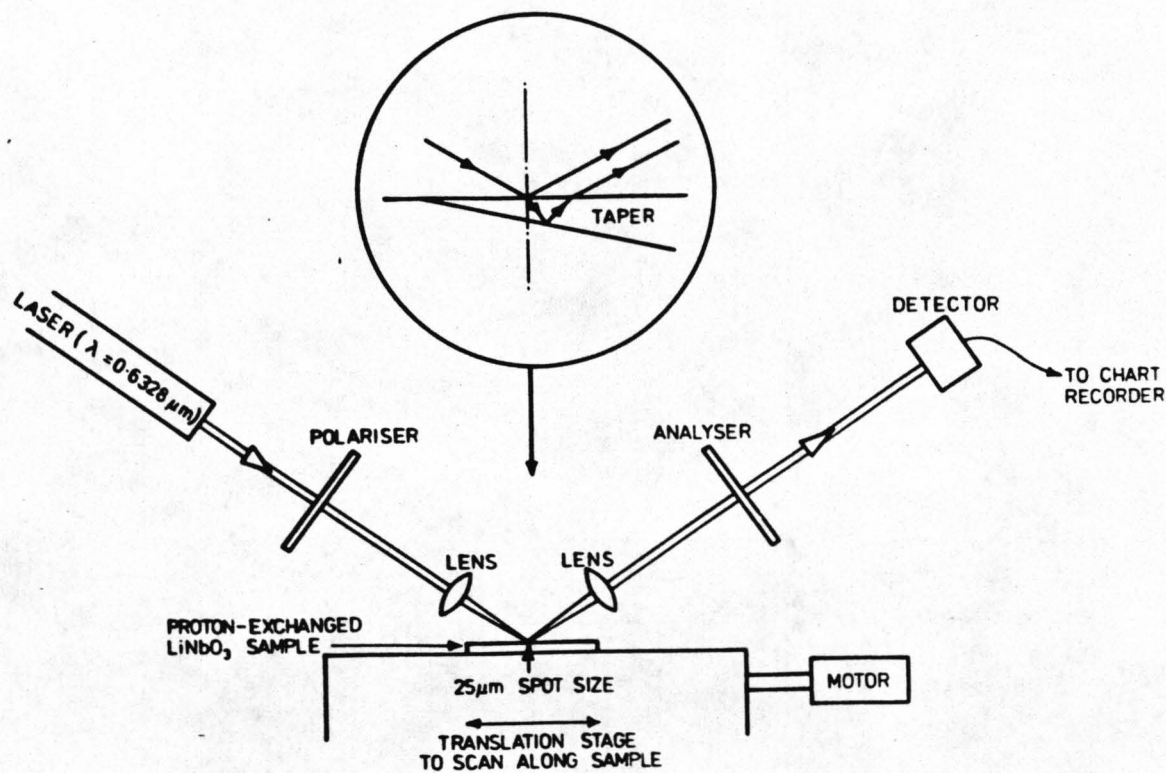
Figure (5.12): Schematic Diagram of Film Thickness Monitor (FTM) used for Proton Exchanged Waveguide Taper Evaluation.
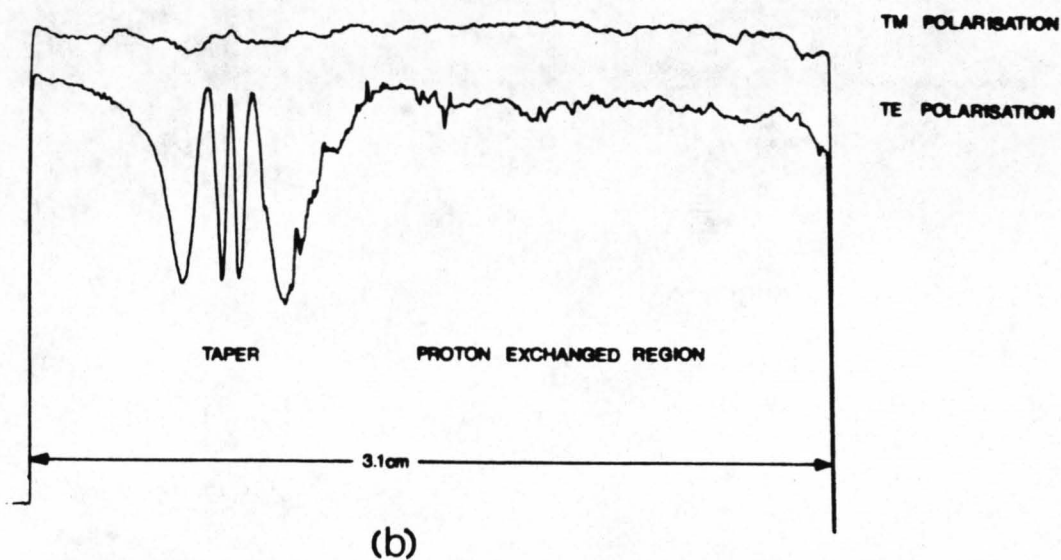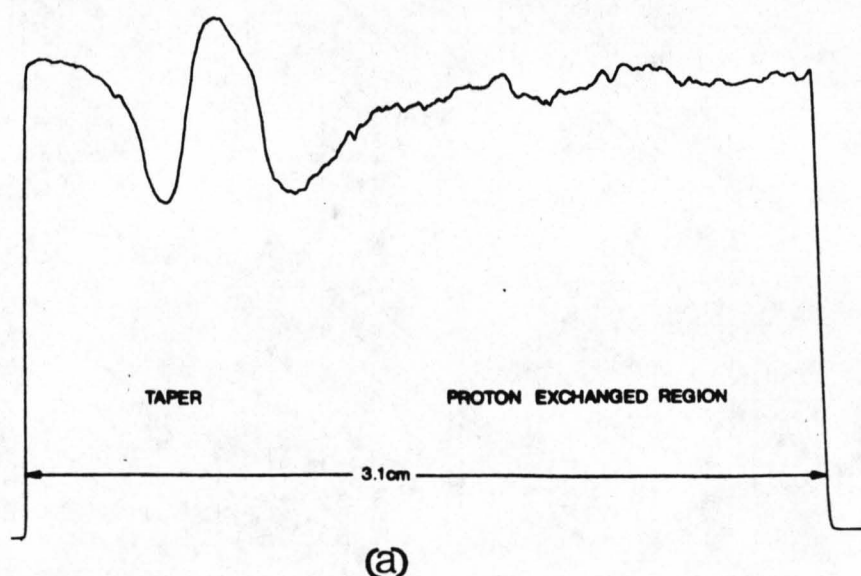
TAPER   PROTON EXCHANGED REGION

3.1cm

(a)

TM POLARISATION

TE POLARISATION

TAPER   PROTON EXCHANGED REGION

3.1cm

(b)

Figure (5.13): Experimental Results (from FTM) showing the Taper
Region as a Sinusoidal Variation in Intensity. All
Tapers Exchanged at 202°C for (a) 15min, (b) 1h
(c) 2hrs 15min and (d) 3hrs 20min

(c)

(d)
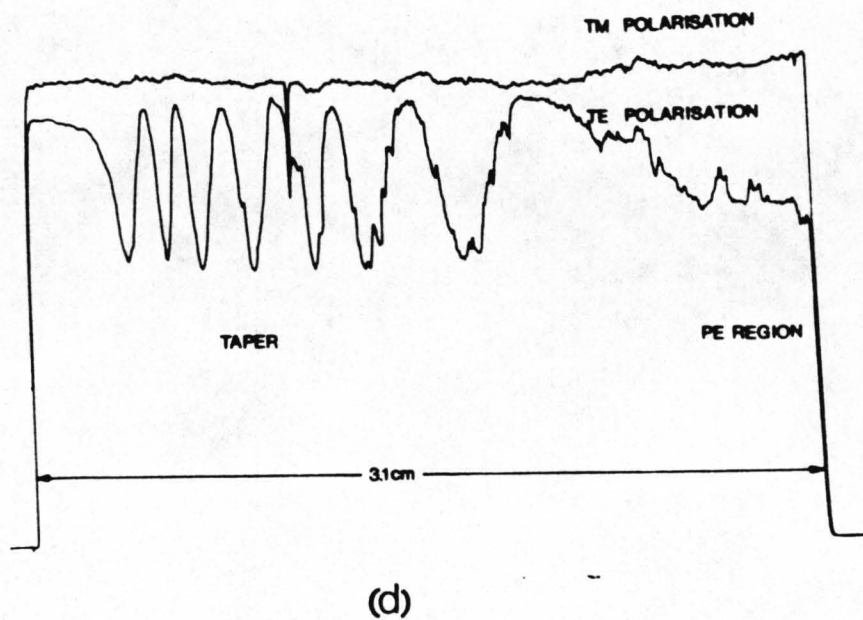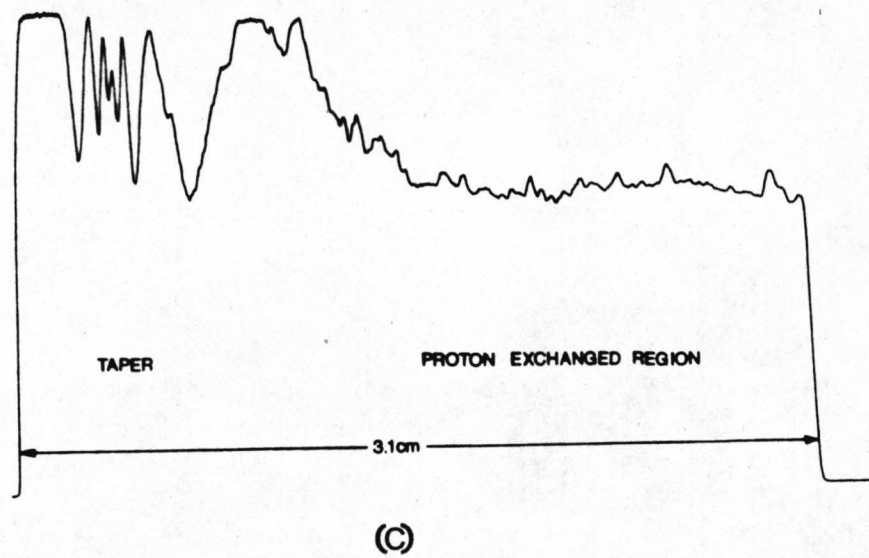
Figure (5.13): Experimental Results (from FTM) showing the Taper Region as a Sinusoidal Variation in Intensity. All Tapers Exchanged at 202°C for (a) 15min, (b) 1h (c) 2hrs 15min and (d) 3hrs 20min

air/waveguide interface, r_{23} is the amplitude of the reflected light from the waveguide/substrate interface and B, the phase difference between the two light rays, is defined as:

$$B = 2.\pi.N_f.d.\cos(\theta_2)/\lambda \qquad (2)$$

where N_f is the waveguide refractive index, d is the film thickness (at that point of the taper), θ_2 is the angle the incident light ray enters the waveguide at and λ is the wavelength of the incident light.

For an incidence angle of 70° and with values for film (N_f) and substrate index (N_s) of 2.3295 and 2.2025 on proton exchanged X-cut lithium niobate, the reflectivity is given by the expression:

$$R = \frac{0.525 - 0.049\cos(2.B)}{1.0 - 0.049\cos(2.B)} \qquad (3)$$

$$\text{with} \qquad B = 3.368 \ (2.\pi.d) \qquad (4)$$

Figure (3.13) shows experimental plots of reflectivity obtained from four samples which were exchanged at a temperature of 202^oC for times of (a) 15 mins (b) 1 hour (c) 2 hrs 15 mins (d) 3hrs 20 mins. The interference fringes indicate the form and extent of the tapered region. Fringes are only obtained with TE polarisation of the input beam as shown in (b) and (d) of figure (3.13). Table 5.4 shows values of film thickness calculated from equation (3) and (4) compared with thicknesses obtained from waveguiding measurements. When the distance along the taper (obtained from the calibrated motor driven translation stage, see figure (5.12)) is plotted against film thickness at a series of points the taper shape is traced. Figure (5.14) shows the shape of a PE taper in X-cut lithium niobate when exchanged at 210^oC for 30min, 1h and 2h 15min[!].

It is evident from figures (5.13) and (5.14) that the taper lengths vary quite considerably and can be as long as 30mm. It

TABLE 5.4

Comparison between waveguide depths estimated by optical and
reflectivity measurements for PE waveguide tapers
exchanged at 202°C

PE Time	Waveguide Depth Measurement (μm)	Reflectivity Depth Measurement (μm)
15 min	0.28	< 0.3
30 min	0.36	0.37
1 hr	0.677	0.6
2 hr 15 min	0.97	0.97
3 hr 20 min	1.14	1.12
6 hr 15 min	1.65	1.65
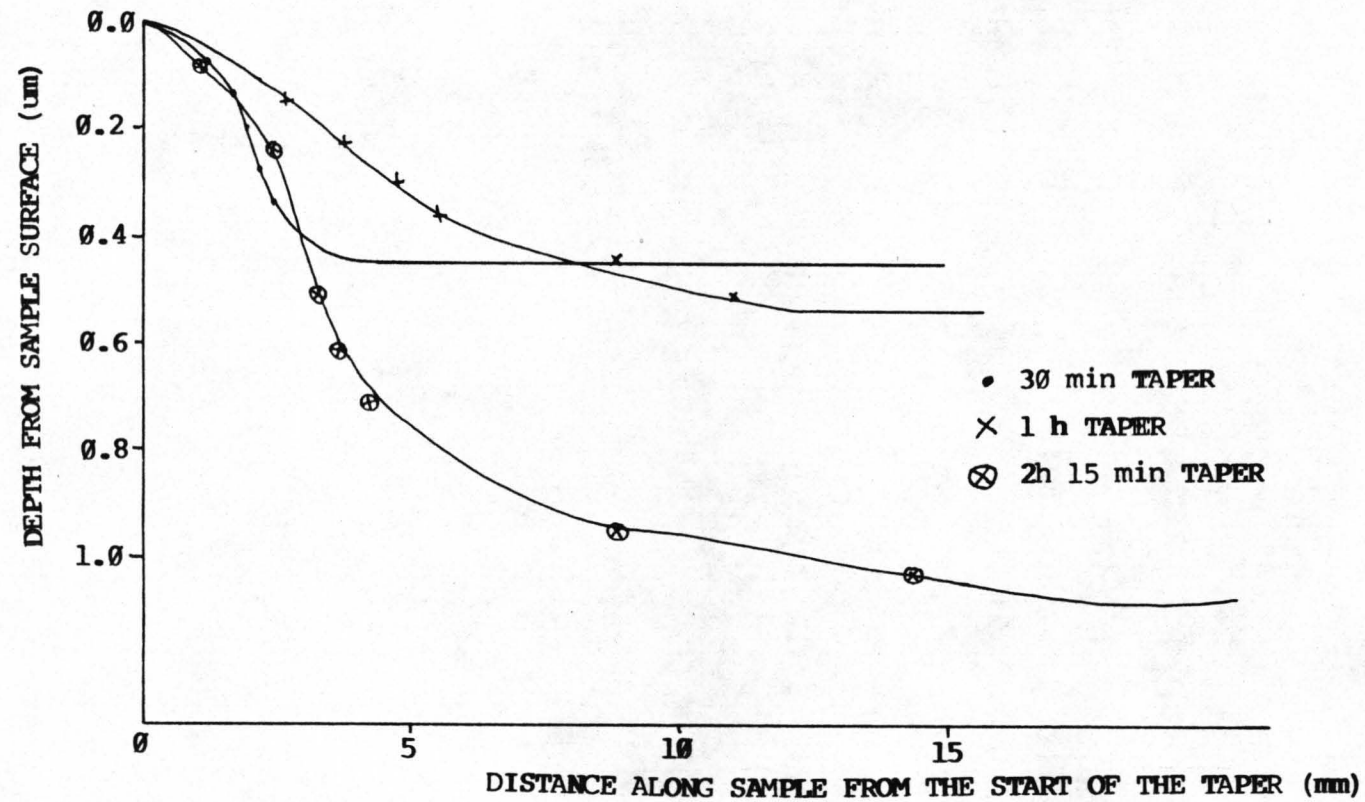
Figure (5.14): Plots of Proton Exchanged Waveguide Taper Regions. Tapers Exchanged at 210°C for 30 min, 1h and 2h 15min in Pure Benzoic Acid.

has been shown that taper lengths of 1/2 - 1mm are suitable for efficient hybrid coupling between PE tapers and As_2S_3 films [5.36,5.37]. Proton exchange tapers will therefore allow directional coupling techniques to be employed in the construction of hybrid integrated optical systems if the length of the taper can be controllably shortened. The length of the taper can be controlled as a function of the exchange time and also possibly by the exchange temperature, and it is hoped that with further investigation useful taper lengths suitable for hybrid coupling can be realised.

5.10 Conclusions

The advantages of forming high index waveguides on lithium niobate are large and such guides have many potential applications in integrated optics. However, although the process has been optically well defined for planar waveguides, there is still serious questions about the usefulness of such waveguides. The problems with PE waveguides such as stability [5.51,5.52], possible reduced electro-optic and acousto-optic effect [5.39,5.41] (although there is some contention about the electro-optics effect [5.71]), problems with D.C. drift [5.38] and high waveguide scattering losses have to be tackled before they will pass a working specification.

Recently, although initially TIPE was thought to be an answer to waveguide stability and scatter problems [5.25,5.26], there has been considerable interest in PE waveguides using dilute melts. Already with dilute melts the waveguide quality and stability has been considerably improved and electro-optic device operation has been shown to be more comparable with Ti:diffused waveguide technology [5.72]. Other possibilites for waveguide components such as polarisers, hybrid integration, ring resonators and temperature sensors [5.35,5.36,5.37,5.74,5.77,5.73] suggest that the technology is still of immense interest.

$^!$The plots were taken by C.A. MacRae under my supervision [5.75]

In order to gain an understanding of the chemistry of the PE process it is necessary to initiate an in depth materials and chemical analysis, and compare the results with the optical properties. An attempt is made to do this in the next few chapters.

CHAPTER 5 — REFERENCES

[5.1]   D. Botez and G.J. Herskowitz
          Components for Optical Communications Systems: A Review
          Proc. IEEE, vol 68, No.6, pp689-731, June 1980

[5.2]   P.K. Tien
          Integrated Optics and New Wave Phemonena in Optical
              Waveguides
          Reviews of Modern Physics, vol 49, No.2, pp361-420
          April 1977

[5.3]   F.J. Leonberger
          High-Speed Integrated Opto-Electronic Signal Processing
              Devices
          7th Top. Meet. on Integrated and Guided-Wave Optics,
          High-Speed Signal Processing Session, WA1, April 1984
          Kissimmee, Florida, U.S.A.

[5.4]   A. Rauber
          Chemistry and Physics of Lithium Niobate
          Current Topics in Materials Science, vol 1, Ch 7
          F. Kaldis   1978

[5.5]   A.D. McLachlan
          Ph.D. Thesis, University of Glasgow, 1981

[5.6]   W.K. Burns, P.H. Klein, L.E. Plew and E.J. West
          Ti diffusion in Ti:LiNbO$_3$ planar and channel optical
              waveguides
          J. Appl. Phys., vol 50, No.10, pp6175-6182, Oct 1982

[5.7]   J.P. Nisius, P. Hertel, E. Kratzig and H. Pape
          Optical Damage Effects in LiNbO$_3$:Ti Waveguides
          Proc. S.P.I.E., vol 408, Integrated Optics III,
          Virginia April 1983

[5.8]   R.L. Holman P.J. Cressman
          Optical Damage Resistance of Lithium Niobate Waveguides
          Opt. Engineering, vol 21, pp1025-1032, 1982

[5.9]   P. Vandenbulcke and P.E. Lagasse
          Static Field Analysis of Thin Film Electro-Optic Light
          Modulators and Switches
          Wave Electronics, vol 1, pp295-308, 1974/76

[5.10]   A. Dawar et al.
          Acousto-optic techniques in Integrated Optics
          Proc S.P.I.E., vol 517, paper 09, 1984

[5.11]   W. Doldissen, H. Heidrich and D. Hoffmann
          Reduction of Bend Losses in Integrated Optic Devices
          3rd E.C.I.O., pp210-214, Berlin(west), Germany 1985

[5.12]   S.K. Korotky, E.A.J. Marcatili, J.J. Veselka
          R.H. Bosworth
          Greatly Reduced Losses for Small-Radius Bends in
          Ti:LiNbO$_3$ Waveguides
          3rd E.C.I.O., pp207-209, Berlin(west), Germany 1985

[5.13]   J.L. Jackel, C.E. Rice and J.J. Veselka
          Proton Exchange for High Index Waveguides in LiNbO$_3$
          Technical Digest of Integrated and Guided Wave Optics
          Pacific Grove U.S.A. PDP-1, 1982

[5.14]   J.L. Jackel and C.E. Rice
          Topotactic LiNbO$_3$ to Cubic Perovskite Structural
          Transformation in LiNbO$_3$ and LiTaO$_3$
          Ferroelectrics, vol 38, pp801-804, 1981

[5.15]   J.L. Jackel, C.E. Rice and J.J. Veselka
          Proton Exchange for High Index Waveguides in LiNbO$_3$
          Appl. Phys. Lett., vol 41, No.7,pp607-608, Oct 1982

[5.16]   M. Goodwin and C. Stewart
          Proton-Exchanged Optical Waveguides in Y-cut Lithium
          Niobate
          Electronics Lett., vol 19. No.6, pp223-225, March 1983

[5.17]   W.B. Spillman, N.A. Sanford and R.A. Soref
          Optical Waveguides in $LiTaO_3$ formed by Proton Exchange
          Optics Letts., vol 8, No.9, pp497-498, September 1983

[5.18]   D.F. Clark, A.C.G. Nutt, K.K. Wong, P.J.R. Laybourn and
          R.M. DeLaRue
          Characterisation of Proton Exchanged Slab Optical
          Waveguides on Z-cut Lithium Niobate
          J. Appl. Phys., vol 54, No.11, pp6218-6220, Nov. 1983

[5.19]   K.K. Wong, A.C.G. Nutt, D.F. Clark, P.J.R. Laybourn and
          R.M. DeLaRue
          Characterisation of Proton Exchanged Slab Optical
          Waveguides in X-cut $LiNbO_3$
          Submitted to I.E.E. Proc., Part J

[5.20]   M. DeMicheli, J. Botineau, P. Sibillot, D.B. Ostrowsky
          M. Papuchon
          Fabrication and Characterisation of Titanium Indiffused
          Proton Exchanged (TIPE) Waveguides in Lithium Niobate
          Optics Commun., vol 42, No.2, pp101-103, June 1982

[5.21]   M. DeMicheli, J. Botineau, P. Sibillot, D.B. Ostrowsky
          M. Papuchon
          Independent Control of Index and Profiles in Proton
          Exchanged Lithium Niobate Waveguides
          Optics Letts., vol 8, No.2, pp114-115, Feb 1983

[5.22]   A.C.G. Nutt
          Experimental Observations of Light Propagation in
          Proton Exchanged Lithium Niobate Waveguides
          J. Opt. Comm., vol 6, pp8-9, March 1985

[5.23]   J.L. Jackel, C.E. Rice and J.J. Veselka
          Compositional Control in Proton Exchanged $LiNbO_3$
          Electron. Lett., vol 19, pp 387-388,   1983

[5.24]   S.M. Al-Shukri et al.
          Proton Exchanged Optical Waveguides on Lithium Niobate:
          Devices, Characterisation and Future Prospects
          Proc. S.P.I.E., vol 578, paper No.9, Boston Symp. 1985

[5.25]   M. DeMicheli
          Non-linear Effects in TIPE-$LiNbO_3$ Waveguides for
          Optical Communications
          J. Opt. Comm., vol 4, pp25-31,   March 1983

[5.26]   C. Canali, A. Carnera, P. Mazzoldi, R.M. DeLaRue
          $LiNbO_3$ Optical Waveguides Fabricated by Ti Indiffusion
          and Proton Exchange: Process, Performance and Stability
          Proc. S.P.I.E., vol 517, paper-15,   1984

[5.27]   S.M. Al-Shukri et al.
          Analysis of Annealed Proton-Exchanged Waveguides on
          Lithium Niobate by Optical Waveguide Measurements and
          Microanalytical Techniques
          7th Top. Meet. on Integrated and Guided Wave Optics,
          PD71, Kissimmee, Florida,   April 1984

[5.28]   J.L. Jackel and R.J. Holmes
          Recent Advances in $LiNbO_3$ Processing
          2nd E.C.I.O., IEE conf. publ. 227, pp38-41, Florence
          Italy October 1983

[5.29]   E.Y.B. Pun, K.K.Wong, I. Andonovic, P.J.R. Laybourn and
          R.M. DeLaRue
          Efficient Waveguide Bragg-Deflection Grating on $LiNbO_3$
          Elect. Lett., vol 18, No.17, pp740-742, August 1982

[5.30]   M. DeMicheli, J. Botineau, S. Neveu, P. Sibillot
          D.B. Ostrowsky and M. Papuchon
          Extension of Second-Harmonic Phase-Matching Range in
          Lithium Niobate Guides
          Optics Letts., vol 8, No.2, pp116-118,   Feb 1983

[5.31]   D.B. Ostrowsky
          Parametric Processes in $LiNbO_3$
          3rd E.C.I.O., pp 146-151, Berlin(West), Germany May 1985

[5.32]   S.K. Yao and T. Findakly
          The State of Art of Chirp Grating Lenses on $LiNbO_3$
          Proc. S.P.I.E., Vol 408, Integrated Optics III, pp90-94
          Virginia April 1983

[5.33]   Zang De Yu
          Waveguide Optical Planar Lenses in $LiNbO_3$-Theory and
          Experiments
          Optics Commun., vol 47, No.4, pp248-250, Sept 1983

[5.34]   C. Warren, S. Forouhar, W.S.C. Chang, S.K. Yau
          Double Ion Exchange Chirp Grating Lens in Lithium
          Niobate Waveguides
          Appl. Phys. Lett., vol 43, pp424-426, April 1983

[5.35]   M. Papuchon and S. Vatoux
          Integrated Optical Polarisers on $LiNbO_3$:Ti Channel
          Waveguides using Proton Exchange
          Electron. Lett., vol 19, pp612-613   March 1983

[5.36]   G. Stewart and A.C.G. Nutt
          Formation and Analysis of Tapers in Proton-Exchanged
          Lithium Niobate Waveguides
          3rd E.C.I.O., pp58-61, Berlin(west), Germany, May 1985

[5.37]   G. Stewart, R.H. Hutchins, P.J.R. Laybourn C.A. MacRae
          Construction of Hybrid Integrated Optical Circuits
          IOOC/ECOC 85, Integrated Optical Waveguide Fabrication,
          Venice, Italy , October 1985

[5.38]   K.K. Wong, R.M. DeLaRue and S. Wright
          Electro-optic Waveguide Frequency Translator in Lithium
          Niobate Fabricated by Proton Exchange
          Opt. Lett., vol 7, pp546-548,   June 1982

[5.39]   R.A. Becker
          Comparison of Guided Wave Interferometric Modulators
          Fabricated via Ti indiffusion and Proton Exchange
          Appl. Phys. Lett., vol 43, No.2, pp131-133, July 1983

[5.40]   A. Dawar, S.M. Al-Shukri and R.M. DeLaRue
          Surface Acoustic Wave- Guided Optical Wave Interaction
          in Y-cut $LiNbO_3$ annealed Proton Exchanged Waveguides
          IEEE Int. Workshop on Integr. Opt. and Related Technol.
          for Sig. Proc., Addendum, Florence, Italy   Sept. 1984

[5.41]   R.L. Davis
          Acousto-Optic Bragg Diffraction in Proton Exchanged
          Waveguides
          Proc. S.P.I.E., vol 517, paper-10,   1984

[5.42]   V. Hinkov, E. Ise and W. Sohler
          Low Frequency Collinear Acoustooptic TM_0-TE_0 Conversion
          and Single Sideband Modulation in Proton Exchanged
          $LiNbO_3$
          3rd E.C.I.O., pp169-173, Berlin(west),Germany, May 1985

[5.43]   J.L. Jackel, A.M. Glass, G.E. Peterson, C.E. Rice,
          D.H. Olson and J.J. Veselka
          Damage Resistent Lithium Niobate Waveguides
          J. Appl. Phys., vol 55, pp269-270   Oct 1984

[5.44] M. DeMicheli, J. Vollmer, J.P. Baretti and S. Neveu
        Proton Exchange in LiNbO$_3$:
        Temperature and Water Influence During the Process
        2nd E.C.I.O., session 9/a, PDP-1, Florence, Italy
        October 1983

[5.45] P.K. Tien and R. Ulrich
        Theory of Prism-Film Coupler and Thin-Film Light Guides
        J. Opt. Soc. Am., vol 60, No.10, pp1325-1350, Oct 1970

[5.46] H. Kogelnik and V. Ramaswamy
        Scaling Rules for Thin-Film Optical Waveguides
        Applied Optics, vol 13, No.8, pp1857-1862, August 1974

[5.47] J. Finak and H. Jerominik
        Planar Diffusion Glass Waveguides Obtained by Immersing
        in Molten KNO$_3$
        Optica Applicata, vol XII, No.1, pp11-17, 1982

[5.48] W.L. Bond
        Measurement of the Refractive Indices of Several
            Crystals
        J. Appl. Phys., vol 36, No.5, pp1674-1677, May 1965

[5.49] J.R. DeVore
        Refractive Indices of Rutile and Sphalerite
        J. Opt. Soc. Am., vol 41, No.6, pp416-419, June 1951

[5.50] J. Crank
        The Mathematics of Diffusion
        Oxford University, Clarendon Press, London (2nd Ed.)
        1979

[5.51] A. Yi-Yan
        Index Instabilities in Proton Exchanged LiNbO$_3$
            Waveguides
        Appl. Phys. Lett., vol 42, No.8, pp633-635, April 1983

[5.52]   J.L. Jackel and C.E. Rice
          Short-and Long-Term Stability in Proton Exchanged
              Lithium Niobate Waveguides
          Proc. S.P.I.E., vol 460, Processing of Guided Wave
          Optoelectronic Materials,   1984

[5.53]   S.K. Sheem, W.K. Burns and A.F.Milton
          Leaky-mode Propagation in Ti-diffused $LiNbO_3$ and $LiTaO_3$
              Waveguides
          Optics Lett., vol 3, No.3, pp76-78, Sept 1978

[5.54]   J. Ctyroky and M. Cada
          Generalised WKB Method for the Analysis of Light
          Propagation in Inhomogeneous   Anisotropic Optical
              Waveguides
          IEEE J. Quant. Elect., vol QE-17, No.6, pp1064-1070
          June 1981

[5.55]   W.K. Burns, S.K. Sheem and A.F. Milton
          Approximate Calculation of Leaky-Mode Loss Coefficients
          for Ti-Diffused $LiNbO_3$ Waveguides
          IEEE J. Quant. Elect., vol QE-15, No.11, pp1282-1289
          November 1979

[5.56]   J. Ctyroky
          Light Propagation in Proton Exchanged $LiNbO_3$ Waveguides
          J. Opt. Comm., vol 5, No.1, pp16-19,   March 1984

[5.57]   J. Ctyroky
          Rigorous Calculation of Light Propagation in Proton
          Exchanged $LiNbO_3$ Waveguides
          J. Opt. Comm., vol 6, No.3, pp100-102, Sept 1985

[5.58]   Y. Okamura, S. Yoshinaka and S. Yamamoto
          A Simple Method for Measuring Mode Propagation Losses
          of Integrated Optical Waveguides
          Appl. Opt., vol 22, pp3892-3895, 1983

[5.59]   C. DeBernardi, A. Loffredo and S. Morasca
          Optimization of Waveguide Attenuation Measurements by
          Scattered Radiation Detection
          Presented at W.I.O.C.S. (FACE-RC), Rome, Italy,
          November, 1984

[5.60]   Y.H. Won, P.C. Jaussaud and G.H. Chartier
          Three-Prism Loss Measurements of Optical Waveguides
          Appl. Phys. Lett., vol 37, No.3, pp269-271, Aug. 1980

[5.61]   M.N. Armenise et al.
          Dependence of Inplane Scattering Levels in Ti:LiNbO$_3$
          Optical Waveguides on Diffusion Time
          I.E.E. Proc., vol 131, Part H, No.5, pp295-298,
          October 1984

[5.62]   M.N. Armenise et al.
          Evaluation of Planar Titanium Diffused LiNbO$_3$ Optical
          Waveguides by Micro-Analytical Techniques and
          Measurements of Inplane Scattering Levels
          Techn. Digest of 4th Int. Conf on Integrated Opt. and
          Opt. Comm., June 1983, Tokyo, Japan

[5.63]   A.C.G. Nutt, K.K. Wong, D.F. Clark, P.J.R. Laybourn
          and R.M. DeLaRue
          Proton-Exchange Lithium Niobate Slab and Stripe
          Waveguides: Characterisation and Comparisons
          2nd E.C.I.O., IEE Conf. Publ. No.227, pp53-56, Oct 1983
          Florence Italy

[5.64]   T. Findakly, S.K. Yao, C. Warren, S. Forouhar, W. Chang
          Chirp Grating Lenses on LiNbO$_3$ by Benzoic Acid
              Treatment
          ibid ref [5.62]

[5.65]   Discussions with R.L. Holman,
          Battelle Research Labs, Columbus, Ohio, U.S.A.
          are gratefully acknowledged.

[5.66]   M.N. Armenise et al.
         Optical Characterisation of Proton Exchanged and
         Titanium-Diffused Proton Exchanged Slab Waveguides on
         Lithium Niobate
         IEEE Int. Workshop on Integr. Opt and Related Technol.
         for Sig. Proc., Technical Digest, pp21-24, Sept. 1984
         Florence, Italy

[5.67]   A. Dawar, A.C.G. Nutt, S.M. Al-Shukri et al.
         Strain and Surface Damage Induced by Proton Exchange in
                 Y-cut Lithium Niobate
         To be Published in Journal of Materials Science

[5.68]   G. Stewart, R.H. Hutchins, P.J.R. Laybourn
         Controlled Growth of Arsenic Trisulphide Films for
         Coupling Integrated Optical Devices
         J. Phys. D: Appl. Phys., vol 14, pp323-331,   1981

[5.70]   G. Stewart, R.H. Hutchins, P.J.R. Laybourn
         Hybrid Integration of Active and Passive Devices
         3rd Int. Conf. on Int. Opt. and Opt. Fibre Commun.,
         paper WE-1, San Fransisco, April 1981

[5.71]   R.L. Holman, D. Hicks and J. Busch
         Laser Power Handling and Electro-optic Performance of
         Proton Exchanged Lithium Niobate Waveguides
         Proc S.P.I.E., vol 460, paper No. 19, Los Angeles
         California, U.S.A.,   January 1984

[5.72]   K.K. Wong, N.J. Parsons, A.R. Olderoyd
         and A.C. O'Donnel
         High Quality Optical Waveguides in $LiNbO_3$ by Dilute
         Melt Proton Exchange
         IOOC/ECOC'85, Integrated Optical Waveguide Fabrication,
         Venice, Italy   October 1985

[5.73]   M. Haruna, H. Nakajima and H. Nishihara
          Optical π-arc Waveguide Interferometer in Proton
          Exchanged Lithium Niobate for Temperature Sensing
          Applied Opt., vol 24, No.16, pp2483-2484, Aug 1985

[5.74]   A. Mahapatra and W.C. Robinson
          Integrated-Optic Ring Resonators Made by Proton
          Exchange in Lithiun Niobate
          Applied Opt., vol 24, No.15, pp2285-2286, Aug 1985

[5.75]   C.A. MacRae
          Fabrication and Analysis of Tapered Waveguiding Regions
          in Lithium Niobate for Taper Velocity Coupling.
          Final Year Project Report, Dept E&EE, University of
          Glasgow, 1985

[5.76]   D.Y. Zang and C.S. Tsai
          Single-Mode Waveguide Microlenses and Microlens Arrays
          Fabrication in $LiNbO_3$ using Titanium Indiffused Proton
          Exchange Technique
          Appl. Phys. Lett., vol 46, No.8, pp703-705, April 1985

[5.77]   M. Mahapatra and W.C. Robinson
          Proton Exchanged Ring Resonators in Lithium Niobate:
          Operation at $0.79\mu m$ and $1.3\mu m$
          Proc. S.P.I.E., vol 578, Integrated Optical Circuit
          Engineering II, pp70-74, Cambridge, Sept. 1985

CHAPTER 6

MATERIALS ANALYSIS TECHNIQUES

Acknowledgments

6.1 Introduction

The formation of anisotropic optical waveguides in lithium niobate by the immersion of substrates in a hot carboxylic acid (benzoic acid) has been analysed and characterised optically (see chapter 5). However, there is little information on the chemical kinetics of the process. What little materials analysis that has been published by authors such as Jackel et al. and others was based mainly on the chemical analysis of lithium niobate in the powdered state which may not be fully applicable to an analysis in the bulk crystalline form [6.1,6.2,6.3,6.4,6.5,6.6]. With this in mind a comprehensive series of analysis techniques have been adopted to analyse the PE process on lithium niobate, in order to generally understand the PE process and try and explain such phenomena as surface cracking [6.7,6.8] and the D.C. effect [6.9]. These materials analysis techniques were initially adopted to investigate Ti-indiffused waveguides on lithium niobate and involved collaboration with research colleagues in Italy. This collaboration was continued to make use of the considerable expertise amassed in the structural analysis of lithium niobate [6.10,6.11,6.12].

What follows in chapter 6 is an outline of the materials analysis techniques used. It is not the purpose of this chapter to examine each process in detail, but to give the reader a basic understanding of each technique and therefore to be able to understand the results discussed in chapters 7 and 8.

6.2 Infra-red Absorption

When broadband radiation is directed through a crystal, certain frequencies will be absorbed by the crystal. Absorption occurs when the stretching moment, or bond strength, between two atoms in the crystal has the same resonant energy as one frequency of the incident radiation. Thus the frequency of the absorbed radiation indicates probable inter-atomic bonds in the crystal and the amount of absorption gives an indication of the amount of

the particular type of bond in the crystal [6.13,6.14,6.18].

In the following chapter the near infra-red absorption spectra of lithium niobate crystals, both virgin and proton exchanged, are examined. The samples are typically $1cm^2$ in area and polished on both faces to reduce background scatter noise. The sample thickness is typically 1mm. The wavelength range of radiation of interest is from about 0.8 μm to about 6 μm. In this region virgin lithium niobate is basically transparent except for the OH‾ absorption peak at about 2.864 microns or about $3485cm^{-1}$ [6.15]. This absorption peak or band is completely polarised perpendicular to the c-axis of lithium niobate. The absorption band is composed of at least two sub-bands which cannot be resolved completely, even at very low temperatures [6.16].

The main interest of infra-red absorption spectrometry is that some information is available on the incorporation of hydrogen (or protons) in lithium niobate resulting from the PE process. These protons will always be associated with oxygen ions to form OH‾ groups and/or weak hydrogen bonds, as they cannot exist chemically isolated in a material[6.16,6.17]. Thus monitoring the changes in the OH‾ absorption band will yield information on the rate of hydrogen migration into the lattice during the PE process. Polarisation measurements will also yield information on the direction of the O-H bond in the lattice so that comparisons can be made between the proton exchange process and the OH‾ present in the bulk crystal. Normal IR absorption is carried out with randomly polarised broadband radiation, however the chemical bonds only absorb the radiation which is polarised parallel to the bond since only then will the bond resonance be excited and the radiation absorbed. If polarised radiation is used, the axis of which can be varied, information may be obtained about the way the O-H bonds are positioned or alternatively, the extent to which they are random in their orientation in the crystal [6.15,6.16].

6.3 Rutherford Back Scattering

Rutherford Back Scattering (RBS) in PE $LiNbO_3$ can be used to determine the amount of 'irregularity' in the exchanged region and was also a tool which had proved itself with Ti-indiffused waveguides [6.11,6.12]. The method (RBS) [6.19,6.20] is based on elastic scattering of ions of known energy incident onto the nuclei of atoms in a crystal structure. A schematic of a typical RBS machine can be seen in figure (6.1). $^4He^+$ ions are formed into a plasma and focused through a particle accelerator into a high energy beam (alpha particles are normally used in RBS), typically in the range 1.5-2.5MeV, which is filtered into an ion beam of a specific energy by a powerful magnet (which acts like an energy selector and is normally termed an Energy Analyser). The energy resolution is 15-20keV. The beam of ions is then allowed to impinge on the sample surface. A small fraction of the incoming particles are backscattered and measured to determine the number of particles and particle energy after Rutherford collisions [6.19] with sample atoms. For a standard Rutherford type collision, (see figure (6.2)) the energy of the incident ions E_O is proportional to the energy of the scattered ions thus;

$$E = KE_O$$

where E is the energy of the scattered ion and the proportionality constant, K, is defined thus;

$$K = f(\Theta, M)$$

where K is a function of Θ, the angle of scatter, and also a function of M, the mass of the scattering nucleus. Therefore energy analysis of the primary ions backscattered from the sample provides a mass analysis of the atoms near the surface. The relative sensitivity of the process to different atoms is determined by the Rutherford scattering cross section (proportional to Z^2, where Z is the atomic number) and this permits a determination of ion concentration. Due to energy loss
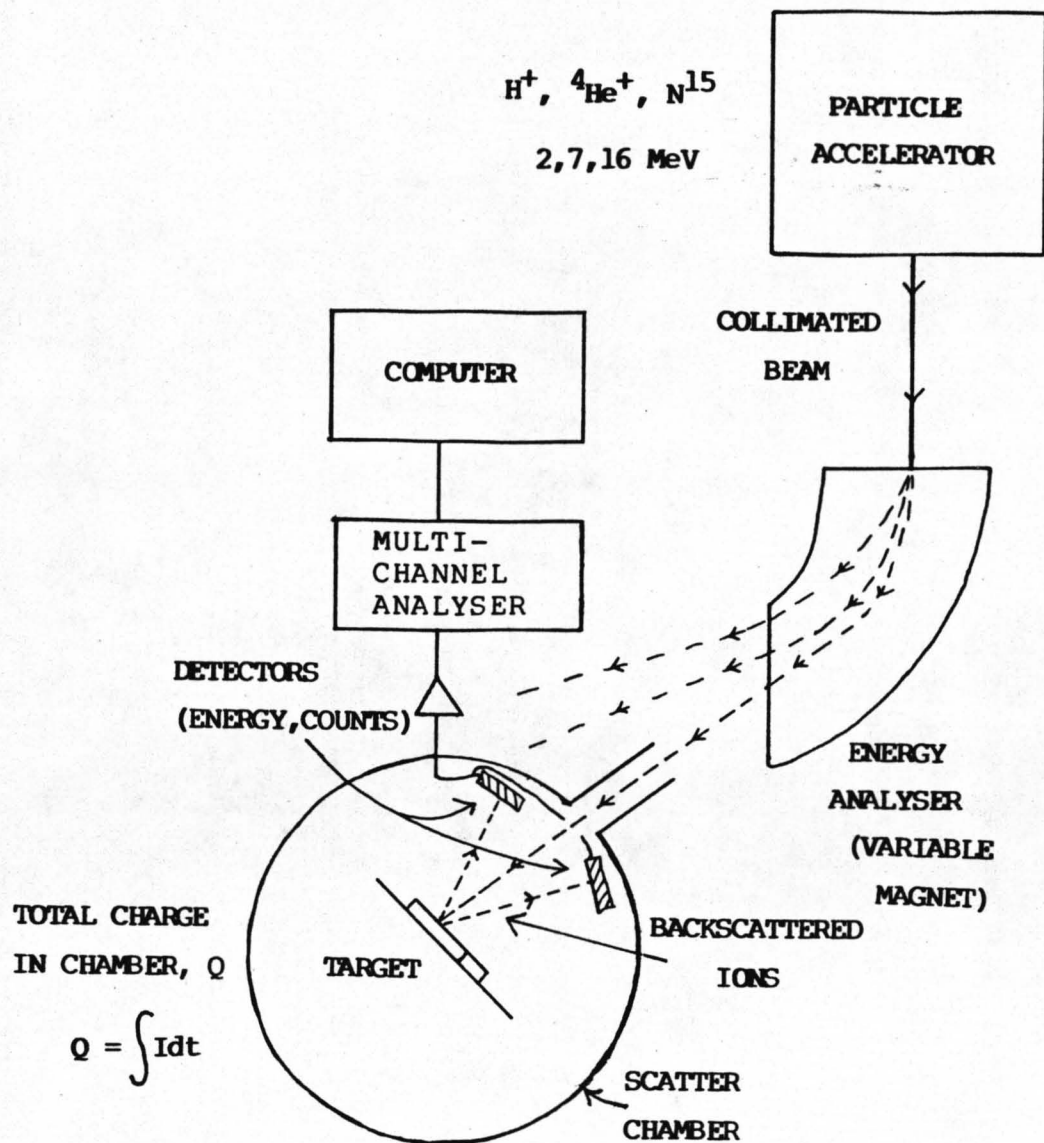
Figure (6.1): Schematic Representation of Experimental Apparatus for Rutherford Back Scattering and Nuclear Interactions
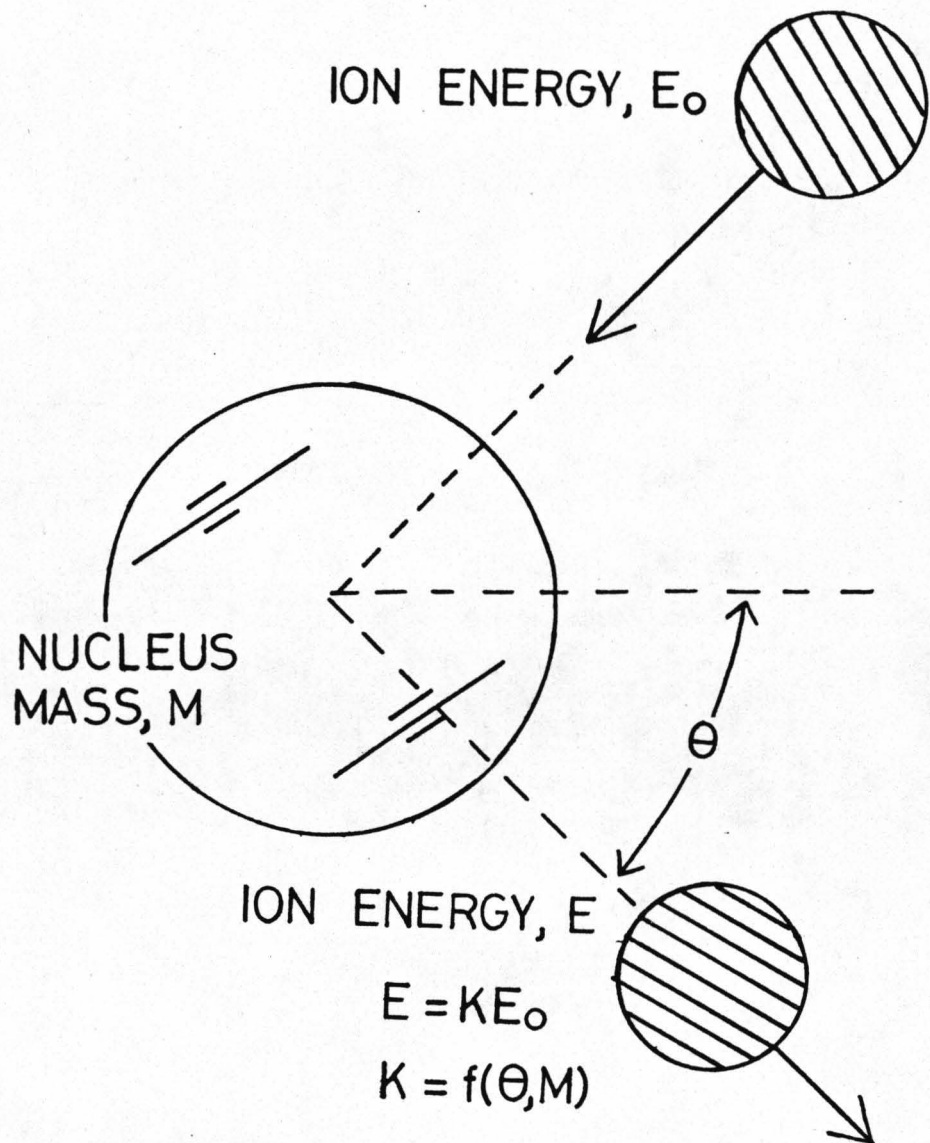
Figure (6.2): Representation of a Rutherford-type Collision (elastic ion scattering by an atomic nucleus).

suffered by the probing particles as they traverse successively deeper atomic layers, energy analysis of the backscattered particles also provides distributional information with respect to depth.

A typical plot of an RBS spectrum of Yield against Energy is shown in figure (6.3). The yield is the number of scattered particles detected, which is derived from the charge collected on the silicon detectors normalised to the total charge collected from the scattering chamber (see figure (6.1)). The Energy is the energy of each scattered ion.

As was established above the energy of the scattered ion is proportional to the mass of the scattering point and can be related to depth in the sample. In backscattering θ is reduced to a minimum and therefore the dependence of E on θ is also reduced to a minimum which makes the mass estimations much more accurate. The backscattered yield is however a much more complex function [6.19,6.20,6.21];

$$\underline{\text{Yield} \propto dQ/Q, \ \theta, \ d\Omega, \ \sigma, \ \delta E/s, \ A, \ N}$$

where dQ is the total charge incident upon the detector, Q is the total charge of the incident particle beam (coulombs), θ is the scattering angle, $d\Omega$ is the solid angle of the beam incident upon the detector (steradians), σ is the Rutherford scattering cross section (steradians), δE is the energy resolution of the incident ion beam in the target (quoted above), s is the channel width of the counter (keV) and is proportional to the stopping power of the sample atoms in the detector, A is the incident beam area (mm^2) and N is the sample atom density (atoms/vol).

The computer and the multichannel analyser however simplify the output information so that the Yield can give the number of sample atoms at a given depth. Figure (6.4) shows schematically the resultant RBS spectrum from a particular incident beam energy in bulk $LiNbO_3$. The energy of the output beam determines the depth in the sample surface and the particle count determines the
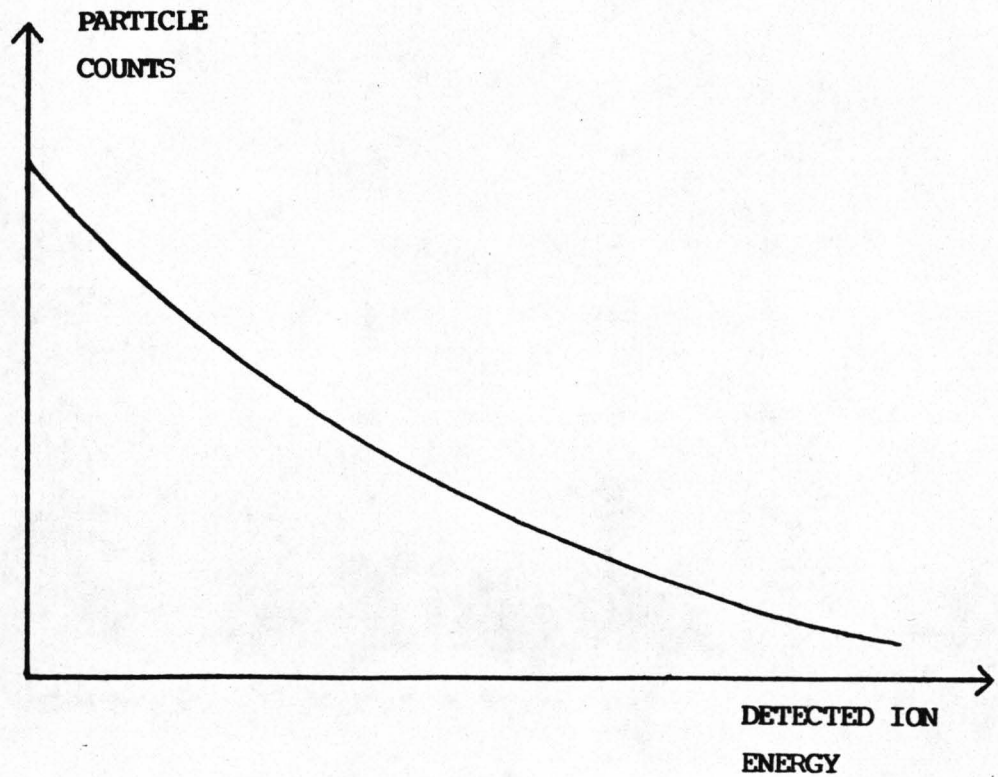
Figure (6.3): Typical Plot of Raw Data Obtained from a RBS
Process. Number of Particle Counts is Plotted
against Detected Scattered Ion Energy.
Neither the Particle Counts nor the Detected Ion
Energy can be Directly Related to Depth or Number
or Type of Ion without Complex Computation.
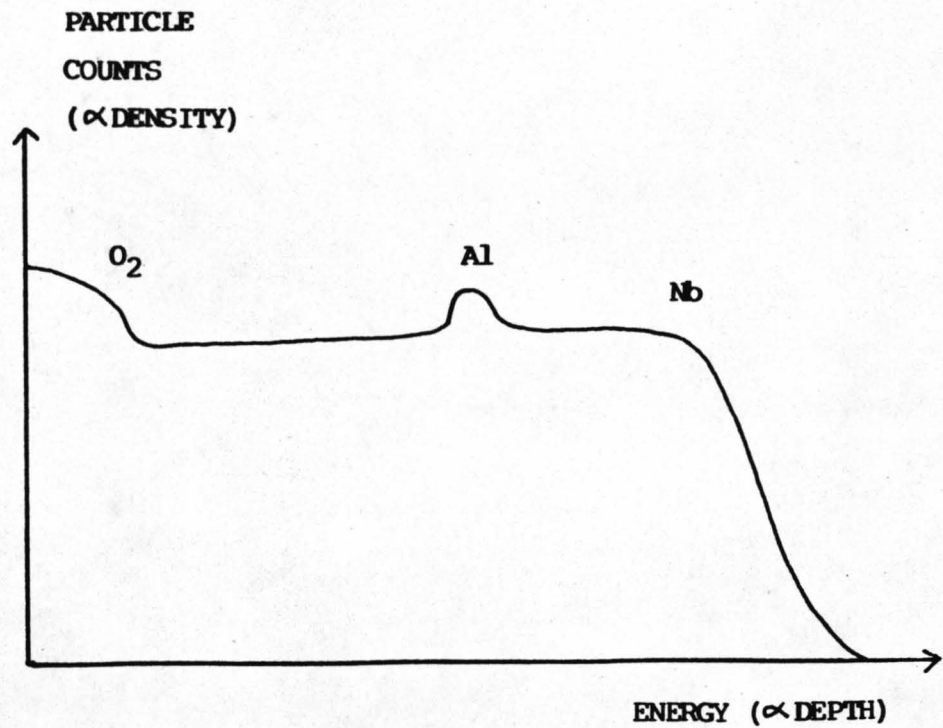
Figure (6.4): Plot of Refined RBS Data Obtained from a Virgin Piece of $LiNbO_3$. The Graph now Yields Depth Information and Information on the Different Types of Atomic Species.

density at that depth.

The measurement technique used in the analysis of proton exchanged layers on lithium niobate is a special case of RBS. When ions are incident on a single crystal, such as lithium niobate, within 1° of a high symmetry axis, they can be steered down an open channel in the lattice by the repulsive potential of atomic strings, as shown in figure (6.5). This effect, called channeling, reduces the probability of nuclear scattering by as much as two orders of magnitude. In such channeling conditions, surface damage due, for example, to mechanical polishing, the epitaxial nature of surface layers and lattice distortion can easily be studied. Channelling can be used as a measure of crystal disorientation, atomic misalignment, interstitial ions and point defects.

RBS in the aligned mode (channeling) does not result in sample crystal damage, assuming correct operation of the machine. In strongly piezoelectric dielectrics (or even insulators) such as lithium niobate, a large increase in surface charge (caused by the bombardment of alpha particles) can cause the incident ion beam to be deflected or slowed down which corrupts the information. The samples are therefore coated with a thin conducting film of aluminium.

Figure (6.5) also shows, schematically, backscattering spectra in the channeling mode for a perfect lithium niobate crystal and for a lithium niobate crystal substrate with a surface layer whose atomic positions are distorted with respect to those of a perfect crystal because of, for example , an ion exchanged surface layer. In the latter case the backscattering spectrum shows an increase in the backscattering yield for an energy range δE which is related to (and approximately proportional to) the thickness W of the exchanged (distorted) layer.

An experimental spectrum would require an incident beam density of approximately $10nA/mm^2$. Higher current densities tend to heat up the substrate and change the properties of the proton
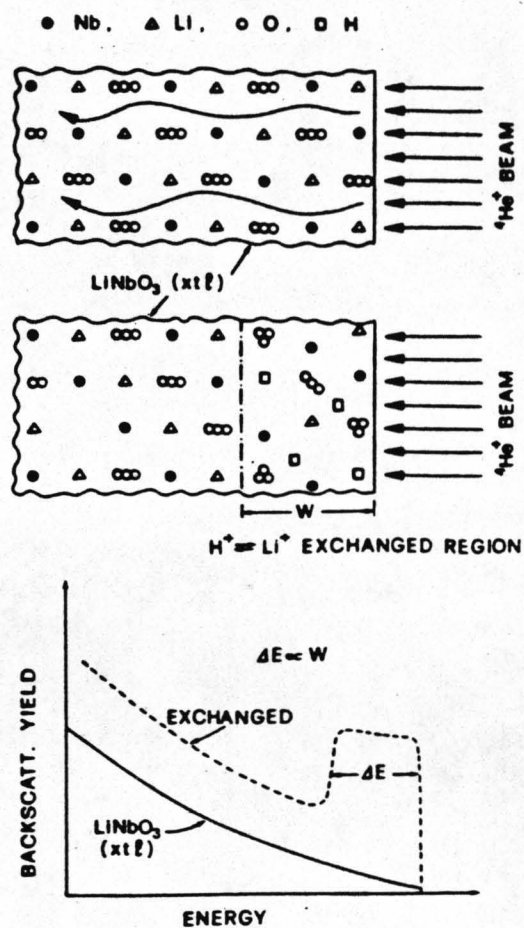
Figure (6.5): Schematic RBS Spectra taken in Channeling Mode for a Perfect LiNbO$_3$ Crystal and for One with a Distorted Surface Layer Due to the Proton Exchange Process.

exchanged layer as it is being measured. The depth resolution of the system is 100-150 angstroms, being inversely proportional to the size of the incident ion and proportional to the energy resolution of the energy analyser (15-20keV). For scattered particle detection the ion has to slow down in the target crystal by the resolution of the analyser to detect any difference, and the required distance is the depth resolution. If a larger incident ion than an alpha particle were used the ion would interact to a greater extent with the crystal structure, and hence it would lose the 15-20keV energy required for resolution in a much smaller path length, as it traverses through the lattice and thus the depth resolution would be improved.

The main information obtained from RBS channeling spectra, as described in the following chapters, is the exchanged layer depth 'W' and an indication of the amount of 'damage' or atomic misalignment in the exchanged region.

6.4 Hydrogen Profiling and Lithium Concentration Analysis by Nuclear Reactions

Since it is assumed that the immersion of lithium niobate crystals in hot benzoic acid , as well as in other carboxylic acids, hydrate melts etc. [6.22,6.23,6.2], produces some form of exchange between the Li atoms in the crystal and the protons in the acid (hence the term proton exchange [6.7]), a method of determining the proton depth profile and concentration in the exchanged layer would be highly advantageous in understanding the exchange process.

The use of Nuclear Reactions (NR) [6.24,6.25,6.26,6.27,6.43] gives a technique complementary to RBS, especially useful for the analysis of elements of low atomic number (where RBS loses sensitivity owing to the z^2 dependence of the cross section), and is based on the analysis of nuclear reaction products induced by bombardment with charged particles. NR can provide isotope sensitive information [6.25]. The observed reaction products are

NUCLEAR REACTION
$$H^1(N^{15}, \alpha, \gamma)C^{12}$$

(4.4 MeV)

N^{15}

$E = E_R$

LITHIUM NIOBATE

$H^1 \rightleftharpoons Li$

(4.4 MeV)

N^{15}

$E > E_R$

LITHIUM NIOBATE

$H^1 \rightleftharpoons Li$

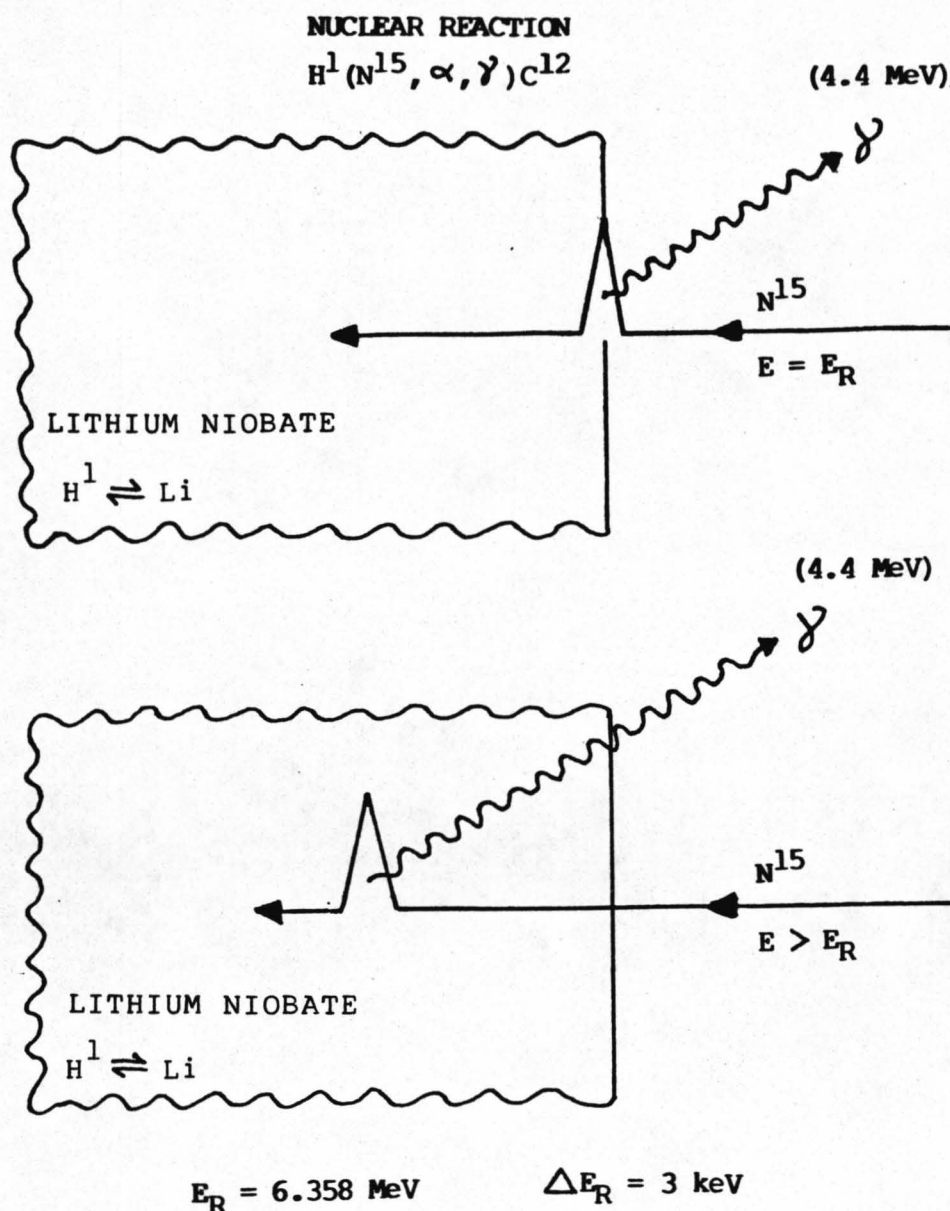$E_R = 6.358$ MeV $\triangle E_R = 3$ keV

Figure (6.6): Schematic of the N^{15} Resonance Profiling Method. The N^{15} Beam Bombardes the Target a) with $E = E_R$ and b) with $E > E_R$. The Number of &-rays is Proportional to the Hydrogen Concentration a) at the Surface and b) at the Depth where the N^{15} Beam Slows Down to $E = E_R$ Passing through the Target

usually charged particles which are detected and analysed by means of nuclear detectors. In NR the choice of the projectile, its energy, the element to be analysed, angle of detection and detector arrangement must all be carefully considered.

If the differential cross-section for a nuclear reaction is nearly constant as a function of projectile energy, the nuclear reaction which occurs is particularly suitable for determining the total number of investigated nuclei. However, a resonance in the cross section can be most useful for depth profiling. In particular the N^{15} hydrogen profiling technique uses a narrow isolated resonance in the process

$$N^{15} + H^1 \rightarrow C^{12} + He^4 + 4.43 MeV \, \gamma\text{-ray}$$
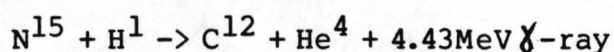
to measure the hydrogen content versus depth. Furthermore the off-resonance cross section of this nuclear reaction is three orders of magnitude smaller than the peak value, and thus the depth profiling resolution is very good (see below).

The experimental set up is similar to that of RBS in figure (6.1). To use this resonance as a probe for hydrogen, the exchanged sample surface is bombarded with N^{15} and the yield of the characteristic 4.43MeV γ-rays is measured with a NaI detector. When the sample is bombarded with an N^{15} beam at the resonant energy, $E_R = 6.385 MeV$, the yield of the characteristic γ-rays is proportional to the hydrogen content at the surface of the target. When the beam energy is raised above the resonant energy, the surface hydrogen is no longer detected because the N^{15} is above the resonant energy but as the N^{15} beam slows down in energy while passing through the target it reaches the resonant energy at a particular depth. The γ-ray yield is now proportional to the hydrogen concentration at this depth, which can be estimated accurately because of the known energy loss behaviour for ions in solids [6.19,6.20]. Hence, by measuring the γ-ray yield versus the energy of the incident N^{15} beam , the concentration of hydrogen versus depth in the target can be determined. The interaction between the N^{15} beam and the target

discussed above is shown schematically in figure (6.6). The depth resolution of this method is finite because the resonance has a finite energy width, 6keV, which for lithium niobate corresponds to a depth resolution of 20 angstroms. The sensitivity of this method for H^+ detection is about 0.1 at%, a hydrogen concentration of 5×10^{19} cm^{-3} [6.26,6.27].

It should be emphasised that the above method can give a signal only from hydrogen in the target. The N^{15} beam is below the Coulomb barrier for nuclear interactions with any element other than hydrogen and this is its particular attraction.

An NR technique has also been established for the detection of Li in a crystal [6.24]. The reasons why Li composition analysis is intrinsically more desirable than hydrogen profiling are discussed in section 6.6. To determine the amount of Li atoms present in the exchanged layer of lithium niobate a second nuclear reaction;

$$H^1 + Li^7 \rightarrow He^4 + \alpha$$
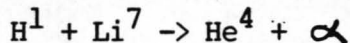
already used for this purpose, was employed [6.4]. The above reaction is not a resonant reaction so that the achievable depth resolution is quite poor, about 1000 angstroms. To use this NR to detect Li, the sample is bombarded with a proton beam, having 1.5MeV energy (in our experiments), and the yield of the emerging alpha particles is measured. The main information obtained from this analytical technique is the lithium concentration in the exchanged region since, as mentioned above, the low resolution of the technique allows only a poor estimation of the concentration profile, but can give satisfactory total lithium concentration information.

6.5 X-Ray Diffractometry Measurements on PE $LiNbO_3$

X-Ray analysis techniques have been used extensively in the analysis of titanium diffused surface layers in single crystal

lithium niobate [6.28,6.10,6.11,6.12]. The information readily available from this type of analysis is crystallographic i.e. lattice parameters, strain, crystal phase information and crystal quality (defects etc.) [6.31,6.32].

Strains and crystal structure modifications induced by proton exchange in the lithium niobate crystal have been analysed in a form akin to the analysis of titanium diffusion in lithium niobate. In particular, a double crystal diffractometer (DXD) was used to measure strains present in the waveguiding region [6.28,6.31,6.32], X-ray diffraction topography (XT) was used to detect defects and dislocations [6.31,6.32], while glancing angle X-ray diffraction measurements, taken in a Wallace-Ward cylindrical texture camera [6.29,6.30], were used to investigate the presence of new phases formed during the proton exchange process.

If X-rays are passed through a well ordered crystal (such as single crystal lithium niobate) they are Bragg diffracted by the grating like structure formed by the crystal planes and atomic strings, assuming that one or more of the planes is at the Bragg angle. The resultant diffraction patterns when carefully analysed can yield comprehensive structural information.

Single crystal X-ray diffractometry (XD) is sensitive to strains in the order of 1 part in 10^5 (see figure (6.7) a)). The data used in the following chapters is in the form of 'Rocking Curves' [6.30,6.31]. As a crystal is rotated through the Bragg condition for a particular crystal plane the intensity of the diffracted beam changes. The intensity vs. angle curve is known as a Rocking Curve. If the crystal is a 'perfect' crystal then there will be a plot in the form of curve (a) in figure (6.8), with a single peak, centred on the Bragg angle. The peak width is limited only by the divergence of the input beam incident on the crystal grating. If there is surface strain in the crystal, the Rocking Curve will be in the form of curve (b) in figure (6.8). The extra peaks, at much smaller intensity, are created by a secondary Bragg reflection obtained from the stressed surface

Figure (6.7): a) Schematic Diagram of the Set-up for Single
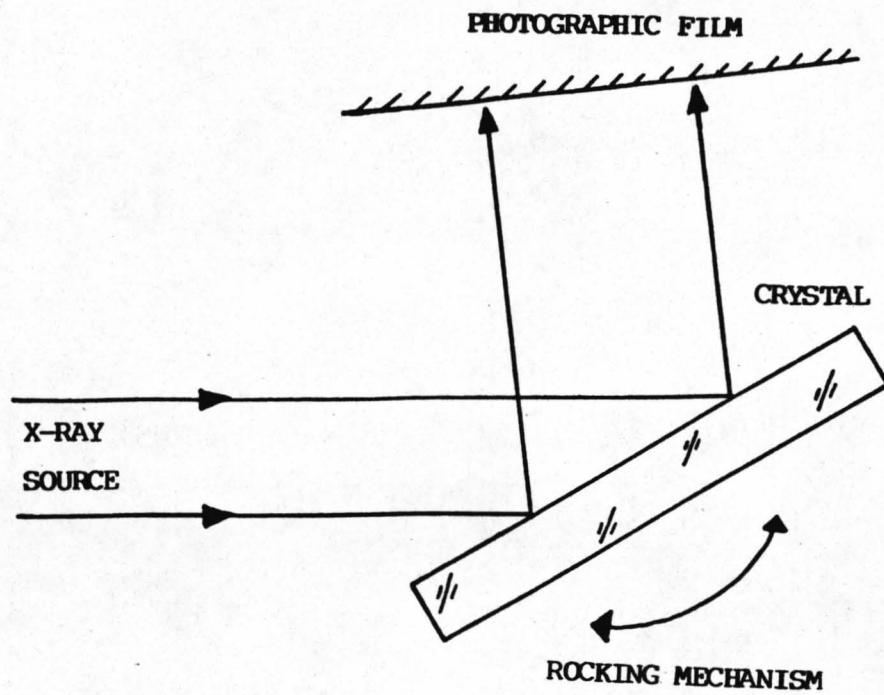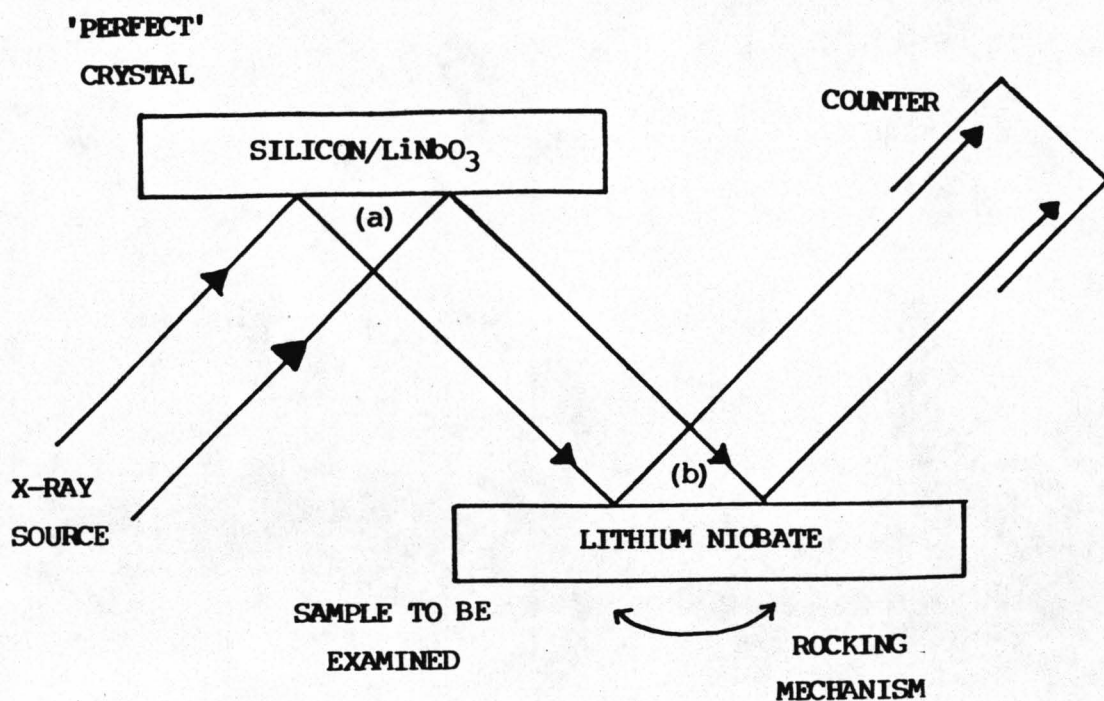Crystal X-Ray Diffraction Topography

Figure (6.7): b) Schematic Diagram of the Set-up for Double
Crystal X-ray Diffraction Topography
(a) Bragg Diffraction
to collimate X-ray beam
(b) Bragg Diffraction
to analyse surface layers
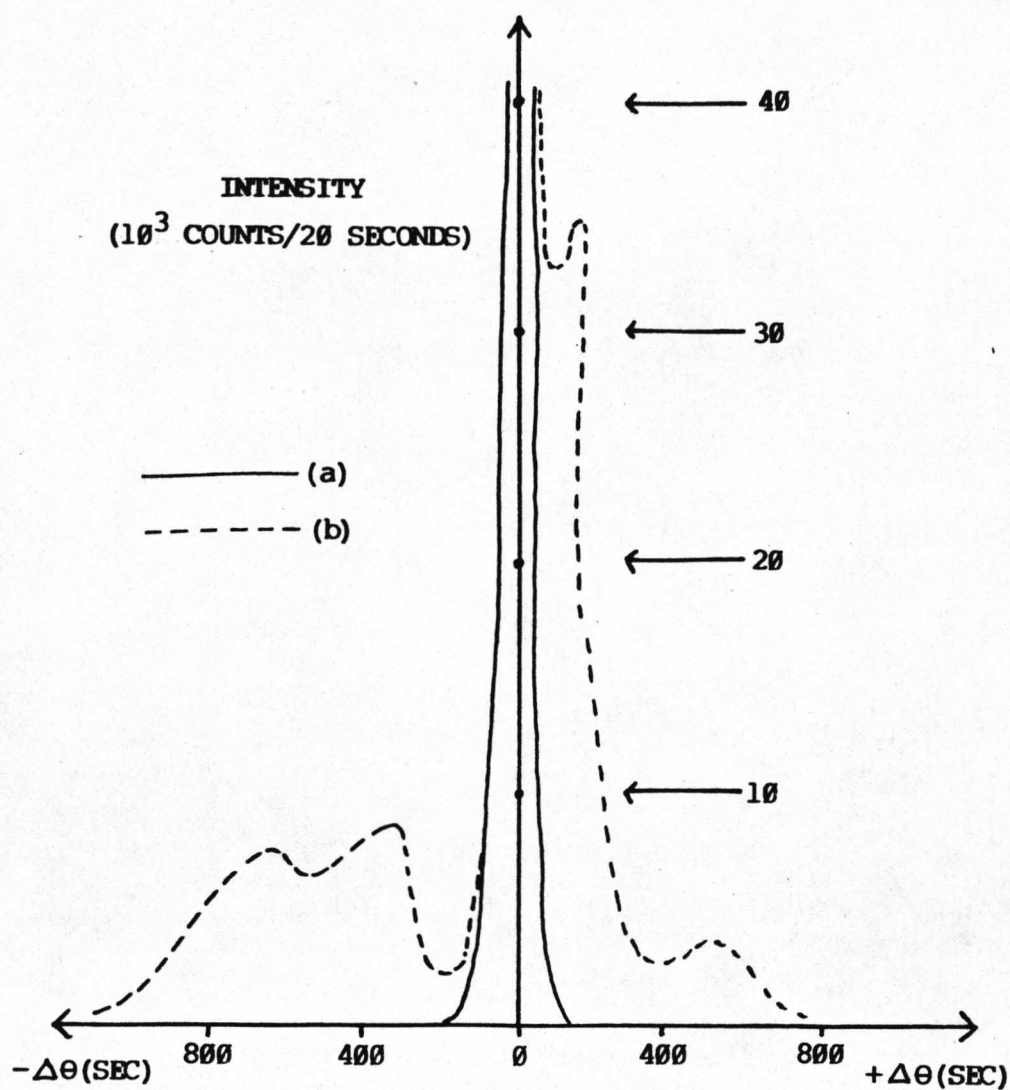
Figure (6.8): Diagram Depicting X-Ray Rocking Curves of a Perfect Crystal '(a)' and of a Crystal with a Stressed Surface Layer '(b)'

layer which has slightly different crystal parameters.

The data which can be obtained is as follows;

a) the sign of the strain (positive or negative depending on which side of the main peak the secondary peaks occur),
b) the intensity of the secondary peaks giving an indication of the amount of crystal which is stressed,
c) the position of the secondary peaks relative to the main peak giving the magnitude of the strain (the bigger the deviation the higher the strain),
d) The number and position of the secondary peaks, forming a picture of the total stress situation (which in some instances can be modelled on a computer).

Although the single crystal diffractometry technique is fairly accurate, in practice [6.32] it is found to be insensitive to slow variations in lattice parameters, because of the large angular divergence of the X-ray beam. Using two crystals, giving Double-crystal X-ray Diffractometry (see figure (6.7) b)), the first crystal Bragg diffracts and provides a collimated beam to analyse the second crystal which increases the sensitivity. For high sensitivity it is essential that both crystals are of the same material or that the first crystal is 'perfect' (silicon can be grown almost defect free and is, therefore, commonly used), since the image for DXD is the superposition of defects from the two crystals. Fortunately the first crystal is some distance from the photographic plate and hence any defect from the first diffraction will appear blurred and as a result poses little problem. This method is not suitable for crystals with high dislocation densities, since its high sensitivity causes saturation of the data on the photographic film.

Single crystal X-ray diffraction topography was used to detect defects in the proton exchanged layer in lithium niobate (see above) when investigating the surface cracking so prevalent on Y-cut substrates. Direct projection of the X-ray beam, which reflects off the crystal surface (i.e. not at an angle at which
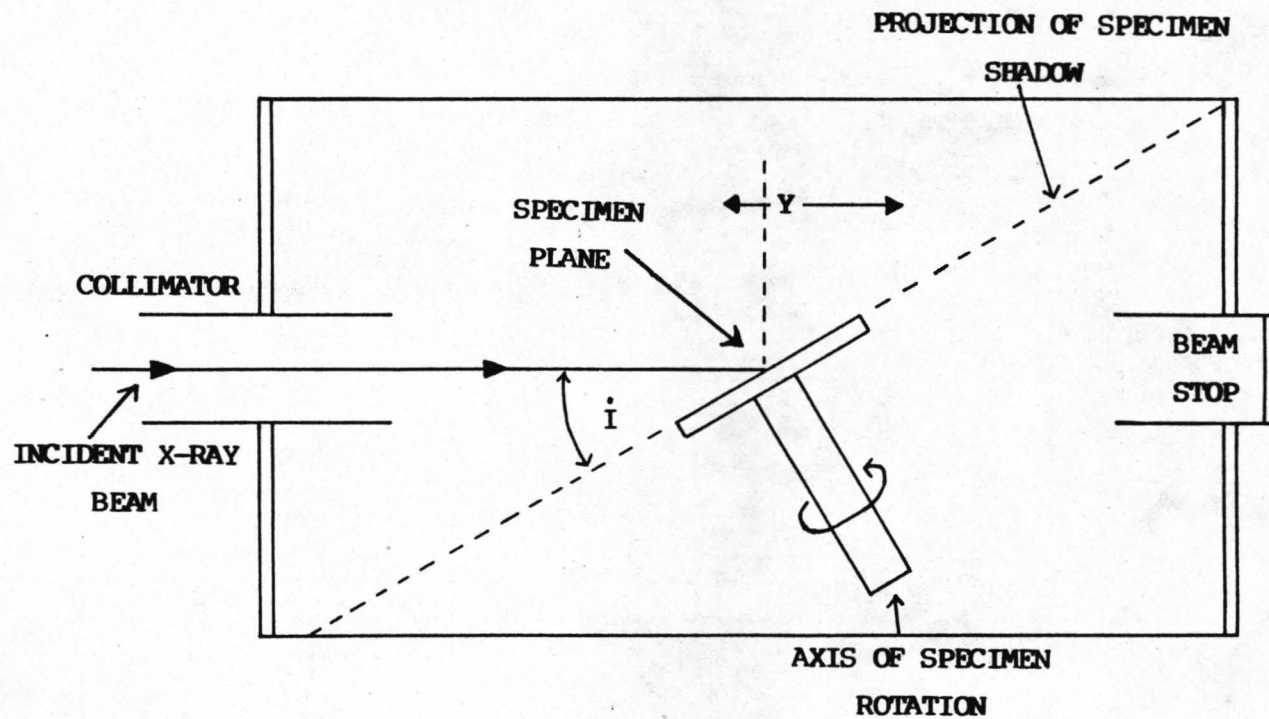
Figure (6.9): Schematic Diagram of a Wallace-Ward Cylindrical
Texture Camera

i = angle of incidence, can be up to 45°

Y = specimen plane longitudinal axis of movement

Bragg reflection/diffraction occurs) onto a photographic plate yields a strain picture of the crystal [6.28,6.31,6.32]. The results obtained with this method will be compared with those from methods discussed in section 6.7.

X-ray diffraction measurements taken with a Wallace-Ward cylindrical texture camera [6.29,6.32,6.30,6.28] give crystallographic information on any new phases which may be evident in the exchanged layer. A schematic diagram of the experimental set-up can be seen in figure (6.9). As the sample is rotated the orientation of the incident X-ray beam changes. Thus only at specific positions in the sample rotation will the incident X-rays be at the Bragg angle of a crystallographic plane. Hence, the photographic film (which surrounds the sample) will only be exposed at specific points. The film, when developed and printed, shows a large number of white spots on a black background, and each spot corresponds to a crystallographic plane. On comparing traces taken from virgin lithium niobate and those from exchanged samples the presence of extra 'spots' would indicate a different set of lattice parameters i.e. a different crystal phase. If the spots are distorted it indicates that there is strain in the lattice.

6.6 Chemical Analysis of Li Content in Exchange Melt

Although the Nuclear Reaction experiments could give an accurate representation of the hydrogen content and profile in the exchanged layer, it was evident that the index change mechanism for the proton exchange process was much more likely to be related to loss of lithium. It has been well established that the stoichiometry of the melt, before the pulling of lithium niobate single crystal, affects the crystal indices. In particular the Li/Nb ratio [6.33,6.34] in the melt, if reduced (to form a lithium deficient crystal), affected the ordinary index of the single crystal only slightly whereas the extra-ordinary index exhibited a substantial increase , this situation is fairly similar to that obtained in the proton exchange

process. Furthermore, in the formation of Ti-indiffused stripe waveguides, when the diffusion atmosphere is not controlled to limit lithium or possibly lithium oxide outdiffusion, a planar outdiffused waveguide is formed which has optical properties such as an anisotropic index change that is again comparable with proton exchanged waveguides [6.35,6.36,6.37]. These outdiffused waveguides have also been investigated in their own right [6.34,6.38,6.39]. The fact that the outdiffused waveguides have been shown to be lithium deficient and that these guides/layers can be suppressed by using an overpressure of Li and LiO_2 (obtained, e.g., by placing congruent lithium niobate powder with the substrate in the diffusion furnace) does point to the hypothesis that it is the lack of lithium in the proton exchanged layer that is important, with the main function of hydrogen being to maintain a charge balance and/or allow the lithium to diffuse out of the crystal at a considerably lower temperature than that which it is possible to form outdiffused waveguides.

The ability of an NR to determine the lithium content in the lithium niobate crystal being a recent development in the materials analysis of proton exchanged waveguides, discussions with Dr J. Winfield of the Chemistry Dept., University of Glasgow, resulted in a method being developed to determine the amount of lithium in the exchange melt, after the PE process, and hence determine the amount of lithium leaked from the crystal. This process is described below.

Z-cut lithium niobate material was cut into $1cm^2$ pieces 1mm thick and polished on both sides (partly so that I.R. measurement could be run concurrently and partly to provide smooth exchanged regions of a known surface area). Each sample was accurately measured in all dimensions, using a micrometer, and scrupulously cleaned. Instead of the normal stainless steel exchange beaker, separate and ultra-clean silica beakers and lids were used for each sample. The amount of pure benzoic acid in each beaker, V_m, was accurately weighed. A small PTFE sample holder was designed to give the maximum freedom for acid to circulate about the exchanging sample, the sample holder being scrupulously cleaned
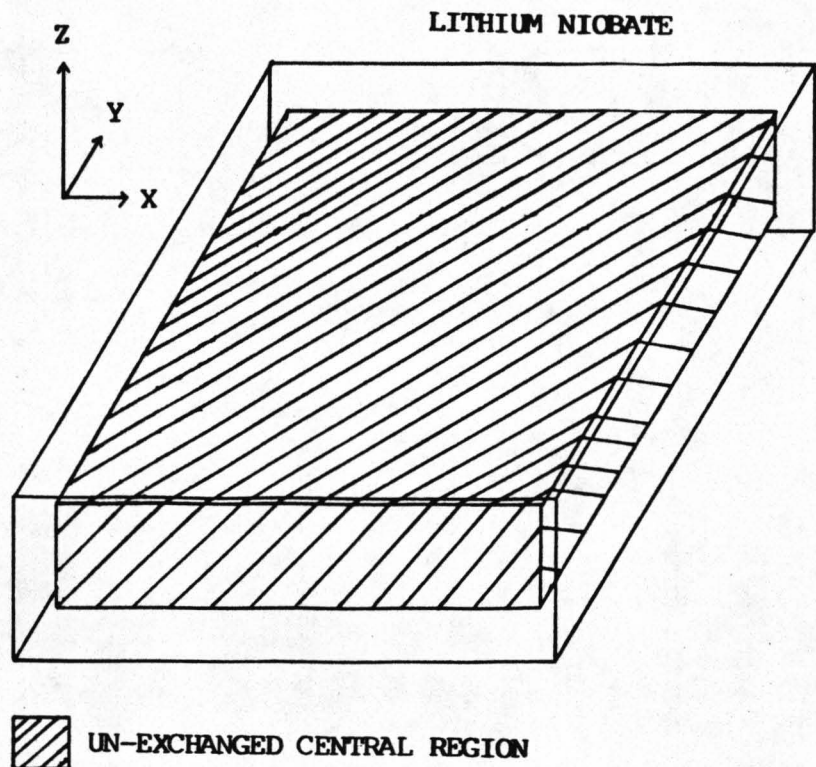
Figure (6.10): Schematic Representation of Exchanged and Un-exchanged Regions in a PE Lithium Niobate Sample Specially Prepared i.e. Polished on all Faces

before each exchange. Each sample was exchanged isothermally but for increasing periods of time. The temperature and times were accurately measured for each exchange.

The chemical formula of lithium niobate is $LiNbO_3$, however a more accurate representation of the chemical formula of a lithium niobate obtained from a congruent melt is;

$$Li_{0.957}Nb_{1.0086}O_3$$
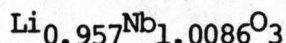
Molecular Weight Li - 6.94 x 0.957
Nb - 92.91 x 1.0086
O - 16.0 x 3

TOTAL   148.35061

Density of lithium niobate for a congruent melt is 4.628 g/cm^3

Therefore the density of lithium ions in the crystal is;

$$(6.642/148.351) \times 4.628 = 0.2072 \ g/cm^3$$

Thus, since the diffusion coefficients of the proton exchange process are known and the resultant exchanged depth can be calculated, an estimate of the total volume of lithium niobate which has been exchanged can be calculated (see figure (6.10)). The assumption must also be made that the diffusion coefficient along the Y-axis is the same as that for the X-axis, which is known. The total exchanged volume V_T can then be used, assuming all the lithium is removed into the exchange melt, to calculate the total weight of lithium in the exchange melt W_{Li};

$$V_T \times 0.2072 \ g/cm^3 = W_{Li}$$

Therefore the theoretical maximum concentration of Li in the exchange melt for a given temperature and time is;

$$\text{fraction of Li in melt} = W_{Li} / W_m$$

These theoretical results can then be compared to the analysis of the lithium content in the exchange melt. The analysis first used to determine the lithium content in the exchanged melt was Flame Emission [6.40]. A weighed sample from the exchange melt was diluted in 50% aqueous solution of ethanol up to a predetermined volume. The sample was then burned in a flame photometer and the Li emission spectrum monitored. This spectrum was then compared to a set of calibration measurements of known Li doping (the standards being made up from lithium nitrate). The characteristic absorption wavelength to detect lithium is 6707.8 angstroms, and the sensitivity of the method is 0.03μg/ml in the pre-diluted exchange melt.

Flame Emission is more sensitive to lithium than Atomic Absorption [6.42,6.40]. However, subsequent measurements (to corroborate the first series of results) were made using Atomic Absorption [6.40,6.41,6.42]. Flame emission gives high sensitivity information but the results are not accurately repeatable due to the noise levels inherent in the process. Although Atomic Absorption is less sensitive, the information can be consistently repeated. Atomic Absorption is similar to Flame Emission in some respects. However, Atomic Absorption is not directly related to the Li concentration, although standard solutions are made up in a similar way. To alleviate the problem of the trade off between reduced sensitivity and result repeatability, when the process was repeated the temperature and the exchange time of the process were increased and the volume of acid decreased, ensuring a much higher lithium concentration in the melt.

6.7 S.E.M. and Phase Contrast Microscope

The scanning electron microscope was used to give a clear and magnified picture of the damaged surface regions in proton exchanged waveguides, particularly on Y-cut lithium niobate which exhibited severe surface damage. A phase contrast microscope was also used to view the surface stress (through index changes)

before the crystal was at the point where localised cracks formed
to alleviate the stress. These methods gave an insight to the
directionality and severity of surface cracking caused by stress
associated with the PE process.

6.8 Conclusions

The materials analysis techniques outlined in chapter 6 give a
comprehensive and wide ranging source of data which when brought
to bear on the analysis of proton exchanged waveguides on lithium
niobate should yield a full materials characterisation of the
process. Some of the materials analysis techniques used have
been tried and tested in the analysis of titanium indiffused
waveguides and their use has been adapted for proton exchange
waveguides.

The data when compared with the optical characterisation of
proton exchanged waveguides should yield information on the index
change mechanism and the optical loss mechanism, as well as
possibly giving an indication of how it is possible to counteract
waveguide stability and stress problems.

CHAPTER 6 - REFERENCES

[6.1]   J.L. Jackel and C.E. Rice
        Topotactic $LiNbO_3$ to Cubic Perovskite Structural
        Transformation in $LiNbO_3$ and $LiTaO_3$
        Ferroelectrics, vol 38, pp801-804, 1981

[6.2]   C.E. Rice and J.L. Jackel
        $HNbO_3$ and $HTaO_3$: New Cubic Perovskites from $LiNbO_3$ and
        $LiTaO_3$ via Ion Exchange
        J. Solid State Chem., vol 41, pp308-312, 1982

[6.3]   C.E. Rice and J.L. Jackel
        Structural Changes with Composition and Temperature in
        Rhombohedral $Li_{1-x}H_xNbO_3$
        Mat. Res. Bull., vol 19, pp591-597, 1984

[6.4]   Y.X. Chen, W.S.C. Chang and S.S. Lau
        Characterisation of $LiNbO_3$ Waveguides Exchanged in
        $TlNO_3$ Solution
        Appl. Phys. Lett., vol 40, No.1, pp10-12, Jan. 1982

[6.5]   J.L. Jackel and C.E. Rice
        Variation in Waveguides Fabricated by Immersion of
        $LiNbO_3$ in $AgNO_3$ and $TlNO_3$: The Role of Hydrogen
        Appl. Phys. Lett., vol 41, No.6, pp508-510, Sept. 1982

[6.6]   Y.X. Chen, X.Y. Zhang, S.M. Fang and M.L. Chen
        $LiNbO_3$ Waveguides by Electrically Enhanced Ion
        Migration
        4th Int. Conf. I.O.O.C., paper 29A1-2, pp66-67
        June 1983, Tokyo, Japan

[6.7]   J.L. Jackel, C.E. Rice and J.J. Veselka
        Proton Exchange for High-Index Waveguides on $LiNbO_3$
        Appl. Phys. Lett., vol 41, No.7, pp607-608, Oct. 1982

[6.8]   M. Goodwin and C. Stewart
          Proton-Exchanged Optical Waveguides in Y-cut Lithium
          Niobate
          Electr. Lett., vol 19, No.6, pp223-225, March 1983

[6.9]   K.K. Wong, R.M. DeLaRue and S. Wright
          Electro-Optic Waveguide Frequency Translator in $LiNbO_3$
          Fabricated by Proton Exchange
          Opt. Lett., vol 7, pp 546-548,   March 1982

[6.10]   M.N. Armenise et al.
          Dependence of Inplane Scattering Levels in $Ti:LiNbO_3$
          Optical Waveguides on Diffusion Time
          I.E.E. Proc., vol 131, part H, No.5, pp295-298,
          October 1984

[6.11]   M.N. Armenise et al.
          Characterisation of TiO_2, $LiNb_3O_8$ and $(Ti_{0.65}Nb_{0.35})O_2$
          Compound Growth Observed During $Ti:LiNbO_3$ Optical
          Waveguide Fabrication
          J. Appl. Phys., vol 54, pp6223-6231, 1983

[6.12]   M.N. Armenise et al.
          Evaluation of Planar Titanium Diffused $LiNbO_3$ Optical
          Waveguides by Micro-analytical Techniques and
          Measurements of In-Plane Scattering Levels
          Tech. Digest of 4th Int. Conf. I.O.O.C., pp67-70
          June 1983, Tokyo, Japan

[6.13]   N.B. Colthup, L.H. Daly and S.E. Wiberley
          Introduction to Infrared and Raman Spectroscopy
          Academic Press, New York, 2nd Edition, 1975

[6.14]   K. Nakamoto
          Infrared and Raman Spectra of Inorganic and
          Coordination Compounds
          Academic Press, New York, 3rd Edition, 1978

[6.15]   A. Rauber
          Chemistry and Physics of Lithium Niobate
          Current Topics in Materials Science, vol 1, Chpt 7
          Edited by E. Kaldis, 1978

[6.16]   J.R. Herrington et al.
          An Optical Study of the Stretching Absorption Band Near
          3 Microns from OH^- Defects in $LiNbO_3$
          Solid State Comm., vol 12, pp351-355, 1973

[6.17]   K.K. Wong et al.
          Characterisation of Proton-Exchange Slab Optical
          Waveguides in X-cut $LiNbO_3$
          Accepted for publication in I.E.E. Proc., Part J, 1985

[6.18]   I.W. Donald and P.W. McMillan
          Review: Infrared Transmitting Materials
          Part 1 Crystalline Materials
          J. Mat. Science., vol 13, pp1151-1176, 1978

[6.19]   W.K. Chu, J.W. Mayer and M-A Nicolet
          Backscattering Spectrometry
          Academic Press, New York, 1978

[6.20]   J.W. Mayer and E. Rimini (eds.)
          Ion Beam Handbook for Materials Analysis
          Academic Press, New York, 1977

[6.21]   Discussions with A. Carnera
          Dipartimento di Fisica, Padova, Italy
          are gratefully acknowledged

[6.22]   M.L. Shah
          Optical Waveguides in $LiNbO_3$ by Ion Exchange Technique
          Appl. Phys. Lett., vol 26, No.11, pp652-653, June 1975

[6.23]   J. Jackel
High-Δn Optical Waveguides in $LiNbO_3$: Thallium-Lithium
Ion Exchange
Appl. Phys. Lett., vol 37, No.8, pp739-741, Oct 1980

[6.24]   W.K. Chu, J.W. Mayer, M.A. Nicolet et al.
Review Paper: Principles and Applications of Ion Beam
Techniques for the Analysis of Solids and Thin Films
Thin Solid Films, vol 17, No.1, pp1-41, 1973

[6.25]   P. Mazzoldi and G. Della Mea
The Use of Nuclear Techniques for the Analysis of
Thin Films on Glass
Thin Solid Films, vol 77, pp181-193, 1981

[6.26]   W.A. Lanford
^{15}N Hydrogen Profiling: Scientific Applications
Nuclear Instruments and Methods, vol 149, pp1-8
Part 1. Light Element Profiling, 1978

[6.27]   C. Canali et al.
Proton Exchanged $LiNbO_3$ Waveguides: Materials Analysis
and Optical Characteristics
Proc. S.P.I.E., vol 460, Los Angeles Symposium, Calif.
22-26 January 1984

[6.28]   K. Sugii, M. Fukuma and H. Iwasaki
A Study on Titanium Diffusion into $LiNbO_3$ Waveguides by
Electron Probe Analysis and X-ray Diffraction Methods
J. Materials Science, vol 13, pp523-533, 1978

[6.29]   C.A. Wallace and R.C.C. Ward
An X-ray Cylindrical Texture Camera for the Examination
of Thin Films
J. Appl. Cryst., vol 8, pp255-260, 1975

[6.30] C.A. Wallace and R.C.C. Ward
X-ray Diffraction Techniques for the Analysis of
Epitaxic Thin Films
J. Appl. Cryst., vol 8, pp545-556, 1975

[6.31] P. Luger
Modern X-Ray Analysis on Single Crystals
Walter de Gryter, Berlin, New York, 1980

[6.32] B.K. Tanner
X-Ray Diffraction Topography
International Series in the Science of the Solid State
vol 10, Pergammon Press, 1st Ed., 1976

[6.33] J.G. Bergmann et al.
Curie Temperature, Birefringence and Phase Matching
Temperature Variations in $LiNbO_3$ as a Function of Melt
Stoichiometry
Appl. Phys. Lett., vol 12, No.4 , pp92-95, 1968

[6.34] J.R. Carruthers, I.P. Kaminow and L.W. Stulz
Diffusion Kinetics and Optical Waveguide Properties of
Outdiffused Layers in Lithium Niobate and Lithium
Tantalate
Applied Optics, vol 13, No.10, pp2333-2342, Oct 1974

[6.35] R.J. Esdaile
Closed Tube Control of Out-Diffusion During Fabrication
of Optical Waveguides in $LiNbO_3$
Appl. Phys. Lett., vol 33, No.8, pp733-734, Oct 1978

[6.36] W.K. Burns, C.H. Bulmer and E.J. West
Application of Li_2O Compensation Techniques to Ti-
Diffused $LiNbO_3$ Planar and Channel Waveguides
Appl. Phys. Lett., vol 33, No.1, pp70-72, July 1978

[6.37]   J.L. Jackel, V. Ramaswamy and S.P. Lyman
         Elimination of Out-Diffused Surface Guiding in Titanium
         -Diffused $LiNbO_3$
         Appl. Phys. Lett., vol 38, No.7, pp509-511, April 1981

[6.38]   I.P. Kaminow and J.R. Carruthers
         Optical Waveguiding Layers in $LiNbO_3$ and $LiTaO_3$
         Appl. Phys Lett., vol 22, No.7, pp326-328, April 1973

[6.39]   R.L. Holman
         The Optical Properties and Processing of Lithium
         Niobate Optical Waveguides
         Proc. S.P.I.E., vol 408, Integrated Optics III,
         pp14-20, Virginia, April, 1983

[6.40]   G.F. Kirkbright and M. Sargent
         Atomic Absorption and Flourescence Spectroscopy
         Academic Press, New York, 1974

[6.41]   G.D. Christian and F.J. Feldman
         Atomic Absorption Spectroscopy
         Wiley-Interscience, London, 1970

[6.42]   W.T. Elwell and J.A.F. Gidley
         Atomic - Absorption Spectrophotometry
         Pergammon Press, Second (revised) Edition, 1966

CHAPTER 7

MATERIALS ANALYSIS OF PROTON EXCHANGED WAVEGUIDES
AND OPTICAL COMPARISONS

7.1 Introduction

In chapter 6 some of the materials analysis techniques for the
investigation of proton exchanged planar waveguides have been
discussed extensively. Therefore, in this chapter, the
techniques will only be mentioned by abbreviations. The aims of
this analysis are to define the proton exchange process and, as
well as attempting to understand the index change mechanism, to
investigate possible phase changes, examine the causes of surface
damage in the crystals and discuss why the waveguides are
intrinsically unstable. It is hoped that if a clear
understanding of the process is achieved the information will
increase the probability of achieving stable low loss waveguides.

7.2 Analysis of Infra-red Absorption Measurements

Infra-red transmission absorption spectra have been obtained on
PE waveguides on X-cut, Y-cut and Z-cut lithium niobate. The
results obtained are similar to those already reported in the
literature [7.1,7.2,7.3].

IR measurements on proton exchanged X-cut lithium niobate use the
acid temperature as the exchange temperature as discussed in
chapter 5. All other techniques in this chapter are consistent
with the usual method of taking the oil temperature as the
exchange temperature.

Measurements of IR spectra in PE waveguides were usually carried
out with the spectrum from the bulk crystal subtracted from the
output, thus enabling the effect of PE on the crystal to be
examined without the superposition of the OH^- spectrum from the
bulk crystal. This was the case except for figure (7.2).

After proton exchange in lithium niobate two absorption bands are observed in the IR spectrum. From figure (7.1) it can be seen that one is a sharp and strong peak at 3505 cm^{-1} and the other is a small broad absorption band at 3250 cm^{-1}, in close agreement with other researchers [7.6,7.7]. Figure (7.1) shows IR absorption spectra for PE waveguides formed on a) X-cut, b) Y-cut and c) Z-cut lithium niobate. All spectra show absorption peaks for electric field parallel and perpendicular to the c-axis (in the case of X-cut and Y-cut samples) and to the X-axis and Y-axis (in the case of Z-cut samples). From figure (7.1) it is evident that, as in the bulk case, the large absorption peak is polarisation dependent whereas the low broad band is substantially independent of polarisation.

The spectra of figure (7.1) indicate that in the PE reaction at least two new OH groups are formed which differ in their hydrogen bonding environment. The spectrum, compared with that of virgin lithium niobate [7.4,7.5] (or more accurately the main peak of the spectrum), is of a much greater intensity than the residual water peak although they both have the same polarisation characteristics. The peak is also asymmetric and consists of at least two peaks overlapping which may arise from more than one type of OH group. The second peak, much weaker and broader than the main peak, is unpolarised and its position in the lower resonant energy range suggests that it is due to OH groups which participate in extensive hydrogen bonding. The spectra obtained appear to be very similar to those obtained from treating X-cut lithium niobate with a hydrate melt and nitric acid. In the latter work, the peak was attributed to the formation of a secondary phase, possibly $HNbO_3$ [7.6,7.7].

Figure (7.2) shows that the large absorption peak grows in proportion to the thickness of the exchanged layer, as would be expected. In figure (7.2) Z-cut lithium niobate samples are a) exchanged isothermally for differing exchange times and b) exchanged isochronally for differing exchange temperatures. From figure (7.2) it can be seen that there is a transition period during which the peak shifts position from $3486 cm^{-1}$ (the residual

Figure (7.1): a) Polarised IR Absorption Spectra of a X-cut
Lithium Niobate Sample Exchanged at 180°C for 1
hour. Main Peak is at 3505 cm^{-1}.
(A) Radiation Polarised Normal to c-axis
(B) Radiation Polarised Parallel to c-axis
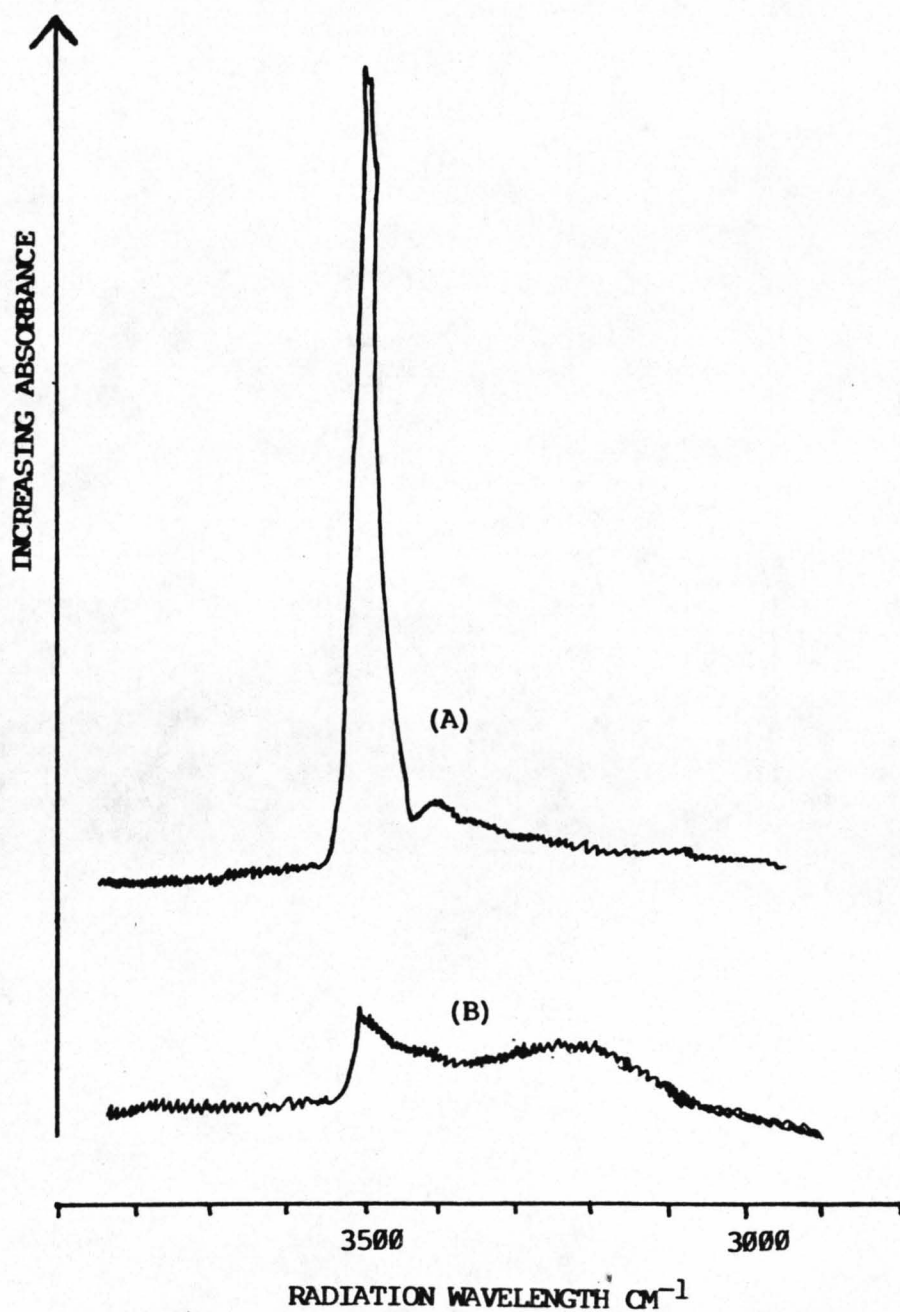
Figure (7.1): b) Polarised IR Absorption Spectra of a Y-cut
Lithium Niobate Sample Exchanged at 171°C for
20 min. Main Peak is at 3504 cm^{-1}.

(A) Radiation Polarised Normal to c-axis

(B) Radiation Polarised Parallel to c-axis

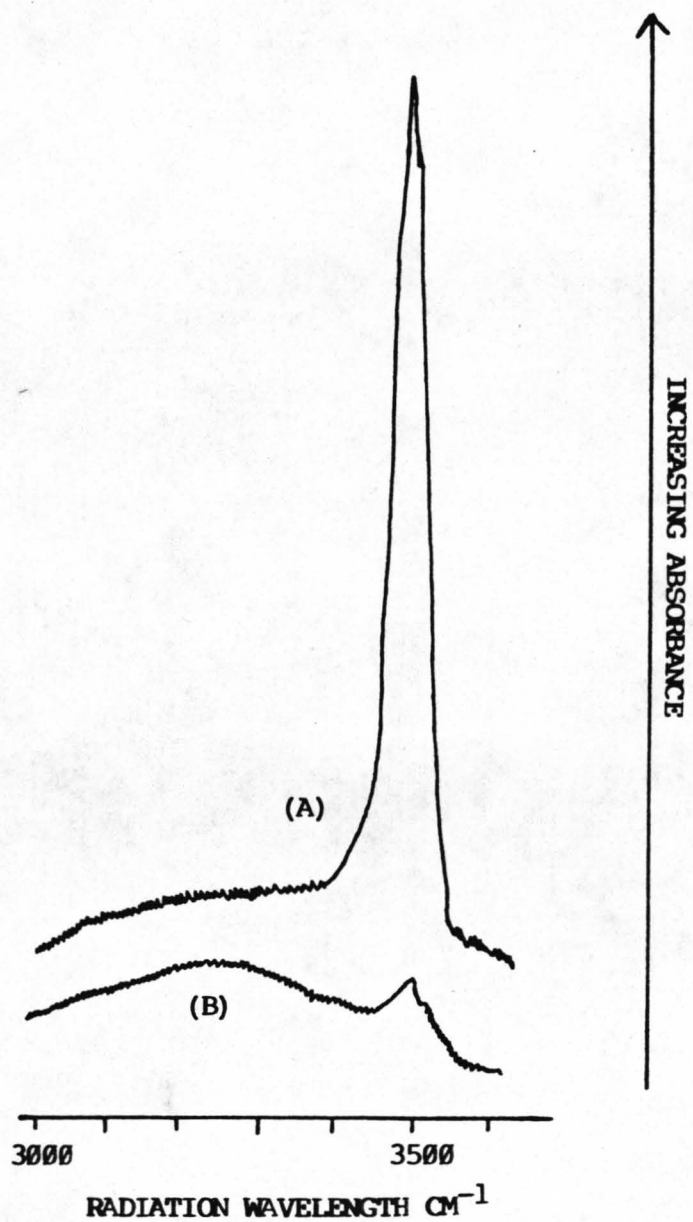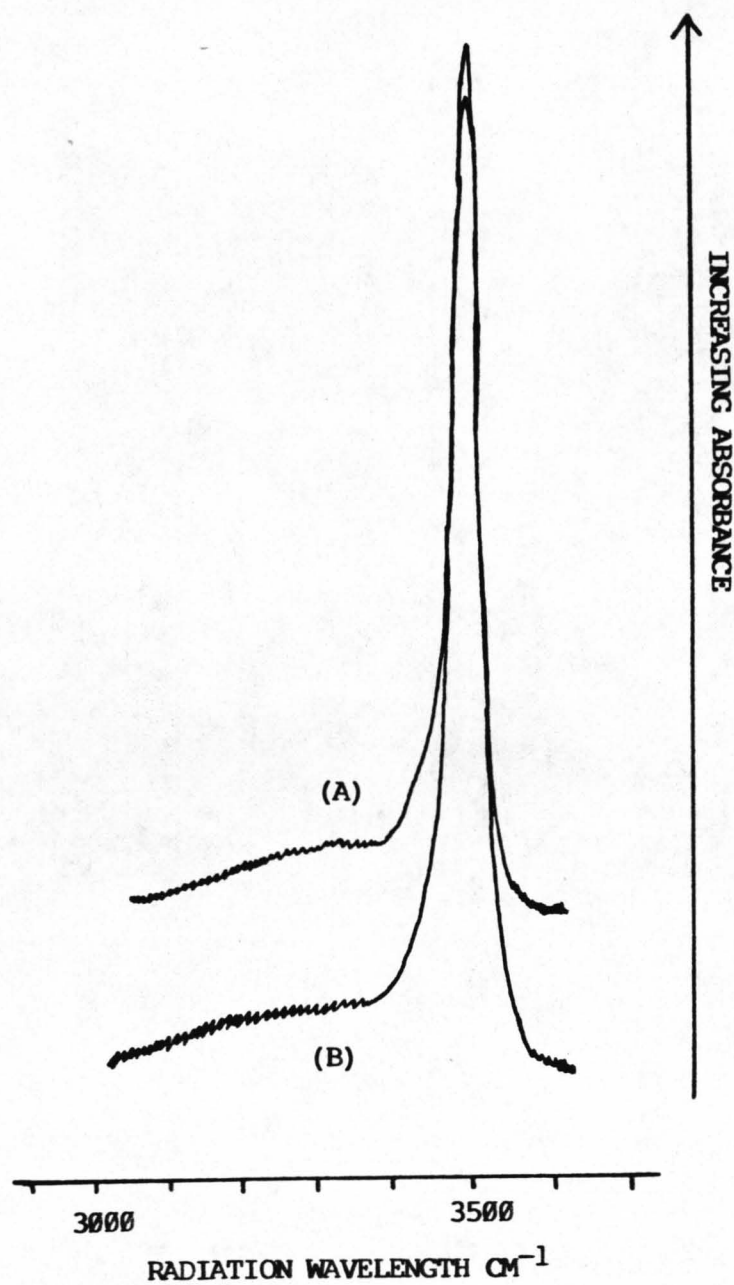**Figure (7.1):** c) Polarised IR Absorption Spectra of a Z-cut
Lithium Niobate Sample Exchanged at 180.5°C for
2 hours. Main Peak is at 3507 cm^{-1}.
(A),(B) Radiation Polarised Normal to the c-axis
and Orthogonally to Each Other.
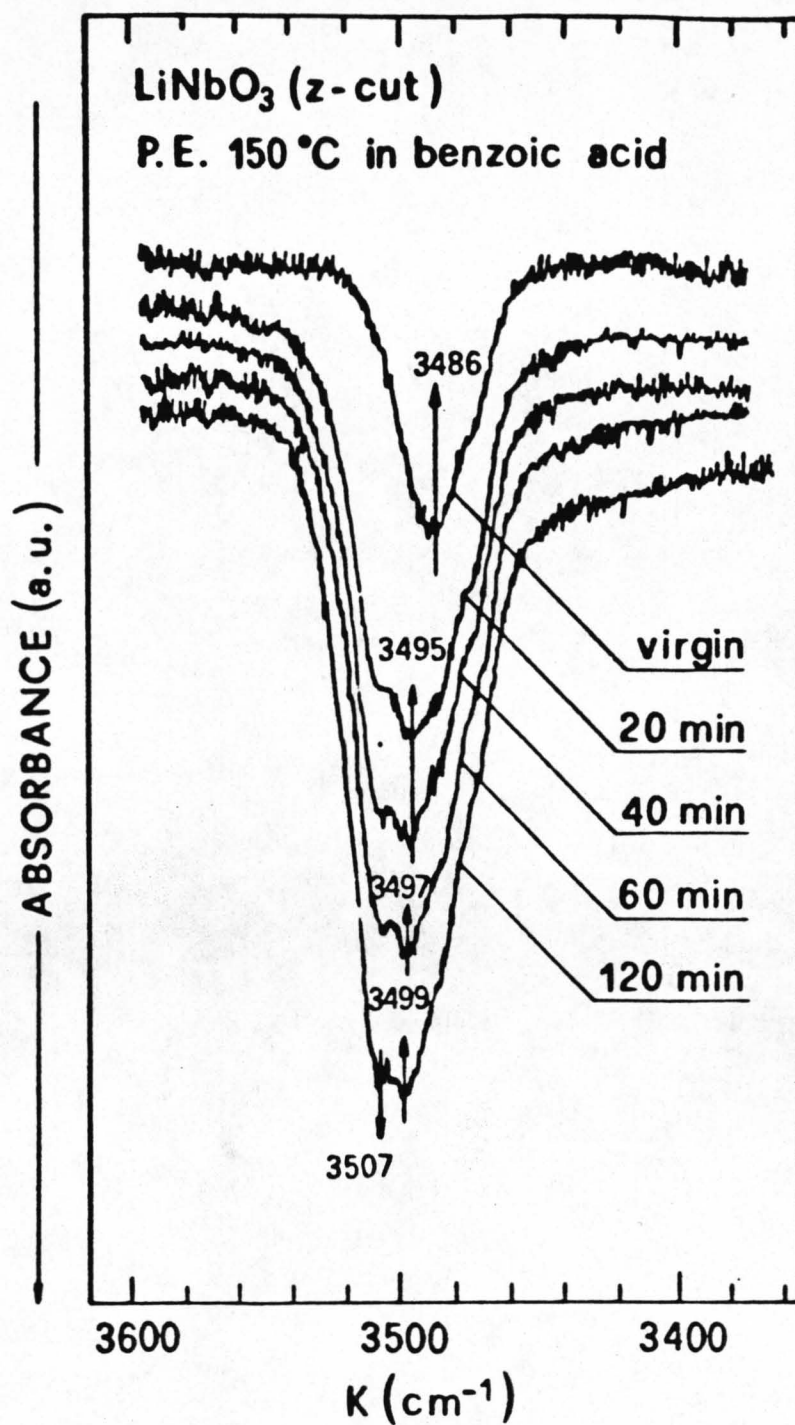
Figure (7.2): a) Random IR Spectra of Z-cut Lithium Niobate Samples Exchanged at 150°C for Various Times plus an IR Spectrum from Virgin Lithium Niobate. K - Radiation Wavelength

Figure (7.2): b) Random IR Spectra of Z-cut Lithium Niobate Samples Exchanged for 2 hours at Various Temperatures plus an IR Spectrum from Virgin LiNbO₃. K – Radiation Wavelength

water) peak to the 3505cm^{-1} position. It is evident that the shift in the peak is due to the overpowering effect the PE strong OH bond has on the small bulk water peak when the exchanged layer gets deeper. Assuming, as can be seen from figure (7.2) , th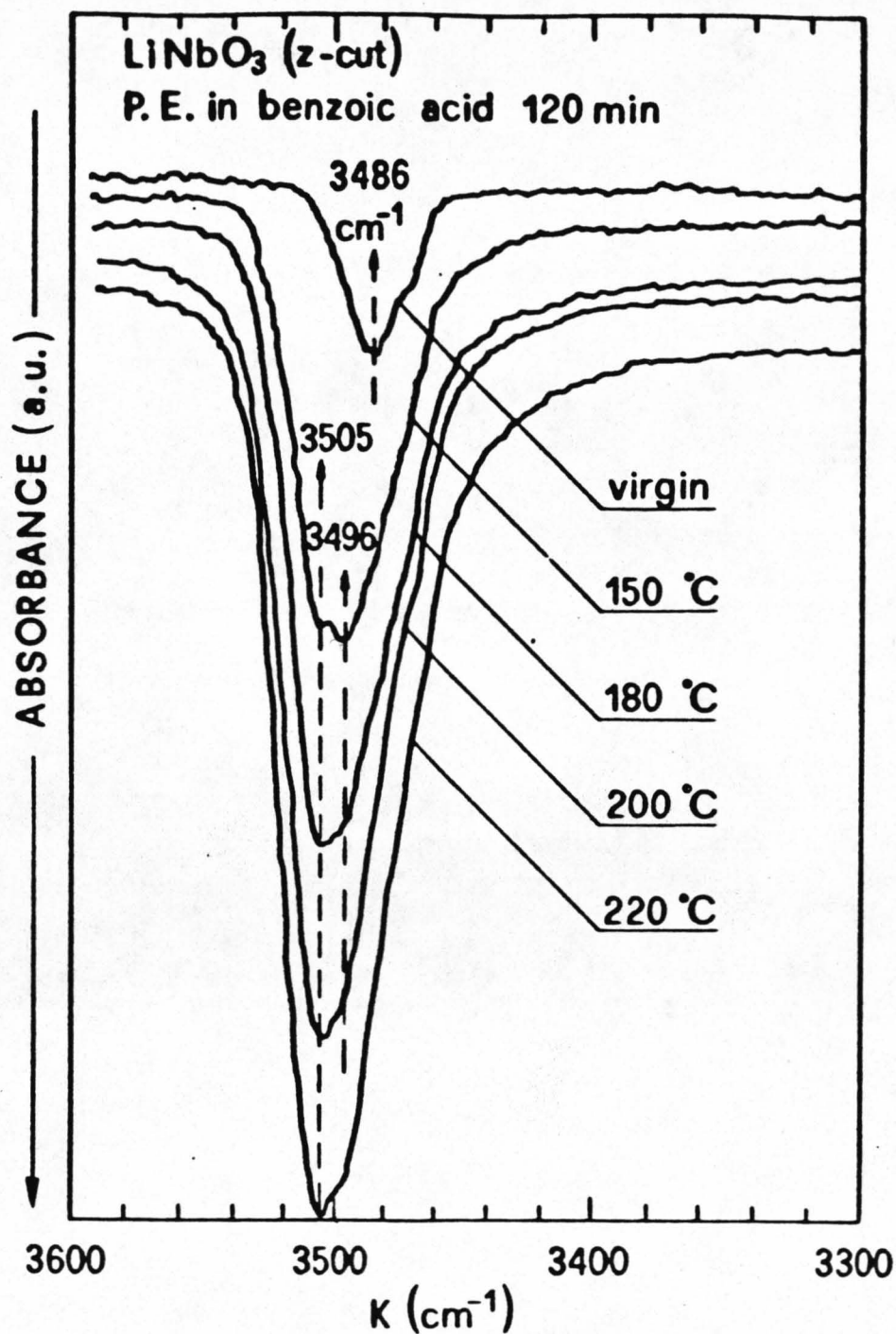at there is proportionality, it should be possible to monitor the exchange process by monitoring the rate of change of the OH$^-$ absorption band.

The information that can be gained from the above spectra is that substantial amounts of hydrogen enter the lattice during the proton exchange process. The hydrogen entering the lattice bonds with the oxygen in the lattice. Most of the O-H bonds are in a plane normal to the c-axis, although there is a small number of O-H bonds whose directions are varied throughout the crystal axes (contrary to the bulk water peak). The amount of hydrogen entering the lattice is a function of the exchange time and/or temperature of the PE process. The randomly bonded hydrogen in the lattice is bonded somewhat more weakly (hydrogen bonding).

Figure (7.3) shows OH absorbance as a function of exchange layer depth, on X-cut lithium niobate samples. It is evident that there is a small data spread suggesting that the hydrogen concentration in the exchanged layer is to some degree variable (possibly the difference between exchanging with pure and used benzoic acid), although no visible changes in waveguiding properties have been noted.

Figure (7.4) shows the peak absorption values for a series of PE waveguides on X-cut lithium niobate plotted against, exchange temperature (for a series of exchange times)[!].

On examining figure (7.4) it appears that at high temperatures (>200°C) or long diffusion times (>1 hour) the exchange process is non-linear [7.8]. This reasoning is valid if the assumption,

[!] Figure (7.4) is from reference [7.8] on which I am an author. The data was collected and plotted by Mr K.K. Wong, Marconi Research Centre, Chelmsford, Essex.
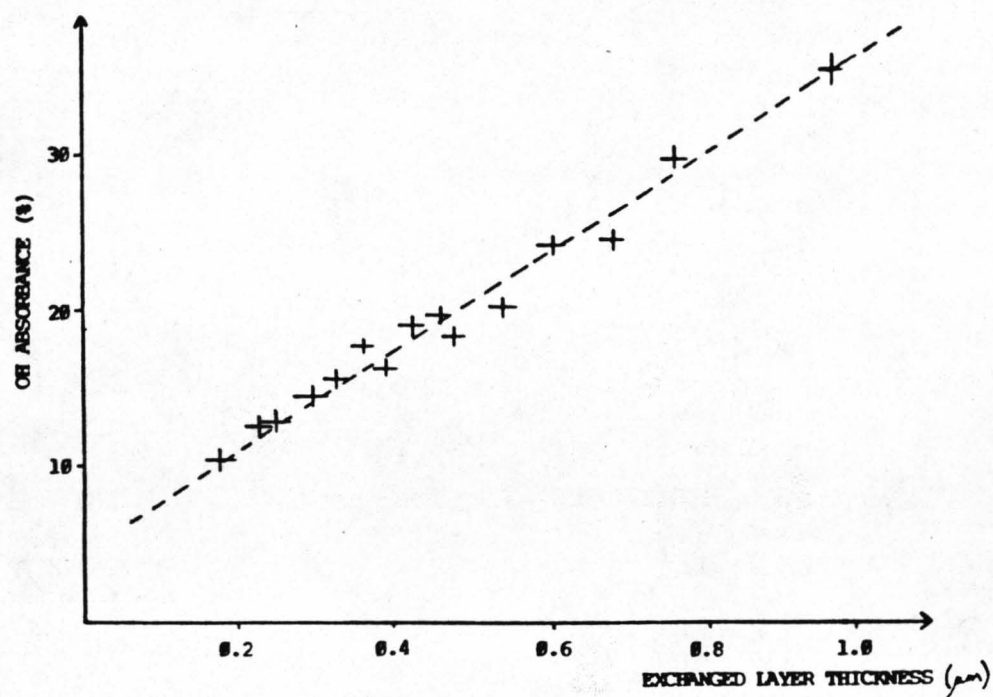
Figure (7.3): Plot of Peak OH Absorbance (3505 cm^{-1}) vs. Depth of Exchanged Layer. Samples Fabricated on X-cut Lithium Niobate for Various Exchange Temperatures and Times.
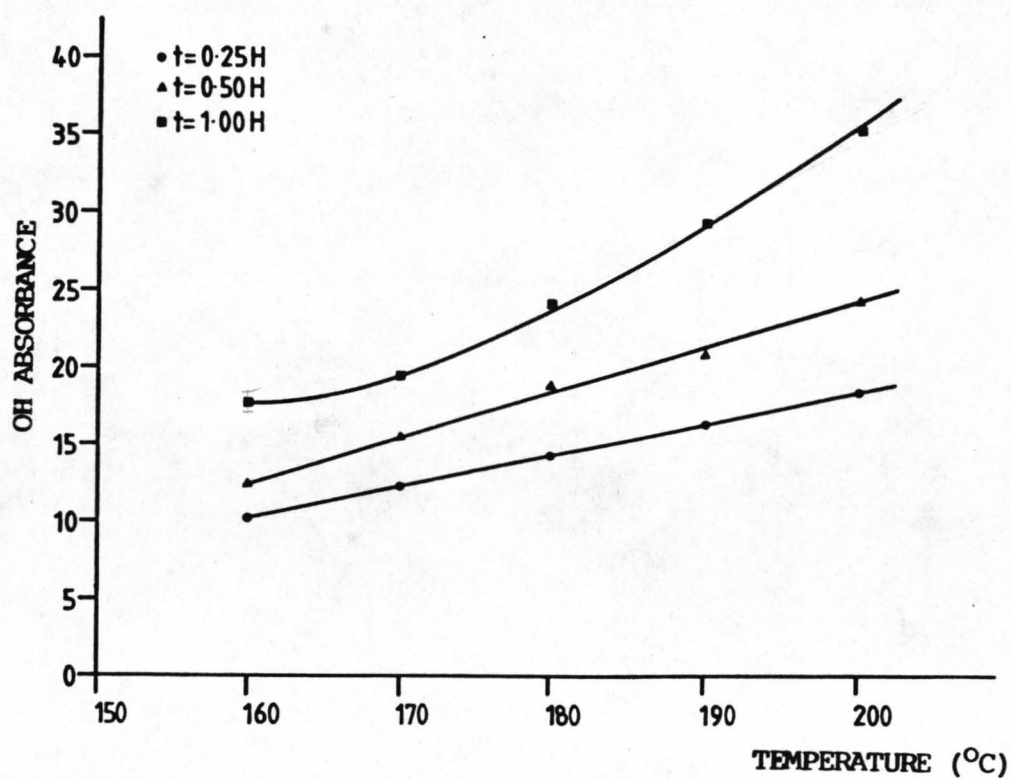
Figure (7.4): Plot of Peak OH Absorbance (3505 cm⁻¹) vs. Exchange Temperature for Various Exchange Times. Samples Fabricated on X-cut Lithium Niobate.

implicit in these plots, is made, that the peak absorption value of each IR spectrum can be related directly to the absorption in the whole band, implicitly suggesting that the absorption peak maintains the same shape for different amounts of exchange i.e. that the area under the peak (the total absorption) can be related directly to the peak value. This is assumed to be true as long as the broad absorption peak remains at a value such that the overlap with the main peak is not sufficent to alter the main peak.

For long exchange times the assumption possibly becomes less tenable because of the observed non linearities in the plots shown in figure (7.4). The non-linearity in OH absorption (in the PE process) may also be due to the formation of cubic $HNbO_3$ which may be monitored by the broad absorption peak at $3250cm^{-1}$ [7.6,7.7]. Although this absorption band has been attributed to the presence of a new crystalline structure, $HNbO_3$, in lithium niobate samples exchanged in pure benzoic acid [7.7] the hypothesis cannot be strengthened by any of the other analytical methods described in this chapter (see section 7.5). Moreover the high concentration of hydrogen and the high distortion in the crystal lattice (see section 7.3) in the exchanged region suggest that not all hydrogen atoms are substitutional with Li atoms in the host lattice (see section 7.4) and that some of the hydrogen may be interstitial. As a consequence, the presence of two absorption bands with different shape and polarisation dependence may be due to the different lattice positions and bondings of H atoms present in the exchange layer.

7.3 Analysis by Rutherford Back Scattering

RBS analysis of proton exchanged waveguide layers was mainly carried out on X-cut and Z-cut lithium niobate wafers. Since RBS in the channeling mode measures the amount of misalignment in the exchanged region, especially of Nb because of its large atomic number, it gives an indication of exchanged layer depth and of the amount of lattice disruption.

Figures (7.5) and (7.6) show RBS channeling spectra taken on three X-cut and three Z-cut lithium niobate substrates exchanged for a constant time, 20 min, and at three different temperatures: 180°C, 200°C and 220°C. The aligned spectra clearly show a surface region with a slightly higher backscattering yield by comparison with the 'perfect' crystal lattice. By comparing the spectra of figures (7.5) and (7.6) the displacement of Nb atoms appears larger along the c-axis than the a-axis, i.e. the backscattering yield is much higher in X-cut crystals than in Z-cut crystals. The depth of the distorted layer clearly increases with increasing temperature when the exchange time is kept constant. For almost all samples the small peak present at the surface suggests a small amount of surface damage essentially due to mechano-chemical polishing of the sample and/or chemical reactions occurring at the sample surface during the exchange process [7.9,7.10,7.11].

In the random spectra the Nb yield does not show any variation going from the exchanged surface layer to the unperturbed substrate thus suggesting that the Nb concentration remains constant across the whole sample.

Figures (7.7) and (7.8) show similar RBS channeling spectra. In figure (7.7) for X-cut lithium niobate the prepared samples are exchanged isothermally (160°C) for 20 minutes, 1h and 3h. In figure (7.8) Z-cut lithium niobate is also exchanged isothermally (160°C) for 20 minutes, 1h, 2h and 3h. By comparing figures (7.7),(7.8) and (7.5),(7.6) the results are essentially the same. However, examining the spectra more closely, it appears that when the exchange time exceeds 1h, the lattice distortion appears to be considerably time dependent, with the disorder increasing with exchange time, and the lattice disorder appears to be relatively insensitive to exchange temperature for short exchange times.

Similar results have been obtained in samples exchanged at different temperatures and/or times and on Y-cut substrates when the thickness of the exchanged layer was smaller than 0.2μm (i.e.
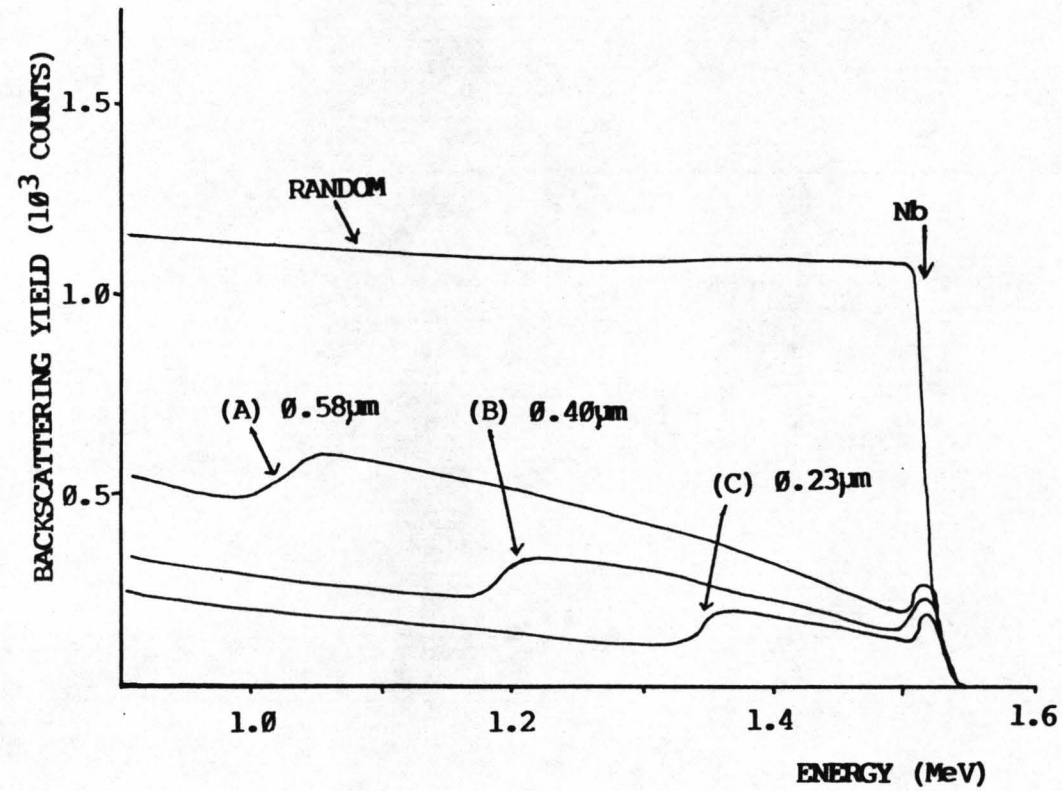
Figure (7.5): Channeling RBS Spectra on X-cut Lithium Niobate
Waveguides, Exchanged for 20 min. at Various
Temperatures (A) 220°C (B) 200°C (C) 180°C.
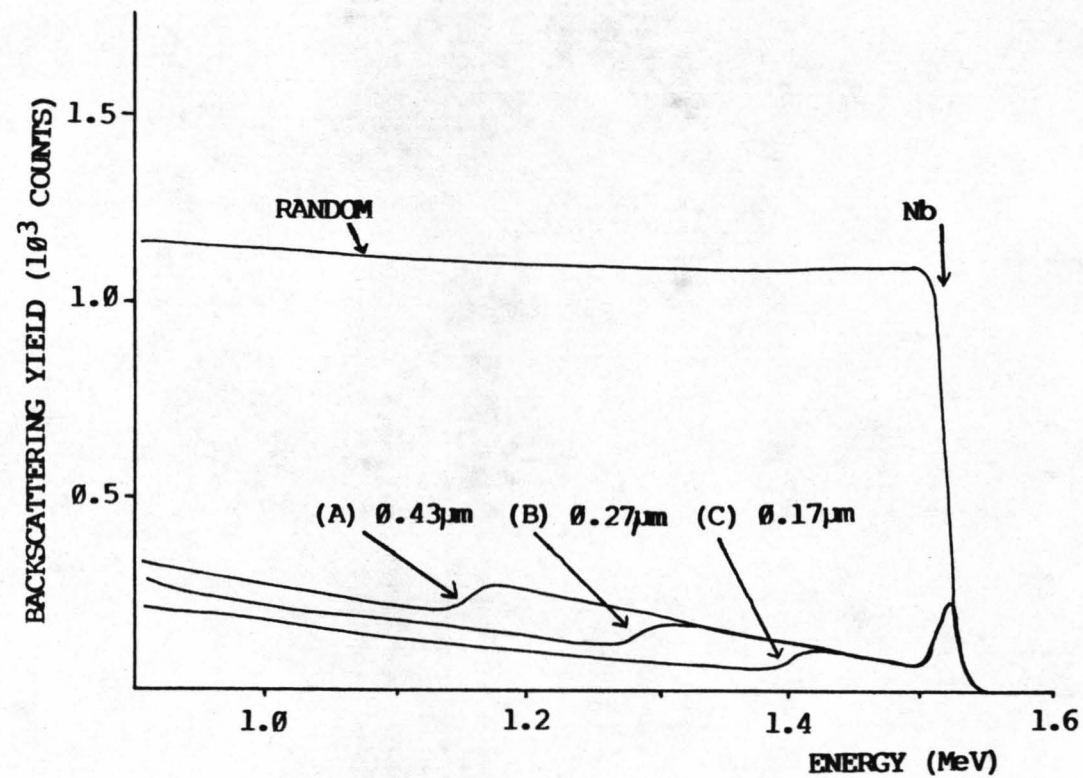
Figure (7.6): Channeling RBS Spectra on Z-cut Lithium Niobate
Waveguides, Exchanged for 20 min. at Various
Temperatures (A) 220°C (B) 200°C (C) 180°C.

Figure (7.7): Channeling RBS Spectra on X-cut Lithium Niobate Waveguides, Exchanged at 160°C for Various Times, (A) 3 hours (B) 1 hour (C) 20 minutes.
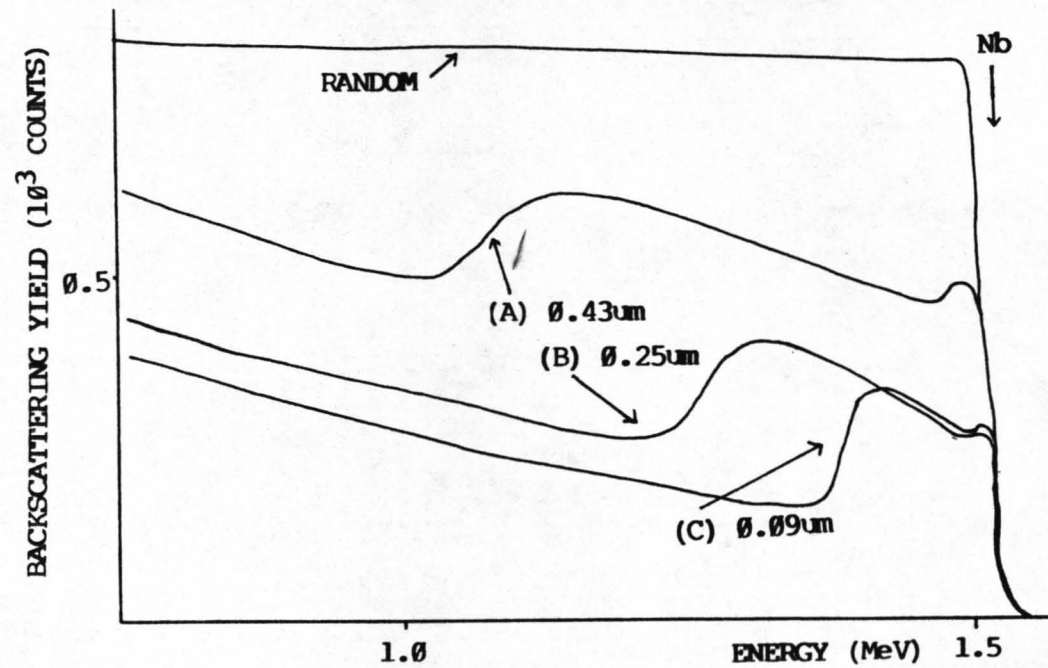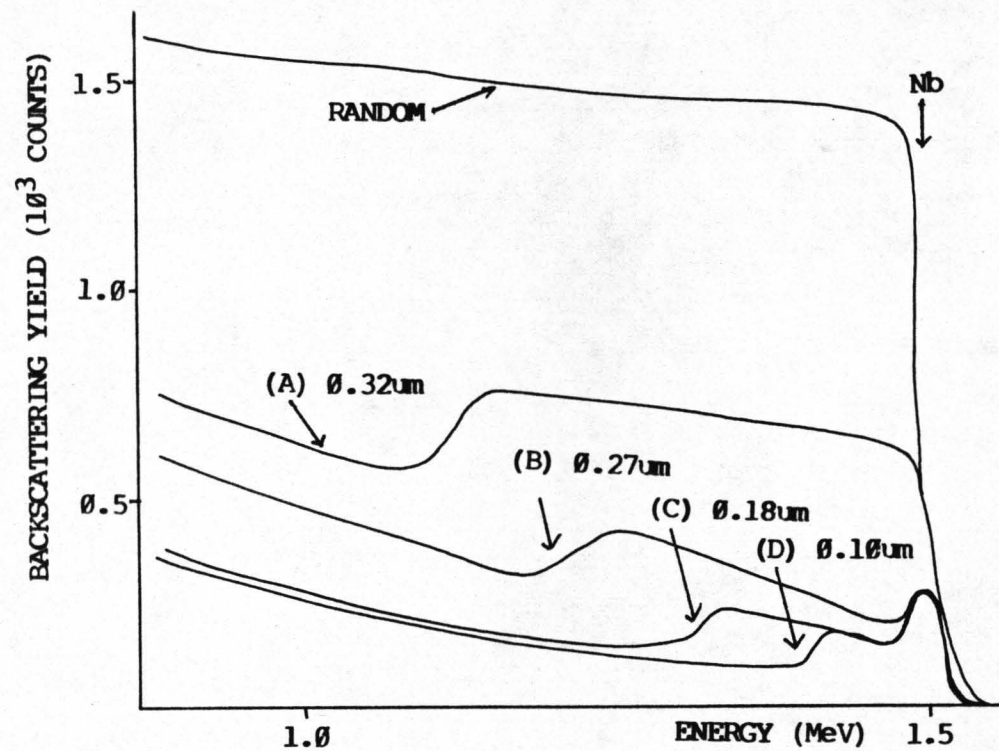
Figure (7.8): Channeling RBS Spectra on Z-cut Lithium Niobate
Waveguides, Exchanged at $160^\circ C$ for Various Times,
(A) 3 hours (B) 2 hours (C) 1 hour (D) 20 minutes.

limited by surface damage, see sections 7.5 and 7.6).

The thicknesses of the perturbed layers measured from the aligned RBS spectra as a function of the exchange time and temperature are shown in figures (7.9) and (7.10) for X-cut and Z-cut substrates repectively. In all cases the measured thicknesses exhibit a square root time dependence indicating, as in the optical analysis, that proton exchange in lithium niobate is a diffusion-limited process. The optical data for waveguide depth w.r.t. the exchange temperature and time are also plotted for comparison on the same figures. As shown on the figures there is good agreement between the depth estimates obtained from optical waveguide measurements and measurements of perturbed layer thicknesses obtained using the RBS technique on Z-cut and X-cut lithium niobate. At high temperatures (> 200°C) the optical estimates appeared to be slightly higher than the RBS estimated values.

As in chapter 5, the graphs plotted in figures (7.9) and (7.10) yield diffusion coefficients and if these values are plotted against inverse temperature, figure (7.11), the values of activation energy, Q, and diffusion constant, D_o, for an Arrhenius Law;

$$D(T) = D_o \exp[-Q/RT]$$

can be defined.

The values of the activation energy calculated from RBS data, approx. 94kJ/mol, are very similar for all crystal orientations (X,Y, and Z) and compare well with the optically estimated values. The main difference between diffusion rates in different crystal orientations is the diffusion constant, D_o. D_o appears larger for X-cut , $D_{ox} = 6.09 \times 10^9$ μm^2/h, than for Z-cut, $D_{oz} = 3.47 \times 10^9$ μm^2/h, with an intermediate value for Y-cut lithium niobate, $D_{oy} = 4.93 \times 10^9$ μm^2/h. Again optical values of D_o compare very favourably with RBS data. A comparison of D_o and Q can be seen in table 7.1.
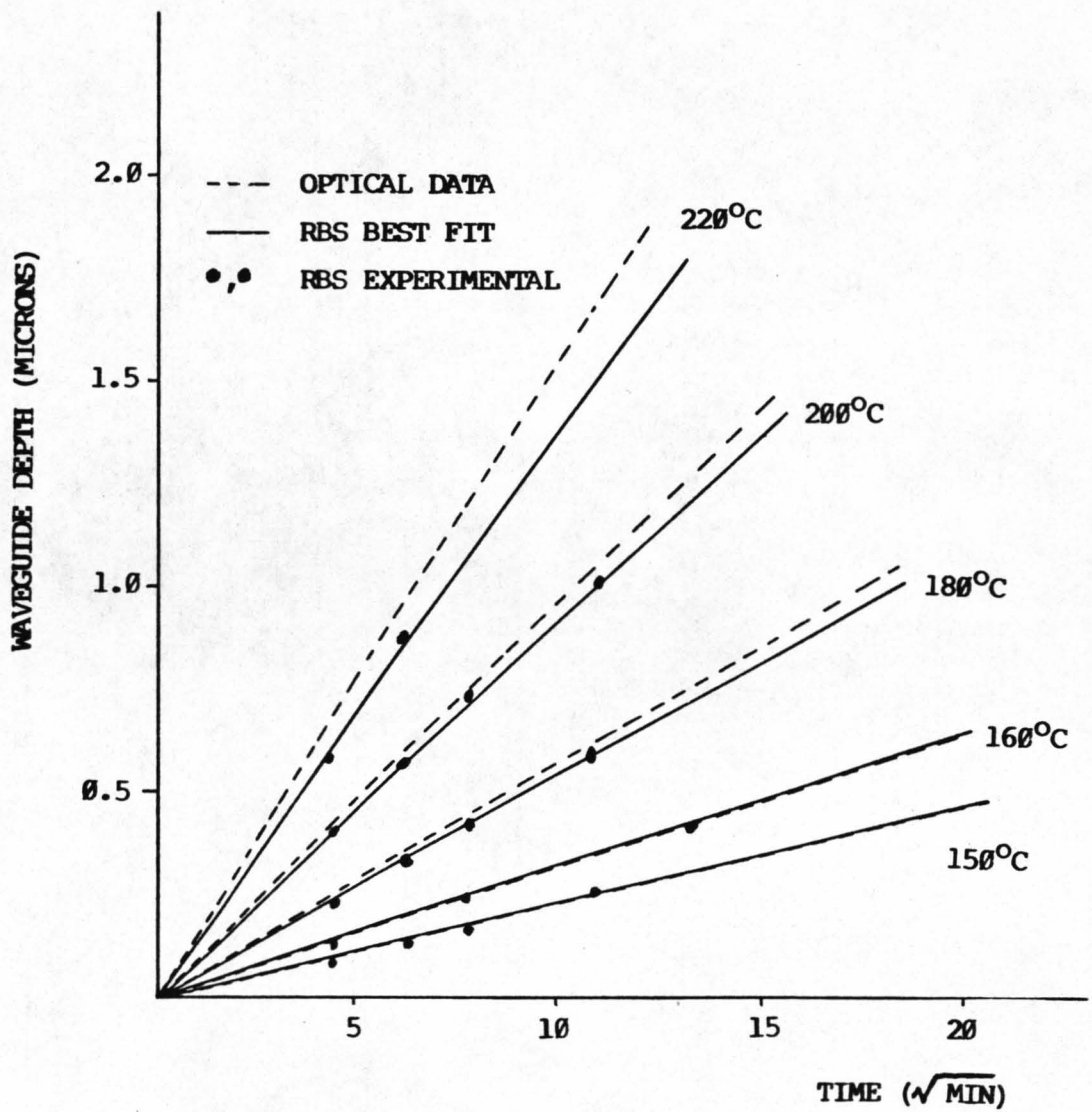
Figure (7.9): Plot of PE Waveguide Depth on X-cut Lithium Niobate vs. Root Exchange Time (for various temperatures). Depths Estimated by RBS and Optical Techniques.
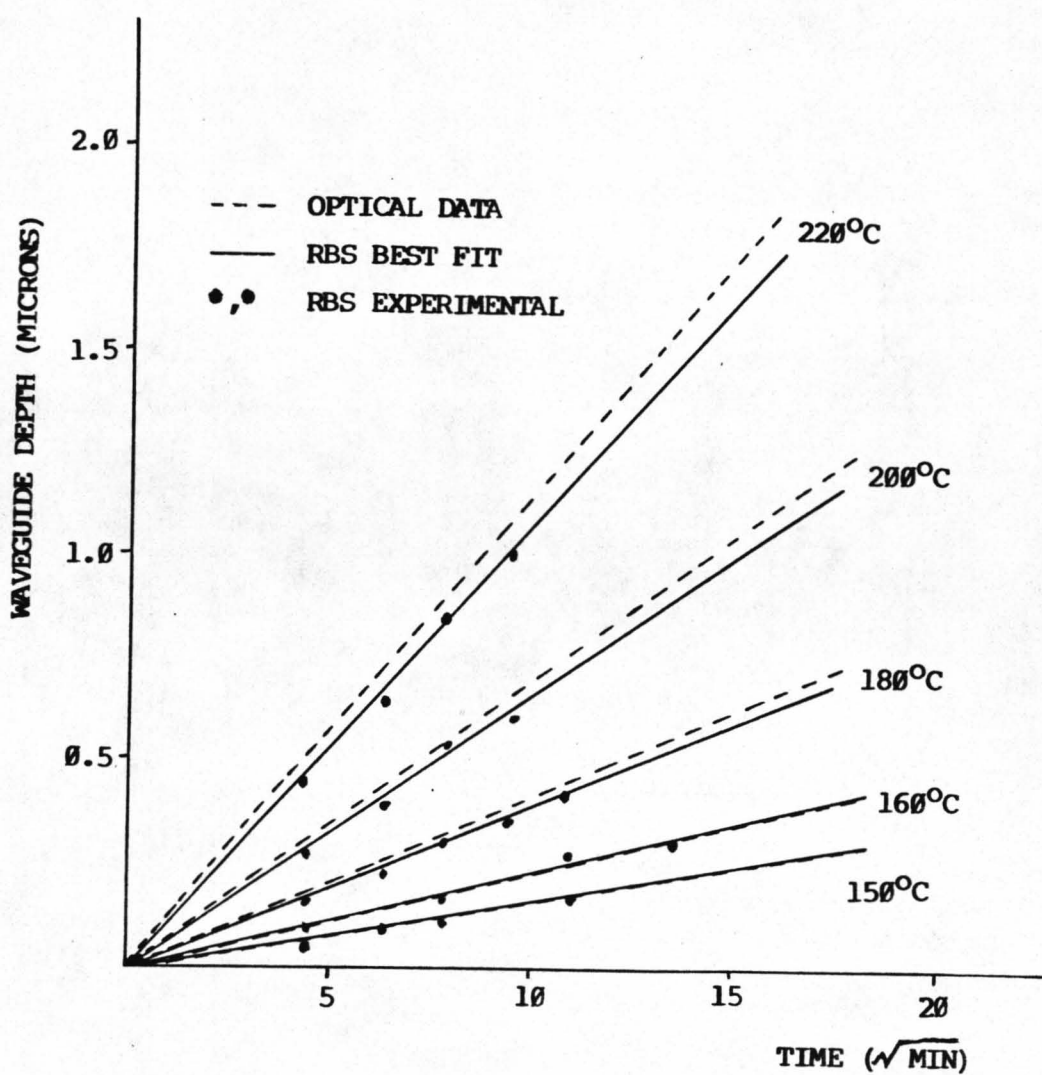
Figure (7.10): Plot of PE Waveguide Depth on Z-cut Lithium Niobate vs. Root Exchange Time (for various temperatures). Depths Estimated by RBS and Optical Techniques.
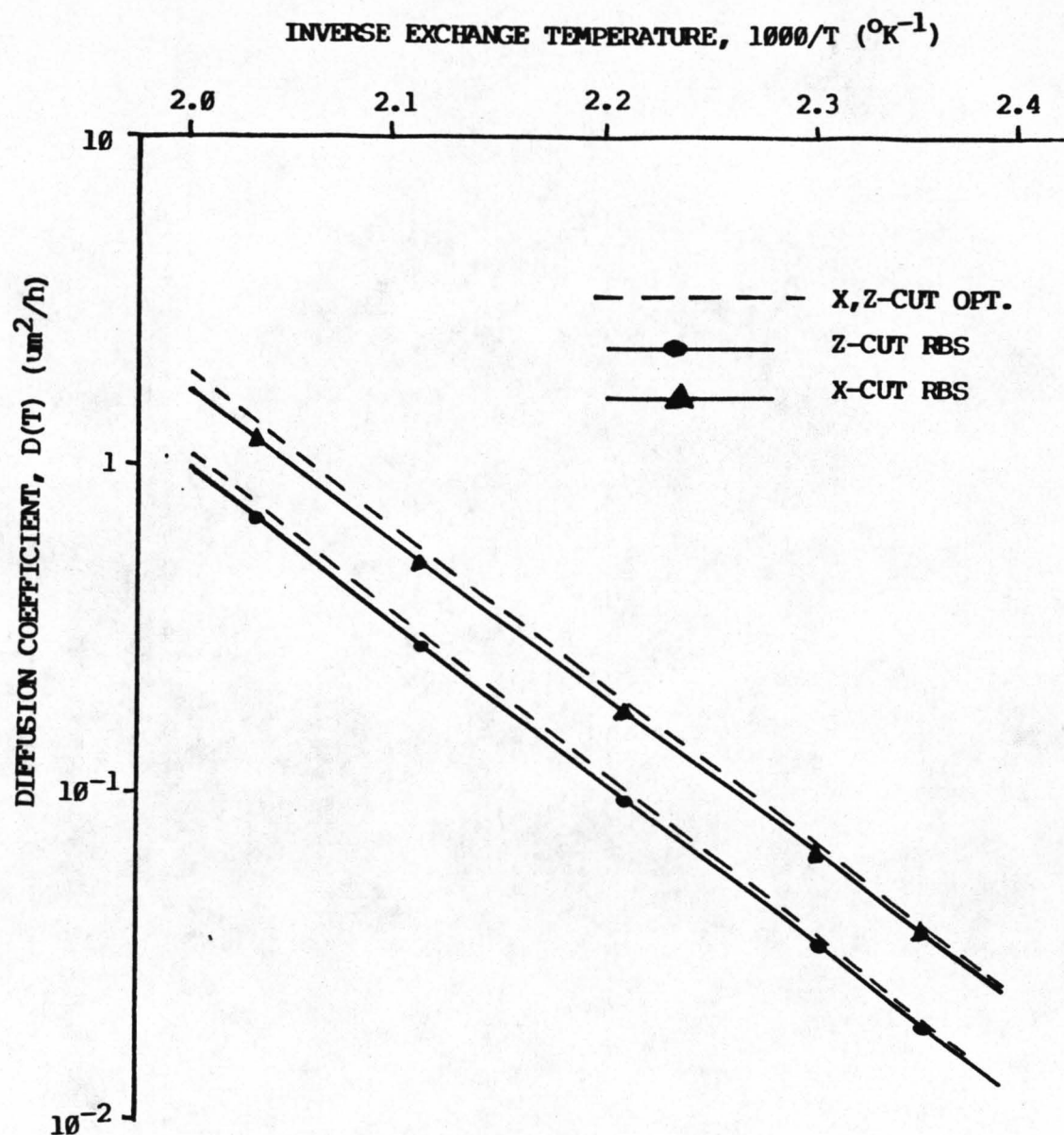
Figure (7.11): Plot of the Logarithm of Diffusion Coefficient
vs. Inverse Exchange Temperature. The Curves are
for X-cut and Z-cut Lithium Niobate and are
Estimated from RBS and Optical Data Obtained from
Figures (7.9) and (7.10).

TABLE 7.1

Comparison of Activation Energy and Diffusion Constant
for the Proton Exchange Process in Lithium Niobate

	OPTICAL	RBS
ACTIVATION ENERGY, Q (kJ/mol)	X-cut, 92.5	91.6
	Z-cut, 94.0	91.6
DIFFUSION CONSTANT, D_O ($\mu m^2/h$)	X-cut, 2.298×10^9	6.09×10^9
	Z-cut, 1.84×10^9	3.47×10^9

The information to be gained from the RBS data is very varied.
The PE process in lithium niobate disrupts the crystal lattice.
The disrupted area defines an area of different higher
anisotropic index change (as the optical and RBS data compare
very closely). In the disrupted region the displacement of
niobium atoms is greatest along the c-axis. The data has shown
that diffusion coefficients on Y-cut lithium niobate are smaller
than on X-cut lithium niobate and hence the severe surface damage
observed on Y-cut lithium niobate is not due to stress caused by
very high diffusion rates (see section 7.6). The RBS information
points to the possibility that the atomic strings of Nb along the
c-axis of lithium niobate misalign and that this misalignment
could play a part in the index change mechanism. The amount of
atomic misalignment (or interstitial ions?) increases for
increasing exchange time but not so obviously for increasing
exchange temperature if the exchange time is kept short (<1h).

7.4 Analysis by Nuclear Reactions

The NR measurements on lithium niobate were mainly carried out on
Z-cut lithium niobate, with a few measurements on X-cut lithium
niobate. The results are not as comprehensive as in RBS because
of the limited time available on the NR facility, and the much
greater operational difficulties.

Figure (7.12) shows the measured hydrogen profiles in Z-cut and
X-cut lithium niobate samples exchanged in pure benzoic acid at
two temperatures, 160°C and 180°C for several different times.
The data clearly shows a step-like hydrogen distribution with a
well defined plateau, where the resultant hydrogen concentration
is in the range 1.1 to 1.3×10^{22} cm^{-3} with, apparently, a small
dependence on exchange temperature and substrate crystallographic
orientation; the concentration is in fact slightly higher for X-
cut material. The resolution of the analysis is, as previously
mentioned, 5×10^{19} cm^{-3} and therefore the small changes in
concentration mentioned above are well within the resolution of
the process and are therefore true values. The depth of the
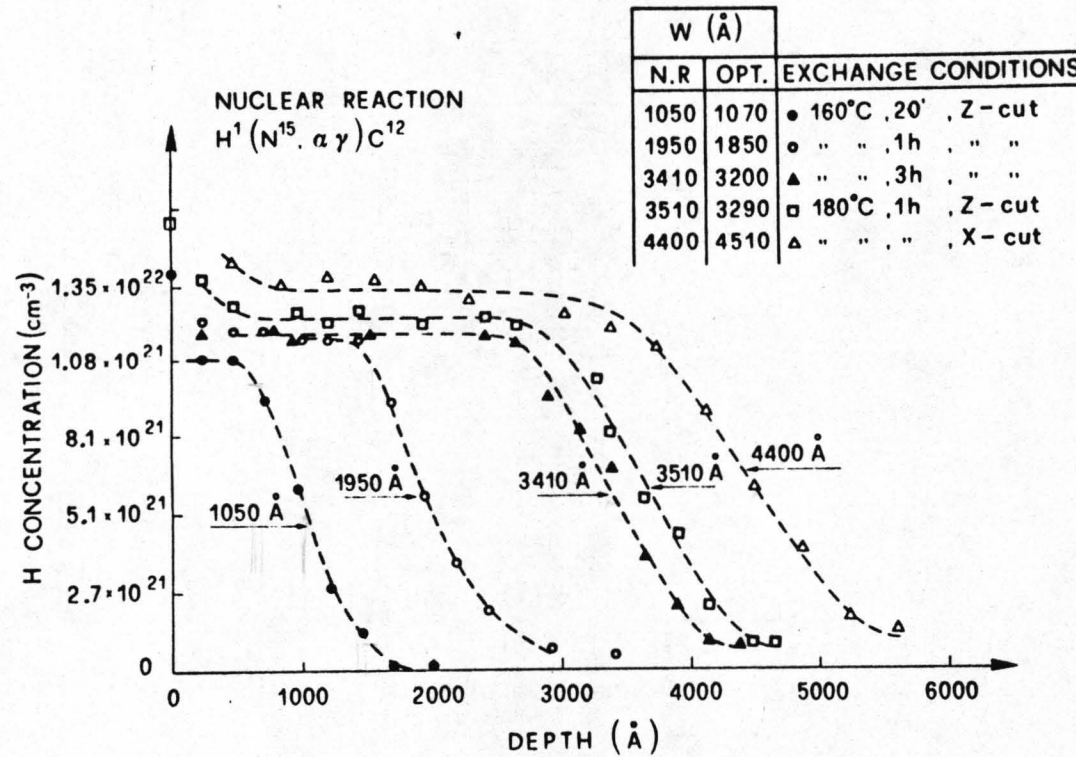
Figure (7.12): Measured Hydrogen Profiles on X-cut and Z-cut
Lithium Niobate Samples Exchanged in Pure Benzoic
Acid at two Temperatures and Different Times.
The Inserted Table Compares NR and Optical Depth
Measurements.

hydrogen profile was taken to be the full-width-half-maximum point on the profile curve. The depths of the exchanged regions measured by NR always agree closely with RBS data. The disorder in the exchange layer is, therefore, clearly related to the presence of protons in the lattice. In comparison with the optically estimated depth of the waveguide, good agreement is found in both X-cut and Z-cut samples.

The maximum depth to which this technique can be employed is in the order of $0.8\mu m$, greater depths cause substrate annealing (ion migration) because of the increase in beam energy required.

The above information alone could point to the index mechanism being controlled by the presence of protons in the lattice. However, as discussed previously, the index change mechanism, having much in common with outdiffused waveguides [7.12,7.13], is more likely to be controlled by the amount of Li atoms in the crystal, with the protons possibly lowering the activation temperature for the Li outdiffusion from $1000^{o}C$ to $200^{o}C$.

It order to give some weight to this hypothesis it was necessary to measure the lithium concentration in the exchange layer. In the PE process, if it can be assumed to be an ion exchange process, the amount of the two exchanging ions, Li^{+} and H^{+} in this case, should be equal. As a consequence, from the measured concentration of H in the exchanged layer, it would be expected that about 65% - 75% of the original Li atoms present in the lithium niobate lattice have been exchanged or substituted by protons. To determine the amount of lithium ions in the exchanged region a second NR was employed, caused by proton bombardment (see chapter 6). Figure (7.13) shows the alpha particle rates from Li atoms in a virgin sample and in an X-cut substrate exchanged at $220^{o}C$ for 1 hour. The shape of the alpha particle signal produced by Li atoms in the exchanged sample clearly indicates that this sample exhibits a surface layer partially depleted of Li atoms. The thickness of the exchanged layer was estimated to be approximately 1.0 μm, in agreement with RBS data and moreover the concentration of Li atoms is about 30%
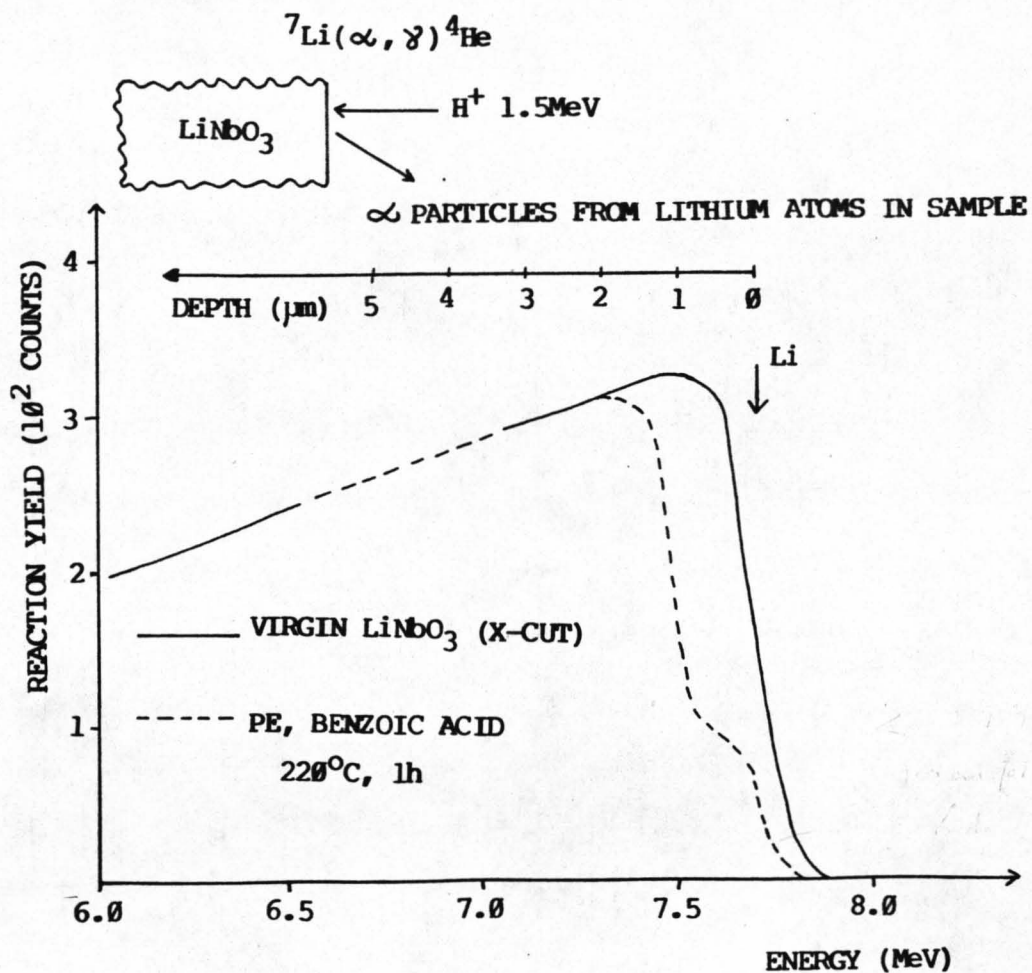
Figure (7.13): α Particles Signal from $^7Li(\alpha, \gamma)^4He$ Nuclear Reaction Obtained on a Virgin X-cut $LiNbO_3$ Sample and on one Exchanged in Pure Benzoic Acid at $220°C$ for 1 hour.

of the original Li concentration of the bulk sample. This 70% lithium depletion of the exchanged layer is in broad agreement with the hydrogen profile measurements which point to the process effectively being an ion exchange process and this supports the theory that the index change is caused by lithium depletion in the exchanged layer.

7.5 An X-Ray Diffractometry Analysis of PE LiNbO$_3$

Few people have attempted full X-ray analysis of the complex proton exchanged lithium niobate structure. Yi-Yan [7.14] measured the effects of phase modification during the waveguide relaxation period and directly related his measurements to instabilities that he previously measured [7.15] but that other authors to some extent have failed to corroborate (see chapter 5). The measurements discussed in this section are of a very basic nature but give information on structural modifications caused by the proton exchange process.

Figure (7.14) shows double crystal X-ray diffraction (DXD), (220) rocking curves, taken on X-cut lithium niobate samples, for a constant exchange time (40 minutes) at four different temperatures exchanged in pure benzoic acid. The presence of satellite peaks, at a negative deviation, $\Delta\Theta$, from the Bragg angle relative to that for the unperturbed substrate, indicates that the exchanged layer exhibits a positive strain. Therefore the strain normal to the surface is defined thus, $\Delta a/a > 0$. The shape and position of the satellite peaks remain the same with increasing exchange temperature. Furthermore, as can be seen in figure (7.14), their intensity increases linearly as a function of exchanged layer thickness. A qualitative estimate of the strain observed in figure (7.14) was 0.8% [7.10].

Positive strains perpendicular to the surface have been observed in Z-cut and Y-cut lithium niobate proton-exchanged substrates. In particular, strains as large as 1.6% have been observed in exchanged Y-cut substrates. Further X-ray information is shown in
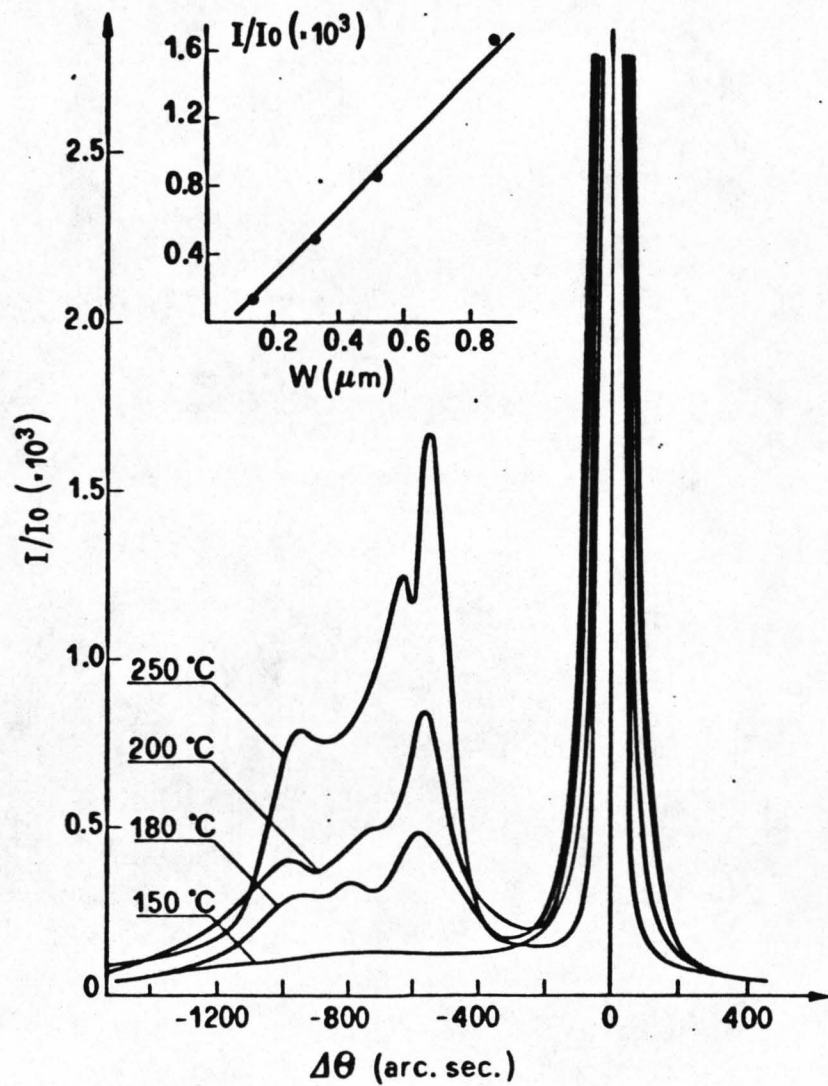
Figure (7.14): Double Crystal X-Ray Diffraction (22Ø) Rocking Curves Obtained on X-cut Samples Exchanged for 4Ø min at Different Temperatures. The Insert shows the Dependence of the Satellite Peak Amplitude on the Thickness of the Exchanged Layer, W.

section 7.6 since it has special relevance in that section. The range of strains observed in the proton exchanged layer are highly complex thus deductions obtained are by their nature qualitative without an accurate computer model (which was not avialable).

Exchanged samples were also measured using a Wallace-Ward cylindrical texture camera. Diffraction patterns confirm the presence of large strains in the exchanged layer but do not reveal the presence of any new phase (Yi-Yan also confirms this [7.15]), such as cubic perovskite, $HNbO_3$, observed in proton exchanged lithium niobate powders [7.7].

7.6 Analysis of Surface Damage

Surface damage on Y-cut lithium niobate, first noticed by Jackel et al. and discussed in more detail by Goodwin et al. [7.16,7.17] has been observed when lithium niobate is immersed in benzoic acid. The literature has concentrated on surface damage on Y-cut lithium niobate as any such effects on X-cut or Z-cut lithium niobate waveguides were not evident at that time. This section discusses the onset of surface damage on each crystal orientation and discusses the effect particularly on Y-cut substrates.

Observations on a phase contrast microscope reveal that before stress relieving cracks occur the crystal surface, on either crystal orientation, exhibits an index perturbation not unlike an index grating. Figure (7.15) a) shows such an effect on X-cut lithium niobate exchanged at 210°C for 5 hours. The lines of the perturbed index grating coincide with the eventual position and direction of the cracks. Figure (7.15) b) shows the damage caused to the exchanged surface layer after cracking occurs in Y-cut lithium niobate. Note that the surface peeling effect appears to be limited to one consistent depth. The direction of the cracks in Y-cut lithium niobate is along the a-axis, and the direction of the cracks on X-cut and Z-cut lithium niobate is along the Y-axis.
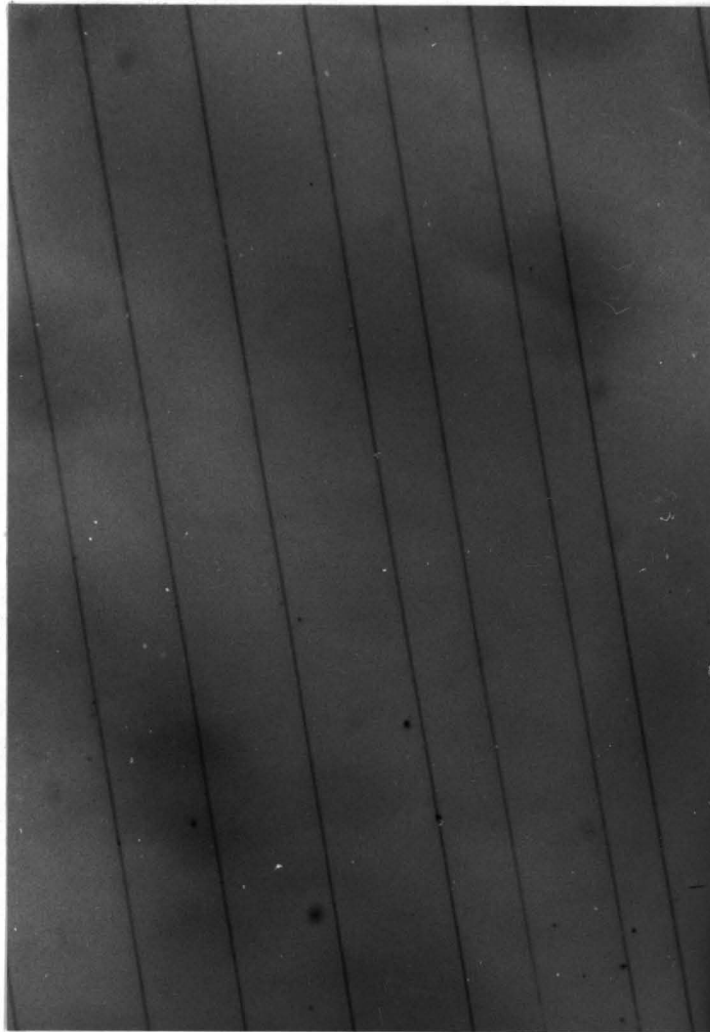
Figure (7.15): a) Photograph Taken from a Phase Contrast Micro-Scope Depicting a Stress Induced Grating Observable before the Onset of Surface Damage. X-cut Lithium Niobate Sample Exchanged at 220°C for 5 hours.

Figure (7.15): b) Scanning Electron Micrograph of Surface Damage
on Y-cut Lithium Niobate Exchanged at 180°C
for 2 hours. (although damage occurs after 20 min)
10 Micron Markers.

As previously mentioned, surface damage is only observed if the exchange process is allowed to proceed for more than a certain time and temperature. Since an optical analysis of PE waveguides on Y-cut lithium niobate was not possible (due to the limited number of available modes) RBS measurements in the aligned condition reveal the thickness of the exchanged layer (as in section 7.3). Results, from observations obtained with an S.E.M. and with RBS techniques, show that PE waveguides on Y-cut lithium niobate appear free from surface damage when the exchanged layer is shallower than about 0.2µm. Figure (7.16) shows the variation in waveguide depth with the exchange time for three different temperatures: the $t^{1/2}$ dependence of the layer thickness is in accordance with similar measurements on X-cut and Z-cut lithium niobate. On X-cut and Z-cut lithium niobate the onset of surface damage occurs at an exchanged-layer depth which makes the waveguides highly multimode at 633nm wavelength. This was one reason that the effect was not noticed on X-cut and Z-cut lithium niobate. X-cut and Z-cut lithium niobate PE waveguides formed to a depth greater than 3µm will exhibit surface damage and although this does not pose a problem for devices and components formed at a wavelength of 0.633µm, at longer wavelengths, such as 1.3µm, the maximum waveguide depth of less than 3µm will prove to be a limitation.

Looking particularly at surface damage on PE waveguides on Y-cut lithium niobate investigations using X-ray analysis techniques the following results were obtained.

Figure (7.17) shows DXD (030) rocking curves taken on three Y-cut samples exchanged at 180°C for three different times: 10, 20, and 40 minutes. One can see from the presence of satellite peaks at negative, $\Delta\theta$, deviations from the Bragg angle relative to the unperturbed substrate, that the exchanged layer exhibits a positive strain $\Delta a/a$, as is well known to occur also for analogous treatment of X-cut and Z-cut lithium niobate crystals (see above).

DXD Rocking Curves give information on the various strains in the
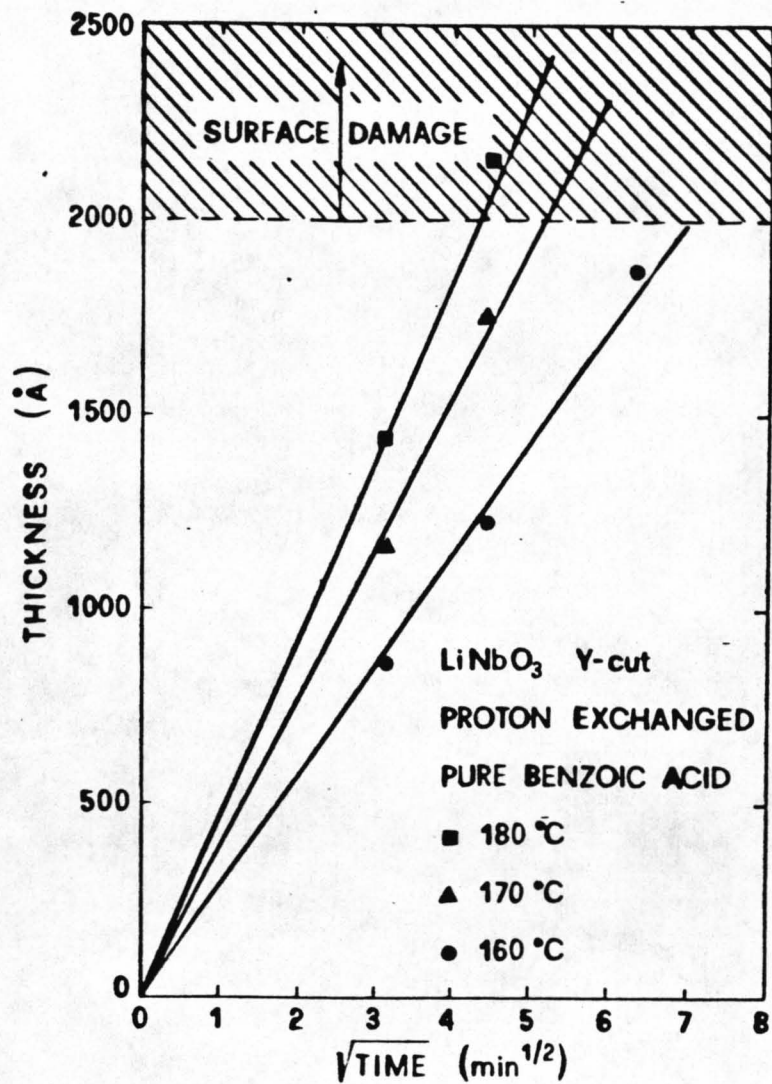
Figure (7.16): Thickness of Exchanged Layers Measures on Y-cut
Lithium Niobate Substrates (RBS Technique) as a
Function of Exchange Time and Temperature. The
Figure Shows the Area Where Surface Damage Occurs.
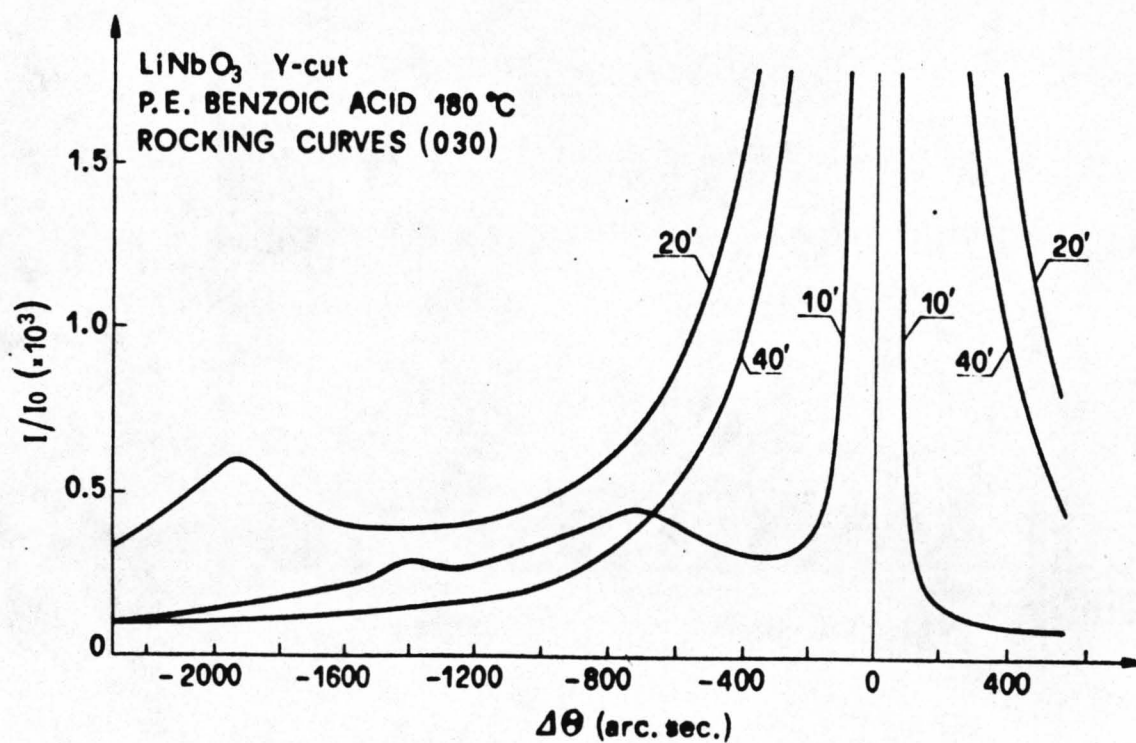
Figure (7.17): Double Crystal X-Ray Diffraction (030) Rocking Curves of Various Y-cut PE Samples Exchanged at 180°C for Various Times.

exchanged region. However, the technique gives no information on the distribution of the strain throughout the exchanged region, i.e. if a high strain peak is at the surface or the base of a perturbed region. Theoretical simulations of the experimental rocking curves are necessary to succeed in this objective. Although a simulation was not available, with careful inspection of the curves shown in figure (7.17), it was possible to make a qualitative estimation of where the lattice strains might have occurred [7.18,7.11].

Remembering that proton exchange is a diffusion limited process from an extended source, the surface proton concentration in the samples should be the same as that of the exchange melt at a given temperature. The strain value at the surface should therefore be the same for all samples in figure (7.17). The observed increase of the satellite peak shift, on-going from 10 to 20 minutes exchange time, indicates that for short exchange times the strain distribution does not reach a step-like profile. In fact the presence of an intensity bump at -1400 arcsec and a broad, but more intense, satellite peak at -700 arcsec indicates that the strain is highest in a thin surface layer and that the strain reduces depthwise into the substrate (from the small -1400 arcsec peak) and combined with this there is a thicker region of less rapidly varying lattice parameter, a_o (from the larger broad -700 arcsec peak). The strain therefore has a high surface value, a central fairly constant strain region and a tail of decreasing strain extending into the substrate. When the exchange time increases, the strain profile appears to form a constant high strain step profile with fewer strain variations over the exchanged region. These characteristics are directly related to the further increase of $\Delta\theta$ separation of the satellite peak and its narrower width in the case of the sample exchanged for 20 minutes. After 40 minutes exchange time, the disappearance of the satellite peak suggests that the large lattice strain has been compensated for, and inspection of the sample indicates that surface cracks have alleviated the lattice strain.

With a combination of X-ray analysis techniques the strain on the

c-axis was also determined [7.18]. Contrary to Yi-Yan [7.15], who quotes lattice strains $\Delta a/a$ = 0.75 % and $\Delta c/c$ = 0.43 %, results[!] indicate the the true lattice strains are $\Delta a/a$ = 1.58 % and $\Delta c/c$ = 0.0 %. Therefore the heavy strain found in the proton exchange lattice, on Y-cut lithium niobate is concentrated exclusively in the a_O lattice parameter (a_O = 5.230A against a normal value of a_O = 5.149A while the c-axis remains practically unchanged (c_O = 13.86 $\pm$ 0.02A).

The reason as to why the surface damage effect is so severe on Y-cut lithium niobate has, as yet, not been determined. The answer is almost certainly linked with the dependence of the elastic properties of lithium niobate on crystal orientation [7.26,7.27,7.4].

7.7 Investigation of Lithium Content by the Examination of Post Exchange Melts

To determine the amount of lithium leaking from the crystal during the PE process the experimental procedure of section 6.6 was adopted. Although the technique is not as elegant as the NR estimation lithium depletion in the exchanged layer, it was assumed that the technique would give similar results.

The first set of samples were $1cm^2$ pieces of Z-cut lithium niobate (polished on both sides). The exchange temperature was 180.5^{O}C and the exchange times were 10 mins, 1/2 h, 1 h, and 2 hrs. A computer programme calculated the total exchanged volume using the Z-cut diffusion coefficient and the X-cut diffusion coefficient (the diffusion coefficient in the Y direction was assumed to be the same as that of the X direction). From the calculated volume the total amount of lithium in the exchanged

---

[!] Results obtained from measurements made by M. Servidori, CNR Bologna, Italy to be published [7.18] to which the author of the thesis has contributed.

Figure (7.18): Plot of the Theoretical and Experimental Li ppm in the Post-Exchanged Melt Obtained from Flame Emission Spectroscopy vs. Exchange Time. Z-cut Lithium Niobate Samples Exchange at 180.5°C for Different Times.

layer was calculated and assumed to be present in the melt. From this information the theoretical fraction of Li in the acid was calculated.

Figure (7.18) shows a plot of the calculated lithium concentration in the acid versus the square root of the exchange time. Superimposed onto the graph is the experimental Li concentration in the exchange melt, measured by flame emission. From the graph it is obvious that the calculated Li ppm in the exchange melt is linear with root time (the calculated concentration is a function of exchanged layer depth). The experimentally measured Li ppm in the exchange melt is not linear and far greater than would be expected even from a total exchange process (NR measurements point to a 70% exchange). Figure (7.18) shows that for very short exchange times both sets of data are in close agreement but as the exchange time increases the experimental values of concentration increase much more rapidly. The results therefore appear to indicate that much more Li outdiffuses than is present in the exchange layer, which may mean that lithium is leaking also from the bulk substrate through the exchange layer and into the melt.

The concentration range for the set of samples was small, less than 3ppm, so for consistency the experiment was repeated by A. Loni. This time the exchange temperature was 210°C and the exchange times were 37 minutes, 4 hrs and 5hrs. The higher temperature and longer exchange times ensured a much higher ppm of lithium in the exchange melt with the intention of making the results more accurate. The results are plotted in figure (7.19) and obtained from atomic absorption spectroscopy. As can be seen from the graph the results follow exactly the same trend as in figure (7.18).

One possibility was that although the two main faces of the sample were polished there were still four edges which were rough and therefore a) could contribute a higher than estimated surface area and b) since the Y edge is prone to surface damage the peeling effect combined with the rough surface may contribute to
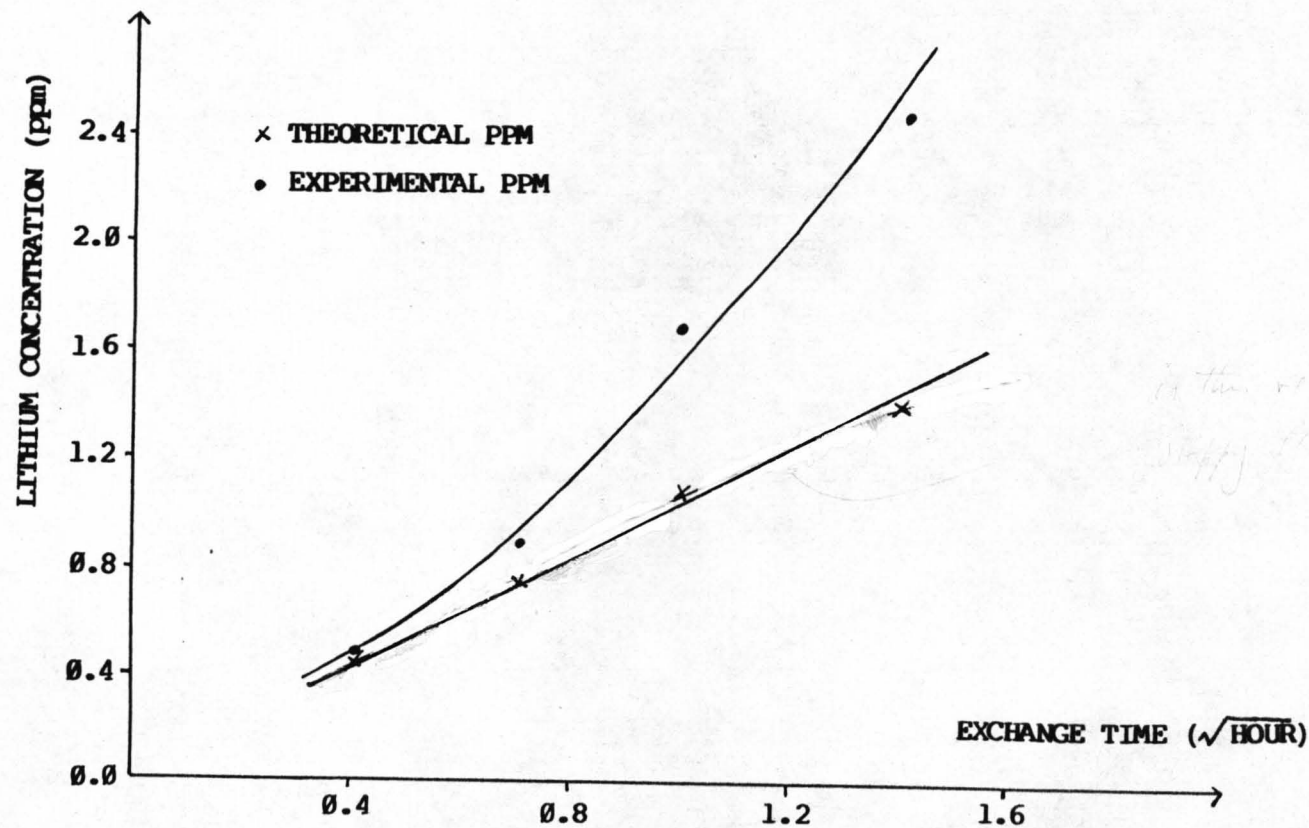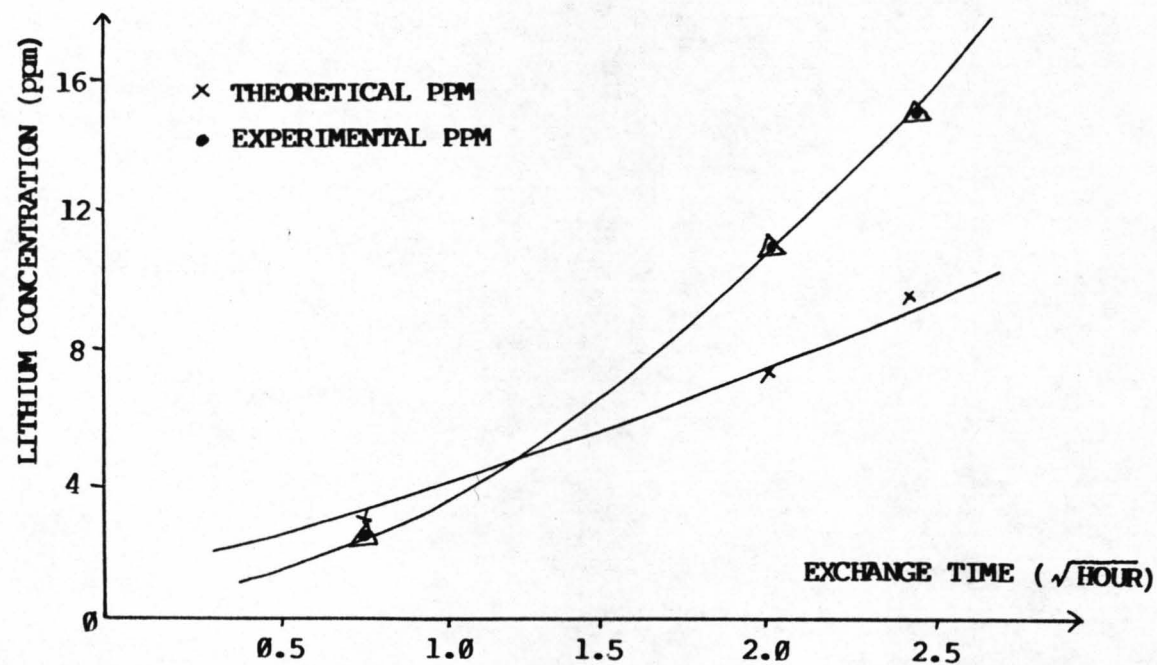
Figure (7.19): Plot of the Theoretical and Experimental Li ppm
in the Post-Exchanged Melt Obtained from Atomic
Absorption Spectroscopy vs. Exchange Time.
Z-cut Lithium Niobate Samples Exchanged at 210°C
for Different Times.
△- Data From Samples Polished on all Sides

a greater than estimated amount of lithium leaching to the acid. To combat this samples were prepared with both faces and all edges polished. The experimental conditions were the same as above, i.e. $210^{\circ}C$ for various exchange times. The results are superimposed on figure (7.19).

It can be seen from the results plotted on figure (7.19) that there is no appreciable change in the measured lithium concentration when the samples are polished on all sides. The results appear to be consistent, therefore there must be an extra source of lithium, not accounted for in the exchange layer. As the experiments were carried out in the strictest of conditions it is assumed that the excess lithium must have been taken from the bulk crystal. It is estimated that about 0.1% of the lithium in the central bulk area of the crystal would have to leak into the melt to cause the non-linear effect. Such a small percentage loss of lithum in the bulk crystal may not be detected by any of the analysis techniques used.

7.9 Conclusions

In this chapter an attempt has been made to analyse the proton exchange process.

Several questions need to be answered about the lattice effects and the index change mechanism. As mentioned in chapter 6, it is probable that the index change mechanism is due to the outdiffusion of lithium from the bulk crystal. The index profile for the PE process can be assumed a step and indeed the proton concentration profile is as much like a step as a diffusion limited process could be. Essentially the same value of exchanged layer depth (in the form of a step) was obtained whether it was estimated by NR, RBS or Optical techniques. The abrupt proton step profile is somewhat of an anomaly however since there is an extremely sharp proton concentration gradient between the exchanged layer and the bulk substrate. It may well be that protons can be considered an extremely mobile ion and the

question that must be posed is why don't protons diffuse into the bulk crystal? Protons are bonded to oxygen atoms in the lattice, however these bonds are OH⁻ and weak hydrogen bonds and should allow the protons to move from their bonding site to an adjacent oxygen atom at room temperature (movement of protons is possible at slightly elevated temperatures, see chapter 8). The step-like profile suggests that there is possibly either some form of reverse electric field attracting the protons to the surface an effect similar to ones noticed with silver ion exchange in glass [7.35] or that a non-linear, depth and concentration dependent diffusion coefficient could account for the proton profile (more work needs to be done to corroborate this hypothesis).

Jackel has suggested the presence of a non-linear or depth dependent diffusion coefficient [7.28] in the proton exchange process. Work in that paper was based on the assumption that deuterated PE waveguides are comparable with pure PE waveguides. This assumption is not rash as deuterium and protons are chemically equivalent (although deuterium is a bigger ion). The paper however based its analysis on experimental information which researchers at the University of Glasgow found to be unrepeatable[!]. A large part of the papers argument was based on the fact that the deuterium profile was not like a step (and hence neither was the proton profile). Our NR measurements have shown the H^+ profile to be very like a step, which is in complete contradiction to Jackel's assumption. The paper also related the index change to the presence of deuterium, when it is obvious that since PE waveguides can be made in many ways the mechanism is lithium depletion, admittedly in my opinion. The non-linear diffusion coefficient was based upon the deuterium profile and therefore although the idea may have been correct the theory was based on debatable experimental results.

[!]Discussions with Dr. J. Winfield of the Chemistry Dept. and A. Loni of the Dept. E.&E.E., University of Glasgow are acknowledged.

One factor which must be considered in Jackel's work is the NR technique she used [7.29];

$$D + {}^{3}He \rightarrow p + \alpha, \quad Q = 18.352 \text{ MeV}$$
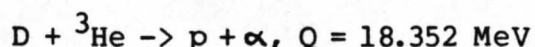
On each atomic collision the resultant species is a proton, an alpha particle and a lot of energy. The amount of energy released on each collision is 18.352 MeV which means that the reaction is highly exothermic (as mentioned by Jackel [7.28]). One can only surmise that there is a strong possibility that the measurement technique is annealing and altering the waveguide structure as it is being measured.

A non-linear effect related to the excess amounts of lithium lost from the substrate (more than is present in the exchanged layer) was measured. A similar effect was noticed in the formation of out-diffused waveguides in lithium niobate [7.12,7.13]. An attempt was made to compare the weight loss occurring during the outdiffusion process to the calculated amount of LiO_2 that should theoretically leak from the crystal. Curiously a much greater weight loss was measured than was calculated [7.12,7.13], which appeared to indicate that either much more LiO_2 was leaving the crystal than was expected (similar to our findings) or that some other factors (such as the loss of niobium) contributed to the weight loss. In the measurements discussed in section 7.8, the excess lithium must come from the bulk substrate, however there is no indication of any change in the bulk substrate directly next to the step-like exchanged layer probably because, as previously mentioned, any effect in the bulk lattice would be very small. Comparing the index anisotropy in both forms of waveguide and the weight loss effects there may be a common factor. The comparison is limited since the formation of outdiffused waveguides is a high temperature process and the formation of PE waveguides is a relatively low temperature process.

The structural changes which occurred in the exchanged layer were analysed in some detail and the measurements from the different

processes are outlined below:

Although there is no evidence which indicates the formation of a new phase in the exchanged layer, there is considerable stress, as high as 1.6%, and this is mainly unidirectional. It has been shown with NR measurements that approximately 70% of the Li in the exchanged region exchanges for protons from the pure benzoic acid. At the moment there is no proof that the exchange process is a pure 'one for one' exchange process. It is possible that the more weakly hydrogen bonded protons are interstitially positioned in the lattice. The OH^- bonds are, in the main, perpendicular to the c-axis, which is the same as the direction of strain in the lattice, resulting in a negative crystallographic index change. The strain is positive which indicates lattice parameter expansion in the a-axis. There is no alteration in the c-axis dimensions compared to the bulk crystal, measurable by X-ray techniques. However RBS data indicates that there is misalignment of Nb atoms in their atomic strings parallel to the c-axis. This misalignment would have to be of a zig-zag form to maintain inter-atom spacing along the c-axis, which indicates movement of lattice planes perpendicular to the c-axis. The amount of lattice distortion appears to be dependent upon exchange time and relatively independent of exchange temperature for short exchange times.

It has been shown that PE induced surface damage can be avoided by titanium pre-diffusion [7.19,7.17]. It is known that Ti-indiffusion causes a negative strain ($\Delta a/a < 0$), which depends on the titanium concentration and ranges from 10^{-3} to 10^{-2} in Ti-diffused waveguides [7.20,7.21,7.22]. Damage is apparently prevented by some form of compensation between the two opposite induced strains. This hypothesis is strengthened by the fact that damage appears if the concentration of Ti in the TIPE layer is reduced [7.19], and obviously, if the thickness of the exchanged layer exceeds the thickness of the Ti-diffused layer [7.18]. Similar effects can be obtained by lowering the proton concentration either by using a dilute exchange melt or by annealing the waveguide before the formation of cracks otherwise

needed to alleviate the stress in the exchanged layer
[7.23,7.24,7.25].

The high stress and disorder in the waveguiding region must be related to the poor quality of the optical waveguides fabricated.

The inherent difficulties encountered with proton exchanged waveguides, such as the D.C. effect [7.30,7.15], suggest that the waveguides have serious stability problems. These problems are likely to be related to the proton concentration since a reduction in proton concentration gives less lossy and more stable waveguides [7.31,7.32,7.33]. It is possible, therefore, that the weakly hydrogen bonded protons are the main cause of undesirable effects observed, since they appear to cause the complex strain patterns in the exchanged layer (this will be discussed in more detail in chapter 8). The presence of protons in lithium niobate is not always to the detriment of the optical properties, however, as they greatly reduce optically induced inhomogeneities in the crystal [7.34].

This chapter has to some extent outlined materials aspects of PE waveguides. However in order to gain a more complete picture of the process and the effects of hydrogen in the lattice, a similar series of experiments would have to be attempted on post-annealed PE waveguides. Chapter 8 deals with this analysis and attempts to discuss the many questions that have arisen from the measurements obtained above.

CHAPTER 7 - REFERENCES

[7.1]   J.L. Jackel and C.E. Rice
          Topotactic $LiNbO_3$ to Cubic Perovskite Structural
          Transformation in $LiNbO_3$ and $LiTaO_3$
          Ferroelectrics, vol 38, pp801-804, 1981

[7.2]   J.L. Jackel and C.E. Rice
          Short- and Long-Term Stability in Proton Exchanged
          Lithium Niobate Waveguides
          S.P.I.E., vol 460, Processing of Guided Wave
          Optoelectronic Materials, 1984.

[7.3]   J.L. Jackel and C.E. Rice
          Variation in Waveguides Fabricated by Immersion of
          $LiNbO_3$ in $AgNO_3$ and $TlNO_3$: The Role of Hydrogen
          Appl. Phys. Lett., vol 41, No.6, pp508-510, Sept. 1982

[7.4]   A. Rauber
          Chemistry and Physics of Lithium Niobate
          Current Topics in Materials Science, vol 1, Ch7
          Edited by F. Kaldis, 1978

[7.5]   J.R. Herrington et al.
          An Optical Study of the Stretching Absorption Near 3
          Microns from OH^- Defects in $LiNbO_3$
          Solid State Comm., vol 12, pp351-355, 1973

[7.6]   C.E. Rice and J.L.Jackel
          Structural Changes with Composition and Temperature in
          Rhombohedral $Li_{1-x}H_xNbO_3$
          Mat. Res. Bull., vol 19, pp591-597, 1984

[7.7]   C.E. Rice and J.L. Jackel
          $HNbO_3$ and $HTaO_3$: New Cubic Perovskites from $LiNbO_3$ and
          $LiTaO_3$ via Ion Exchange
          J. Solid State Chem., vol 41, pp308-312, 1982

[7.8]   K.K. Wong, A.C.G. Nutt, D.F. Clark et al.
        Characterisation of Proton-Exchanged Slab Optical
        Waveguides in X-cut LiNbO$_3$
        Accepted for Publication in I.E.E. Proc. Part J, 1985

[7.9]   C. Canali et al.
        Proton Exchanged LiNbO$_3$ Waveguides: Materials Analysis
        and Optical Characteristics
        Proc. S.P.I.E., vol 460, paper 07, Los Angeles, 1984

[7.10] C. Canali et al.
        LiNbO$_3$ Optical Waveguide Fabrication by Ti Indiffusion
        and Proton Exchange: Process, Performance and Stability
        Proc. S.P.I.E., vol 517, paper 15, 1984

[7.11] A. Carnera et al.
        Structural Characterisation of Proton Exchanged LiNbO$_3$
        Optical Waveguides
        Submitted to J. Mat. Science 1985

[7.12] I.P. Kaminow and J.R. Carruthers
        Optical Waveguiding Layers in LiNbO$_3$ and LiTaO$_3$
        Appl. Phys. Lett., vol 22, No.7, pp326-328, April 1973

[7.13] J.R. Carruthers, I.P. Kaminow and L.W. Stulz
        Diffusion Kinetics and Optical Waveguiding Properties
        of Outdiffused Layers in Lithium Niobate and Lithium
        Tantalate
        Applied Optics, vol 13, No.10, pp2333-2342, Oct. 1974

[7.14] A. Yi-Yan, J. Primot, J. Burgeat and R. Guglielmi
        Proton Exchanged LiNbO$_3$ Waveguides: An X-Ray Analysis
        2nd E.C.I.O., I.E.E. Conf. Publ. No.227, Post-Deadline
        Papers, Florence, Italy, 1983

[7.15]   A. Yi-Yan
         Index Instabilities in Proton Exchanged $LiNbO_3$
         Waveguides
         Appl. Phys. Lett., vol 42, No.8, pp633-635, April 1983

[7.16]   J.L. Jackel, C.E. Rice and J.J. Veselka
         Proton Exchange for High Index Waveguides in $LiNbO_3$
         Appl. Phys. Lett., vol 41, No.7, pp607-608, Oct 1982

[7.17]   M. Goodwin and C. Stewart
         Proton Exchanged Optical Waveguides in Y-cut Lithium
         Niobate
         Electr. Lett., vol 19, No.6, pp223-225, March 1983

[7.18]   S.M. Al-Shukri at al.
         Strain and Surface Damage Induced by Proton-Exchange
         in Y-cut $LiNbO_3$
         Submitted to J. Appl. Phys.

[7.19]   M. DeMicheli, J. Botineau, P. Sibillot et al.
         Fabrication and Characterisation of Titanium Indiffused
         Proton Exchanged (TIPE) Waveguides in Lithium Niobate
         Optics Comm., vol42, No.2, pp101-103, June 1982

[7.20]   M.N. Armenise et al.
         Characterisation of TiO_2, $LiNb_3O_8$ and $(Ti_{0.65}Nb_{0.35})O_2$
         Compound Growth Observed During $Ti:LiNbO_3$ Optical
         Waveguide Fabrication
         J. Appl. Phys., vol 54, pp6223-6231, 1983

[7.21]   M.N. Armenise et al.
         Evaluation of Planar Titanium Diffused $LiNbO_3$ Optical
         Waveguides by Micro-Analytical Techniques and
         Measurements of In-plane Scattering Levels
         Tech. Digest of 4th Int. Conf. I.O.O.C., pp67-70
         June 1983, Tokyo, Japan

[7.22]   K. Sugii, M. Fukuma and H. Iwasaki
          A Study of Titanium Diffusion into LiNbO$_3$ Waveguides by
          Electron Probe Analysis and X-ray Diffraction Methods
          J. Materials Science, vol 13, pp523-533, 1978

[7.23]   M. DeMicheli, J. Botimeau, P. Sibillot et al.
          Independent Control of Index and Profiles in Proton
          Exchanged Lithium Niobate Waveguides
          Optics. Lett., vol8, No.2, pp114-115, Feb 1983

[7.24]   S.M. Al-Shukri et al.
          Analysis of Annealed Proton-Exchanged Waveguides on
          Lithium Niobate by Optical Waveguide Measurements and
          Microanalytical Techniques
          7th Top. Meet. on Integrated and Guided Wave Optics,
          PD71, Kissimmee, Florida, April 1984

[7.25]   S.M. Al-Shukri et al.
          Proton Exchange Optical Waveguides on Lithium Niobate:
          Devices, Characterisation and Future Prospects
          Proc. S.P.I.E., vol 578, paper 05, Boston Symposium
          September, 1985

[7.26]   J. Hornstra and W.J. Bartels
          Determination of Lattice Constants of Epitaxial Layers
          in III-V Compounds
          J. Cryst. Growth., vol 44, pp513-517, 1978

[7.27]   R.T. Smith and F.S. Welsh
          Temperature Dependence of the Elastic, Piezoelectric,
          and Dielectric Constants of Lithium Niobate and Lithium
          Tantalate
          J. Appl. Phys., vol 42, No.6, pp2219-2230, May, 1971

[7.28]   C.E. Rice, J.L. Jackel and W.L. Brown
          Measurement of the Deuterium Concentration Profile in a
          Deuterium-Exchanged LiNbO$_3$ Crystal
          J. Appl. Phys., vol 57, No.9, pp4437-4440, May 1985

[7.29]   D. Dieumegard, D. Dubreuil and G. Amsel
         Depth Profiling of Deuterium with the $D(^3He,p)^4He$
         Reaction
         Nuclear Instruments and Methods, vol 168, Part III.
         Methods and Apparatus, pp223-225 1980

[7.30]   K.K. Wong, R.M. DeLaRue and S. Wright
         Electro-Optic Waveguide Frequency Translator in Lithium
         Niobate Fabricated by Proton Exchange
         Opt. Lett., vol 7, pp546-548,   June 1982

[7.31]   M.N. Armenise et al.
         Optical Characterisationof Proton Exchanged and
         Titanium Diffused Proton Exchanged Slab Waveguides on
         Lithium Niobate
         IEEE Int. Workshop on Integr. Opt. and Related Technol.
         for Sig. Proc., Technical Digest, pp21-24, Sept. 1984
         Florence, Italy

[7.32]   K.K. Wong, N.J. Parsons, A.R. Olderoyd, A.C. O'Connel
         High Quality Optical Waveguides in $LiNbO_3$ by Dilute
         Melt Proton Exchange
         IOOC/ECOC'85, Integrated Optical Waveguide Fabrication,
         Venice, Italy, October 1985

[7.33]   J.L. Jackel, C.E. Rice and J.J. Veselka
         Compositional Control in Proton Exchanged $LiNbO_3$
         Electron. Lett., vol 19, pp387-388,   1983

[7.34]   R.G. Smith et al.
         Correlation of Reduction in Optically Induced
         Refractive-Index Inhomogeneity with OH Content in
         $LiTaO_3$ and $LiNbO_3$
         J. Appl. Phys., vol 39, No.10, pp4600-4602, Sept, 1969

[7.35]   R.G. Walker
         Ph.D. Thesis, University of Glasgow,   1982

CHAPTER 8

**OPTICAL CHARACTERISATION AND MATERIALS ANALYSIS
OF POST ANNEALED PROTON EXCHANGED WAVEGUIDES**

8.1 Introduction

The formation of PE waveguides in lithium niobate is a
comparatively low temperature process (<240°C) [8.1,8.2]. It is
therefore not surprising that the process is amenable to low
temperature annealing, as was shown by De Micheli [8.3].
Altering the step index profile in this manner is desirable for
the following reasons:

Proton exchanged waveguides have a high index change. As a
result of this, single mode waveguides (at 633nm) are very
shallow, of the order of 0.2 microns deep [8.4]. Single mode
stripe waveguides therefore have a very small field intensity
distribution (compared to that of a standard single mode fibre).
The resultant field mismatch between fibre and PE waveguide
would be the cause of large power losses if butt-coupling between
the two lightguides was attempted. A method of increasing the
size of the PE field distribution while maintaining single mode
operation would be desirable as this would improve the fibre
waveguide coupling loss. The problem is similar to that of fibre
coupling to single mode ion exchanged waveguides in glass
[8.5,8.6].

The PE process creates severe surface damage on Y-cut
substrates for all but very short exchange times [8.7] and it is
shown in this chapter that low temperature annealing of such
waveguides forms multimode waveguides without surface damage.
Annealed waveguides retain the high waveguide index and
polarisation properties of the unannealed waveguides [8.3].

As well as creating a range of index profiles and hence
waveguide properties on PE waveguides, the annealing of PE slab
waveguides on lithium niobate and subsequent materials analysis
may provide useful information on waveguide surface index
relaxation and stability problems in general. The modification

of the waveguide surface index after the PE process appears to take the form of a low temperature anneal since the overall waveguide depth increases and the waveguide refractive index decreases during both processes. This will be discussed in more detail.

The annealing of PE waveguides has been shown to result in waveguides of a generally higher quality i.e. lower propagation losses, lower in-plane scattering and more stable [8.8,8.9,8.10,8.11].

This chapter describes the analysis of post annealed PE on X-cut, Y-cut and Z-cut lithium niobate including investigations of the modification of modal indices, index profile and waveguide quality associated with the variation of the five main fabrication parameters, the temperature and time for PE waveguide formation and the temperature, time and atmosphere of the annealing process.

8.2 Post Annealing Procedure and Conditions for PE Waveguides

In the formation of titanium indiffused waveguides on lithium niobate, the atmosphere in which the annealing occurred has been found to be an important factor in the resulting waveguide properties [8.12,8.13]. It thus seemed reasonable that in a low temperature process, such as proton exchange, the subsequent post annealing of such waveguides could produce optical properties that were dependent on the post annealing atmosphere, as well as depending on annealing temperature and time.

Initial measurements, which were undertaken to gain a working range for the analysis, used the IWKB method [8.14,8.15] as an indication of index profile modification, yielded the following;

PE waveguides should be formed over the usual range of temperatures to give waveguide depths of up to 2 microns, which provided a sufficient number of guided modes (more than three) so that the IWKB method could be implemented. This excluded PE
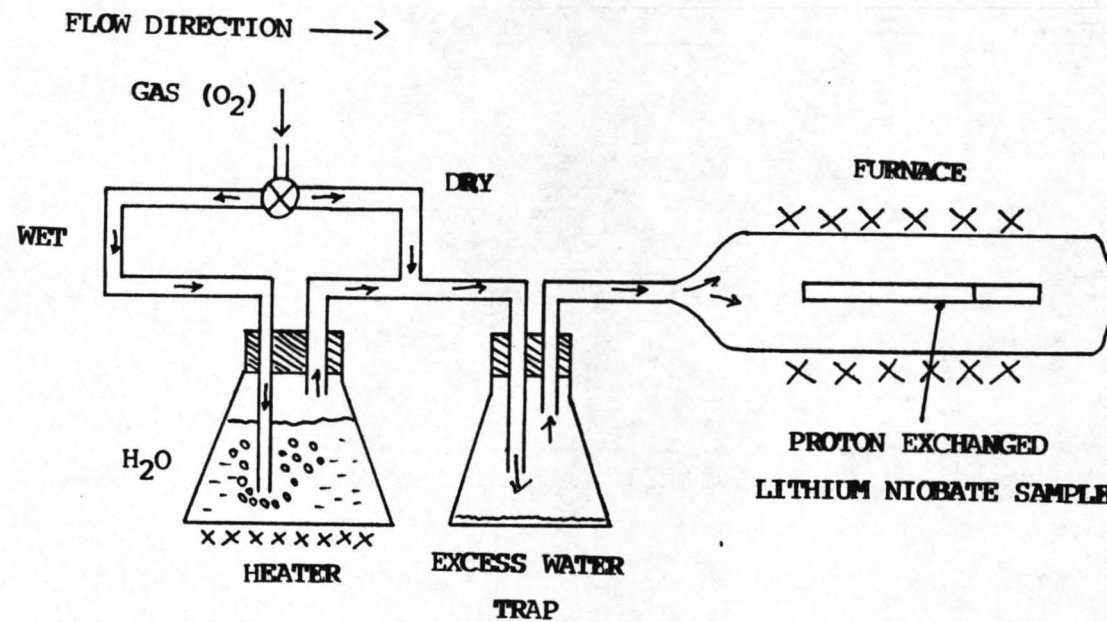
Figure (8.1): Schematic Diagram of Apparatus used in the
Annealing of Proton Exchanged Waveguides in LiNbO$_3$

waveguides formed on Y-cut plates (due to surface damage) and those required for subsequent materials analysis. The maximum depth measurable by RBS and NR being 1 micron (see chapters 6,7) pre-annealed waveguides had to be of the order of 0.3μm deep, allowing subsequent depth increases, due to post annealing, to be in an acceptable and measurable range.

Post-annealing was undertaken in flowing oxygen with wet and dry atmospheres. The flow rates chosen were 500cc/min and 2000cc/min. The gas bubbler water temperature was set to 45°C. The annealing temperatures were chosen in the range 250°C to 500°C. The main temperatures used were 325°C and 400°C. A diagram of the post-annealing apparatus can be seen in figure (8.1). In all cases, pre-annealed waveguides were allowed to relax to their stable condition before annealing took place.

8.3 Optical Characterisation of Annealed Waveguides

To investigate the effects of post-annealing on the optical properties of PE waveguides, two methods were adopted. The first was to plot the variation of modal effective indices against annealing time for various annealing conditions. The second method was to make use of the IWKB method to give a representation of the change in waveguide refractive index profile with respect to the annealing conditions. In some cases the index profiles estimated by the IWKB method were checked by using the profile as an input for a programme based on the method described by Vassel [8.16]. This programme yields theoretical mode effective indices of a waveguide whose refractive index profile has been defined. The comparisons were made by S.W.C. Wong and the results indicated that the measured IWKB refractive index profiles were in very close agreement with the Vassel theory thus confirming the accuracy of the annealing profiles obtained with the IWKB method.

Observations of modal effective refractive index (obtained by the prism coupling technique [8.17]), at λ = 0.633um, as a function of annealing time is represented in figure (8.2) a) and b) for Z-

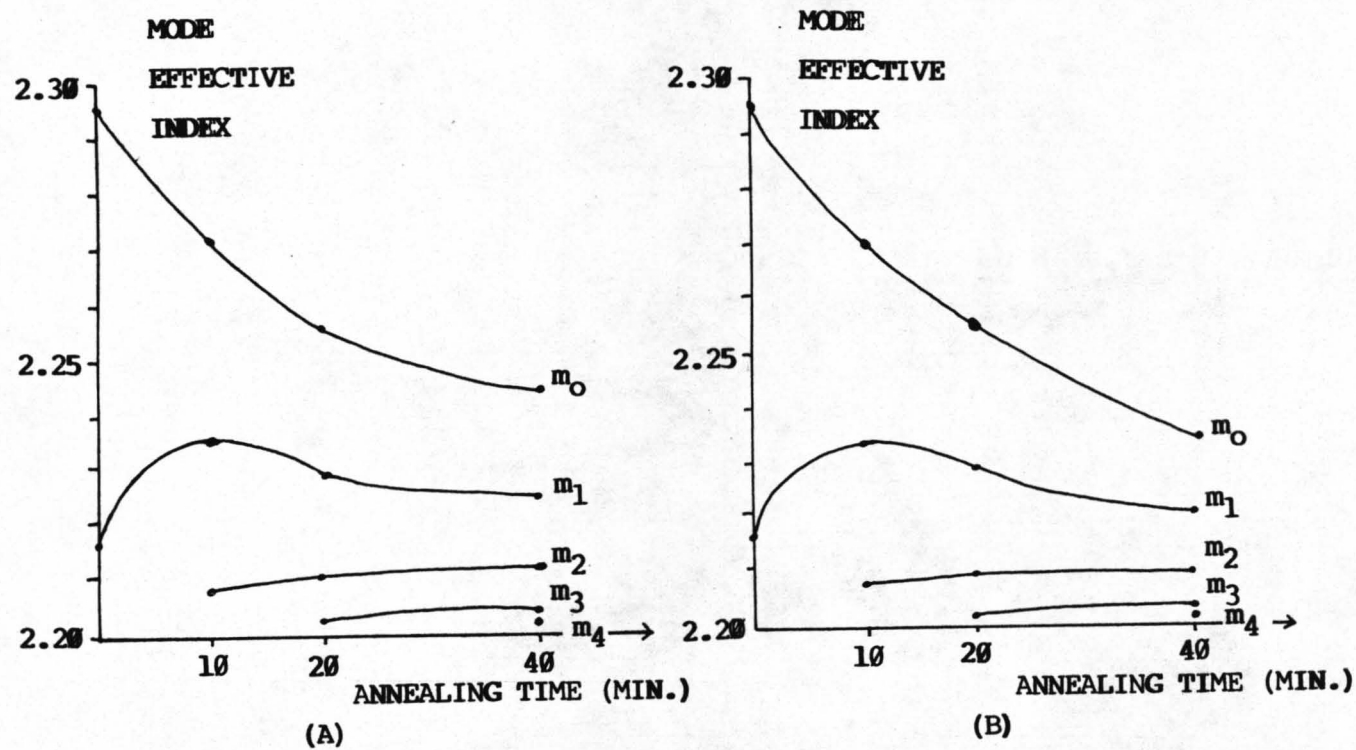**Figure (8.2):** Plots of Mode Effective Index vs. Annealing Time
for Z-cut LiNbO$_3$ (PE 210°C for 96 min.). Samples
Annealed at 400°C in (A) Wet and (B) Dry Oxygen
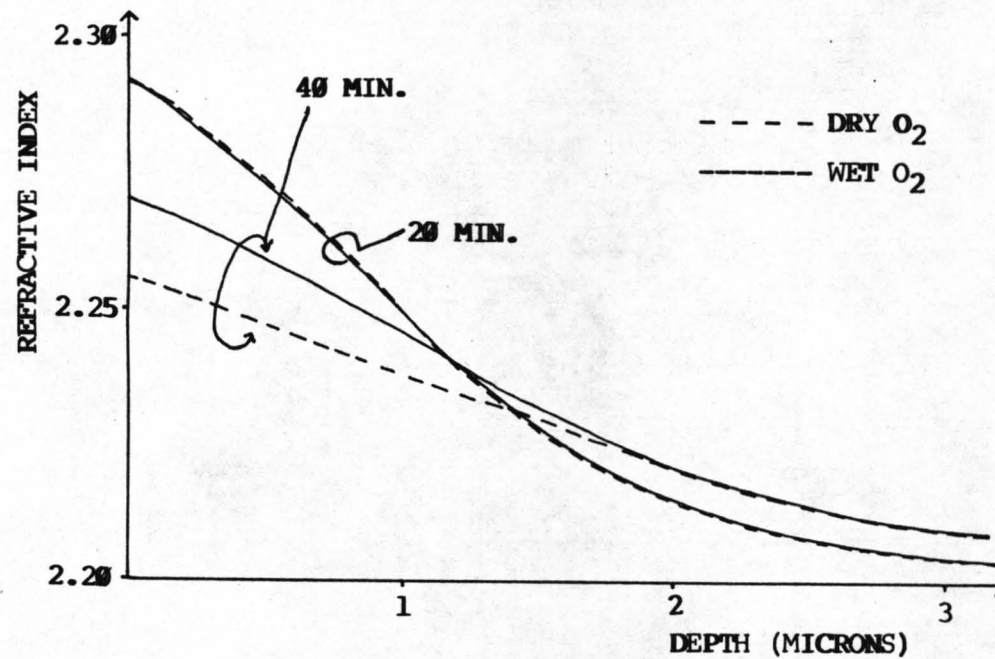Flowing at 2000 cc/min.

Figure (8.3): IWKB Generated Refractive Index Profiles for Annealed Z-cut LiNbO$_3$ (PE 210°C for 96 min.). Samples Annealed at 400°C for 20 and 40 minutes in Wet and Dry Oxygen Flowing at 2000 cc/min.

cut substrates. The samples were initially exchanged at 210°C for 1h 36min and had an optically estimated waveguide depth of 0.73μm. Initially the waveguide supported two modes. The samples were annealed at 400°C in a) wet and b) dry oxygen flowing at 2 litre/min. Note, from figure (8.2), that the results for wet and dry atmospheres are practically indistinguishable. However if the resultant index profiles are examined (see figure 8.3), estimated by the IWKB method, as the annealing time increases a discrepancy between the index distributions of the waveguides annealed in wet and dry atmospheres emerges indicating that dry atmospheres possibly have more effect in altering the waveguide index distribution for the above annealing conditions. The data on figure (8.3) are limited because there were not enough waveguide modes after annealing for 10 minutes to extract an index profile from the IWKB method. The effects of the annealing atmosphere will be discussed in more detail later on in this section.

In figure (8.2) it can be seen that the second mode, m_1, has a maximum effective index at about 10 minutes annealing and then the mode index decays in annealing time in a manner similar to that for the fundamental mode. This effect can be seen more clearly in figure (8.4). Figure (8.4) shows the effect of annealing temperature and time on the TE_0 mode index of PE waveguides formed on Y-cut lithium niobate at 210°C and exchanged for 5 min (1,1'), 10 min (2,2') and 3 min (3,3'), respectively. It is evident from the figure that at 325°C the modal effective index of the two deeper waveguides, 1 and 2, show a peak similar to that of m_1 in figure (8.2). The same effect was seen in X-cut substrates. This phenomenon can be explained if the various stages of annealing in a proton exchanged waveguide are examined carefully. Figures (8.5) a) and b) show the relative changes in waveguide refractive index distribution for a) changing annealing time and constant temperature and for b) constant annealing time and changing temperature. It can be seen from figure (8.5) a) that the waveguide distribution, which is originally a step-like profile, initially goes deeper while maintaining a similar step-like distribution. The profile subsequently modifies towards a
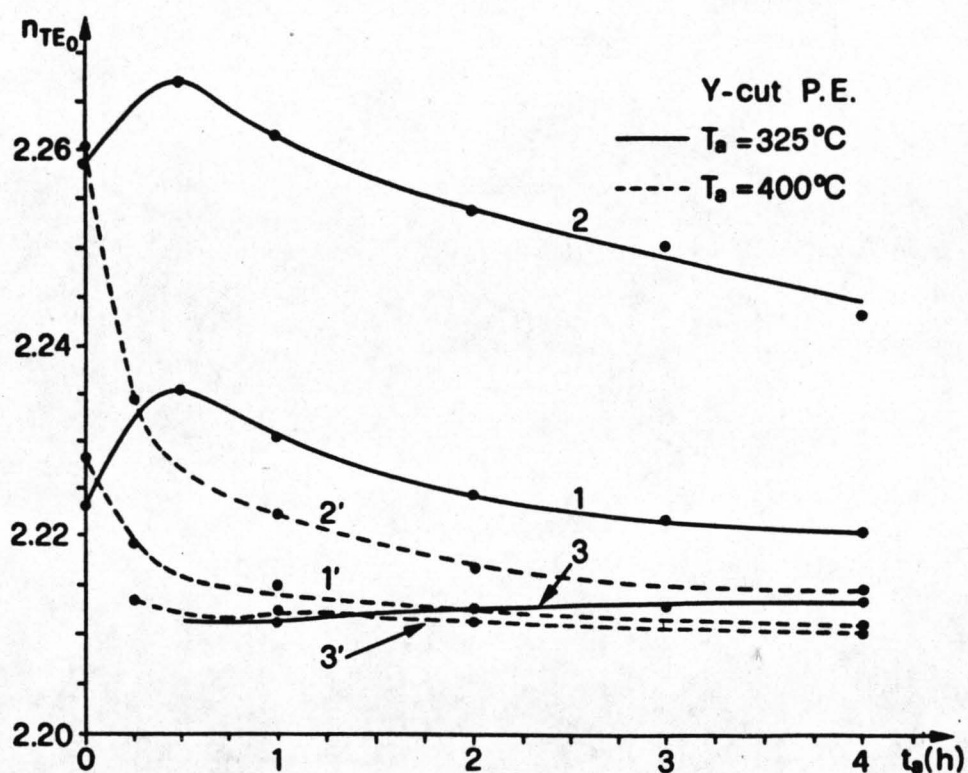
Figure (8.4): Plots of Mode Effective Index (n_{TE}) vs. Annealing
Time (t_a) for Y-cut LiNbO$_3$ PE waveguides.
All Curves Exchanged at 210°C for (1,1') 5 min.;
(2,2') 10min. and (3,3') 3 min. All Samples
Annealed in Dry O$_2$ Flowing at 2000 cc/min.

Figure (8.5): a) IWKB Generated Refractive Index Profiles for Annealed Z-cut LiNbO$_3$ (PE 200°C for 8h). Samples Annealed at 325°C for 1,3 and 6 hours. All Samples Annealed in Dry Oxygen Flowing at 500 cc/min.

Figure (8.5): b) IWKB Generated Refractive Index Profiles for Annealed X-cut LiNbO$_3$ (PE 210°C for 4h). Samples Annealed for 3h at Temperatures of 325°C and 400°C and for 0.5h at 500°C. Samples Annealed in Dry Oxygen Flowing at 2000 cc/min.

gaussian like profile in which the peak value decreases and the width (depth) of the distribution increases as the annealing time increases. Keeping the annealing time constant and increasing the temperature, figure (8.5) b), indicates that the rate of this diffusion process is critically controlled by the annealing temperature. Figure (8.6) shows the effect of the same annealing conditions on waveguides of different initial depth, and indicates that the rate of change of waveguide distribution is also dependent on the initial diffusion source [8.18]. Therefore the rate of change of the waveguide distribution is dependent on the initial waveguide depth with the rate of profile modification being inversely proportional to the initial waveguide depth

The short-term increase in modal effective index can be explained by the change in index distribution. Examining the 325°C annealing of Y-cut substrates in figure (8.4) it is now evident that the initial increase in effective indices is caused by an increase in the depth of the guiding region with at most only a small change in the waveguide index. Eventually the index profile spreads out to assume a profile closer to a standard diffusion profile, the index maximum decreases, and thus the modal effective indices also decrease. A simple analysis of the normalised dispersion curves for index profiles of step and gaussian distributions yields similar results.

Annealing at 400°C in figure (8.4) does not show the index increase which is associated with the lower temperature anneal. This was because the range of annealing times chosen to plot the curves were too large to accommodate the rapid initial increase and subsequent decrease in the modal indices at the higher temperature, the rate of index profile modification being higher at higher temperatures, see figure (8.5).

The possibility of the annealing atmosphere and gas flow rate playing an important role in the annealing process and hence in the resultant waveguide properties, as discussed above, was one that had to be examined. The effects of modifying the above parameters is far from straightforward. At an annealing
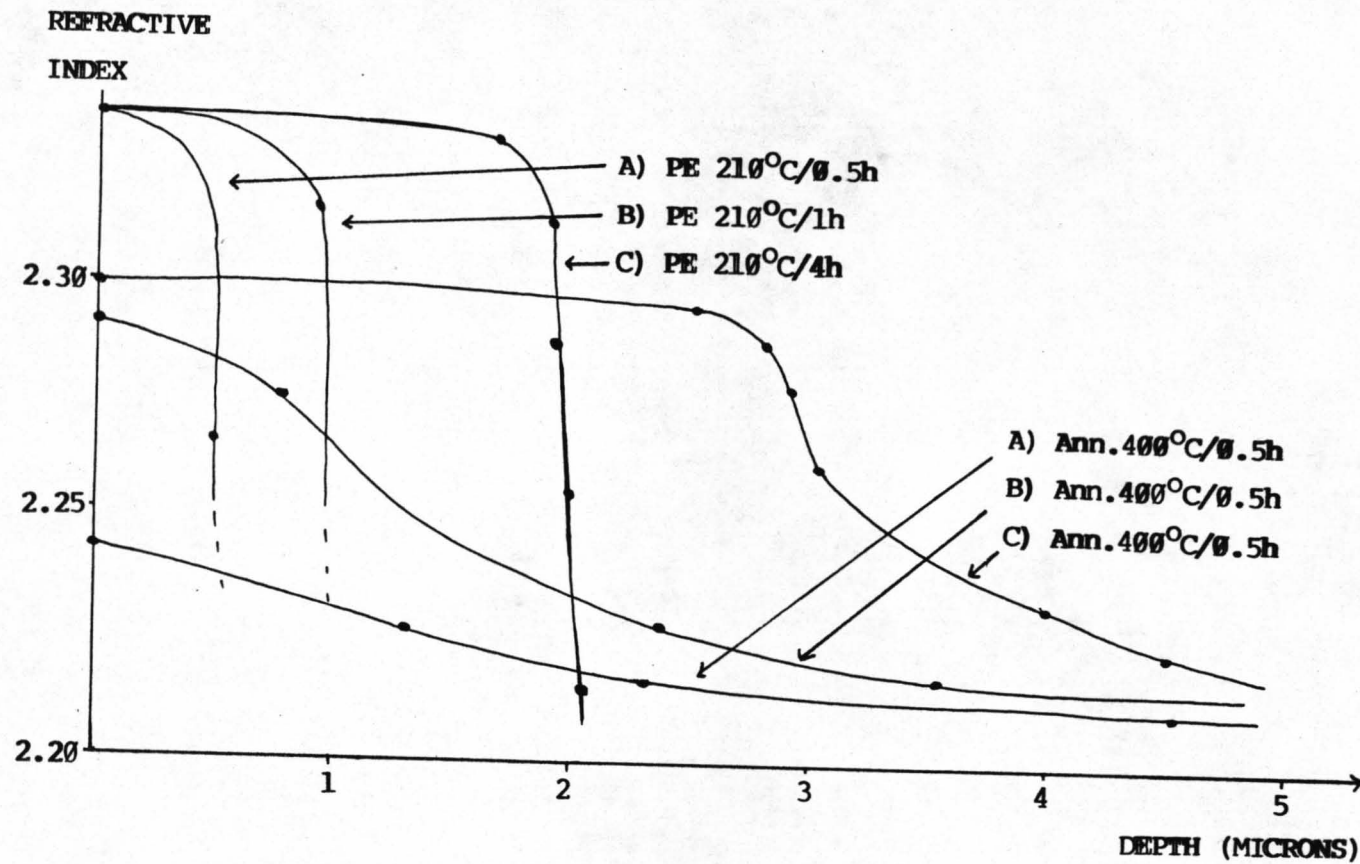
Figure (8.6): IWKB Generated Refractive Index Profiles for
Annealed X-cut LiNbO$_3$ (PE 210°C for 0.5,1,4h).
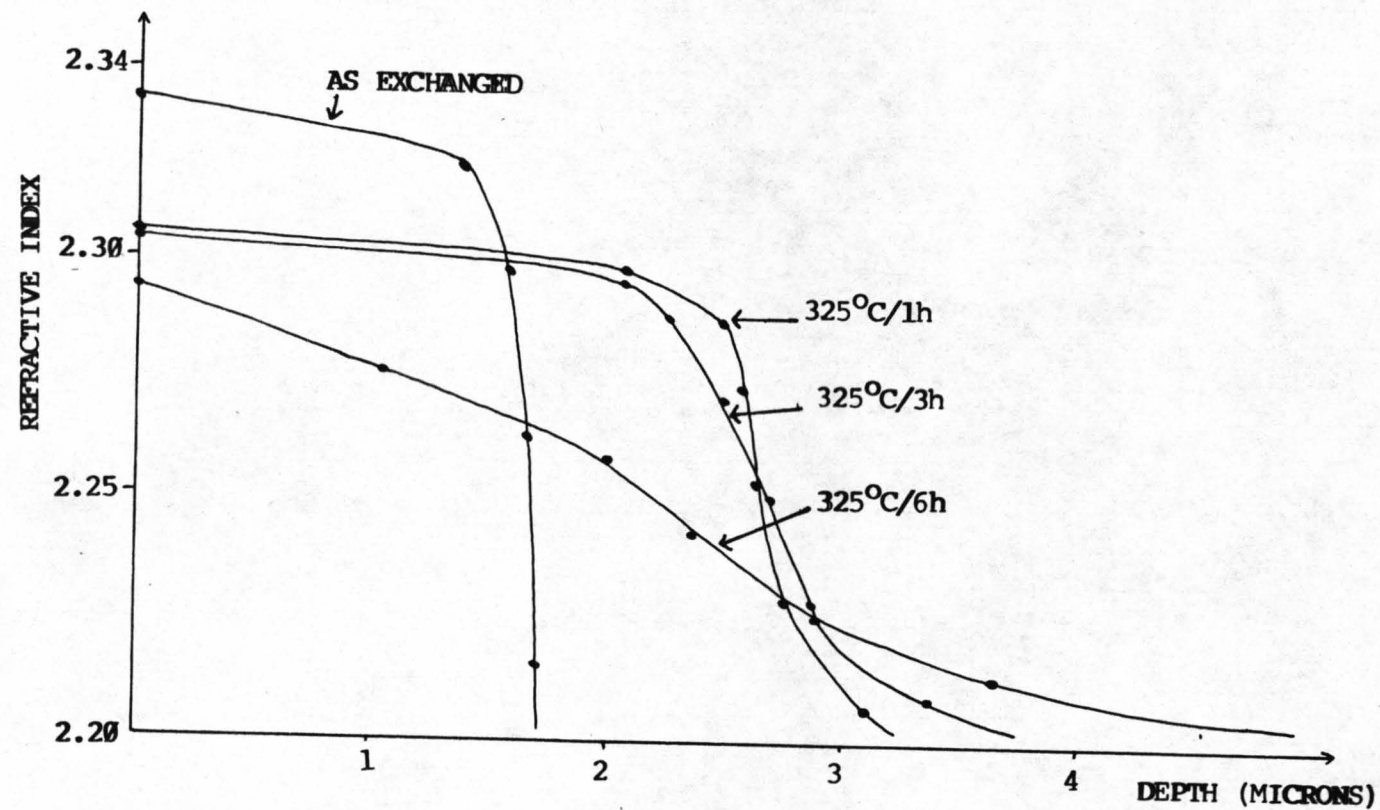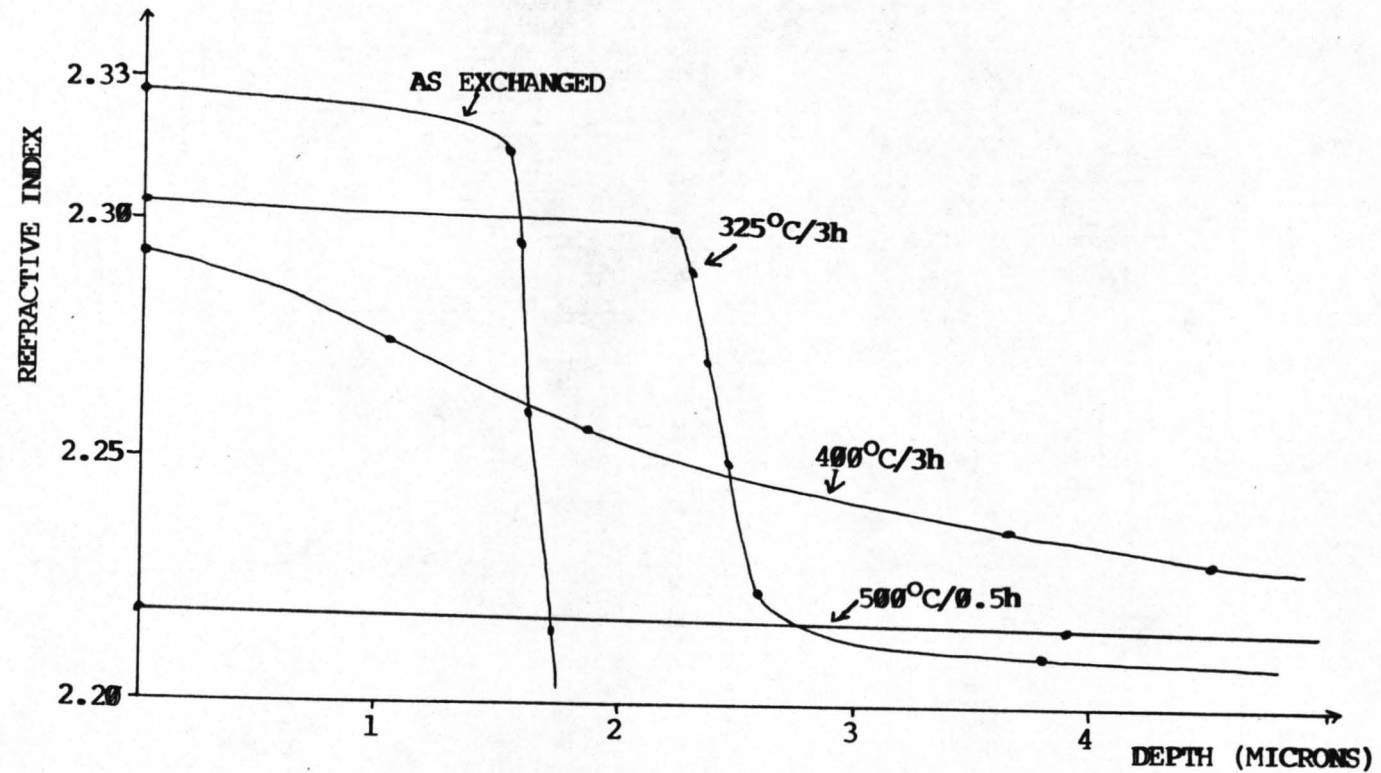All Samples Annealed at 400°C for 30 minutes in Dry
Oxygen Flowing at 2000 cc/min.

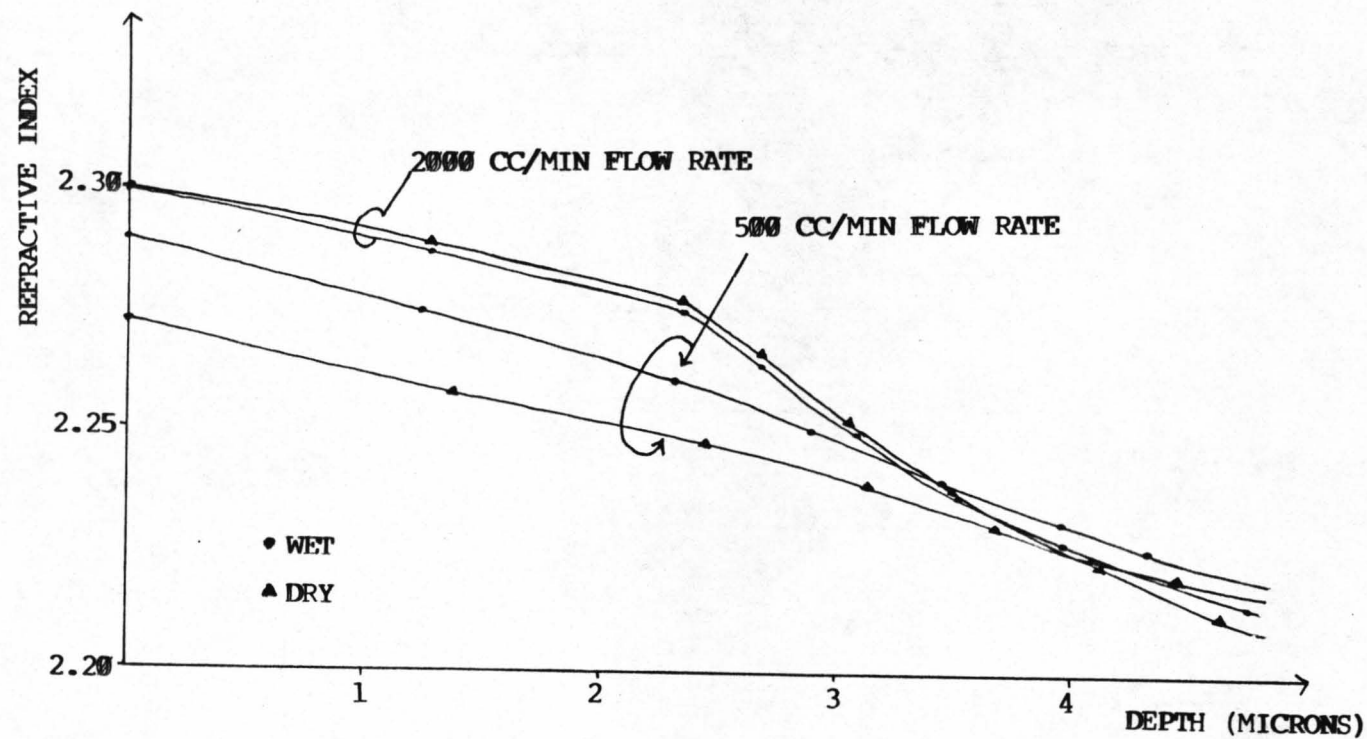**Figure (8.7):** IWKB Generated Refractive Index Profiles for
Annealed Z-cut LiNbO$_3$ (PE 210°C for 8h). Samples
Annealed at 400°C for 1h in Wet and Dry Oxygen
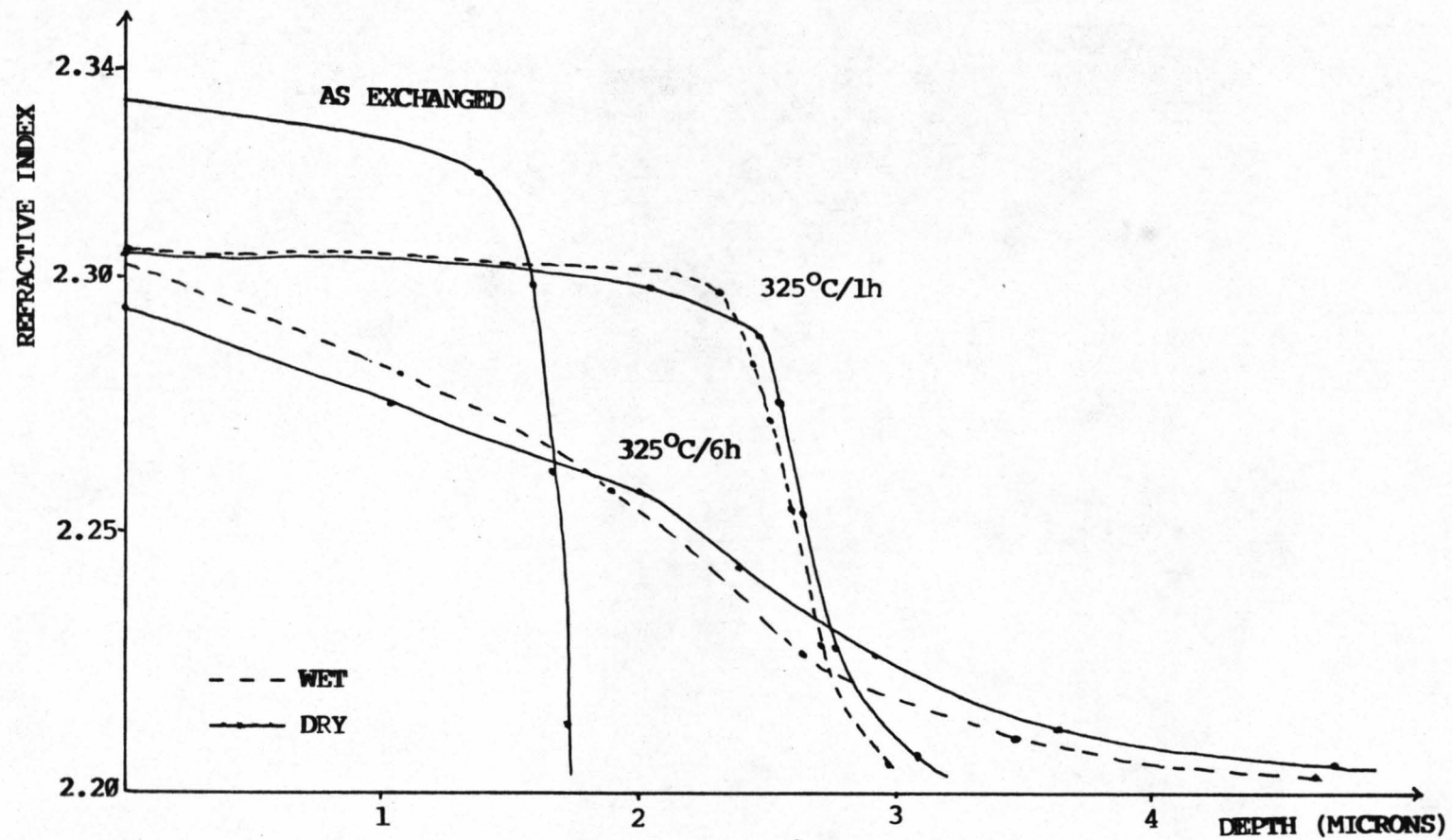Flowing at 500cc/min and 2000 cc/min.

Figure (8.8): IWKB Generated Refractive Index Profiles for Annealed Z-cut LiNbO$_3$ (PE 200°C for 8h). Samples Annealed at 325°C for 1 and 6 hours Wet and Dry Oxygen Flowing at 500 cc/min.

temperature of $400^{\circ}C$, on any crystal orientation, a flow rate of 2 litres/min yields no appreciable difference in waveguide properties for wet and dry O_2 gas flow (see figure (8.7)), whereas at a flow rate of 500 cc/min the dry flowing atmosphere affects the waveguide index profile to a greater extent (see figure (8.7)). Annealing at $325^{\circ}C$ yields similar results, except that the profile discrepancy between wet and dry atmospheres when annealing at a 500cc/min flow rate was much less (see figure (8.8)).

Unfortunately the above information is also misleading. It is most probable that different flow rates in the system will result in small changes in the actual annealing temperature causing discrepancies in the results. It may also be that the annealing atmosphere (i.e. wet/dry) also causes temperature discrepancies, so conclusions obtained from the above information must be acknowledged to be inherently weak.

Annealing at $250^{\circ}C$ produced a very slow rate of annealing and annealing at $500^{\circ}C$ produced an extremely high rate of annealing, acknowledging that the annealing rate is also dependent on the exchange layer depth. The main information to be deduced is that annealing is possible at $250^{\circ}C$ (admittedly the effect is small) and therefore the possibility of stability problems occurring with PE waveguides at low temperatures is great. The initial waveguide relaxation is too fast a diffusion process to be explained purely by a room temperature annealing process, and it is thought that another mechanism plays a role in the process - this will be discussed in more detail in section 8.6.

8.4 Materials Analysis of Post Annealed PE Waveguides

The techniques used in the analysis of post-annealed PE waveguides are discussed in chapter 6. Due to the limited period of time allocated to use the Nuclear Reaction technique the materials information on post-annealed PE waveguides is mainly based on RBS measurements and X-ray crystallographic techniques,

however sufficient data is available from all techniques to discuss trends in the annealing process.

Figure (8.9) shows results of RBS observations on X-cut lithium niobate samples. All the traces in figure (8.9) were obtained from aligned samples proton-exchanged for 15 minutes at 210°C. Trace '0' shows the non-annealed RBS curve with its characteristic sharp demarcation between the distorted and normal lattice regions. Traces 1, 2 and 3 were obtained on samples subsequently annealed for times of 15 and 30 minutes and for 1 hour at 325°C in wet oxygen flowing at 2 litre/min. The traces all show essentially the same decrease in lattice distortion compared with the non-annealed sample. It must be noted that the overall drop, at lower energies, corresponding to the normal substrate lattice is merely an artefact of the measurement technique. The distorted region still exhibits a sharp boundary and has, as expected, increased considerably in depth (an increase from 0.37 µm to 0.6 µm after 15 minutes annealing). Remarkably, however, the distorted region decreases in depth for longer annealing times to 0.446µm after 1 hour.

Figure (8.10) shows examples of RBS spectra obtained in Z-cut lithium niobate samples under similar conditions to those of figure (8.9). Many of the features of the two figures are similar but it is evident that there is actually a small increase in the apparent lattice distortion occurring when annealing is carried out. It can be speculated that figures (8.9) and (8.10) taken together indicate the relocation of interstitial hydrogen atoms to more closely substitutional positions in the lattice or vice versa - this will be discussed in more detail in section 8.6.

A notable feature of both X-cut and Z-cut samples is the appearance of a pronounced peak at the surface of the sample. Figure (8.11) shows the peak formation in more detail. Figure (8.11) shows annealing trends of X-cut samples at 400°C and illustrates the formation of a surface peak as it increases substantially in height and width with increasing annealing time
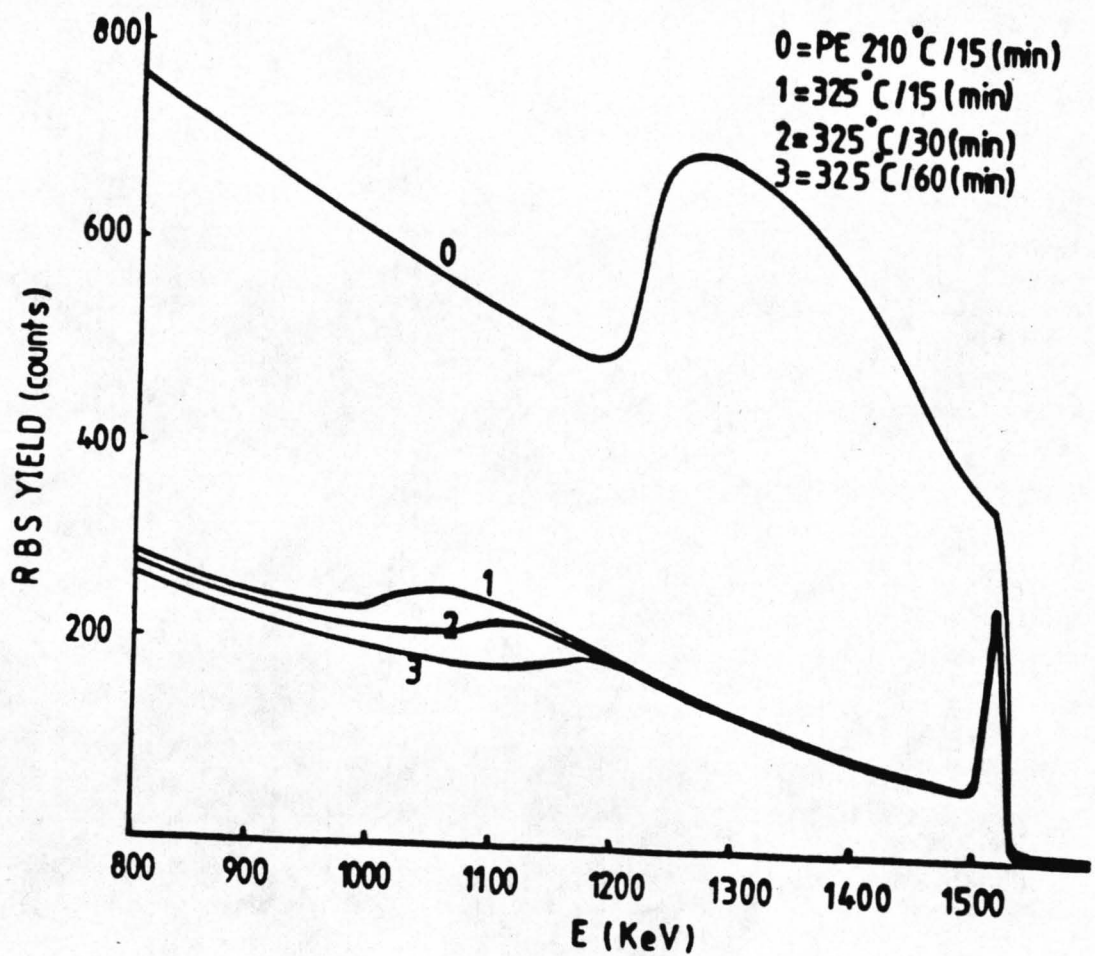
Figure (8.9): Aligned RBS Spectra of As-Exchanged and Annealed Waveguiding Layers on X-cut LiNbO$_3$. PE Waveguides Initially Exchanged for 15 min at 210°C and Annealed at 325°C for 15, 30 and 60 min in Wet Oxygen Flowing at 2000 cc/min.
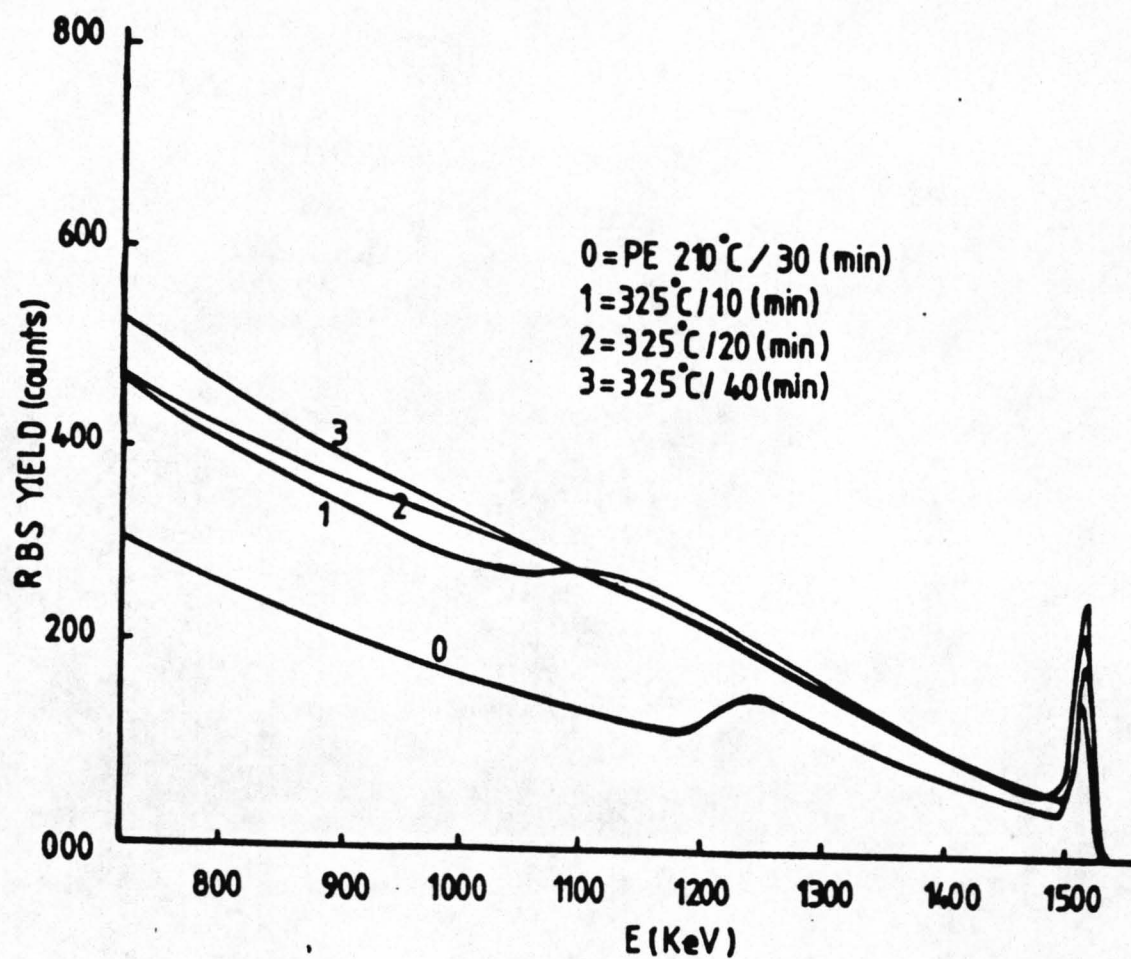
Figure (8.10): Aligned RBS Spectra of As-Exchanged and Annealed Waveguiding Layers on Z-cut LiNbO₃. PE Waveguides Initially Exchanged for 30 min at 210°C and Annealed at 325°C for 10, 20 and 40 min in Wet Oxygen Flowing at 2000 cc/min.

Figure (8.11): Expanded RBS Spectra of the Surface Region in
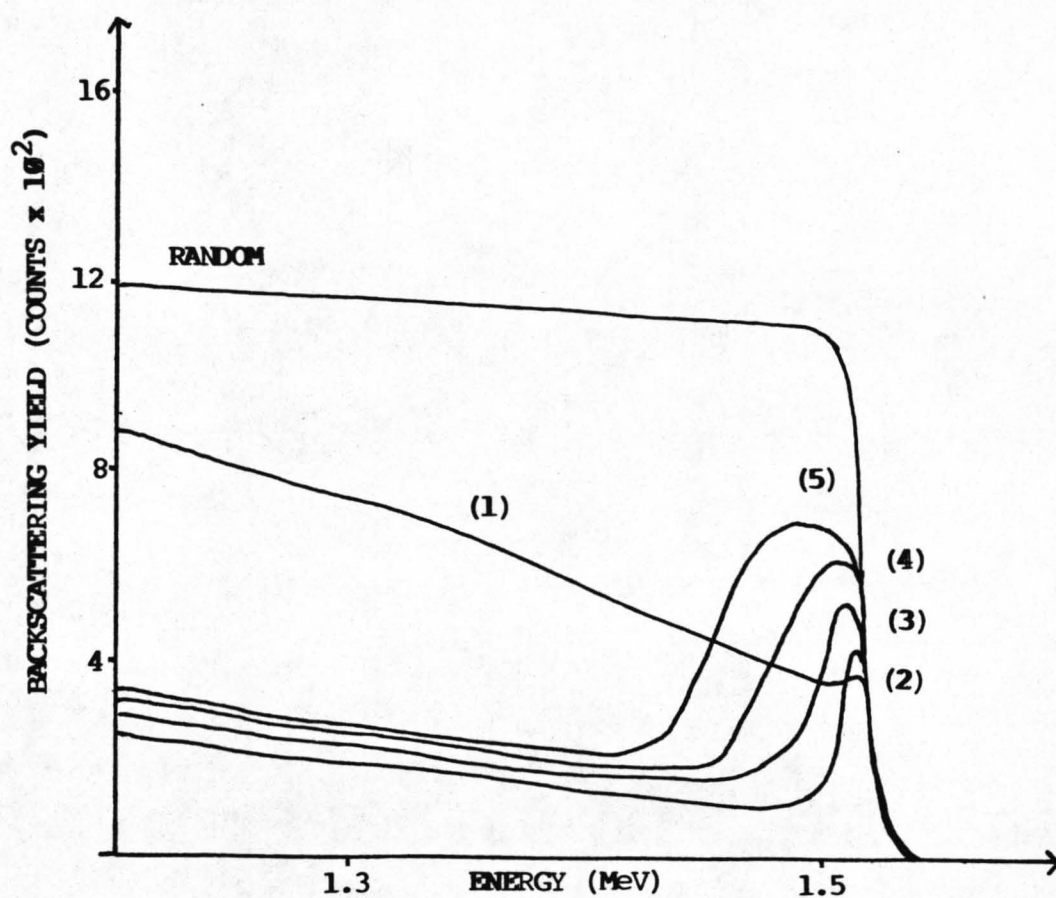As-Exchanged and Annealed PE Waveguiding Layers on
X-cut $LiNbO_3$. Waveguides Initially Exchanged for
1h at $210^{O}C$, (1), and Annealed at $400^{O}C$ for
(2) 15min, (3) 30min, (4) 2h and (5) 4h in Wet
Oxygen Flowing at 2000 cc/min.

- being about 0.1μm thick after 4 hours. This peak may be
attributed to the formation of a niobium-rich $Li_xH_{1-x}Nb_3O_8$ phase
or to irreparable damage caused by the initial exchange at the
sample surface and will be discussed in more detail later on in
this section. It is not thought that the damage can be caused by
surface polishing as it is unlikely that such damage could be
modified during the low temperature annealing process.

From observations on RBS spectra, annealing in a wet or dry
atmosphere produces no remarkable differences in the post-
annealed regions (either in peak distortion or depth). The
trend, admittedly small, is that annealing in dry atmospheres
does slightly increase the depth of the effective annealed
region. Observations of RBS spectra for differing oxygen flow
rates during the annealing process are inconclusive due to the
small amount of data available, but there is some indication that
an increase in flow rate increases the depth but not the
magnitude of the distorted region. The change in depth of the
distorted region is, at the most, only a few percent.

Figure (8.12) shows NR hydrogen profiles of exchanged and
annealed PE waveguides on X-cut lithium niobate substrates. The
samples were exchanged at 180°C for 25 minutes and subsequently
annealed in wet flowing oxygen, 500cc/min, for 30 minutes at
temperatures ranging from 200°C to 400°C. The figure clearly
shows the form of the change in hydrogen distribution throughout
the annealing process, the profiles take a form not unlike the
IWKB index profiles of similarly annealed waveguides.
Unfortunately these results are the only ones available at the
present time, however they do give a remarkable insight into the
hydrogen migration and point to the hypothesis that the RBS
measured disorder is not directly related to the hydrogen profile
and that the presence of the hydrogen atoms does not always
disrupt the lattice structure.

The effects of the annealing process are similar when comparing
the optical, NR and RBS results, and can be divided into three
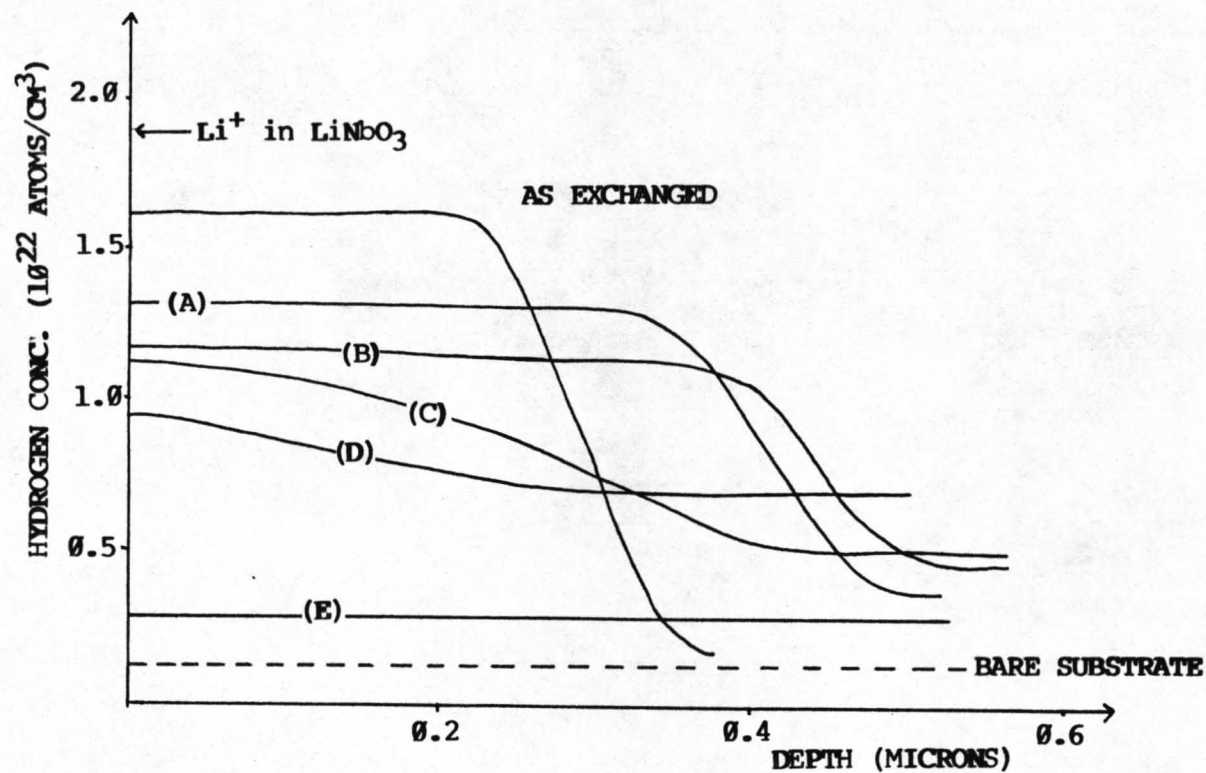stages. At the first stage of annealing the index profile keeps

Figure (8.12): Measured Hydrogen Profiles on As-Exchanged and
Annealed PE Waveguides on X-cut LiNbO$_3$. All
Samples Exchanged at 180°C for 25 minutes.
Samples Annealed for 30min in Wet Oxygen Flowing
at 2000 cc/min at Temperatures of (A) 200°C,
(B) 250°C, (C) 300°C, (D) 350°C and (E) 400°C

a step-like shape with an increased depth and a lower value of waveguide index. Similarly the lattice distortions observed by RBS decrease in amplitude but propagate deeper into the crystal. Afterwards, for intermediate annealing periods, the waveguide index decreases further, caused by hydrogen diffusing into the substrate. As a consequence of the hydrogen movement the proton concentration profile decreases in a similar manner to that of the waveguide index profile resulting in the proton profile interface with the substrate becoming less abrupt i.e. the waveguide profile remains mainly step-like with a long tail. A similar movement in the RBS measured distorted layer is observed. For longer annealing periods (or higher temperatures) we see from figure (8.12) that hydrogen goes deeper and deeper into the substrate and the step-like proton profile and the waveguide profile change to one much more like a gaussian profile.

The annealing behaviour agrees with the data obtained by double crystal X-ray diffraction. Figure (8.13) shows rocking curves from a series of X-cut samples proton exchanged and then post-annealed for 30 minutes at increasing temperatures, i.e. similarly to those used for the NR and RBS measurements. The effect of the first annealing stage is reflected in the strong modification from the broad and low intensity satellite peak produced by the 'as-exchanged' sample to the sharp and high peak observed in the 250°C, 30 min annealed sample. The shape of this peak indicates a unique and well defined strain value (0.6%) with a step-like depth profile. Increasing the annealing temperature gradually reduces the height of the satellite peak and a tail appears at the left side of the unperturbed substrates Bragg diffraction peak. This feature indicates that the step-like strain distribution decreases in intensity and a region of lower strain appears in the lattice (most probably at the exchanged-layer/substrate interface). In other words the strain profile is smoothed out similarly to the refractive index (figure (8.3)) and distortion profiles (figure (8.10)).

Even though no work on examining the annealed layer by IR absorption was attempted, other authors[8.10,8.19] have examined
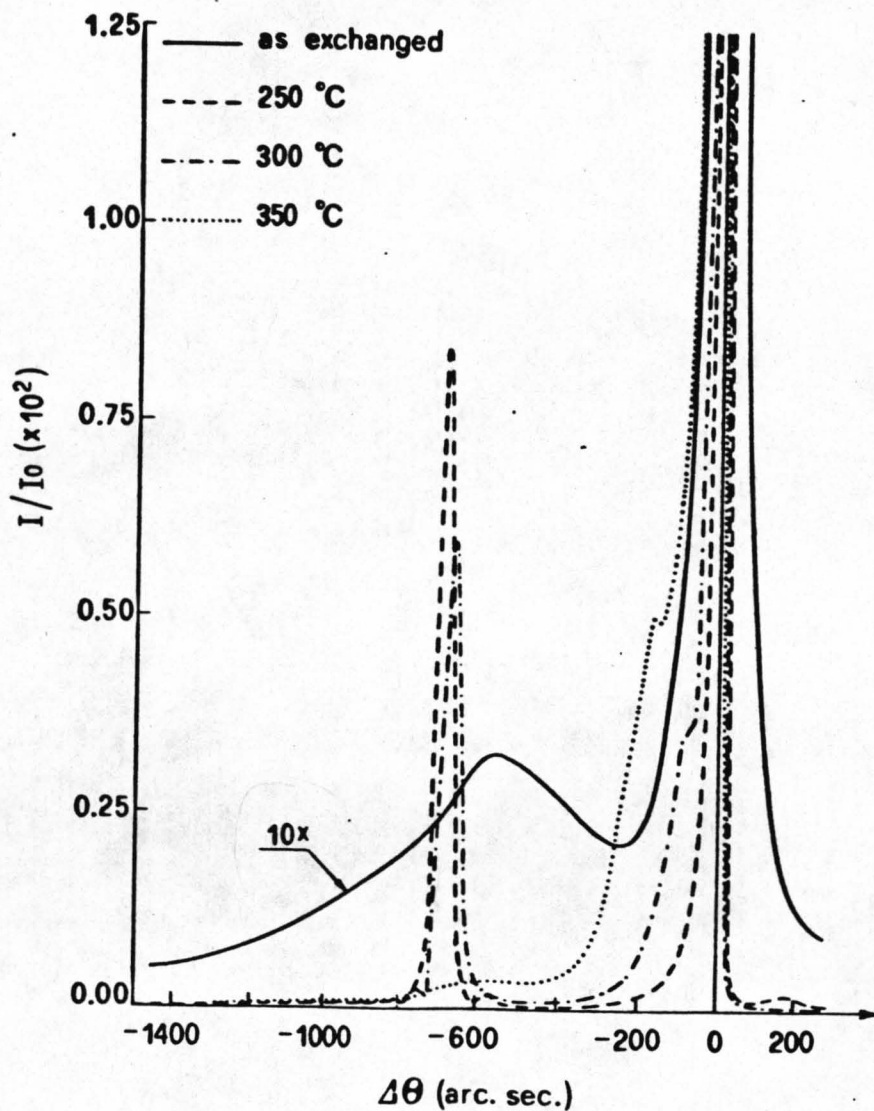
Figure (8.13): Double Crystal X-Ray Diffraction (220) Rocking Curves Obtained on As-Exchanged and Annealed PE Waveguides on X-cut LiNbO$_3$. Samples Exchanged at 180°C for 25 min and Annealed for 30min in Wet Oxygen Flowing at 2000 cc/min at temperatures of 250°C, 300°C and 350°C - as in Figure (8.12).

the effects, to some extent, and the following conclusions can be extracted. PE layers on lithium niobate have infrared spectra in the form of a main absorption peak at 3505 cm^{-1} and a broad absorption band at 3250 cm^{-1}. After annealing the main absorption peak only reduces in intensity (by a few percent), whereas the broad absorption band almost disappears. The broad peak is due to lower energy hydrogen bonding, supposed to be interstitial hydrogen, not positionally ordered like the OH bonds of the main peak. It is possible therefore that during the annealing process the unsited H^+ ions move into the bulk crystal finding sites for bonding with the oxygen in positions of a more ordered form i.e. a stronger OH bond with an absorption band the same as the main peak. This initial proton migration to more ordered sites must be directly related to the first stage of index profile modification in the annealing process and to the creation of a single strain in the exchanged layer. The initial stage is that the profile maintains its step-like distribution but is deeper and has a shallower index than the initial step. The protons in the exchanged layer forming random bonds must therefore be thought of as excess protons, and have been attributed elsewhere to the inherent waveguide instabilities and to the presence of a possible new phase $HNbO_3$ [8.10]. The next stages of index modification during the annealing process can be attributed to the OH bonded hydrogen atoms migrating deeper into the substrate and allowing Li atoms to transfer to shallower regions, reducing the index change in the normal manner of diffusion.

8.5 Improvement of In-Plane Scattering in Post Annealed PE Waveguides

As was mentioned previously in chapter 5, in-plane scattering can give an indication of the waveguide quality. Using in-plane scattering levels as such an indicator, the post-annealing of PE waveguides was investigated in a limited series of experiments. The experiments were limited because large sample lengths are needed for in-plane scattering measurements (ch.5,sect.7).

Preliminary measurements were made on annealed proton exchanged waveguides on all three major axes, but mainly on Y-cut lithium niobate [8.9].

Observations on in-plane scattering levels and waveguiding modes for samples exchanged on Y-cut lithium niobate for the same conditions as for the samples in figure (8.4) were as follows: waveguides proton-exchanged for 5 and 10 minutes supported very faint waveguide modes which were difficult to couple out with a prism coupler. In waveguides exchanged for 10 minutes and annealed at 325°C the second mode became apparent after thirty minutes of annealing and the third mode after 4 hours. For annealing at 400°C the third mode appeared after 15 minutes and a fourth mode after 2h. In waveguides exchanged for 5 minutes and annealed at 325°C the second mode becomes apparent after 2h. For annealing at 400°C a second mode becomes visible after 30 minutes and a third after 1h.

In all the above Y-cut samples, post-annealing did not improve the high in-plane scattering levels, except for the sample exchanged for 5 minutes and annealed at 400°C which exhibited an improvement in m-line quality after 30 minutes of annealing.

The sample exchanged for three minutes and annealed at 325°C remained single mode after 4h of annealing, while, with annealing at 400°C, the sample showed a clear single mode after 15 minutes. In either case the samples exhibited improvements in in-plane scattering levels after annealing. Annealing at 325°C for 2h the ΔI value was 3.6dB/cm, while a similar value (3.9dB/cm), has been measured for samples annealed at 400°C for 15 min. In either case a monomode waveguide still results with effective index equal to 2.213.

It may be that the poor m-line quality observed for most of the Y-cut samples proton exchanged for 5 and 10 minutes is due to the near-surface damage (or high strained region) caused by the initial exchange process, such damage (or surface regions of high strain) only being modified in the case of the 5 min exchange and

annealing at high temperature (400°C for 30 min).

A three minute exchange at 180°C may be short enough and at a low enough temperature that the waveguide has not been stressed to the point where annealing redresses the situation. It has been observed that the best quality single mode waveguides are fabricated with an initial PE that forms an exchanged region shallower than the fundamental mode cut-off depth. The subsequent annealing of the layer into the guiding region attains the best results (in all crystal orientations) [8.20]. This information coupled with the above observations on Y-cut lithium niobate suggests that after a certain exchange depth, permanent damage to the crystal surface layer occurs for which post-annealing cannot compensate.

If the above hypothesis were true it would explain the poor quality of most proton exchanged waveguides and can be related possibly to the initial high proton surface concentration, since exchanges in lower proton concentration melts do not exhibit such poor waveguide quality [8.10,8.21,8.22].

Limited observations on X-cut and Z-cut lithium niobate indicate that annealing does not improve the in-plane scattering levels unless the initial exchange depth is below the fundamental mode cut-off depth [8.20].

8.6 Conclusions

The initial change in waveguide refractive index profile during the annealing process can be explained in the following manner. The pre-annealed PE waveguide, as well as having OH bonds (protons) in well defined sites, has a percentage of protons randomly in the exchanged region (hydrogen bonded as can be noted from the broad absorption band centred at 3250 cm^{-1}). On annealing the first occurrence is that these randomly sited protons move through and modify the substrate/waveguide interface to take up positions similar to those defined by the polarised

peak at 3505 cm^{-1}. Thus the waveguide is deeper, and if the small amount of Li (in the transition region) disperses throughout the exchanged region (which it probably does) then the resultant index profile is still a step but with a slightly reduced index due to the small increase in %Li in the exchanged region. This theory is supported by the following observations;

1) after annealing the broad absorption peak at 3250 cm^{-1} disappears, indicating that there are no longer any randomly (probably interstitial protons) in the exchanged region

2) before annealing there is a complex series of strains in the exchanged region. After the first stage of annealing all the strains disappear except for one well defined strain with a step like profile in the exchanged layer (the complex series of strains being caused by the random series of hydrogen bonds in the pre-exchanged sample)

3) the NR measurements indicate the migration of protons described above.

Further modification of the waveguide index profile, to a step with a tail and finally to a gaussian form, are directly related to the migration of the OH bond into the substrate and to the subsequent movement of Li into the exchanged (Li depleted) region. It is improbable that the OH bond actually moves, it seems more likely that the protons 'hop' from an oxygen atom in the exchanged region to a near neighbour in the substrate, since:

1) the NR proton profiles do indicate that the protons move deeper into the lattice. The profiles are very much like the change in refractive index profiles discussed above.

2) the step strain profile (obtained after the first stage in the annealing process) is modified in a manner akin to the the index distribution changes. The step strain reduces in amplitude and magnitude and also shows a small tail of reducing strain near that of the unperturbed substrate. On further annealing the step

profile disappears and is replaced by a series of strains, tailing off from the unperturbed peak, indicating a series of strains reducing in magnitude as the the exchange region merges with the adjacent substrate.

The PE waveguide relaxation effect is most probably caused by the migration of the interstitial protons evenly throughout the exchanged layer (directly after the exchange process there must be an excess proton concentration at the surface). The protons still remain in unaligned bonding sites (as can be seen from IR data) but the redistribution throughout the exchanged layer may cause the slight increase in depth and the reduction in surface index observed. To move the interstitial protons out of the exchanged region needs a much higher temperature than the room temperature where relaxation occurs, although measurements have been made by NR (see section 8.4) techniques on PE waveguides annealed at 200°C and have monitored a substantial change in hydrogen position (admittedly the initial waveguide was very shallow). There may also be an associated even redistribution of Li throughout the exchanged layer. Initially after exchange an ion gradient will most probably exist.

Device instabilities such as the D.C. effect [8.23] will most probably also be caused by the movement of the interstitial protons under the influence of the applied field. The reduction of strain in the lattice after annealing may explain the improved quality of some waveguides.

The RBS data has yielded some interesting information. In Z-cut PE waveguides annealing caused an increase in the depth of the perturbed region (which is not unreasonable since the waveguide also gets deeper). However, in X-cut lithium niobate the perturbed region after initially increasing in depth as annealing commences subsequently reduces in depth. Obviously there is an increase in lattice order along the X-axis in the waveguide substrate interface region. Whether it is the increase of Li atoms back into, or the loss of protons from, the exchanged region/substrate interface that causes this effect is open to

conjecture.

Finally, from RBS data it was noticed that the surface peak (initially thought to be surface damage caused by polishing) grew as the exchanged layer was annealed. The temperatures used in the annealing process are too low to be able to modify the crystal lattice directly, therefore the peak must be due to the exchange process. It is thought that the PE process causes irreparable damage to the surface of the exchanged layer (due possibly to the high proton concentration). The damaged layer may only be in the order of 100 angstroms thick, and may be a totally different phase ($HNbO_3$ or $Li_xH_{1-x}Nb_3O_8$). This surface layer could result in waveguides which exhibit considerable scattering (PE waveguides are very prone to optical scatter).

The surface layer damage, if caused by high proton concentration, might be averted by either reducing the proton concentration (as in dilute melts) or by exchanging for very short periods of time and annealing the waveguide above mode cut-off (this effect has been noticed with Y-cut samples). The RBS surface peak is also observed from RBS plots obtained from PE waveguides formed by dilute melts (0.5% lithium benzoate) [8.22] so this theory does not appear to be substantiated, although it may be that the proton concentration is still too high (RBS spectra of 1% lithium benzoate melts (and greater) have not, as yet, been taken).

CHAPTER 8 - REFERENCES

[8.1]   J.L. Jackel, C.E. Rice and J.J. Veselka
        Proton Exchange for High Index Waveguides in $LiNbO_3$
        Appl. Phys. Lett., vol 41, No.7, pp607-608, Oct 1982

[8.2]   D.F. Clark, A.C.G. Nutt, K.K. Wong, P.J.R. Laybourn
        and R.M. DeLaRue
        Characterisation of Proton Exchanged Slab Optical
        Waveguides on Z-cut lithium niobate
        J. Appl. Phys., vol 54, No.11, pp6218-6220, Nov. 1983

[8.3]   M. DeMicheli, J. Botineau, P. Sibillot, D.B. Ostrosky
        M. Papuchon
        Independent Control of Index and Profiles in Proton
        Exchanged Lithium Niobate Waveguides
        Optics Lett., vol 8, No.2, pp114-115, Feb 1983

[8.4]   A.C.G. Nutt, K.K. Wong, D.F. Clark, P.J.R. Laybourn
        and R.M. DeLaRue
        Proton Exchange Lithium Niobate Slab and Stripe
        Waveguides: Characterisation and Comparisons
        2nd E.C.I.O., IEE Conf. Publ. No.227, pp53-56, Oct 1983
        Florence, Italy

[8.5]   G. Stewart, R.H. Hutchins, P.J.R. Laybourn, C.A. MacRae
        Construction of Hybrid Integrated Optical Circuits
        IOOC/ECOC'85, Integrated Optical Waveguide Fabrication,
        Venice, Italy, October 1985

[8.6]   G. Stewart, R.H. Hutchins, P.J.R. Laybourn
        Hybrid Integration of Active and Passive Devices
        3rd Int. Conf. on Int. Opt. and Opt. Fibre Commun.,
        paper WE-1, San Fransisco, April 1981

[8.7]   M. Goodwin and C. Stewart
          Proton-Exchanged Optical Waveguides in Y-cut Lithium
          Niobate
          Electronics Lett., vol 19, No.6, pp223-225, March 1983

[8.8]   M.N. Armenise et al.
          Optical Characterisation of Proton Exchanged and
          Titanium-Diffused Proton Exchanged Slab Waveguides on
          Lithium Niobate
          IEEE Int. Workshop on Integr. Opt. and Related Technol.
          for Sig. Proc., Technical Digest, pp21-24, Sept. 1984
          Florence, Italy

[8.9]   S.M. Al-Shukri et al.
          Analysis of Annealed Proton Exchanged Waveguides on
          Lithium Niobate by Optical Waveguide Measurements and
          Microanalytical Techniques
          7th Top. Meet. on Integrated and Guided Wave Optics,
          PD71, Kissimmee, Florida, April   1984

[8.10]   J.L. Jackel and C.E. Rice
          Short-and Long-Term Stability in Proton Exchanged
          Lithium Niobate Waveguides
          Proc. S.P.I.E., vol 460, Processing of Guided Wave
          Optoelectronic Materials, 1984

[8.11]   C. Canali et al.
          $LiNbO_3$ Optical Waveguide Fabrication by Ti Indiffusion
          and Proton Exchange: Process, Performance and Stability
          Proc. S.P.I.E., vol 517, paper 15, 1984

[8.12]   A.D. McLachlan
          Ph.D. Thesis, University of Glasgow, 1981

[8.13]   W.K. Burns, P.H. Klein, L.E. Plew and E.J. West
          Ti Diffusion of $Ti:LiNbO_3$ Planar and Channel Optical
          Waveguides
          J. Appl. Phys., vol 50, No.10, pp6175-6182, Oct 1982

[8.14]   J.M. White and P.F. Heidrich
Optical Waveguide Refractive Index Profiles Determined
from Measurement of Mode Indices: A Simple Analysis
Applied Optics, vol 15, No.1, pp151-155, Jan 1976

[8.15]   J.Finak and H. Jerominek
Planar Diffusion Glass Waveguides Obtained by Immersing
in Molten KNO_3
Optica Applicata, vol XII, No.1, pp11-17, 1982

[8.16]   M.O. Vassel
Structure of Optical Guided Modes in Planar Multilayers
of Optically Anisotropic Materials
J. Opt Soc. Am., vol 64, No.2, pp166-173, Feb 1974

[8.17]   P.K. Tien and R. Ulrich
Theory of Prism-Film Coupler and Thin-Film Light Guides
J. Opt. Soc. Am., vol 60, No.10, pp1325-1350, Oct 1970

[8.18]   J. Crank
The Mathematics of Diffusion
Oxford University, Clarendon Press, London (2nd Ed.)
1979

[8.19]   J.L. Jackel, C.E. Rice and J.J. Veselka
Compositional Control in Proton Exchange $LiNbO_3$
Electron. Lett., vol 19, pp387-388, 1983

[8.20]   Discussions with R.L. Holman of Battelle Research Labs,
Colombus, Ohio, U.S.A. are gratefully acknowledged.

[8.21]   K.K. Wong, N.J. Parsons, A.R. Olderoyd and
A.C. O'Donnel
High Quality Optical Waveguides in $LiNbO_3$ by Dilute
Melt Proton Exchange
IOOC/ECOC'85, Integrated Optical Waveguide Fabrication,
Venice, Italy   October 1985

[8.22]   S.M. Al-Shukri et al.
          Proton-Exchange Optical Waveguides on Lithium Niobate:
          Devices, Characterisation and Future Prospects
          Proc. S.P.I.E., vol 578, paper No. 9, Boston 1985

[8.23]   K.K. Wong, R.M. DeLaRue and S. Wright
          Electro-Optic Waveguide Frequency Translator in Lithium
          Niobate Fabricated by Proton Exchange
          Opt. Lett., vol 7, pp546-548, June 1982

PART 3

CONCLUSIONS
AND FUTURE WORK

CHAPTER 9

CONCLUSIONS AND FUTURE WORK

9.1 Introduction

This thesis has presented theoretical and experimental observations on the ion beam etching of lithium niobate (chapters 2,3), a fibre/waveguide coupler using ion milled alignment grooves (chapter 4) and a materials and optical analysis of proton exchanged and post-annealed planar waveguides including tapered regions for a hybrid coupler (chapters 5,6,7,8).

9.2 Ion Etching of Lithium Niobate

Various ion etching techniques have been examined for the purpose of etching deep groove structures in lithium niobate substrates. Thick masking layers are required to protect the lithium niobate substrate when ion beam etching deep structures. AZ 1350J could not be used as a masking layer for ion beam etching due to the relatively thin layers which can be spun onto the substrate surface. Polyimide XU 218 [9.1] is an acceptable masking layer since the substrate can be coated with a thick polymer layer (up to 20µm) on one spin. The resultant polymer layer is free from striations and can be patterned with a high degree of finesse by oxygen reactive ion etching. The anisotropic oxygen RIE process ensured vertical walls in the masking layer, the only problem with the masking layer was shown to be the small ripples in the side walls which could not be removed by altering process parameters. The wall ripples are either thought to be caused by ripples in the aluminium masking layer created at the photolithographic stage or structure inherent in the polymer layer itself. If the former is the case the ripples could be alleviated by using a metal with a smaller grain size (such as chromium) or by electron beam pattern writing on the photoresist.

In the future, photosensitive polyimides could be used (such as

Polyimide HTR-2 [9.2]) which will remove the need for the oxygen
RIE process since their specification shows that they can be
patterned to even layers of up to 100um thick and which will
produce a vertical and smooth wall quality after exposure and
development. At the moment however these polyimides are
prohibitively expensive.

The quality of the resultant ion beam etched slot on lithium
niobate substrates appears to be directly related to the quality
of the masking layer. The four main drawbacks encountered were
1) the relatively slow etch rate (approx. 500Å/min), 2) the
uncontrollability of the etch rate, 3) redeposition and 4) the
need for a very thick and high quality masking layer.

Although good groove quality was achieved, suitable for ion
milled alignment groove fibre/waveguide coupling on lithium
niobate, the above problems will still have to be addressed if
the process is to be fully adaptable for industrial
implementation. The etch rate achievable is limited by the ion
energy used and by the fact that the substrate can be damaged by
thermal shock if too high a beam energy is used. The
uncontrollability of the etch rate coupled with the length of
time required to etch grooves to the required depth means that
the final groove depth cannot be accurately predicted. Thus to
improve the system some form of depth monitor or end-point
detector is required. The most practical monitor would have to
be some form of laser interferometer [9.3,9.4] to monitor the
depth of the substrate as it changes and close the beam shutter
when the required etch depth is achieved. In this manner the
actual etch duration is no longer critical and the etch rate can
vary without affecting the final groove depth. The addition to
the system of this type of monitor will alleviate problems 1) and
2) above.

In a purely physical etching process, redeposition will always be
a problem. With IBE on lithium niobate the formation of ears
degrades the quality of the rim of the groove, and the groove
wall ripples are also related to redeposition. A reactive ion

etching process would theoretically solve problems 3) and 4) above. Although metal masking layers such as aluminium are very resilient to reactive gases such as Freon 12, lithium niobate is not suitable for reactive ion etching due to its high lithium content. The main reason for wanting to use reactive gases is that the etched substrate forms volatile products which can be removed by the pumping system. However, compounds such as lithium fluoride are very hard and have very high partial pressures (i.e. they only can be removed under very low pressure conditions) [9.5, 9.8].

The solution to the problem of reactive ion etching lithium niobate is to proton exchange the region before etching. Over 70% of the lithium in the exchanged region is removed during the process and hence the exchanged region should etch readily in reactive gases which contain fluorine or chlorine (since the formation of the lithium salt which acts as an inhibitor is greatly reduced). The process would only entail one extra process step. The prepared sample to be reactive ion etched in lithium niobate would have a patterned metal mask (such as aluminium) on the substrate surface. The sample when proton exchanged would only be altered in the etch aperture as the metal acts as a buffer protecting the surface that is coated.

Future work should also include the investigation of other ion etching processes such as IBAE and RIBE on lithium niobate substrates. Especially when using IBAE the process would be at least as good as inert gas ion beam etching. It would be expected that the presence of a reactive gas could increase the etch rate and should also considerably reduce the problems encountered with redeposition.

9.3 Fibre Chip Coupling

An ion milled groove fibre/waveguide coupler was examined. The coupling component consisted of an ion milled groove longitudinally aligned to a Ti:diffused waveguide, the etched

fibre could then be placed in the groove which aligned it to the waveguide, negating any need for optimising the fibre position to the waveguide. Working at a wavelength of 1.3μm the best total insertion loss measured was 3.1dB which is a net insertion loss from fibre to waveguide of 2.58dB. From the loss analysis the major part of this loss was estimated to be Fresnel reflection loss and with index matching, the net insertion loss could be lowered theoretically to 1.82dB. Of the 1.82dB net insertion loss 0.5dB was found to be scatter loss from the side wall and base of the groove, 0.51dB was estimated to be field mismatch losses and the remainder consisted of a combination of alignment loss, waveguide propagation loss and scatter loss from the end-face of the ion milled alignment groove. Although the fibre field profile modifies considerably when traversing from the unetched to etched portions of the fibre no power is lost in the transition region.

By increasing the groove depth, and hence fibre width, it is envisaged that the scatter losses can be reduced. Improving the quality of the ion milled groove (reducing the wall ripples), possibly by a reactive etch process, should reduce the side wall, base and end-face scatter losses. If the groove depth can be accurately controlled with the aid of an end-point detector the alignment losses could be improved. The field overlap loss is considered to be acceptable since Ti:diffused waveguides always have some degree of anisotropy, however if proton exchanged stripe waveguides can be made single mode with dimensions comparable to fibre dimensions (possibly by annealing) this loss could also be reduced. Instabilities have been shown to occur when a polished fibre end is in close proximity to a polished waveguide end. The dips in waveguide output power have been shown to be greater than that which occurs if the effect is assumed to be a localised Fabry-Perot effect. An explanation for this phenomenon was not found.

There is, therefore, considerable scope for insertion loss improvement in the groove coupler and, as its losses are already low, the future prospects for this type of coupling component are

bright. The coupler is rigid in design (the fibre is supported), more stable than silicon V-groove coupler technology and most of the processes involved are amenable to industrial implementation. Fibre/waveguide coupling using ion milled alignment grooves in the waveguide substrate theoretically could be used in any substrate material, such as semiconductors or glass, with little modification. The etching processes used are purely physical and and the groove quality is dependent on the masking layer so that if a different material was used as a substrate the resultant etch should not be material specific. The component negates the need for the end-polishing of lithium niobate waveguides, required for end-fire coupling and fibre/waveguide butt coupling, and thus a complex process step is removed.

Future work should involve the investigation of both input and ouput port coupling possibly related to array coupling. Since the fibre outside diameter is much less than that of a standard fibre it allows a much higher fibre density at the device interface allowing multiport integrated optical devices to become practical. Couplers using arrays of ion milled alignment grooves do not increase the number of process steps, as the total number of grooves are defined at the photolithographic stage (i.e. the number of grooves are defined by the optical mask pattern). It should be interesting to try to implement a microprocessor based machine that will place the fibres in the groove array and bond them (possibly with fast curing epoxy).

Using the ion milling technology described it has been possible to design and make other novel components. Bristow et al. [9.6] have used the process to form novel TM polarisers on lithium niobate substrates, and recent research work by the author has shown that integrated optical stripe waveguide reflectors (IOR) can be made using the ion milling process. The IOR is similar in form to that described using rib waveguides on semiconductor substrates [9.7]. Initial measurements on the type of stripe waveguide reflector shown in figure (9.1) have yielded a total insertion loss of 17.5dB for a 6µm Ti:diffused stripe waveguide operating single mode at 1152nm wavelength. The reflector,
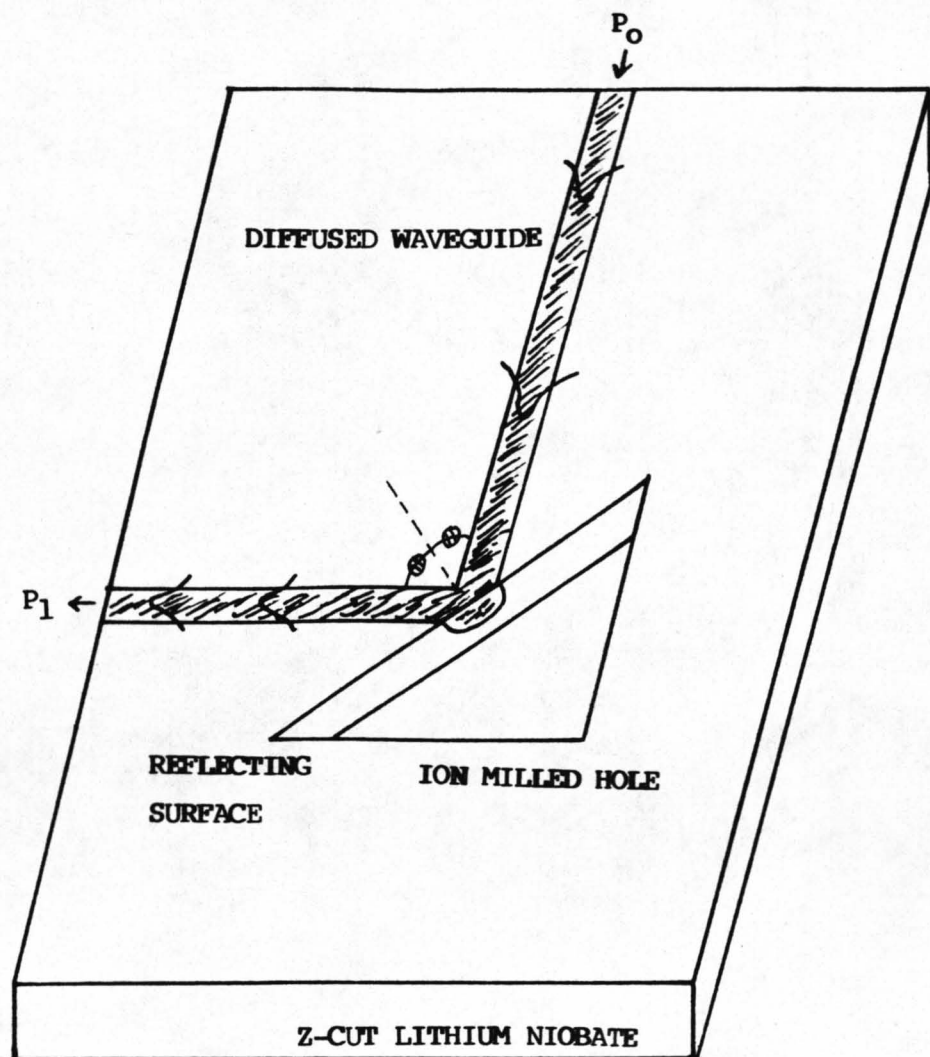
FIGURE (9.1): Diagram Depicting the Form of the Integrated
Optical Reflector. Insertion Loss is Measured as
$10.\log(P_1/P_0)$. Light is Reflected at Interface
by Total Internal Reflection.

operating by total internal reflection, has a high total insertion loss but if the typical insertion loss for straight waveguide section is subtracted from that value we find that the loss at the reflection interface is approximately 6dB. Although this value is still high the measurements were made with reflection faces which were much rougher than was observed for the ion milled alignment grooves. An RIE process would be ideal to form the reflection interface, because the process also polishes the etched surface [9.8]. A post-graduate research student has been sponsored by Barr & Stroud Ltd. to investigate this type of reflection component.

9.4 PE and Post Annealed Planar Waveguides on LiNbO$_3$

The characteristics of proton exchanged (pure benzoic acid) planar waveguides on X-cut and Z-cut lithium niobate have been investigated in the laboratory. The waveguides have been shown to be anisotropic with index changes of approximately 0.125 and 0.096 at wavelengths of 633nm and 1152 respectively along the c-axis (extra-ordinary axis) and −0.04 along the ordinary axes (at 633nm wavelength). The refractive index profile is a step. The diffusion characteristics, with respect to exchange temperature and duration, have been shown to follow the form of an Arrhenius type diffusion equation. The mode effective refractive indices decrease after exchange by 0.0075 and the waveguide depth increases, however the optical waveguide does stabilise after a two week period. The effects of off-axis light propagation have been investigated in PE waveguides on X-cut lithium niobate. The experiments showed the ordinary index change to be close to −0.04 and this negative change in ordinary index was related to the creation of leaky modes. Waveguides were shown to have high propagation and in-plane scattering losses when compared to Ti:diffused waveguides. Surface damage occurs when substrates are exchanged to a depth greater than approximately 3μm for X-cut and Z-cut lithium niobate while on Y-cut lithium niobate surface damage occurs after a depth of approximately 0.2μm. The formation of waveguide tapered regions in proton exchanged waveguides has been shown to be feasible and these tapers may

prove invaluable in a hybrid coupling component. Although, at the moment, a method of decreasing the taper length is needed, so that tapers will be suitable for a practical hybrid coupling component.

A high index waveguide in lithium niobate would be extremely useful in the formation of integrated optical components. However proton exchanged waveguides exchanged in a pure melt are not of sufficient quality. Techniques are needed for forming waveguides which are less lossy, more stable, that do not have doubts about their electro-optic and acousto-optic efficiencies and have no instabilities when D.C. electric fields are applied to them [9.9].

The optical properties of post-annealed proton exchanged waveguides have been discussed. Annealing PE waveguides does alleviate some of the waveguide scatter problems. It allows the formation of multimode waveguides on Y-cut lithium niobate. However it appears that, for initial exchange depths which support a strong single mode or are multimode, annealing cannot redress the damage that causes the waveguide scatter. The annealing process makes the waveguide stable in as much as it accelerates the relaxation process (as it appears to be like a low temperature anneal). The step-like refractive index profile can be modified in various stages to a gaussian form. Annealed waveguides become very multimode and to form single mode waveguides using annealing the initial exchange depth has to either close to or below cut-off depth. The rate of change of the waveguide profile and hence its optical characteristics are proportionately related to the annealing temperature, annealing time and inversly proportional to the initial exchanged depth.

Future work should and will be directed towards the investigation of PE waveguides formed with dilute melts. These waveguides have been shown to have superior waveguiding properties to those of waveguides exchanged with pure benzoic acid and could prove to be suitable for the manufacturing of devices [9.10,9.11].

9.5 Materials Analysis of the Proton Exchange Process

Materials properties of the proton exchange process on lithium niobate were discussed. The depth of the step index profile has been shown to be equivalent to the depth as measured by the proton concentration profile, the lithium depletion depth and the depth of the distorted region as measured by RBS techniques in the aligned mode. About 70% of the lithium is exchanged for protons in the waveguide region however although the bulk of the protons are substitutional some are also interstitial showing that the process cannot be expressed thus:

$$Li_{1-x}H_xNbO_3$$
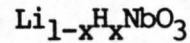
The index change mechanism is almost undoubtedly the depletion of lithium from the lattice. However it is easier to talk about proton movement in the lattice and it should be remembered that there is an associated reverse lithium movement.

The interstitial protons cause the waveguide relaxation effect. Initially after the exchange process the highest proton concentration must be at the surface, and as the proton concentration gradient evens out in the exchanged region the waveguide properties are modified. Although the waveguide does get slightly deeper during this process the excess protons still remain interstitial. During the annealing process it is evident that the first stage (when the index still remains step-like but is deeper and has a lower surface index), is characterised by the excess protons finding ordered bonding sites in the substrate region adjacent to the waveguide. The subsequent release of lithium into the exchanged region lowers the refractive index. Further annealing causes the protons to redistribute deeper into the lattice similar in form to the index redistribution (when a tail in the step index profile forms and then modifies towards a gaussian form). X-Ray Topographical measurements and NR measurements on proton concentration support this theory.

It is evident that the high optical waveguide scatter is caused

by the complex series of strains in the proton exchanged region. There is a possibility that the problems observed when using D.C. fields on proton exchanged waveguides may be due to the weakly bonded interstitial hydrogen migrating under the field effects and thus moving the lithium in the lattice.

Measurements on the amount of lithium in the melt after the exchange process strongly suggest that much more lithium is removed from the crystal than can be accounted for in the depleted exchanged region. It can only be suggested that in some way a small percentage of lithium (approximately 0.1%) is being removed from the bulk crystal making up the factor of two discrepancies in the measured and estimated amount of lithium in the melt.

RBS measurements on annealed waveguides showed that in Z-cut waveguides annealing caused an increase in the depth of the distorted region (not unreasonable since the optical waveguide depth increases). However in X-cut lithium niobate waveguides, after initially increasing in depth as annealing commences, the perturbed region then gets shallower. This suggests that there is an increase in lattice order along atomic strings in the a-axis at the merging waveguide/substrate interface which may be related to much reduced strain observed in that region. It is not surprising that the lattice distortion is anisotropic since most of the lattice strain appears to be along the X-axis (a-axis), with no measurable strain along the c-axis.

It is difficult to define a process as complex as PE; however the observations mentioned suggest that a great deal of the stress and instabilities are caused by high proton concentrations in the crystal, although no change of phase has been observed, and that a reduction in the proton concentration reduces strain and improves waveguide quality (assuming the crystal can redress the damage caused). One solution to these problems is to use dilute melts so that the proton concentration is never high enough to cause crystal damage.

Future materials analysis research should be directed to the investigation of the proton exchange process using dilute melts as it is probable that this type of waveguide will prove to be of much more use than those exchanged in pure benzoic acid.

In this thesis it has been shown that ion etched slots in lithium niobate can be successfully fabricated. The possibility of forming good quality ion etched grooves has allowed the realisation of a fibre/waveguide coupler which has shown very encouraging properties including net insertion loss, ease of fibre alignment, rigidity and process compatibility to industrial implementation. Using the ion milling technique a novel waveguide TM polariser and integrated optical reflector have been realised. The thesis has also outlined the first detailed materials and optical analysis of a new form of high index waveguide in lithium niobate formed by the immersion of substrates in hot benzoic acid. The analysis has defined the optical properties of such waveguides and has to some extent determined why waveguide properties will be better in waveguides exchanged in benzoic acid which is diluted with a small amount of lithium benzoate to reduce the proton concentration. The formation of waveguide taper regions has shown that hybrid coupling using lithium niobate substrates could now be a practical alternative to butt-coupling, if more research is undertaken in this area.

CHAPTER 9 - REFERENCES

[9.1]   Polyimide XU 218
        Specification Sheet and Laboratory Coating
        Recommendations
        Resins and Additives Division, Ciba-Geigy Corp.,
        Ardesley, New York, 1981

[9.2]   Polyimide 'Selectilux' HTR-2
        Polyimide Precursor Photoresist: Preliminary Data Sheet
        E. Merck, R&D Dept., Frankfurter Str. 250, D-6100
        Darmstadt 1, FRG, 1984

[9.3]   P.J. Marcoux and Pang Dow Foo
        Methods of End-Point Detection for Plasma Etching
        Solid State Techn., vol 24, No.4, pp115-122, April 1981

[9.4]   H.H. Busta
        End-Point Detection with Laser Interferometry
        Proc. S.P.I.E., vol 276, pp164-169, Calif.   1981

[9.5]   C.L. Lee and C.L. Lu
        CF_4 Plasma Etching on $LiNbO_3$
        Appl. Phys. Lett., vol 35, No.10, pp756-758, Nov. 1979

[9.6]   J.P.G. Bristow, A.C.G. Nutt and P.J.R. Laybourn
        Novel Integrated Optical Polarisers using Surface
        Plasma Waves and Ion Milled Grooves in Lithium Niobate
        Electr. Lett., vol 20, No.25/26, pp1047-1048, Dec. 1984

[9.7]   P. Buchmann et al.
        Totally Reflecting Mirrors: Fabrication and Application
        in GaAs Rib Waveguide Devices
        3rd E.C.I.O., pp135-139, Berlin(West), Germany,
        May 1985

[9.8]   I. Andonovic
        Ph.D. Thesis, University of Strathclyde, 1984

[9.9]   K.K. Wong, R.M. DeLaRue and S. Wright
           Electro-Optic Waveguide Frequency Translator in Lithium
           Niobate Fabricated by Proton Exchange
           Opt. Lett., vol 7, pp546-548, June 1982

[9.10]   K.K. Wong et al.
           High Quality Optical Waveguides in LiNbO$_3$ by Dilute
           Melt Proton Exchange
           IOOC/ECOC'85, Integrated Optical Waveguide Fabrication,
           Venice, Italy   October 1985

[9.11]   S.M. Al-Shukri et al.
           Proton Exchange Optical Waveguides on Lithium Niobate:
           Devices, Characterisation and Future Prospects
           Proc. S.P.I.E., vol 578, paper No.9, Boston 1985

PUBLISHED PAPERS RESULTING FROM RESEARCH

1) Characterisation of Proton-Exchanged Slab Optical Waveguides
in Z-cut LiNbO$_3$
D.F. Clark, A.C.G. Nutt, K.K. Wong, P.J.R. Laybourn
and R.M. DeLaRue
J.Appl.Phys., vol 54, NO.11, pp6218-6220, November 1983

2) Proton-Exchanged Lithium Niobate Slab and Stripe Waveguides:
Characterisation and Comparisons
A.C.G. Nutt, K.K. Wong, D.F. Clark, P.J.R. Laybourn
and R.M. DeLaRue
2nd E.C.I.O., Firenze, October 1983, I.E.E. Conf. Publ.
No.227, pp.53-56, 1983

3) Proton-Exchanged LiNbO$_3$ Waveguides: Material Analysis and
Optical Characteristics
C. Canali, A. Carnera, G. Della Mea, R.M. DeLaRue,
A.C.G. Nutt and J.R. Tobin
2nd E.C.I.O., Firenze, October 1983, Post-Deadline Session
9/A Post-Deadline Papers 1.

4) Efficient Fiber-Chip Coupling using Ion-Milled Alignment
Grooves on Lithium Niobate at λ = 1.3um
A.C.G. Nutt, J.P.G. Bristow, A. McDonach and P.J.R. Laybourn
7th Topical Meeting on Integrated and Guided Wave Optics,
Kissimmee, Florida, April 1984, ThC3

5) Analysis of Annealed Proton Exchanged Waveguides on Lithium
Niobate by Optical Waveguide Measurements and Microanalytical
Techniques
S.M. Al-Shukri, A. Dawar, R.M. DeLaRue, A.C.G. Nutt,
M.R.S. Taylor, J.R. Tobin, G. Mazzi, A. Carnera and
C. Summonte
Post Deadline Paper presented at 7th Top. Meet. on Integrated
and Guided Wave Optics, Kissimmee Florida, April 1984, PD71-4

6) Proton-exchanged LiNbO$_3$ Waveguides: Materials Analysis and
Optical Characteristics
C. Canali, A. Carnera, G. Della Mea, R.M. DeLaRue,
A.C.G. Nutt and J.R. Tobin
Proc. S.P.I.E., vol 460, paper 07, Los Angeles, Calif.
22-26 January 1984

7) Coupling Optical Fibres to Integrated Optical Waveguides
P.J.R. Laybourn, J.P.G. Bristow, A. McDonach and A.C.G. Nutt
Presented at the 1984 I.E.E.E. International Workshop on
Integrated Optical and Related Technologies for Signal
Processing in the Passive Components Session
Florence, Italy, 10-11 September 1984

8) Optical Characterisation of Proton Exchanged and Titanium-
Diffused Proton Exchanged Slab Waveguides on Lithium Niobate
M.N. Armenise, S.M. Al-Shukri, A. Dawar, R.M. DeLaRue
and A.C.G. Nutt
Presented at the 1984 I.E.E.E. International Workshop on
Integrated Optical and Related Technologies for Signal
Processing in the Materials and Fabrication Technology 1
Session, Florence, Italy, 10-11 September 1984

9) Characterisation of Proton Exchanged Slab Optical Waveguides
in X-cut LiNbO$_3$
K.K. Wong, A.C.G. Nutt, D.F. Clark, J. Winfield,
P.J.R. Laybourn and R.M. DeLaRue
To Be Published in I.E.E. Publication Part J, 1985

10) Fibre to Waveguide Coupling using Ion Milled Grooves in
Lithium Niobate at 1.3 Micron Wavelength
A.C.G. Nutt, J.P.G. Bristow, A. McDonach and P.J.R. Laybourn
Optics Letters Vol.9 No.10 pp463-465 October 1984

11) Strain and Surface Damage Induced by Proton-Exchange
in Y-cut LiNbO$_3$
A. Dawar, A.C.G.Nutt, S.M. Al-Shukri, R.M. DeLaRue,
M. Servidori, C. Summonte, C. Ferrari, A. Campari, G. Mazzi
Submitted to Journal of Materials Science

12) Locating and Coupling Fibres to Integrated Stripe Waveguides
P.J.R. Laybourn, A.C.G. Nutt, A. McDonach, J.P.G. Bristow
Workshop on Fibre Optic Gyroscopes and Monomode Optical
Components, Glasgow, 1-2 November 1984   Session 2

13) Experimental Observations of Light Propagation in Proton
Exchanged Lithium Niobate Waveguides
Alan C.G. Nutt
J. Opt. Comm., vol 6, No.1, pp 8-9, March 1985

14) Novel IntegratedOptical Polarisers using Surface Plasma
Waves and Ion Milled Grooves in Lithium Niobate
J.P.G. Bristow, A.C.G. Nutt, P.J.R. Laybourn
Electronics Lett., vol 20, No.25/26, pp1047-1048,
6th Dec 1984

15) Structural Characterisation of Proton Exchanged LiNbO$_3$
Optical Waveguides
A. Carnera, G. Della Mea, P. Mazzoldi, C. Canali,
A.C.G. Nutt and R.M. DeLaRue
Submitted to Journal of Applied Physics

16) Formation and Analysis of Tapers in Proton-Exchanged Lithium
Niobate
G. Stewart, A.C.G. Nutt
3rd E.C.I.O., pp58-61, Berlin(West), Germany, May 1985

17) Locating and Coupling Fibres to Integrated Stripe Waveguides
J.P.G. Bristow, P.J.R. Laybourn, A. McDonach and A.C.G. Nutt
Accepted for publication in I.E.E. Special Issue on
Components for Gyroscopes in Integrated Optics